The Dissertation Committee for Jung Heum Yeon Certifies that this is the approved version of the following dissertation:

Zero-Stress Temperature and Its Implications for Long-Term Performance of Continuously Reinforced Concrete Pavements

Committee:

David W. Fowler, Supervisor

Moon C. Won, Co-Supervisor

Kevin J. Folliard

Maria G. Juenger

Harovel G. Wheat

Zero-Stress Temperature and Its Implications for Long-Term Performance of Continuously Reinforced Concrete Pavements

by

Jung Heum Yeon, B.S.; M.S.E.

Dissertation

Presented to the Faculty of the Graduate School of

The University of Texas at Austin

in Partial Fulfillment

of the Requirements

for the Degree of

Doctor of Philosophy

The University of Texas at Austin
December 2011

Dedication

To My Family

Acknowledgements

First, I would like to express my most sincere gratitude to my supervisors Drs. David W. Fowler and Moon C. Won for their valuable support, guidance, and advice throughout my graduate years. This dissertation could not have been come to realization without their help. It’s the greatest fortune in my life to have them as my supervisors.

Also I would like to thank my dissertation committee members – Drs. Kevin J. Folliard, Maria G. Juenger, and Harovel G. Wheat – who provided me with great comments, guidance, and suggestions for my dissertation work.

My special thanks are extended to all former and current researchers at the Center for Transportation Research (CTR) – Drs. Dongho Kim, Chul Suh, Seongcheol Choi, Soojun Ha, and Byoung Hooi Choi – and Texas Tech University – Drs. Pangil Choi and Seongwoo Ryu. I cannot express in words how much I appreciate their help, advice, encouragement, and friendship.

The contribution from the staffs at CTR – Mr. John Ermis, Ms. Shannon Palmquist, Ms. Amy De La Rosa, and Mr. Adam Finley who is now living in Israel – and all Korean civil engineering graduate students at the University of Texas at Austin is deeply appreciated.

Finally, I owe my deepest and extreme gratitude to my father, mother, and brother for their unconditional love, support, and patience. This dissertation is dedicated to my family.

Jung Heum Yeon

November 2011

Zero-Stress Temperature and Its Implications for Long-Term Performance of Continuously Reinforced Concrete Pavements

Jung Heum Yeon, Ph.D.
The University of Texas at Austin, 2011

Supervisors: David W. Fowler and Moon C. Won

Continuously reinforced concrete pavement (CRCP) is a portland cement concrete (PCC) pavement structure with a continuous longitudinal steel layout. CRCP is forming a major portion of PCC roadway systems in the state of Texas due to its low life cycle cost, ease of maintenance, and durable nature. While the overall performance of CRCP is proven to be excellent, some performance problems are still found as a form of distresses such as punchout and spalling. The current pavement design guide states that these distresses are closely related with the early-age behavior characteristics of CRCP, and various measures are underway to develop to improve the long-term performance of CRCP in terms of initial material design and use, structural design, and quality control.

Understanding the current issues that pavement engineers and researchers face, the primary objective of this dissertation research focuses on sound understanding of the early-age structural behavior characteristics of CRCP and its effect on the long-term performance to provide reliable design and analysis criteria for CRCP. To achieve this main objective, characterizing the early-age structural response in CRCP was a core task of this study. For this purpose, a zero-stress temperature (ZST), one of the design and construction variables considered to have most significant effects on CRCP behavior and performance, was evaluated. As a beginning point of the entire framework, a series of field experiments were conducted in four new PCC pavement construction projects in the state of Texas to evaluate the actual structural response in early-age CRCP since a laboratory experiment would have a critical limitation in simulating the restraint conditions that exist in actual CRCP. To expand this core task to various parametric categories, a computer-aided parametric simulation was performed using valid numerical models. Based on data sets obtained from the parametric investigation, a statistical model to quantify the early-age structural response of CRCP was proposed to implement in codes of practice and pavement design guides.

A secondary task was to identify a correlation between the early-age structural response and the long-term performance of CRCP structures. Since the experimental and analytical investigations tended to provide quite localized information for the time-dependent behavior of CRCP, the overall performance of CRCP could not be properly identified solely based on those results. To overcome this limitation, extensive field condition surveys were performed in seven different old CRCP sections with known material and early-age temperature history to find the implications of early-age behavior characteristics on the long-term performance of CRCP from a macroscopic point of view.

It is expected that this research effort will provide pavement engineers and researchers with useful information to understand the actual time-dependent behavior of CRCP and a solid foundation to improve the sustainability of CRCP structures.

Table of Contents

List of Tables

List of Figures

Chapter 1: Introduction

1.1 BACKGROUND AND MOTIVATION

According to the Federal Highway Administration (FHWA), about 45,000 lane miles of interstate highways have been established to date and a great deal of new construction projects are in progress to provide a safe, comfortable, and economical method of transporting people and goods. Currently, about 60 % of the interstate highway systems were constructed with portland cement concrete (PCC) to ensure the durability and serviceability under harsh traffic and/or weather conditions. In recent decades, the use of PCC for pavement systems is showing an increasing trend nationally, and more and more reconstruction and new construction of PCC pavements are being required to meet the public demand.

Among several different types of PCC pavement, continuously reinforced concrete pavement (CRCP) is forming a major portion of PCC roadway systems in the state of Texas because of its advantages in life cycle cost and maintenance. The CRCP is a PCC pavement structure with a continuous longitudinal steel layout (Nam, 2005). In this type of PCC pavement system, no artificial saw-cut joints are used; rather it allows random non-structural transverse cracks, most of which typically take place within a few days after construction, to relieve the stresses due to variations in temperature and internal moisture. These transverse cracks are controlled by the longitudinal steel reinforcement generally placed at the mid-depth of CRCP slabs.

As a demand for better-performing and longer-lasting CRCP increases recently, it became essential to accurately characterize the behavior and structural responses of CRCP structures. Among the various elements influencing the behavior and structural response of CRCP, zero-stress temperature (ZST) has been receiving significant attention by researchers and practitioners in the past a few decades. According to the Mechanistic-Empirical Pavement Design Guide (MEPDG), one of the most recent pavement design guides developed through under National Cooperative Highway Research Program (NCHRP) 1-37A, the ZST is considered as one of the important input variables affecting the long-term performance of CRCP such as punchout and spalling distresses (ERES, 2004).

Figure 1.1 displays the result of a sensitivity analysis run by the MEPDG software, which indicates substantial effect of ZST on the number of punchouts. The result shows that the number of punchouts is quite sensitive to the ZST of early-age concrete; the higher ZST results in the more number of punchouts, whereas the lower ZST causes the less number of punchouts.

Although the ZST is believed to be an important indicator affecting the long-term performance of CRCP structures, little research effort has been made to propose a reasonable model to estimate ZST. Even in the MEPDG developed by NCHRP, one of the most advanced protocols for pavement designs, the ZST is quite simply estimated by two different parameters, i.e., cement content of the mixture and mean monthly temperature for the month of construction (ERES, 2004), while the thermal behavior and structural response of PCC pavement, particularly at early-age, involve the sophisticated interactions of numerous factors such as material properties, environmental effects, and geometric parameters.

With the sound understanding of the current issues that researchers, practitioners, and engineers are facing, the present research study is purposed to provide an enhanced model to predict ZST based on both experimental and computer-aided analytical approaches. Also, the extent of this doctoral research includes the validation work on how the early-age behavior characteristics affect the long-term performance of CRCP structures based on a series of field condition surveys because the actual impact of ZST on long-term performance of CRCP has been an open question to date.

It is expected that this research effort will provide adequate measures to improve the sustainability of CRCP structures, especially in terms of initial material and structural designs, and environmental conditions at the time of pavement construction.

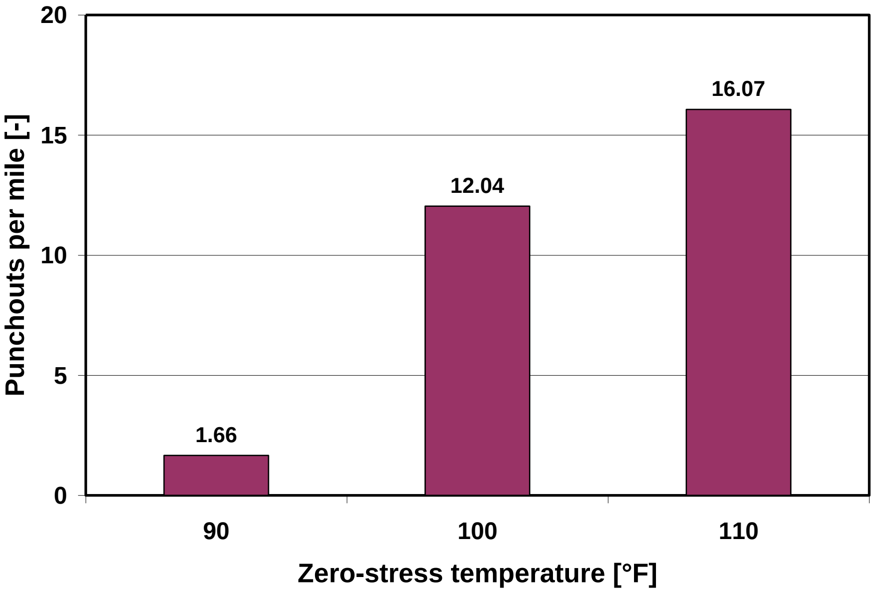

Figure 1.1: *Effect of ZST on punchouts estimated by MEPDG*

1.2 OBJECTIVES

As described previously, the NCHRP model is the most advanced and practical one currently available for the ZST prediction. However, there are several critical limitations tied to this model:

1) The model incorporates only two parameters to predict the ZST of early-age concrete – cementitious material content and mean monthly temperature for the month of construction – while diverse factors such as material properties, environmental conditions, and geometric parameters influence on the formation of ZST.

2) The model did not consider the ZST gradient along the PCC pavement slab depth that may exist due to temperature and moisture differentials. Also, the effect of ZST gradient through slab depth on the behavior and response of CRCP structures is not examined.

3) There is a lack of field evidences to prove that the ZST of early-age behavior characteristics affect the long-term performance of CRCP structures.

Based on the thorough literature review, primary improvements can be made in the following aspects:

1) Provide advanced experimental and computer-aided analytic techniques to accurately evaluate the restrained stress developments in CRCP as well as in typical concrete structures.

2) Develop an accurate and reasonable ZST predictive model which can be implemented in the codes of practice and pavement design guide.

3) Identify the effects of built-in curling (BIC) and the time-dependent CTE on the structural response of CRCP.

4) Investigate the effect of early-age behavior characteristics of CRCP on the long-term performance based on a series of field condition surveys.

1.3 SCOPE

The scope of this dissertation study primarily covers the characterization of early-age behavior of CRCP structures under environmental loading – early-age thermo-hygro-mechanical behavior – using both experimental and analytical methods. Also, the implications of early-age behavior characteristics of CRCP on the long-term performance are studied. An extensive review of past and current research studies in this area was carried out for collection of useful experimental data sets and their interpretation.

Based on the various outputs resulted from this study, ZST, an important indicator which may affect the early-age cracking tendency and the long-term performance of

CRCP, is primarily characterized. Since laboratory testing has critical limitations to simulate the actual CRCP behavior, the main part of the experimental program was performed in the field, with support from the Texas Department of Transportation (TxDOT). Based on the sound understanding of early-age behavior of CRCP, numerical models are developed and validated with the field data sets. Using the verified numerical models, a parametric study is conducted in accordance with a predetermined factorial experiment. The result obtained from the parametric study is statistically modeled to provide an efficient tool to predict ZST in early-age CRCP structures.

The extent of this doctoral research also includes the identification of pavement distress mechanisms and the assessment of the effects of early-age thermo-hygro-mechanical behavior on the long-term CRCP distresses based on extensive field condition surveys.

1.4 OVERALL RESEARCH SCHEME AND ORGANIZATION

This dissertation consists of a total of eleven chapters with different objectives. Discussions of overall CRCP behavior is provided in Chapter 2, and detailed literature review on early-age behavior characteristics of concrete structures is discussed in Chapter 3. The rest of the chapters are categorized into three main phases as illustrated in Figure 1.2.

In the first phase of this research study, an overall experimental program and data analysis methodology to evaluate the stress history of a concrete element is presented. In Chapter 4, the detailed information of a series of field experiments conducted in four different PCC pavement construction sections in the State of Texas are described: testing sites, material properties, and field instrumentation schemes. In Chapter 5, concrete stress histories for each field experimental project are evaluated based on the field measurements. Also, the stress evaluated with the proposed method is compared with the reference stress data measured by a stressemeter to validate the proposed experimental methodology. Furthermore, ZSTs for each project are found based on the evaluated stress histories and the results are compared with the ZSTs estimated by the current ZST predictive models. Chapter 6 investigates the time-dependent variation of coefficient of thermal expansion (CTE) in early-age concrete, which may affect the early-age stress development, in turn, the formation of ZST. In Chapter 7, the effect of creep and built-in curling which can influence the stress history of PCC pavement are examined based on the field measured data sets.

In the second phase of this study, numerical models to evaluate the temperature and corresponding stress histories of a concrete element are developed. The developed analytic model is validated with the experimental data presented in Phase I. Then, a parametric numerical simulation is conducted in terms of various parametric categories (Chapter 8). Once the parametric study is completed, an advanced ZST prediction model is proposed based on a multivariate regression analysis (Chapter 9).

In the third phase, a field condition survey is performed to investigate the effect of ZST on the behavior and long-term performance of CRCP. The field condition survey is carried out in the testing sections described in TxDOT Research Projects 1700-2 and 1244-3. Also, the field testing sections described in a study by Nam (2005) are used for the field condition survey. Since the test sections evaluated in these research projects have been in service for about 10 to 20 years, the data obtained from the field condition survey are expected to provide meaningful and important information to examine the actual impact of ZST on the behavior and long-term performance of CRCP structures. Chapter 10 summarizes the observations, findings, and implications obtained from the field condition surveys.

Finally, Chapter 11 describes overall conclusions made in this study and provides recommendations for further efforts.

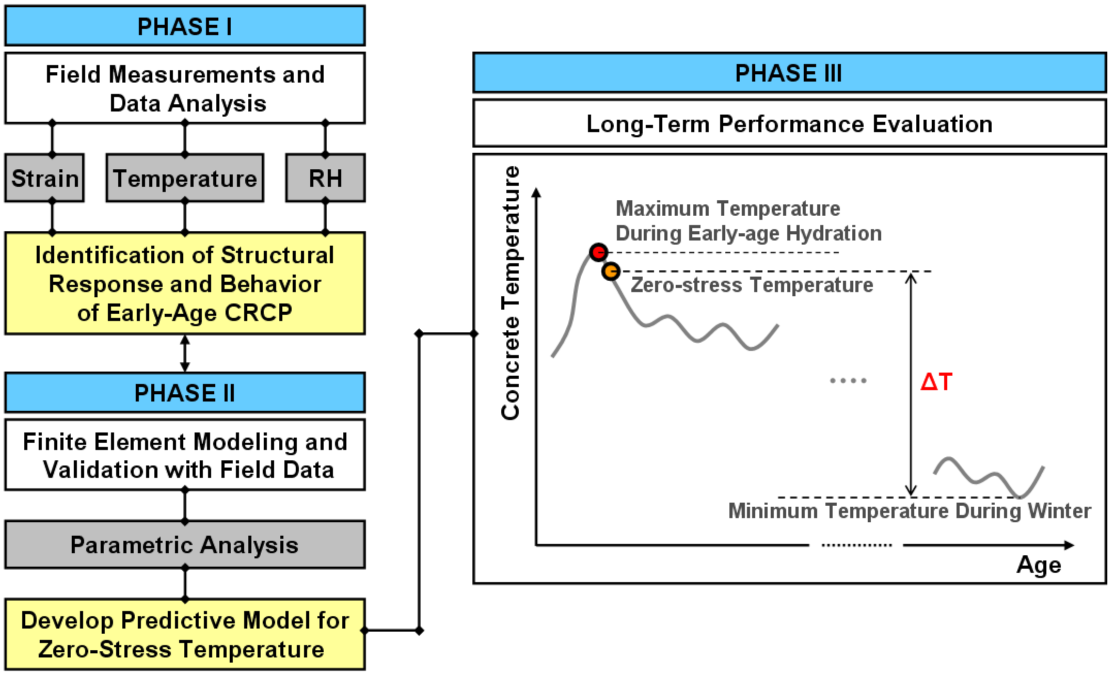

Figure 1.2: Overall structure of research

Chapter 2: Behavior of CRCP

2.1 EARLY-AGE BEHAVIOR

2.1.1 Early-Age Transverse Cracking

A CRCP structure experiences non-structural transverse cracking typically within a couple of days after concrete placement due to restrained volume changes caused by the variations in temperature and moisture. The timing of the transverse cracking depends on several factors such as concrete strength and modulus development, degree of restraint, which includes subbase friction and longitudinal reinforcement, and magnitude of temperature swing and drying shrinkage at early-ages. Previous research indicated that these non-structural cracks could be detrimental to the durability and performance of concrete structures because deleterious ingredients such as sulfate, acid, and salt can penetrate into hydrated cement matrix and steel reinforcement through the crack opening, which can lead to various types of deteriorations such as corrosion of reinforcement, sulfate attack, carbonation, and frost attack (Mehta and Monteiro, 2006; Mindess et al., 2003; Neville, 1996). However, rare cases of these deteriorations have been found in CRCP because longitudinal reinforcing bars in CRCP tend to keep these transverse cracks very tight. Figure 2.1 shows the typical early-age transverse cracking in CRCP.

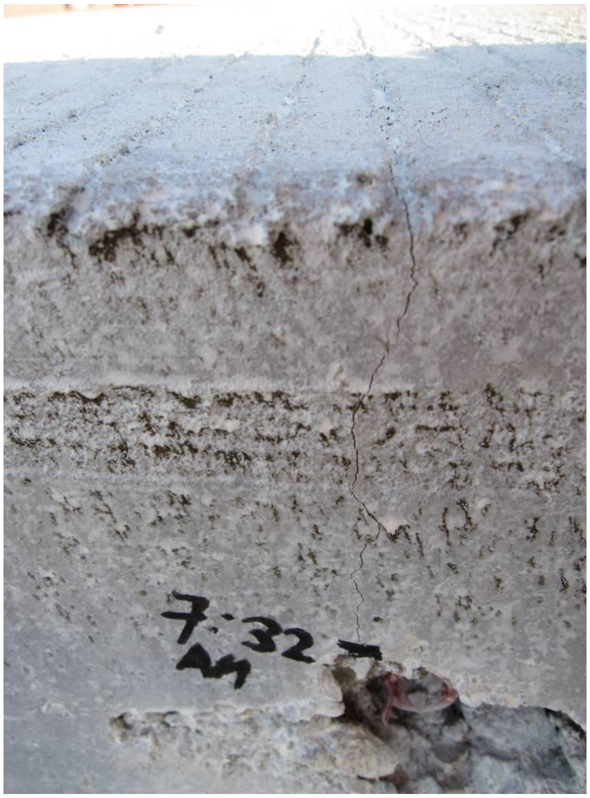

Figure 2.1: *Early-age transverse cracking in CRCP*

2.1.2 Field Observation of Early-Age Transverse Cracking in CRCP

In order to observe the early-age transverse cracking patterns in CRCP, a field survey was conducted in the 2,500–ft.-long newly constructed CRCP section of Brownfield Highway in Lubbock, Texas on August 23rd and 24th, 2009. Figures 2.2 and 2.3 show the overview of the surveyed section and survey scheme, respectively. As seen in Figure 2.3, the observation was conducted from northeast to southwest as the paver moved in that direction. Due to many field restrictions, only the last 1,000 ft. section placed between 6:30 am and noon on the 24th out of total 2,500 ft. was observed with naked eye.

Figure 2.2: *New CRCP construction section in Lubbock, Texas*

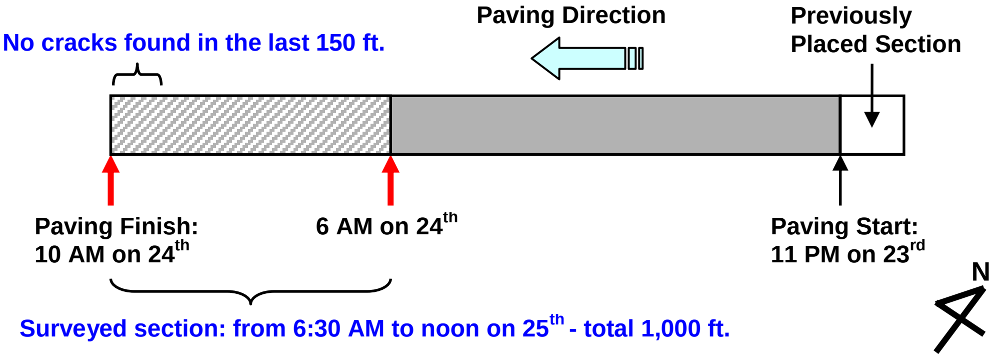

Figure 2.3: *Survey scheme*

Table 2.1 tabulated the result of the early-age transverse crack survey. The coordinate "zero" means the location where the crack survey started. The findings from the field cracking survey can be statistically summarized as follows:

- Total number of transverse cracks found: 64 (no cracks in the last 150 ft.)
- Mean transverse crack spacing: 13.52 ft.

- Standard deviation: 5.09 ft.
- Percentage of transverse cracks occurred around transverse steel: 73.4 % (47 out of 64)
- Percentage of full-depth transverse cracks: 60.9 % (39 out of 64)
- Percentage of transverse cracks closed at steel depth: 12.5 % (8 out of 64)

Table 2.1: *Transverse cracking survey result* (unit: in.)

Coord.	*Spacing*	*Coord.*	*Spacing*	*Coord.*	*Spacing*	*Coord.*	*Spacing*
32	108	2596	146	5295	105	7348	254
140	156	2742	143	5400	106	7602	182
296	100	2885	138	5506	115	7784	112
396	97	3023	154	5621	102	7896	106
493	189	3177	171	5723	148	8002	214
682	147	3348	195	5871	175	8216	142
829	105	3543	134	6046	118	8358	146
934	180	3677	143	6164	154	8504	288
1114	181	3820	181	6318	22	8792	358
1295	248	4001	180	6340	78	9150	130
1543	187	4181	178	6418	141	9280	158
1730	214	4359	141	6559	111	9438	137
1944	144	4500	149	6670	67	9575	325
2088	142	4649	140	6737	214	9900	192
2230	159	4789	155	6951	185	10092	163
2389	207	4944	351	7136	212	10255	-

It is interesting to note two primary survey findings. First, as indicated in Figure 2.3, no transverse crack was observed in the last 150 ft. section. This is probably because the frictional stress was small near the free edge due to the low degree of restraint. This fact also indicates that the contribution of curling and warping stresses was not as significant as to cause transverse cracking in the CRCP. The results from a number of previous field condition surveys conducted under TxDOT Research Project 0-6274 were consistent with this finding; no transverse cracks were found within about 40 ft. to 150 ft.

from the free edge. Second, the majority of transverse cracks, more than 70 %, took place around the transverse steel (or tie bars because tie bars are normally aligned together with transverse reinforcement). The reason for this is not completely understood; however, the following hypotheses can be drawn as the possible mechanisms: 1) the loss of cross-sectional area in concrete slab due to poor finishing quality around tie bars as shown in Figure 2.4 (a), and 2) the stress concentration around transverse steels due to elevated CTE of early-age concrete as presented in Figure 2.4 (b).

Figure 2.4 (a) shows the half-piece of tie bar inserted into concrete slab. It is seen that the slab has poor surface finishing quality around the tie bar. This is because the concrete surface near tie bars is typically cleaned with compressed air after the curing operation to accommodate a socket connection to another half piece of tie bar. During this operation, the fresh concrete around the tie bars loses some aggregates, eventually leading to the reduction of cross-sectional area in concrete slab at tie bar locations. This might make the majority of transverse cracks occur around the tie bars by locally increasing the stress level.

The very high CTE of early-age concrete might cause the majority of transverse cracks at transverse rebar locations. The top figure in Figure 2.4 (b) shows the variation of CTE in early-age concrete measured in the field using a non-stress device; the experimental program and result analysis will be discussed in detail in chapter 6 of this dissertation. It is noted that the CTE of concrete a few hours after setting is about twice as high as that of later-age concrete. Since the concrete CTE at this stage is much higher than the CTE of steel, transverse steel tends to restrain the contraction of surrounding concrete when the concrete temperature drops, which increases the stress level of the concrete near the transverse steels (bottom figure of Figure 2.4 (b)) This local stress increase in concrete around the transverse steel bars might affect the stress state in the concrete slab and might have led to approximately 70 % transverse cracks at transverse rebar locations.

(a) Poor finishing quality around tie bars

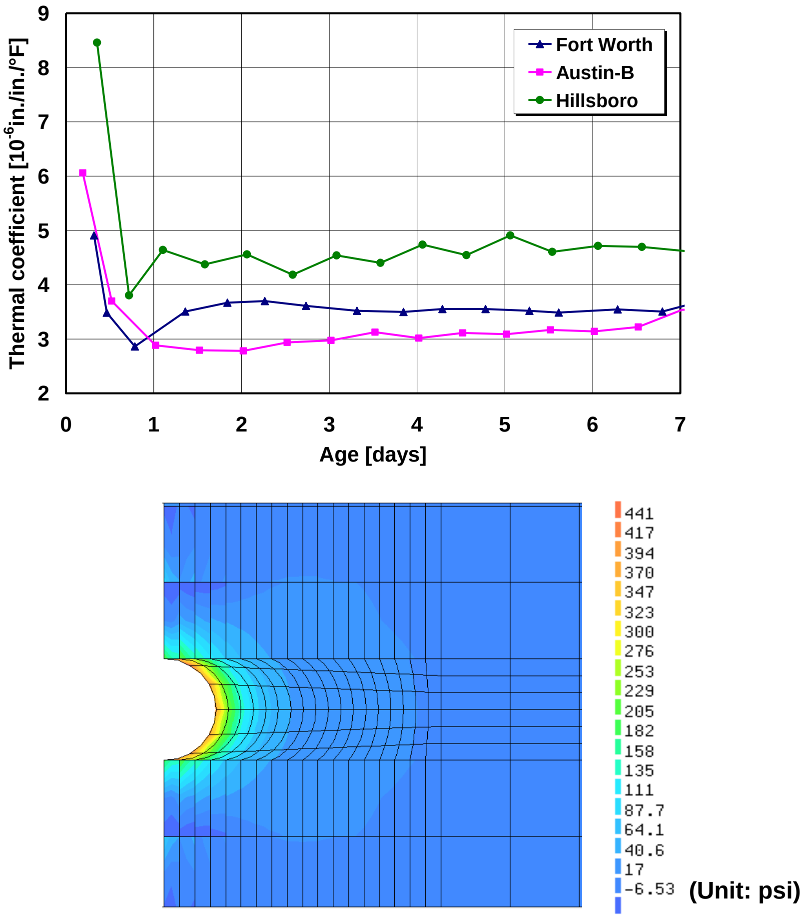

(b) Time-dependent CTE variation and its effect on stress state around transverse bars

Figure 2.4: *Possible early-age transverse cracking mechanisms in CRCP*

2.2 LATER-AGE BEHAVIOR

2.2.1 Horizontal Cracking

As CRCP gets older, later-age cracking starts to take place. One of the most noticeable phenomena in old CRCP is the occurrence of horizontal cracking at the steel depth. The reason for horizontal cracking is still an open question, but some possible causes were suggested by previous research studies (Choi et al., 2011; Kim and Won, 2004; Won et al., 2011). Figure 2.5 shows the clear evidences of horizontal cracking in CRCP structures.

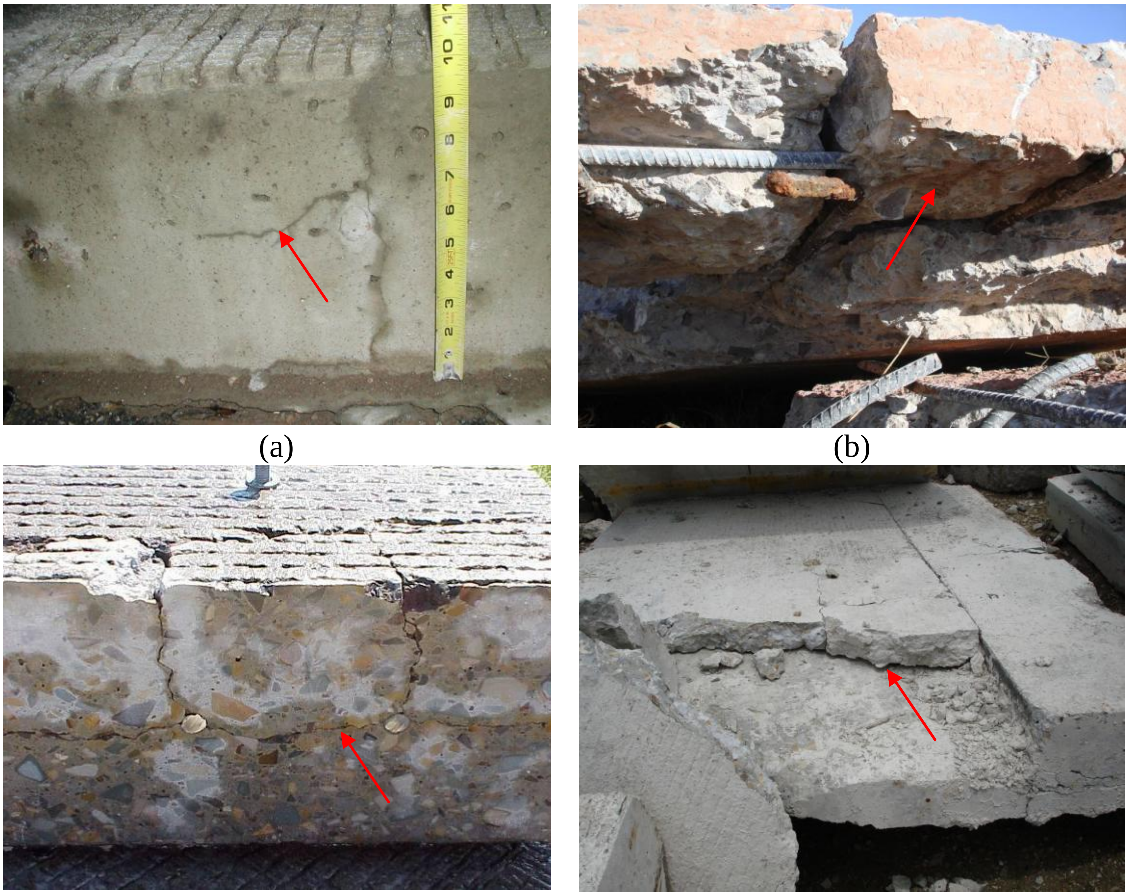

(a) (b)

(c) (d)

Figure 2.5: *Horizontal cracking in CRCP* (photo courtesy: Won)

In order to investigate the possible mechanisms of the horizontal cracking observed in the field, a numerical analysis was performed using DIANA v. 8.1.2 (TNO, 2003), a finite element analysis tool operating on the basis of displacement method. Figure 2.6 shows the two-dimensional finite element model of CRCP employed in this study (Kim and Won, 2004). Table 2.2 summarizes the default input values for geometric and material properties used in the numerical analysis.

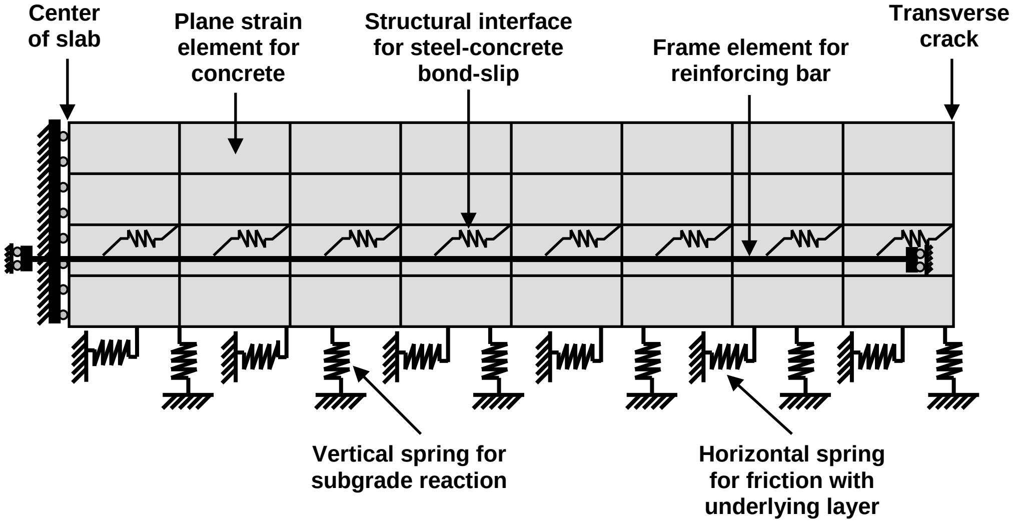

Figure 2.6: *Two-dimensional finite element model for CRCP*

Table 2.2: *Default inputs for geometric and material property used in numerical analysis*

Transverse crack spacing	10 ft.
Slab thickness	13 in.
Amount of steel	# 6 bar (0.75 in.)
Coefficient of thermal expansion of concrete	4 x 10^{-6} in./in./°F
Coefficient of thermal expansion of steel	6.5 x 10^{-6} in./in./°F
Modulus of elasticity of concrete	4 × 10^{6} psi
Modulus of elasticity of steel	29 × 10^{6} psi
Poisson’s ratio of concrete	0.20
Temperature loading	Top: -30 °F ; Bottom: 0 °F

Only a half of the slab and longitudinal reinforcing bar were modeled due to the symmetry of geometry and load condition. For mesh presentations of concrete and longitudinal reinforcement, the eight-node plane strain elements and two-node frame elements were used, respectively. The interfacial interactions at the different material boundaries were considered with the structural interface elements as indicated in the proposed finite element model. Figure 2.7 presents the steel-concrete bond stress-slip relationship, vertical subgrade reaction relationship, and concrete-subbase frictional stress-slip relationship used in the numerical analysis.

Boundary conditions were given to the finite element model based on the sound understanding of CRCP behavior under environmental loading. Since the CRCP section subjected to environmental loading experiences warping/curling behaviors in the mirror image with respect to the mid-slab, vertical degrees of freedom along the mid-slab were released. The CRCP behavior at the transverse crack interface can be affected by the vertical stiffness due to aggregate interlock. However, the aggregate interlock effect was ignored in this study because there will be no vertical relative movement at the transverse crack interface as long as the modeled section is subjected to the environmental loading which is uniformly distributed along the longitudinal direction. To model the vertical reaction from the underlying layers, tensionless springs were installed in the vertical direction along the nodes at the slab bottom surface.

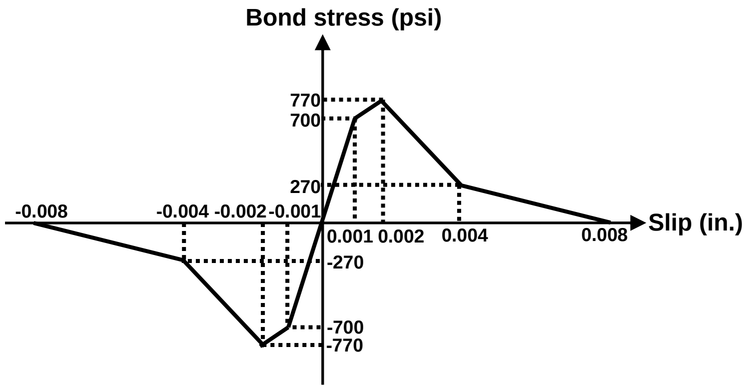

(a) Steel-concrete bond stress-slip relation

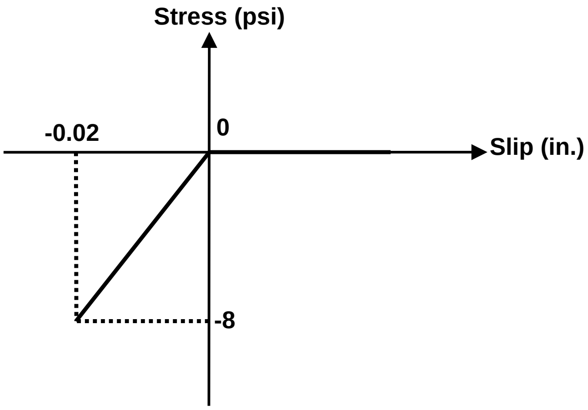

(b) Subgrade reaction relation

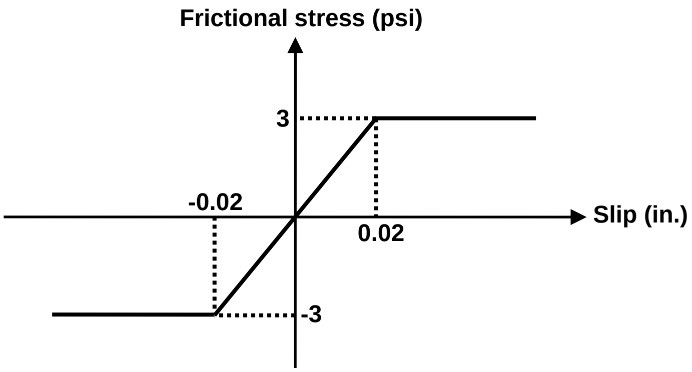

(c) Concrete-subgrade frictional stress-slip relation

Figure 2.7: *Bond-slip, subgrade reaction, and friction-slip relations of CRCP*

Figure 2.8 shows the result obtained from the numerical analysis. As can be seen in the principal stress contour, a significant level of stress occurred in the vicinity of longitudinal steel near crack interface. The directional vector for this stress component was nearly perpendicular to the longitudinal steel layout. This appears to be due to the curing-up movement being restrained by the flexural rigidity of the longitudinal steel (Choi et al., 2011). This restraining behavior raises the vertical stress level in concrete, which may ultimately lead to the initiation of horizontal cracking. It is interesting to note that the estimated results from the numerical analysis showed favorable agreement with the field evidence shown in Figure 2.5 (a).

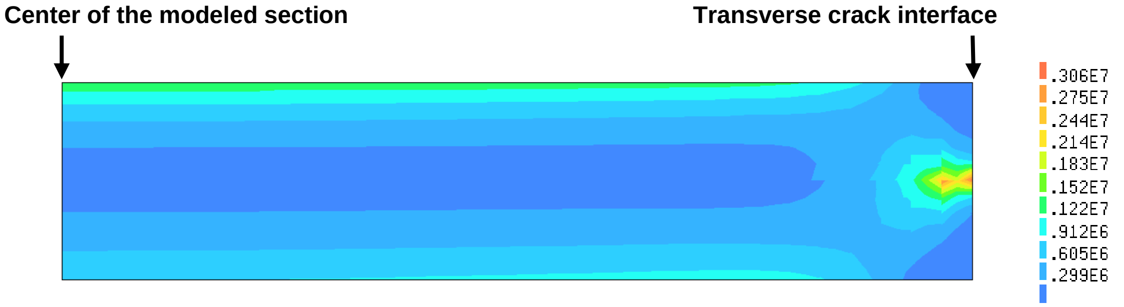

(a) Contour of Principal Stress

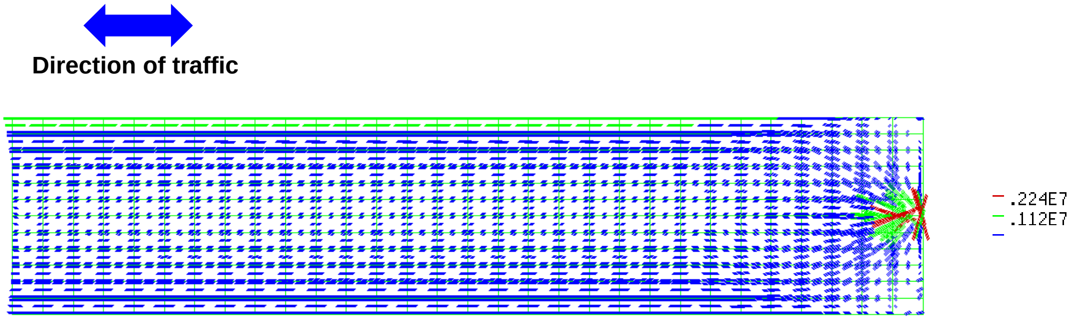

(b) Directional Vector of Principal Stress

Figure 2.8: *Results of two-dimensional finite element analysis for CRCP*

2.2.2 Later-Age Longitudinal and Transverse Cracking

Along with the horizontal cracking, longitudinal cracking occurs as CRCP continues to experience environmental and traffic loadings. Many previous field condition surveys revealed that longitudinal cracks occur along the embedded longitudinal steels. Based on the observation, it might be explained that the interaction between concrete and longitudinal steel due to the environmental loading and wheel loading applications appear to play a critical role in longitudinal crack development. Figure 2.9 illustrates the longitudinal cracking in progress in CRCP.

Figure 2.9: *Longitudinal cracking in progress*

Other than the horizontal and longitudinal cracking, later-age transverse cracks also occur between early-age transverse cracks. It is postulated that the later-age transverse cracking is due to continued increase in concrete modulus and drying shrinkage and wheel loading applications.

2.2.3 Partial-Depth Punchout Distresses in CRCP

The continued propagation of horizontal cracking, longitudinal cracking, and later-age transverse cracking leaves a concrete piece isolated from the slab (Figure 2.10). Under further repetitive traffic loading thereafter, the isolated concrete piece becomes loose and disintegrated as shown in Figure 2.11, ultimately resulting in partial-depth punchout distresses, which could compromise the overall serviceability and durability of CRCP.

(a) (b)

Figure 2.10: *Partial-depth punchout distress in progress* (photo courtesy: Won)

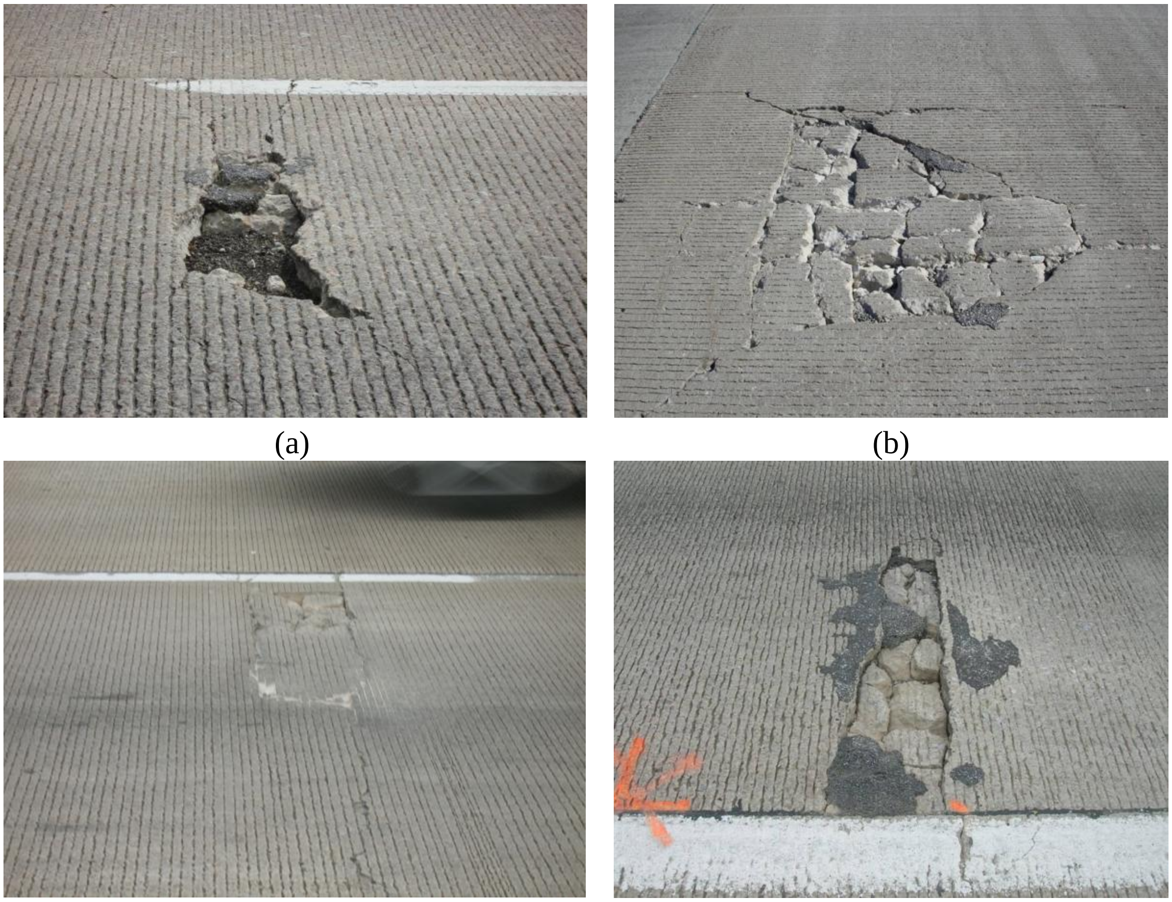

(a) (b)

(c) (d)

Figure 2.11: *Partial-depth punchout distress* (photo courtesy: Won)

Figure 2.12 was taken during the partial-depth punchout repair conducted on US-290 east bound near Hempstead, Texas. In this CRCP section, the ruptured concrete pieces caused by paritial-depth punchout were removed using jackhammers for repair. As expected, there was horizontal cracking at the steel depth, which provides the proof that the horizontal cracking plays a crucial role in partial-depth punchout distresses in CRCP.

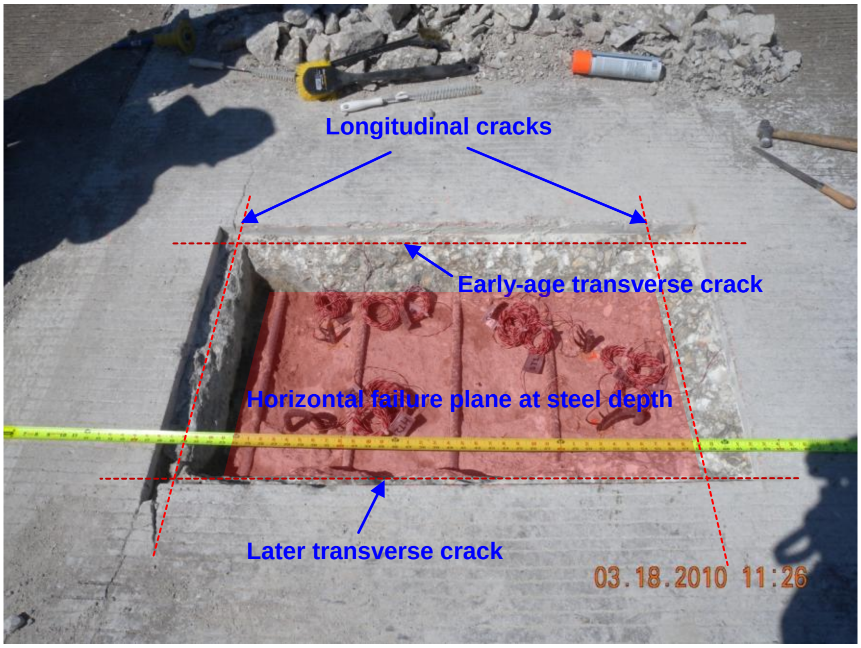

Figure 2.12: *Repair of partial depth punchout in CRCP*

2.3 EFFECT OF MAGNITUDE OF TEMPERATURE LOADING ON PUNCHOUT POTENTIAL

To examine the effect of magnitude of temperature loading on the punchout potential, an additional numerical analysis was conducted using the proposed finite element model in Figure 2.6. Figure 2.13 shows the loading cases for the numerical analysis. The reference temperature (which is comparable to ZST) was changed from 80 °F to 110 °F while the concrete temperature was fixed as 50 °F at the top and 80 °F at the bottom. Figure 2.14 displays the variations in principal stress distribution and directional vector when the loading cases 1 to 7 were imposed to the developed numerical model.

It indicates that as the magnitude of temperature loading (the difference between reference and in-situ concrete temperature) increases, the maximum stress point moves farther from the transverse crack interface. Also, it is observed that the directional vector of the principal stress becomes more perpendicular to the longitudinal axis as the magnitude of temperature loading increase. These findings indicate that the potential of punchout might increase as the difference between ZST and in-situ concrete temperature.

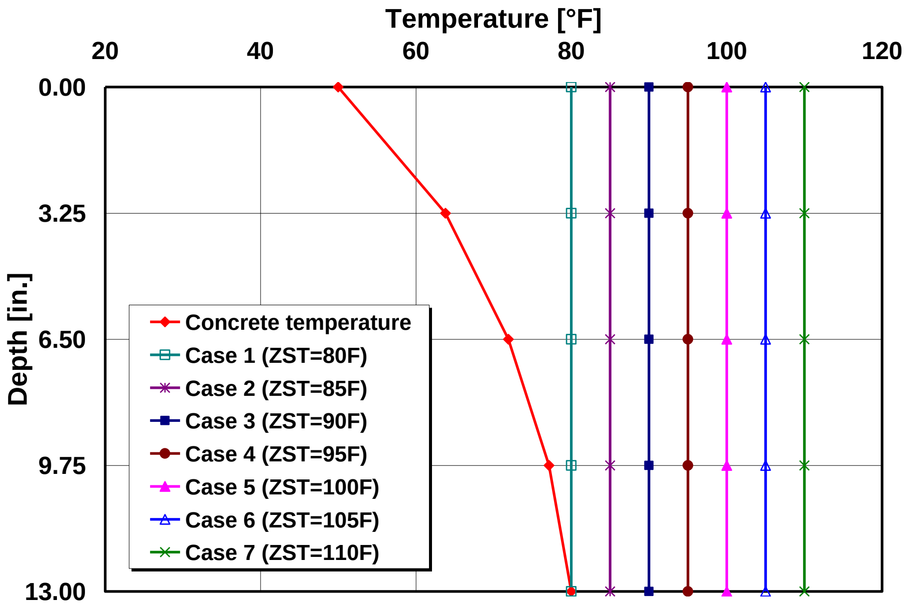

Figure 2.13: *Temperature loading conditions*

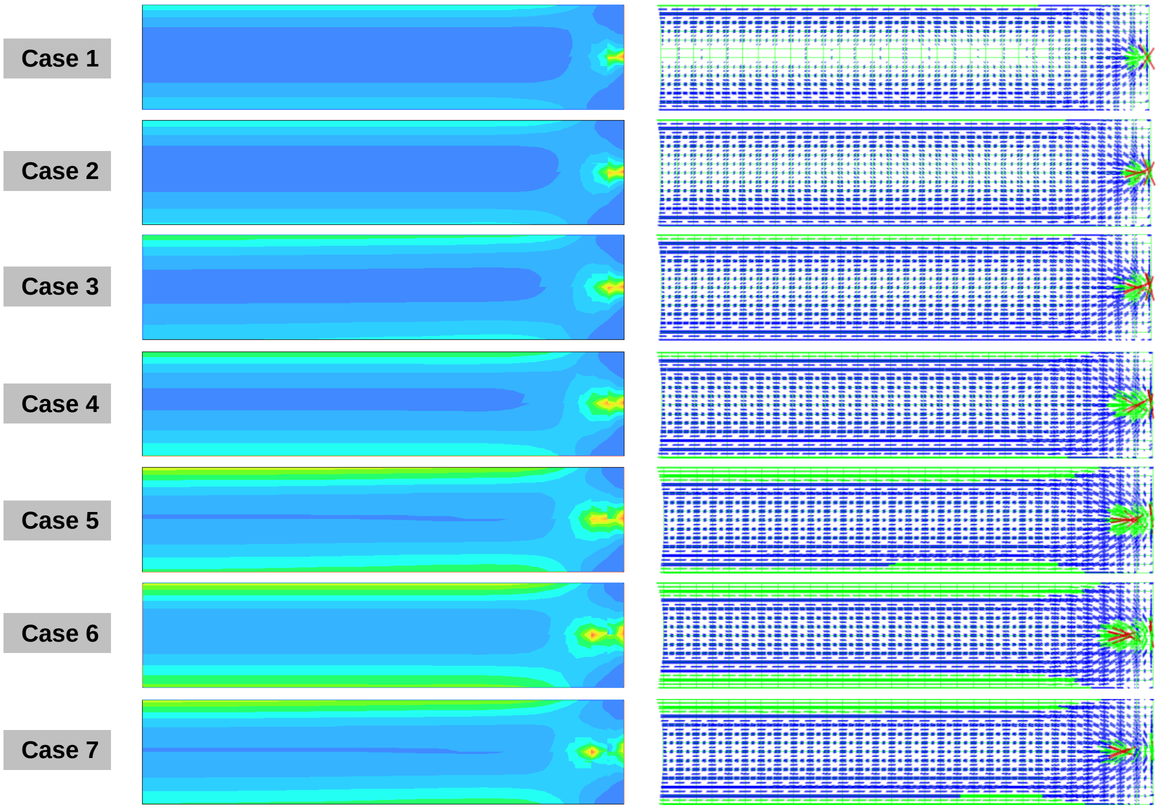

Figure 2.14: *Variations of principal stress state and directional vector*

2.4 SUMMARY

In this chapter, a time-dependent behavior of continuously-reinforced concrete pavement (CRCP) was overviewed along with numerous field evidences. It was identified that CRCP typically experiences the following behavior sequences:

1. Early-age transverse cracks develop to relieve the early-age concrete stresses caused by restraint thermal and hygral volume changes.

2. Horizontal cracking initiates from the transverse crack interface at the steel depth. This behavior appears to be caused primarily by curling resulted from the temperature variations through the concrete slab. On further traffic loading, the horizontal cracks can continue to propagate.

3. Due to the continued incompatible interaction between longitudinal reinforcement and surrounding concrete, later-age longitudinal cracks begin to take place along the longitudinal steel. Also, later-age transverse cracks occur somewhere between previous transverse cracks.

4. The continued propagation of horizontal cracking, longitudinal cracking, and later-age transverse cracking leaves a concrete piece isolated from the slab.

5. Under further repetitive traffic loading thereafter, the isolated concrete pieces are ruptured, ultimately resulting in partial-depth punchout distresses.

Chapter 3: Literature Review

3.1 ZERO-STRESS TEMPERATURE IN HARDENING CONCRETE

3.1.1 Definition of Zero-Stress Temperature

As portland cement hydrates, a significant amount heat is released at early ages. This heat release causes volume expansion in a concrete element. If this volume expansion is restrained internally and/or externally, the induced thermal strain will be converted to compressive stress in proportion to the modulus, coefficient of thermal expansion, temperature variation, and degree of restraint of the concrete element. As the generated heat dissipates to ambient, the initial compression will start to be relieved and then reach the stress-free state. This is called a zero-stress point and the temperature corresponding to this point is a “zero-stress temperature (ZST)” (Breitenbücher, 1990; Nam, 2005; Springenschmid and Breitenbücher, 1998).

Figure 3.1 illustrates the typical temperature and stress developments in early age concretes. Herein, T_s, T_{max}, and T_z refer to the final setting temperature, maximum temperature, and ZST, respectively. As the concrete temperature reduces below the ZST, tensile stress begins to develop in concrete. On further cooling, when the tensile stress exceeds the tensile strength of the concrete, cracking will occur.

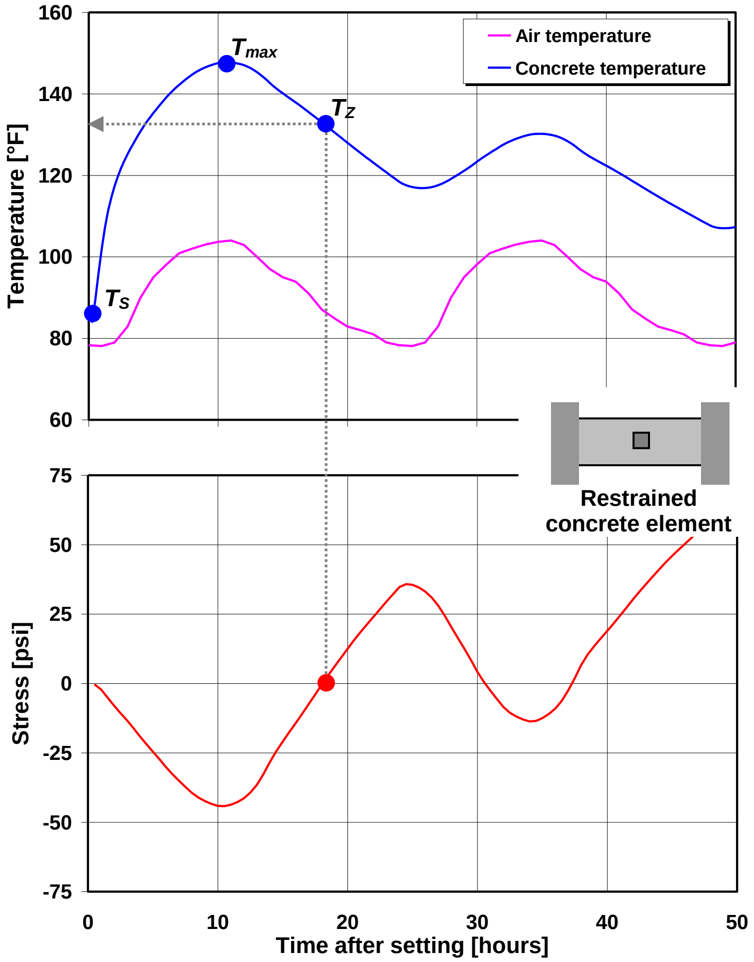

Figure 3.1*: Schematic description of zero-stress temperature*

3.1.2 Implication of ZST in CRCP

It has been suggested by previous research studies that ZST may have substantial effects on the behavior and performance of CRCP.

First, the ZST affects the transverse cracking potential of early-age CRCP (Breitenbücher, 1990; ERES, 2004; Schindler, 2002; Springenschmid and Breitenbücher, 1998). The CRCP with a high ZST will have a high potential of early-age transverse cracking because the instantaneous tensile stress intensity in concrete is proportional to the temperature drop from the ZST. Conversely, when the CRCP has a low ZST, the CRCP will be less sensitive to the early-age transverse cracking.

Second, the ZST may affect the reinforcement design of CRCP (Schinder, 2002). This is because the design amount of steel of CRCP needs to be based on the expected tensile stress level in concrete. If a high ZST is expected during the design stage of CRCP, the amount of steel reinforcement may need to be increased to keep the transverse cracks tight.

Third, the ZST may affect the post-cracking behavior of CRCP such as crack width and load transfer efficiency (LTE). The MEPDG developed under NCHRP 1-37A derived the following mathematical model to predict the transverse crack width due to thermal and drying shrinkage effects (ERES, 2004).

$$cw = Max\left(L \cdot \left(\varepsilon_{sh} + \alpha_{PCC} \Delta T_{\zeta} - \frac{c_2 f_{\sigma}}{E_{PCC}} \right) \cdot 1000 \cdot CC,\ 0.001 \right) \qquad \text{(Eq. 3.1)}$$

where, *cw* is the average crack width at the depth of the steel, mils; *L* is the cracking spacing based on design crack distribution, in.; ε_{shr} is the unrestrained concrete drying shrinkage at the depth of the steel, x10^{-6}; α_{PCC} is the PCC coefficient of thermal expansion, /°F; ΔT_{ζ} is the drop in PCC temperature from the concrete "zero-stress" temperature at the steep depth for each season, °F; c_2 is the second bond stress coefficient; f_{σ} is the maximum longitudinal tensile stress E_{PCC} is the PCC elastic modulus, psi; and *CC* is the local calibration constant (*CC* = 1 for the national calibration).

The above crack width prediction model indicates that the higher ZST leads to the wider crack opening when all other variables are fixed because the contribution of thermal contraction to crack width is proportional to the temperature drop from the ZST. If the crack width becomes larger, according to the conventional punchout distress mechanisms described by NCHRP, the LTE across transverse cracks in CRCP may be reduced as it loses aggregate interlock. As a result of the degraded aggregate interlock at the transverse crack interface, the CRCP can be more prone to suffer from punchout distresses under the repetitive traffic loading thereafter (Figures 3.2 and 3.3).

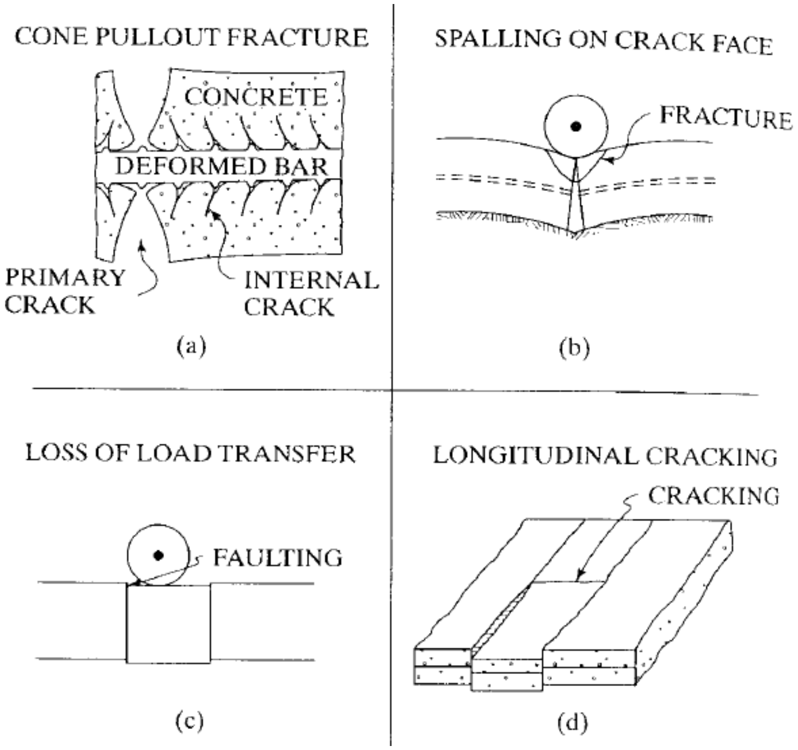

Figure 3.2*: Failure procedures leading to punchout distress* (Huang, 1993)

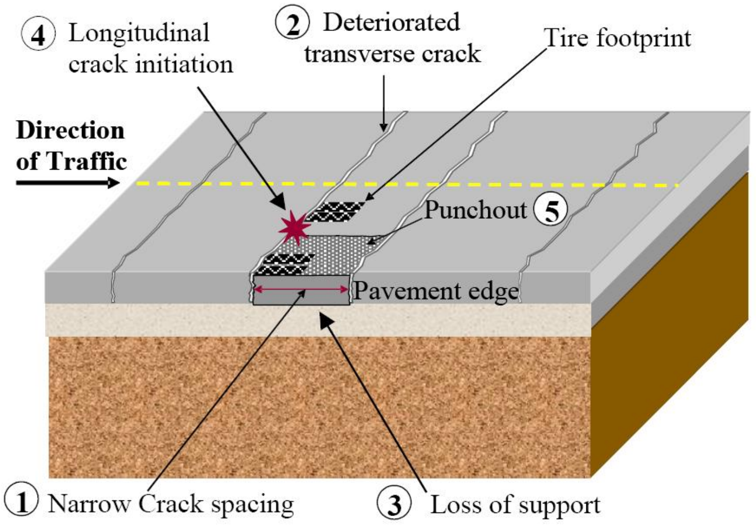

Figure 3.3*: Failure procedures leading to punchout distress* (ERES, 2004)

Lastly, the ZST may influence the residual stress field of later-age concrete. Figure 3.4 shows the unusual but maybe a prevalent case of post-cracking behavior of CRCP. At the right side of the figure (not shown in the figure), the inner lane, the top portion across the longitudinal construction joint, was cut along the transverse direction and the slab segment was completely removed for full-depth repair. Upon removal of the slab segment, the inner lane expanded as much as three and half inches and, caused the bending of retrofitted tie bars as clearly shown in the figure. This behavior may be associated with the concrete's ZST; for instance, in the case of winter placement concrete which has a low ZST, the concrete may be in high compression during hot summer and the significant expansion of CRCP may occur when the slab segment is removed in order to relieve the compressive stress that has existed in the section.

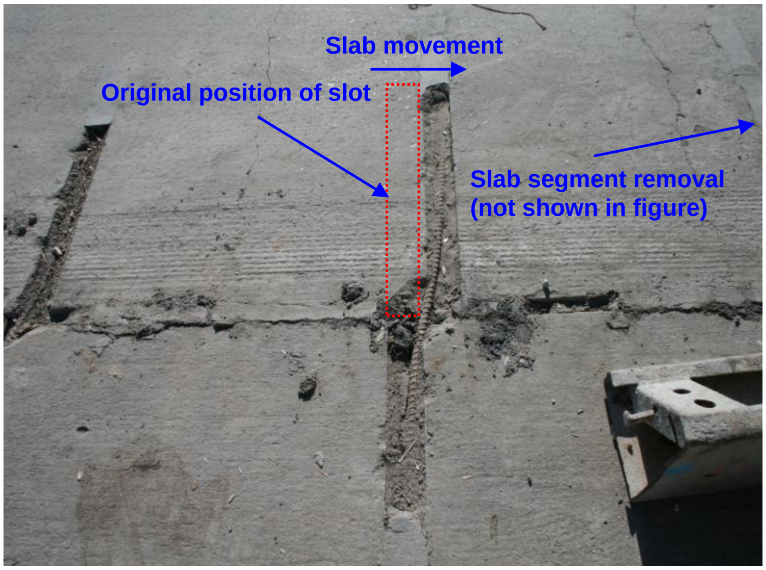

Figure 3.4: *Slab expansion in CRCP* (photo courtesy: Won)

3.1.3 Existing Zero-Stress Temperature Predictive Models

3.1.3.1 NCHRP Model

The MEPDG developed under NCHRP 1-37A suggested the following mathematical model to estimate the ZST in PCC pavements (ERES, 2004). This model was derived based on the enthalpy for hydrating concrete assuming zero heat loss through thermal boundaries (Zollinger, 2011). The function for heat of hydration was based on the data found by Neville (Neville, 1999).

$$T_z = (CC \times 0.59328 \times H \times 0.5 \times 1000 \times 1.8 / (1.1 \times 2400) + MMT) \qquad \text{(Eq. 3.2)}$$

where, T_z is the temperature at which the PCC layer exhibits zero thermal stress (allowable range: 60 to 120 °F), °F; CC is the cementitious content, lb/yd^3; H = -0.0787+0.007×MMT-0.00003×MMT^2; and MMT is the mean monthly temperature for month of construction, F°.

3.1.3.2 Schindler's Model

In Schinder's study (2002), the relationship between ZST and maximum concrete temperature was quantitatively characterized by R_d, the maximum temperature reduction ratio to obtain ZST, based on early-age temperature and stress analyses:

$$R_d = \frac{T_{max} - T_z}{T_{max}} \qquad \text{(Eq. 3.3)}$$

where, R_d is the T_{max} reduction ratio to obtain T_z; T_{max} is the maximum temperature of in-place concrete at early ages, °F; and T_z is the zero-stress temperature, °F.

The results showed that the average R_d for all variable categories were 6 % to 8 %, which indicates that the ZST are, on average, 92 % to 94 % of the maximum concrete temperature.

3.1.3.3 Bernander's Model

Bernander (2004) suggested the following ZST prediction model based on the strain related method. This approach is valid only when an element is subjected to the external restraint, and temperature loading is uniform within the cross-section of a member.

$$T_z = T_{\max} - \frac{\alpha_e}{\alpha_c}(T_{\max} - T_c)(1 - k_0) \qquad \text{(Eq. 3.4)}$$

where, T_z is the zero-stress temperature; T_{max} is the maximum temperature; T_c is the placing temperature; α_e and α_c are the coefficient of thermal expansion and contraction respectively; and k_0 is the ratio of non-elastic strain to total strain during compression phase, $\varepsilon_v / \varepsilon_{tot}$.

3.2 RESTRAINED STRESS DEVELOPMENT IN EARLY-AGE CONCRETE

Cast-in-place concrete experiences significant volume changes especially at early-age due to variations in temperature and internal relative humidity (RH) (Springenschmid 1995; Springenschmid, 1998). In cement-based materials with a low water-to-cementitious ratio such as high-performance concrete (HPC) and ultra high-performance concrete (UHPC), additional volume changes can occur because of self-desiccation (Tazawa, 1999). If these volume changes are internally and/or externally restrained, surface microcracking and visible macrocracking can take place in concrete structures (Springenschmid, 1995; Springenschmid, 1998). These cracks could be detrimental to the durability and performance of concrete structures because deleterious ingredients such as sulfate, acid, and salt can penetrate into hydrated cement matrix and steel reinforcement through the crack opening, which can lead to various types of deteriorations such as corrosion of reinforcement, sulfate attack, carbonation, and frost attack (Mehta, 2006).

3.2.1 Factors Affecting Early-Age Restrained Stress Developments

Many previous research studies revealed that there are three major components that influence early-age cracking in concrete structures: thermal effect, drying shrinkage effect, and autogenous shrinkage effect. All these effects involve the volume changes in concrete and stresses can occur when these volume changes are externally and/or internally restrained.

Figure 3.5 illustrates the overall relationship among the factors affecting the early-age restrained stress development.

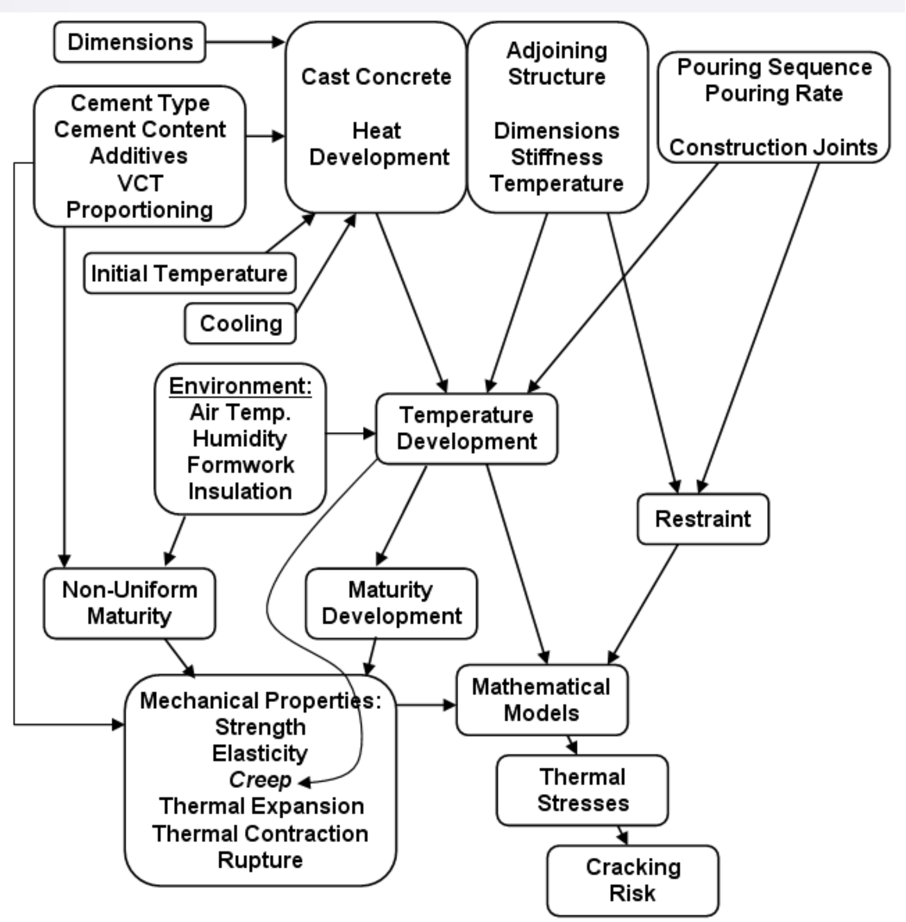

***Figure 3.5**: Overall relationship among the factors affecting the early-age restrained stress development* (Bernander, 1994)

3.2.1.1 Restraints

When a concrete slab interacts with the surround environment, thermal and moisture gradients over the cross-section can occur. These thermal and moisture gradients cause deformations in the slab, and stresses can arise when these deformations are restrained. Figure 3.6 shows the decomposition of a nonlinear strain component into three different strain components: axial, curing, and self-equilibrium (or nonlinear) strains (Ghali et al., 2002). Among these components, the axial and curling strain components are associated with an external restraint while the self-equilibrium component is concerned with an internal restraint.

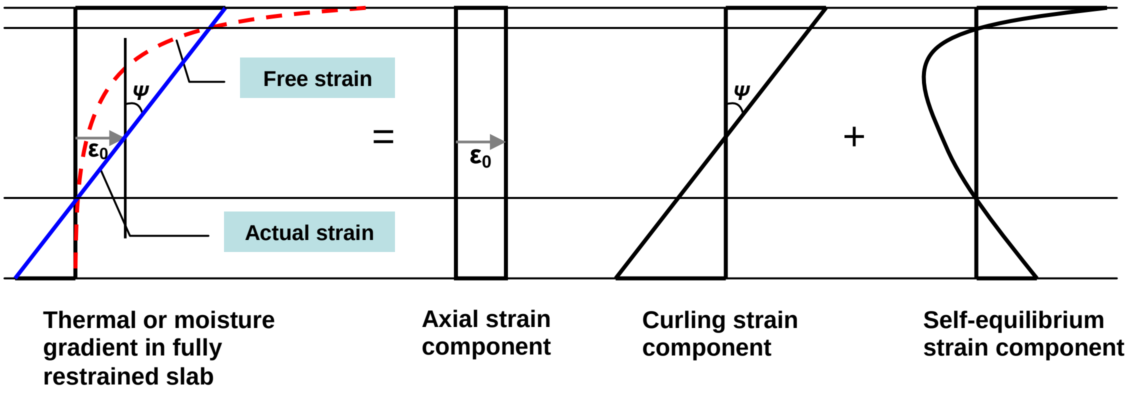

***Figure 3.6**: Decomposition of nonlinear gradients*

The external restraint is the component that is not self-equilibrating and mainly arises when the deformations are hindered by external boundaries such as adjacent existing concrete elements, friction from underlying layer, and self-weight. Figure 3.7 illustrates the typical axial resilient restraint condition in the slab.

***Figure 3.7**: Axial resilient restraint*

The internal restraint, on the other hand, is not related to the external boundaries but the nonlinear gradients of temperature and RH over the cross-section. This implies that stresses can occur, because of the nonlinear gradients, even in the completely unrestrained concrete structures. The self-equilibrium component comes from the Bernoulli’s plane assumption, which is typically made for concrete structure design and analysis. The Bernoulli assumption explains that the plane of concrete member remains the plane after the deformation. As shown in Figure 3.6, the nonlinear temperature or RH gradient induces the discrepancy between the actual strain and free strain, and this component results in self-equilibrium stresses.

Figures 3.8 (a) and (b), respectively, show the stress states in a concrete slab caused by full external and internal restraints when the temperature gradient seen in Figure 3.6 was imposed. Most of typical concrete structures subjected environmental loadings have both external and internal restraints, and the total restrained stresses are, in general, expressed by the sum of the stresses due to external restraint and internal restraint (Rostácy et al., 1998).

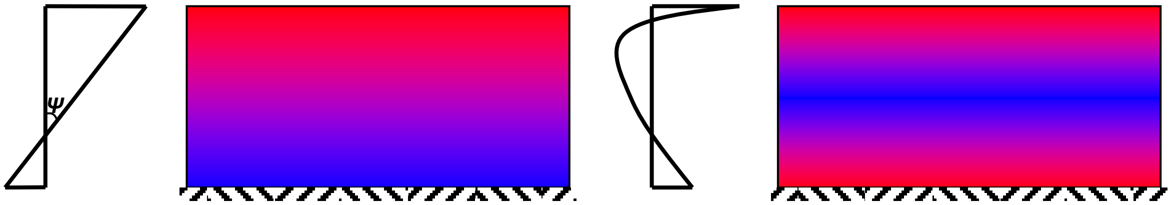

(a) Stress state due to external restraint (b) Stress state due to internal restraint

Figure 3.8*: Stress state due to external and internal restraints*

In order to convert the strain to stress, estimating degree of restraint is of utmost importance because the level of stress linearly depends on the degree of restraint. The degree of restraint of a concrete element can be defined as follows (Choi and Won, 2010):

$$R_i = 1 - \frac{\Delta\varepsilon_i}{\Delta\varepsilon_i^{\,f}} \qquad \text{(Eq. 3.5)}$$

where, R_i is the degree of restraint [-]; $\Delta\varepsilon_i^f$ is the variation of strain of unrestrained concrete; and $\Delta\varepsilon_i$ is the variation of strain of concrete under restraint.

3.2.1.2 Thermal Effect

Among the factors causing volume changes in concrete – thermal, drying, and autogenous shrinkage –, the thermal strain is believed to be dominant in determination of the early-age cracking tendency in normal concrete structures. This is because concrete experiences significant thermal fluctuations at early-age due to liberation of hydration heat and its dissipation, along with rapid material stiffness development (Breitenbücher, 1990; Emborg 1989; Springenschmid 1995; Springenschmid, 1998). Figure 3.9 shows the typical evolutions of temperature and thermal stress in early-age concretes. As can be seen in the figure, cracking may take place within the first a few days after concrete placement solely due to thermal stress.

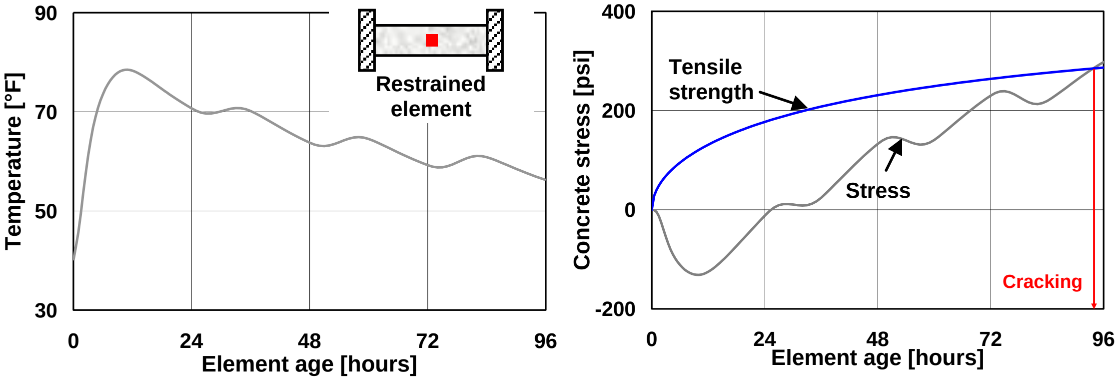

Figure 3.9*: Typical early-age temperature and thermal stress developments*

Also, the thermal effect may affect the post-cracking behavior of concrete structures since a cracked concrete member subjected to successive daily temperature variations undergoes incompatible interaction at the interface between steel reinforcement and surrounding concrete as examined in the previous chapter as well as in the former research efforts (Kim and Won, 2004; Choi et al., 2011).

3.2.1.2.1 Heat of hydration

The four major compounds of portland cement, i.e., C_3S, C_2S, C_3A, and C_4AF, are in a high-energy state and release a significant amount of energy in the form of heat to obtain a low-energy state when they hydrate. Figure 3.10 presents the typical rate of heat generation of portland cement during its early-age hydration period.

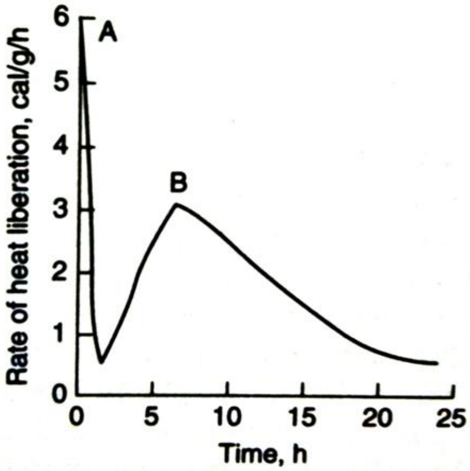

Figure 3.10: *Heat liberation rate of portland cement during early-age hydration,* Mehta (2006)

As can be seen, a very rapid heat generation arises in the first a few minutes of hydration, followed by the second peak in a few hours after that. This indicates that a substantial amount of heat could be liberated during the early-age hydration of portland cement, causing a rapid temperature increase in concrete. It is reported that about 50 to 70 % of the potential heat is generated in the first 3 to 7 days of hydration (Mehta, 2006). The heat of hydration is affected by various factors such as chemical composition of cement, initial concrete temperature, curing temperature, use of SCMs, water-cement ratio, and fineness of cement.

3.2.1.2.2 Coefficient of Thermal Expansion

When a material is subjected to temperature variations, it experiences volume changes, which depends on the magnitude of temperature change and the unique CTE of the material. Their linear relation can be mathematically expressed as follow:

$$\Delta\varepsilon_i^T = \alpha_T \Delta T_i \tag{Eq. 3.6}$$

where, $\Delta\varepsilon_i^T$ is the increment of thermal strain, 10^{-6} in./in.; α_T is the coefficient of thermal expansion, 10^{-6} in./in,/˚F; and ΔT_i is the magnitude of temperature variation, ˚F.

For a realistic prediction of time-dependent behavior of concrete structures under temperature loading, characterizing the CTE is of great importance since the instantaneous stress build-up due to the thermal volume change is in proportion to the CTE of concrete. Previous research studies have described that the CTE of cement-based material can be influenced by several factors.

Grasley and Lange (2007), Meyers (1950), Sellevold and Bjøntegaard (2006), and Yeon et al. (2009) examined the effect of internal RH on the CTE of cement paste and concrete. The results are presented in Figure 3.11. The findings from these studies were nearly consistent in that the maximum CTE occurs around 70% RH, which well coincided with the former research performed by Bažant (1970); the effect of RH on thermal expansion is primarily due to the hygrothermic dilation mechanism in pore structures and it reaches maximum approximately at 70 % RH.

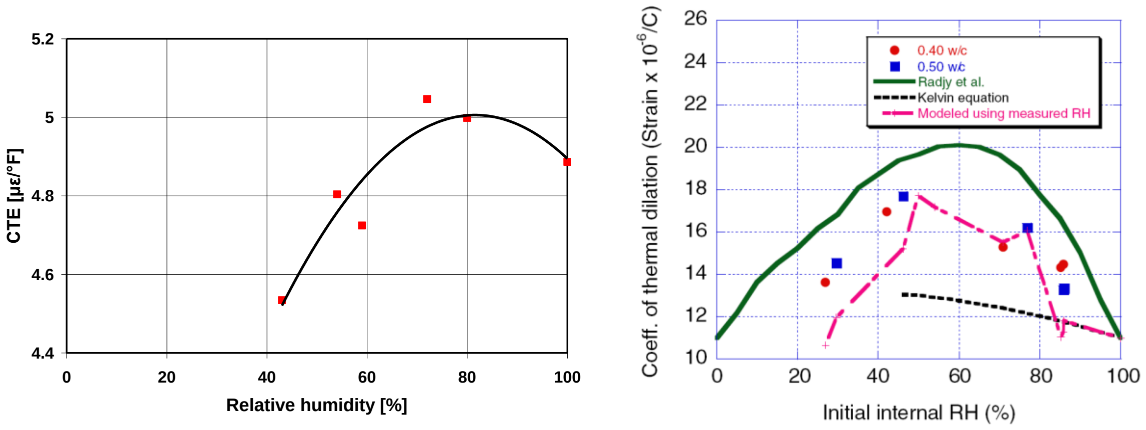

(a) Results from Yeon et al. (2009) (L) and Grasley and Lange (2007) (R)

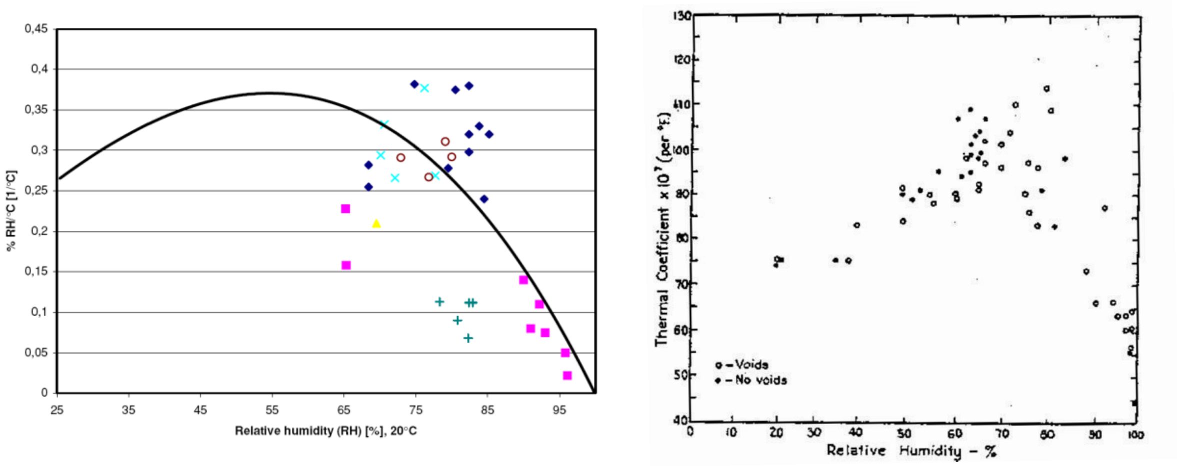

(b) Results from Sellevold and Bjontegaard (2006) (L) and Meyers (1950) (R)

_Figure 3.11__: Effect of RH on CTE in cement-based materials (Note: ℉=1.8× ℃+32)_

The works by Bjøntegaard and Sellevold (2001), Choktaweekarn and Tangtermsirikul (2009), Cusson and Hoogeveen (2007), Kada et al. (2002), Loser et al. (2010), Maruyama and Teramoto (2011), Richardson et al. (2010), and Wittmann and Lukas (1974) showed the strong dependency of CTE on the age of cement-based materials. The results from these studies agreed that the CTE considerably varies within the first a few hours after the final setting, but the trends were contrary to each other; Kada et al. (2002) and Loser et al. (2010) indicated that the CTE at the time of setting was greater than that in the later stage while the other researchers' findings showed that the CTE at the setting time is minimum and the CTE keeps increasing over time thereafter. Figure 3.12 shows the results from the previous research studies.

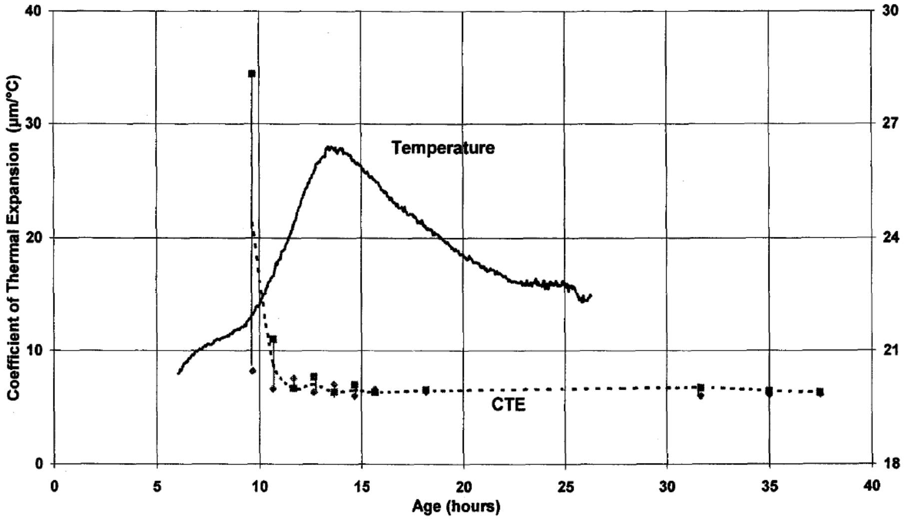

(a) Result from Kada et al. (2002)

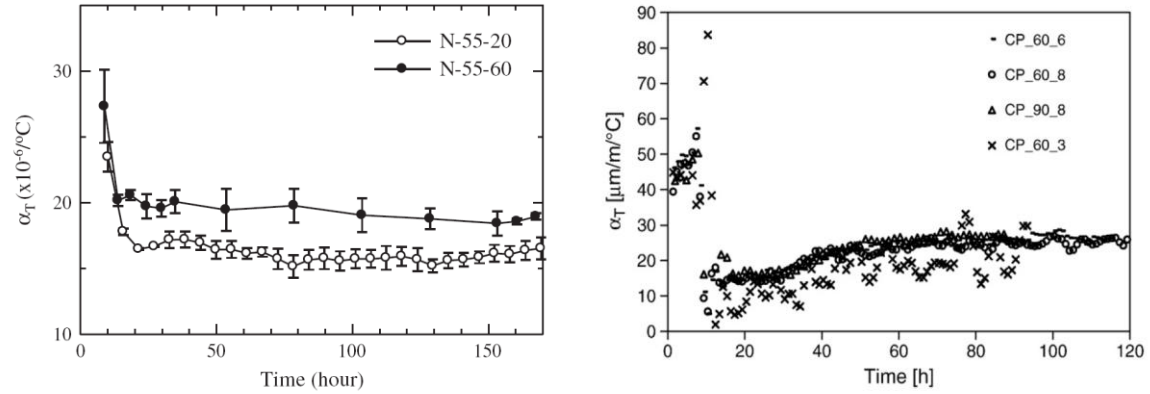

(b) Result from Maruyama and Teramoto (2011)

(c) Result from Loser et al. (2010)

Figure 3.12*: Time-dependent variation of CTE in cement-based materials*
(Note: ℉=1.8× ℃+32)

Emborg (1989), Helmuth (1961), and Wittmann and Lukas (1974) discovered the definite hysteresis loop in temperature-strain curve between heating and cooling paths. This phenomenon may be explained by the contribution of delayed thermal deformation caused by variations in moisture distribution during and after the temperature changes

(Bažant 1970; Helmuth 1961; Sabri and Illston 1982; Scherer 2000; Sellevold and Bjøntegaard 2006).

Also, it is reported that the CTE of hardened cement paste depends on the temperature (Wittmann and Lukas, 1974). The experimental result indicated that the CTE had a minimum value around the freezing point. Yang et al. (2003) stated that the shape of a specimen and the type of a measurement device could affect the CTE of concrete. Their findings showed that the CTE of a prismatic specimen was about 19 % to 23 % higher than that of a cylindrical specimen. Moreover, about 19 % difference in CTE was observed depending on the type of a measurement device even though the same shape of a specimen was used in the testing. The possible cause of the difference in CTE appears to be due to the difference in stiffness of the used measurement devices.

3.2.1.3 Drying Shrinkage Effect

3.2.1.3.1 Mechanism of Drying Shrinkage

When portland cement hydrates, several different types of hydration products are created and the leftover water is trapped in the various sized pores inside concrete: micro, meso, and macropores. It is understood that drying shrinkage occurs when concrete loses this moisture absorbed in the pores through diffusion and evaporation.

Figure 3.13 shows the schematic of drying shrinkage mechanism. As presented in the figure, the leftover water after initial rapid hydration is absorbed among the interconnected hydrated particles. This pore fluid is under capillary tension due to inter-molecular attractive forces, which causes a contraction force among the hydrated particles. The typical hydrated cement system has such configuration continuously in serial, and the compressive forces – as the counter action to the capillary forces – are applied to each hydrated solid particle, resulting in shrinkage in the system.

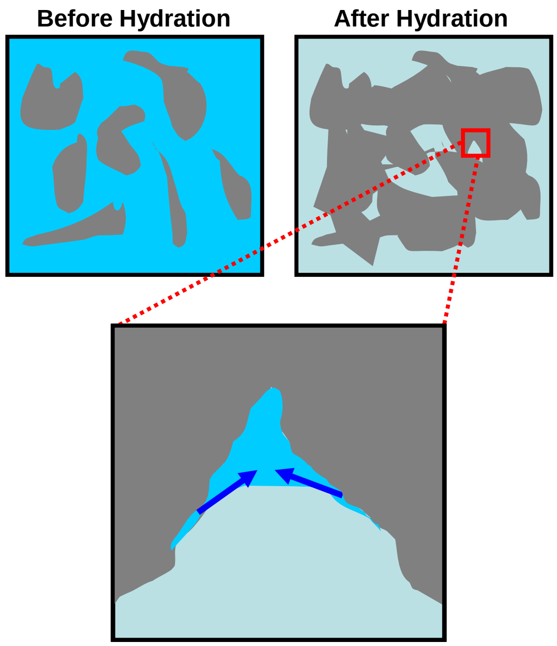

(a) Conceptual presentation of hydration products and absorbed water

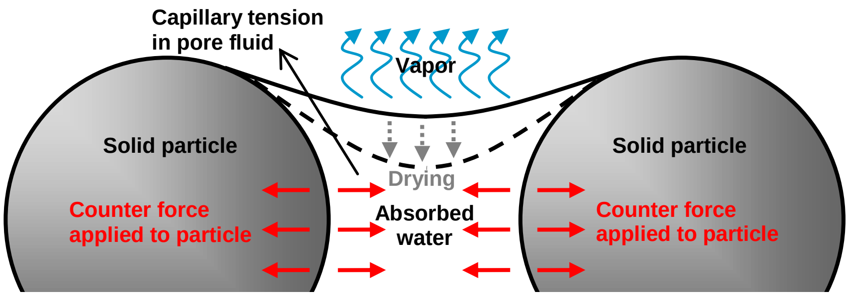

(b) Mechanism of drying shrinkage

Figure 3.13*: Drying shrinkage mechanism*

3.2.1.3.2 Internal RH in Cement-Based Materials

As internal RH is an indicator describing the moisture level of the vapor in the closed system, the RH in the pores is determined by capillary water, absorbed water, and vapor when they are in thermodynamic equilibrium state. The correlation among these terms can be presented by the following differential equation (Bažant and Najjar, 1972):

$$dRH = k\,dw + \kappa\,dT + dH_s \qquad \text{(Eq. 3.7)}$$

where, k is the inverse slope of desorption isotherm $(\partial RH / \partial w)$; w is the mass of water; κ is the hygrothermic coefficient $(\partial RH / \partial T)$; T is the absolute temperature; and H_s is the decrease in RH due to hydration.

The first term indicates the effect of direct moisture movements on the RH changes caused by absorption and desorption process, and the second term presents the temperature-related influence causing RH change (hygrothermic effect in a porous system). The last term stands for the impact of self-desiccation on the RH reduction.

3.2.1.3.3 Mathematical Modeling of Drying Shrinkage

As concrete continues to lose internal moisture, a negative pressure arises in the pore water. This can be expressed using the Laplace equation as follows:

$$p' = \frac{2\gamma}{r} \qquad \text{(Eq. 3.8)}$$

where, p' is the pore pressure of fluid; γ is the surface tension of the pore fluid; and r is the average radius of meniscus curvature.

To correlate the pore fluid and internal RH, the following Kelvin equation can be employed:

$$\frac{2\gamma}{r} = \frac{-\ln(RH)RT}{v'} \qquad \text{(Eq. 3.9)}$$

where, RH is the relative humidity; R is the universal gas constant; T is temperature; and v' is the molar volume of water.

By combining Eqs. 3.8 and 3.9, the Kelvin-Laplace equation, which gives a correlation between pore fluid pressure and RH, is derived as follows:

$$p' = \frac{-\ln(RH)RT}{v'} \qquad \text{(Eq. 3.10)}$$

To relate this pore fluid pressure to the drying shrinkage strain, the following mathematical model can be used (Mackenzie, 1949). To this model to be valid, two basic assumptions should be made: 1) the system is linear elastic, 2) the shape of the pore structure is completely spherical, and 3) the porous system is fully saturated.

$$\varepsilon^S = \Delta p\left[\frac{1}{3k} - \frac{1}{k_s}\right] \qquad \text{(Eq. 3.11)}$$

where, ε^S is the linear shrinkage strain; Δp is the pore pressure; k is the bulk modulus of the porous solid; and k_s is the bulk modulus of the skeleton of the material.

Since Eq. 3.11 is only valid for the fully saturated porous system, a saturation factor term can be added to the equation to make it valid for the partially saturated porous system as well. Then, Eq. 3.11 can be rewritten as follows:

$$\varepsilon^S = \Delta p S\left[\frac{1}{3k} - \frac{1}{k_s}\right] \qquad \text{(Eq. 3.12)}$$

Herein, the saturation factor S can be approximated with the measured RH level (Grasley and Lange, 2007).

3.2.1.3.4 Experimental Method

The drying shrinkage strain also can be modeled using the relationship between the magnitude of internal RH change and the hygral shrinkage coefficient of concrete:

$$\Delta\varepsilon_i^{sh} = \alpha_{sh}(t)\Delta h_i \tag{Eq. 3.13}$$

where, $\Delta\varepsilon_i^{sh}$ is the increment of free drying shrinkage strain, 10^{-6} in./in.; $\alpha_{sh}(t)$ is the hygral shrinkage coefficient at time *t*, 10^{-6} in./in.; and Δh_i is the magnitude of RH change.

As the hygral coefficient indicates the drying shrinkage strain per unit RH changes, laboratory experimental methods to determine the hygral shrinkage coefficient in bulk scale was proposed (Choi and Won, 2010; Grasley and Lange, 2004). In their testing for hygral shrinkage coefficient determination, 2-in.× 2-in. prismatic concrete specimens were used. If this specimen is in the symmetric drying condition, the RH gradient along the depth will be also symmetric with respect to the centerline. The corresponding drying shrinkage strain will remain in the same plane as it moves in accordance with the sectional average RH as indicated Figure 3.14. The slope of the curve between the sectional average RH and the corresponding shrinkage strain was defined as a hygral shrinkage coefficient.

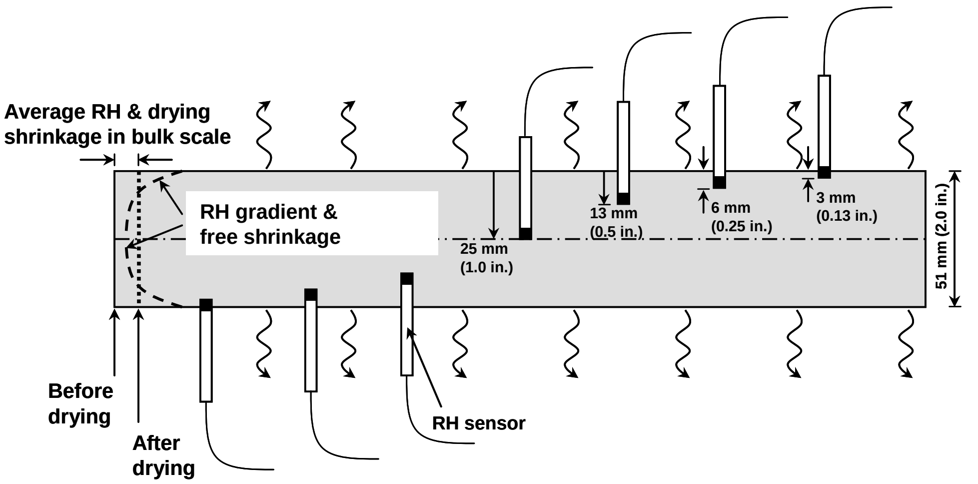

Figure 3.14: *Schematic of prism specimen equipped with RH sensor* (Choi, 2010)

3.2.1.4 Autogenous Shrinkage Effect

Autogenous shrinkage is defined as the apparent volume reduction of cement-based materials occurring when portland cement hydrates after initial setting (Tazawa, 1999). Especially in high-performance concrete which typically has a lower water-cement ratio and incorporates supplementary cementitious materials such as silica fume, the autogenous shrinkage can be highly pronounced. It is well recognized that the autogenous shrinkage arises from self-desiccation; the leftover water trapped in the pores after initial setting is consumed for further hydration of unhydrates existing in the hydrated cement matrix, which increases the capillary tension as drying shrinkage does.

The autogenous shrinkage includes the volume reduction due to cement hydration; the hydration of general portland cement inevitably results in volume-reduction because the volume of products is always lower than the volume of hydration reactants. The volume changes due to temperature variation, moisture loss due to diffusion and evaporation, and external restraint are not included in the extent of autogenous shrinkage. The autogenous shrinkage is different from the chemical shrinkage in that it does not include the volume portion of cumulated voids in the system; the autogenous shrinkage is the apparent volume reduction while the chemical shrinkage is the absolute volume reduction as illustrated in Figure 3.15.

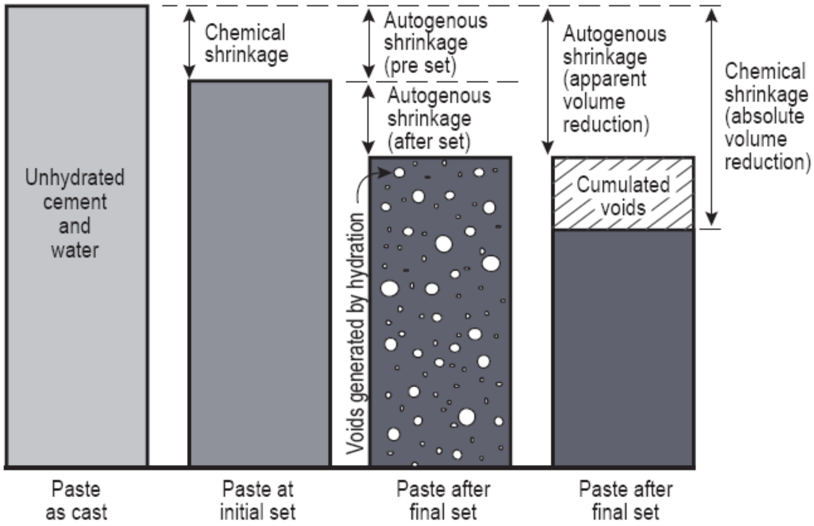

Figure 3.15: *Chemical and autogenous shrinkage volume change of fresh and hardened cement paste* (Kosmatka et al.,2002)

As shown in Figure 3.16, the volume reductions due to autogenous shrinkage and chemical shrinkage were almost identical until the initial setting. This is because the cement paste system has few pores before the initial setting. However, the volume reduction due to chemical shrinkage exceeds that due to autogenous shrinkage after the initial setting. The reason for this is that, as mentioned in the above, the autogenous shrinkage only includes the apparent volume reduction of the system, which does not consider the creation of pore voids inside the system.

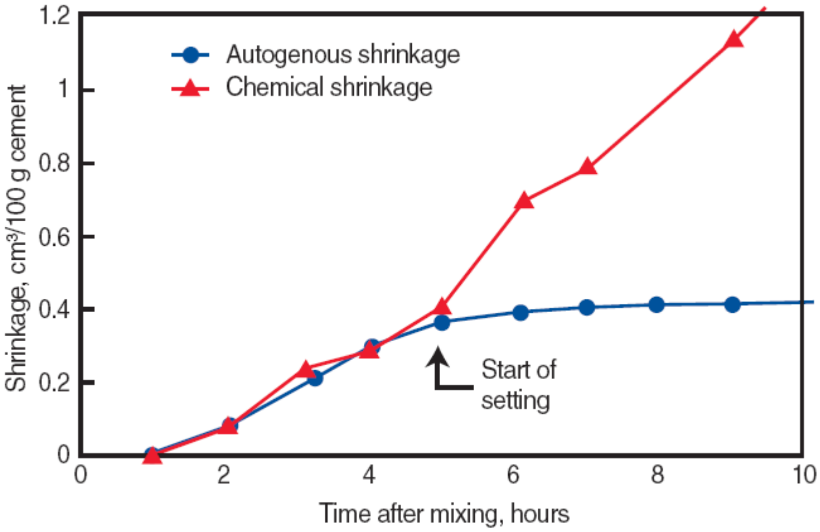

Figure 3.16: *Relationship between chemical and autogenous shrinkage at early ag e cement paste* (Kosmatka et al.,2002)

3.2.1.4.1 Experimental Method

The autogenous shrinkage can be experimentally measured in both linear and volumetric scales. Figure 3.17 illustrates the test setup that is typically used for linear autogenous deformation measurements (Tazawa, 1999). A Polytetrafluoroethylene (PTFE) film and polystyrene sheets are placed in the mold to minimize the restraint from the mold which is rigid, and polyester films are attached onto the PTFE film and polystyrene sheets to reduce the friction from the surroundings. It is quite important that the specimen is completely sealed to prevent the moisture loss during the testing. Also, the testing should be conducted in the controlled temperature to minimize the temperature effect on the length change.

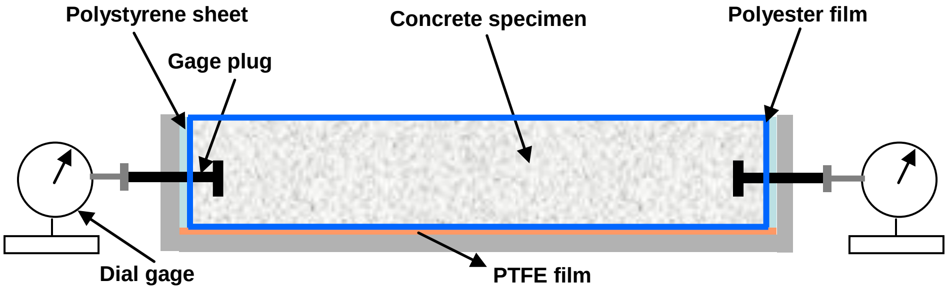

Figure 3.17: *Autogenous shrinkage measurement (linear method)*

The autogenous shrinkage in cement paste can be measured using the volumetric method (Sant et al., 2006). Figure 3.18 illustrates the testing setup for the volumetric method.

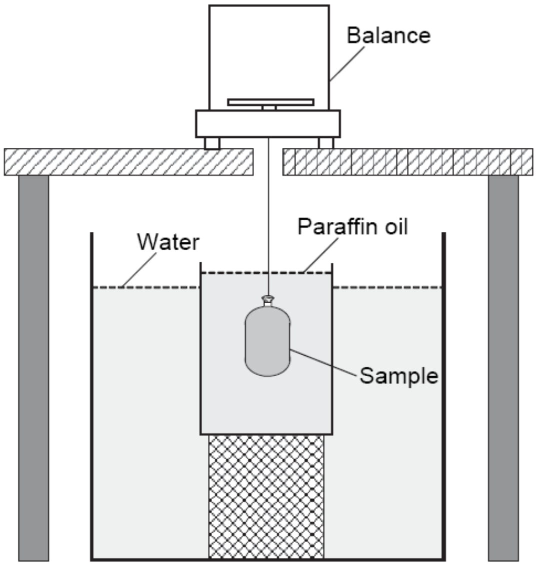

Figure 3.18: *Autogenous shrinkage measurement (volumetric method)* (Sant et al.,2006)

This testing procedure employs the sample sealed with a latex membrane. The sample is submerged into the paraffin oil, and the submerged weight of the sample is continuously measured. The volumetric strain can be computed using the following equations:

$$\varepsilon_{vol} = \frac{\Delta V_{paste}(t)}{V_{paste}(30)} = \frac{W_{sub}(t) - W_{sub}(30)}{\rho_{par} \cdot V_{paste}(30)} \qquad \text{(Eq. 3.14)}$$

where, $\Delta V_{paste}(t)$ is the volume change of the paste at time t; $V_{paste}(30)$ is the initial volume of the paste; $W_{sub}(t)$ is the submerged weight of the paste at time t; $W_{sub}(30)$ is the initial submerged weight of the paste 30 min. after water addition ; and ρ_{par} is the density of the paraffin oil in the buoyancy bath.

The linear strain can be determined with Eq. 3.15, assuming that the material is completely isotropic:

$$\varepsilon_{lin} = \frac{\varepsilon_{vol}}{3} \qquad \text{(Eq. 3.15)}$$

where, ε_{lin} is the linear strain; and ε_{lin} is the volumetric strain.

3.2.1.4.2 Modeling of Autogenous Shrinkage

Miyazawa and Tazawa (1999) proposed a prediction model for linear autogenous shrinkage strain. The variables included in the model were the composition of four major compounds of portland cement, i.e. C_3S, C_2S, C_3A, and C_4AF, along with fineness of cement (Blaine), and water-to-binder ratio.

$$\varepsilon_c(t) = \gamma \cdot \varepsilon_{co} \cdot \beta(t) \qquad \text{(Eq. 3.16)}$$

where,

γ = effects of cement composition

ε_{co} = ultimate autogenous shrinkage $(\times 10^{-6})$

W/B = water-to-binder ratio

a, b = constants

t_0 = initial setting time (days)

t = age (days)

with,

$$\begin{aligned}\gamma &= -0.0042\cdot(C_3S\%) - 0.0049\cdot(C_2S\%)\\ &\quad + 0.125\cdot(C_3A\%) + 0.093\cdot(C_4AF\%)\\ &\quad + 0.00015\cdot(Blaine) - 0.90\end{aligned}$$

$$\varepsilon_{co} = 3070\cdot\exp\{-7.2(W/B)\}$$

$$\beta(t) = 1 - \exp\{-a(t-t_0)^b\}$$

$$a = 3.27\cdot\exp\{-6.83(W/B)\}$$

$$b = 0.251\cdot\exp\{2.49(W/B)\}$$

Figure 3.19 shows the effect of water-cement ratio on the autogenous shrinkage development calculated with the above model.

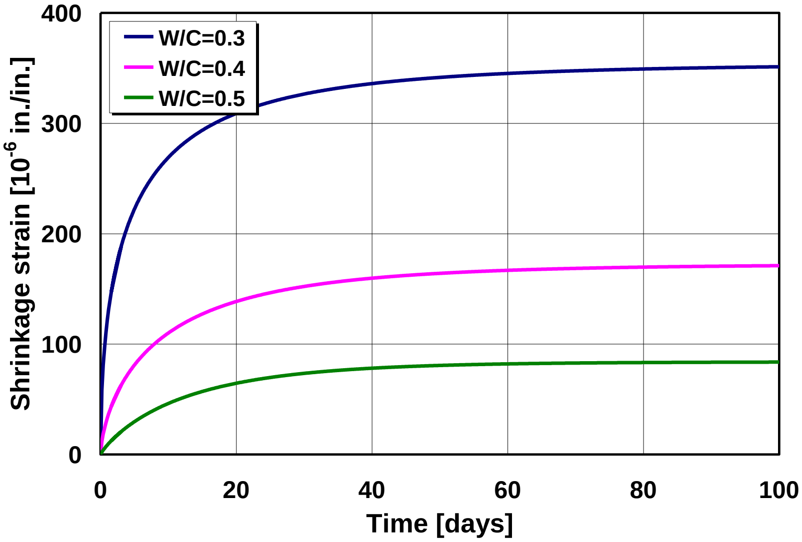

Figure 3.19: *Effect of water-cement ratio on autogenous shrinkage development*

3.2.1.4 Creep Behavior

Creep behavior is defined as the tendency that a solid material continues to deform slowly under a constant load within the service level (Bažant, 1982). The mechanism for concrete creep is not fully identified, but it is generally stated that creep strain occurs when the hydrated matrices lose a large amount of water under the applied stress (Mehta, 2006). Bažant (1982) explained that creep can arise when the solid structure changes because the bond between colloidal sheet (C-S-H) and cement gel is quite unstable.

There are two different types of concrete creep. The creep taking place without moisture exchange with environment is called basic creep. On the other hand, drying creep (or Pickett effect) occurs when concrete is subjected to a sustained load along with a substantial moisture loss. As can be seen in Figure 3.20, the drying creep accompanies additional creep strain other than basic creep and drying shrinkage. The mechanism for this is still being debated. One of the probable causes of drying creep is the mitigation of solid particle when water is diffusing out of the micropores. Stress and microcracking also are believed to be another reason for drying creep (Bažant, 1982).

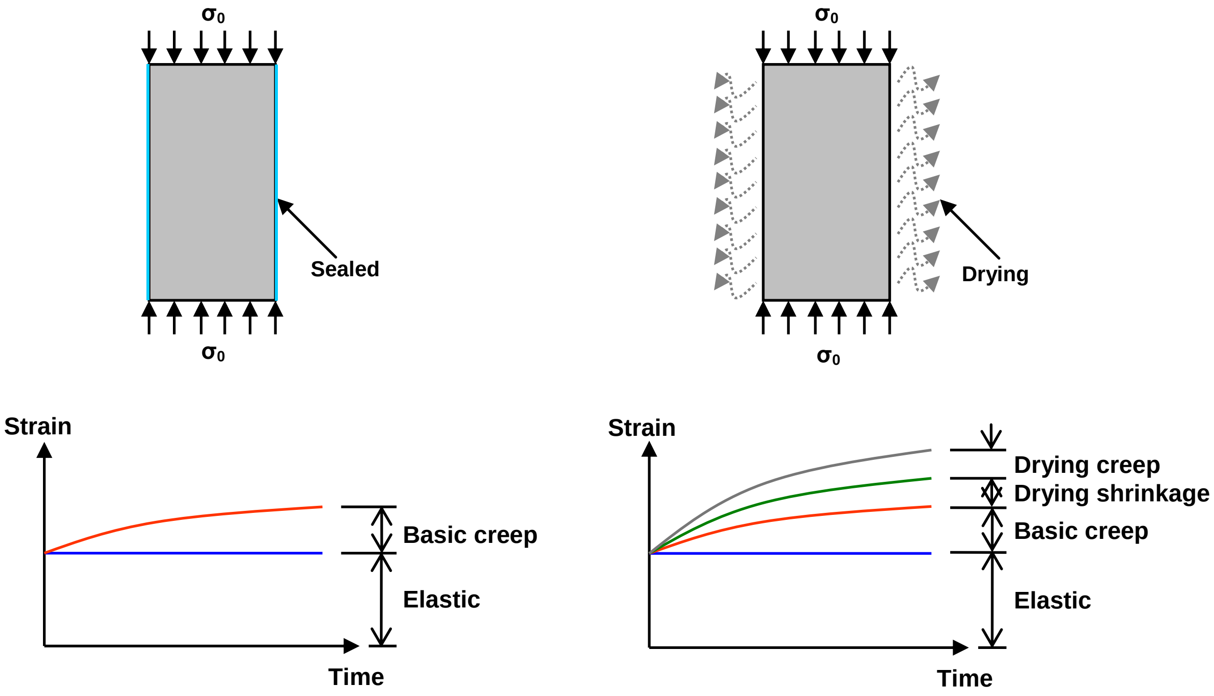

(a) Basic creep (b) Drying creep

Figure 3.20: *Basic creep and drying creep*

Since concrete is a viscoelastic material which shows time-dependent behavior under sustained loads and deformations, the realistic evaluations of strain and stress can be attained when this time-dependent characteristic is taken into account. Figure 3.21 displays the typical time-dependent strain curve of concrete arising under loading and unloading conditions.

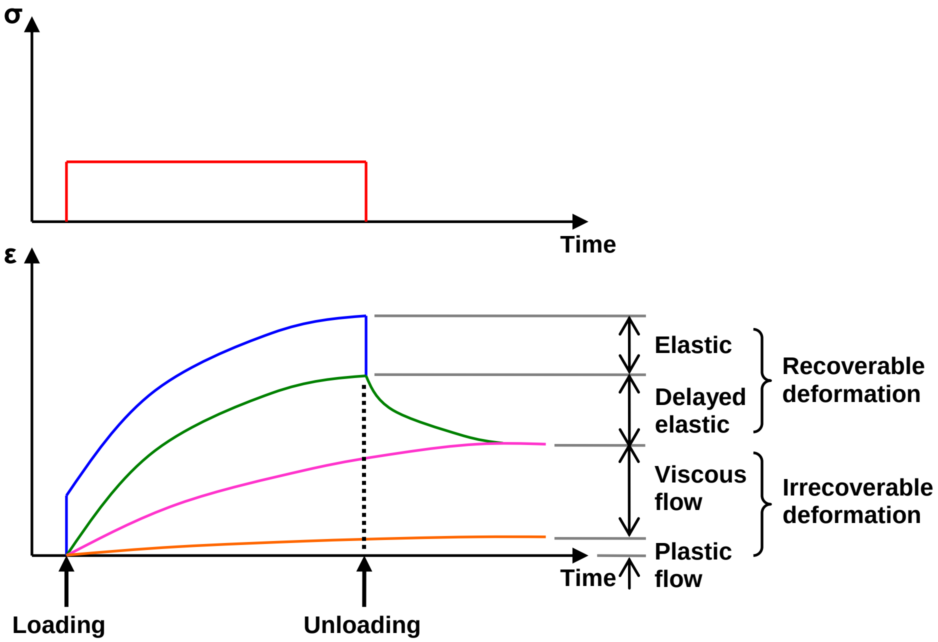

Figure 3.21: *Typical time-dependent strain curve at loading and unloading*

As can be seen in the figure, concrete strains generally incorporate several different rheological phases such as elastic, delayed elastic, viscous and plastic flow. This indicates that the concrete's strain generated upon loading is not fully converted to stress in proportion to its modulus. This characteristic is often described as viscoelastic or elasto-plastic, and considering this component is quite important to calculate the reasonable stress developments in a concrete element.

Figure 3.22 illustrates the rheological model which displays the time-dependent deformation of concrete under a sustained stress. It is seen that the model not only incorporates elastic and viscoelastic portions which are stress-dependent but also the thermal and shrinkage strain portions which are not related with stress. Herein, the viscoelastic portion is often termed Kelvin chain, presenting the time-dependent deformation characteristic of concrete.

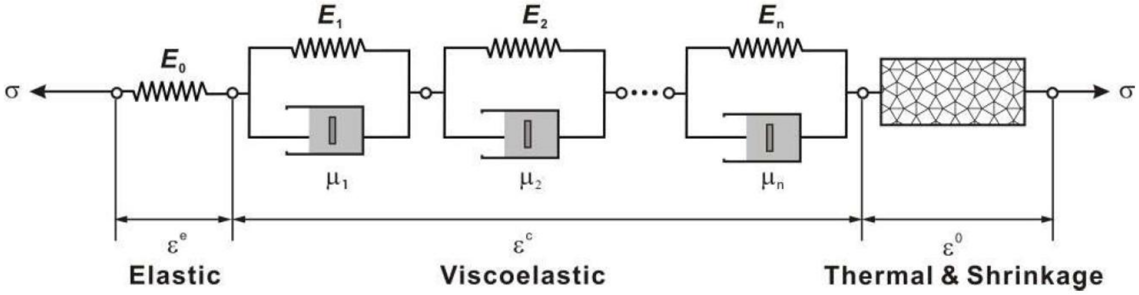

Figure 3.22: *Rheological model for deformation of concrete,* Nam (2005)

3.2.1.4.2 Mathematical Modeling of Concrete Creep

When a concrete element is uniaxially loaded within the service stress range, the total strain at age *t* can be formulated as follows (Bažant, 1982; Bažant, 1988):

$$\begin{aligned}\varepsilon(t) &= \varepsilon^{E}(t)+\varepsilon^{C}(t)+\varepsilon^{S}(t)+\varepsilon^{T}(t)\\ &= \varepsilon^{\sigma}(t)+\varepsilon^{0}(t)\end{aligned} \qquad \text{(Eq. 3.17)}$$

where, $\varepsilon^{E}(t)$ is the instantaneous elastic strain; $\varepsilon^{C}(t)$ is the creep strain; $\varepsilon^{S}(t)$ is the shrinkage strain; and $\varepsilon^{T}(t)$ is the thermal strain. Here, $\varepsilon^{\sigma}(t)$ is the stress-dependent strain, which is produced by stresses, and $\varepsilon^{\sigma}(t)=\varepsilon^{E}(t)+\varepsilon^{C}(t)$. On the other hand, $\varepsilon^{0}(t)$ denotes the stress-independent strain which is not induced by stresses, and $\varepsilon^{0}(t)=\varepsilon^{S}(t)+\varepsilon^{T}(t)$.

In order to mathematically model this behavior, the stress-dependent strain terms in Eq. 3.17 can be replaced by a compliance function *J(t,t')* based on the linearity assumption of the stress-strain relationship (Bažant, 1982; Bažant, 1988):

$$\begin{aligned}\varepsilon(t) &= \sigma J(t,t')+\varepsilon^{0}(t)\\ &= \sigma J(t,t')+\varepsilon^{S}(t)+\varepsilon^{T}(t)\end{aligned} \qquad \text{(Eq. 3.18)}$$

where, t' and t are the concrete ages in days at loading and when the strain is considered. respectively; $\varepsilon(t)$ is the uniaxial strain at time t, μin./in.; σ is the sustained uniaxial stress, psi; $J(t,t')$ is the creep compliance function at age t due to the loading at age t'; and, $\varepsilon^0(t)$ is the stress-independent strain, which is the sum of the shrinkage strain $\varepsilon^S(t)$; and the thermal strain $\varepsilon^T(t)$.

Herein, the compliance function $J(t,t')$ can be subdivided into the instantaneous compliance and the basic creep compliance as follows:

$$
\begin{aligned}
J(t,t') &= \frac{1}{E(t')} + C(t,t') \\
&= \frac{1+\varphi(t,t')}{E(t')}
\end{aligned}
\tag{Eq. 3.19}
$$

where, $J(t,t')$ is described in Eq. 3.18; $E(t')$ is the elastic modulus at time t'; $C(t,t')$ is the creep compliance; and $\varphi(t,t')$ is the creep coefficient at age t due to the loading at age t'.

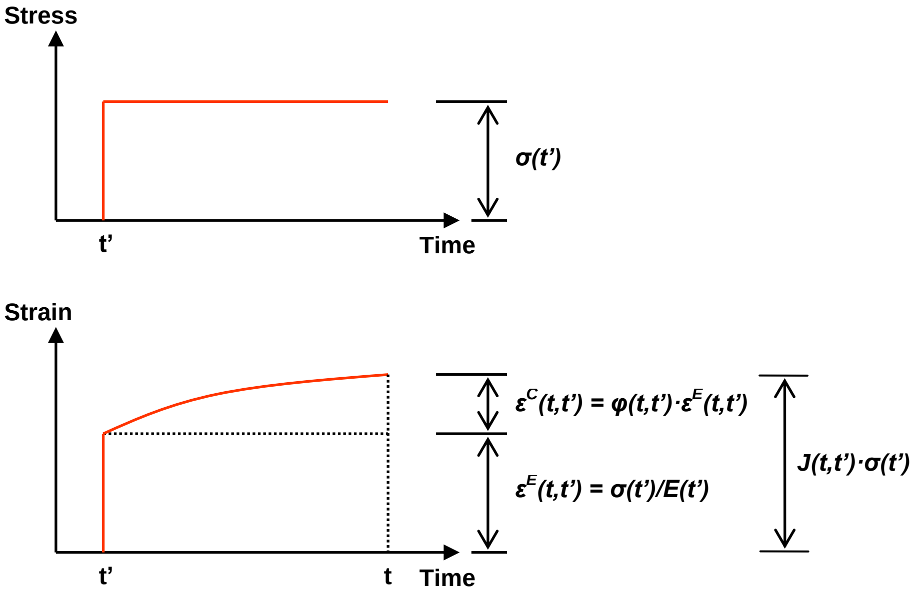

Figure 3.23: *Modeling of creep curve*

The creep strains induced by each stress incremental can be additively combined based on the principle of superposition as shown in Figure 3.24. The principle of superposition is only valid under the assumption that the creep strain is in proportion to the applied stress (assumption of linearity).

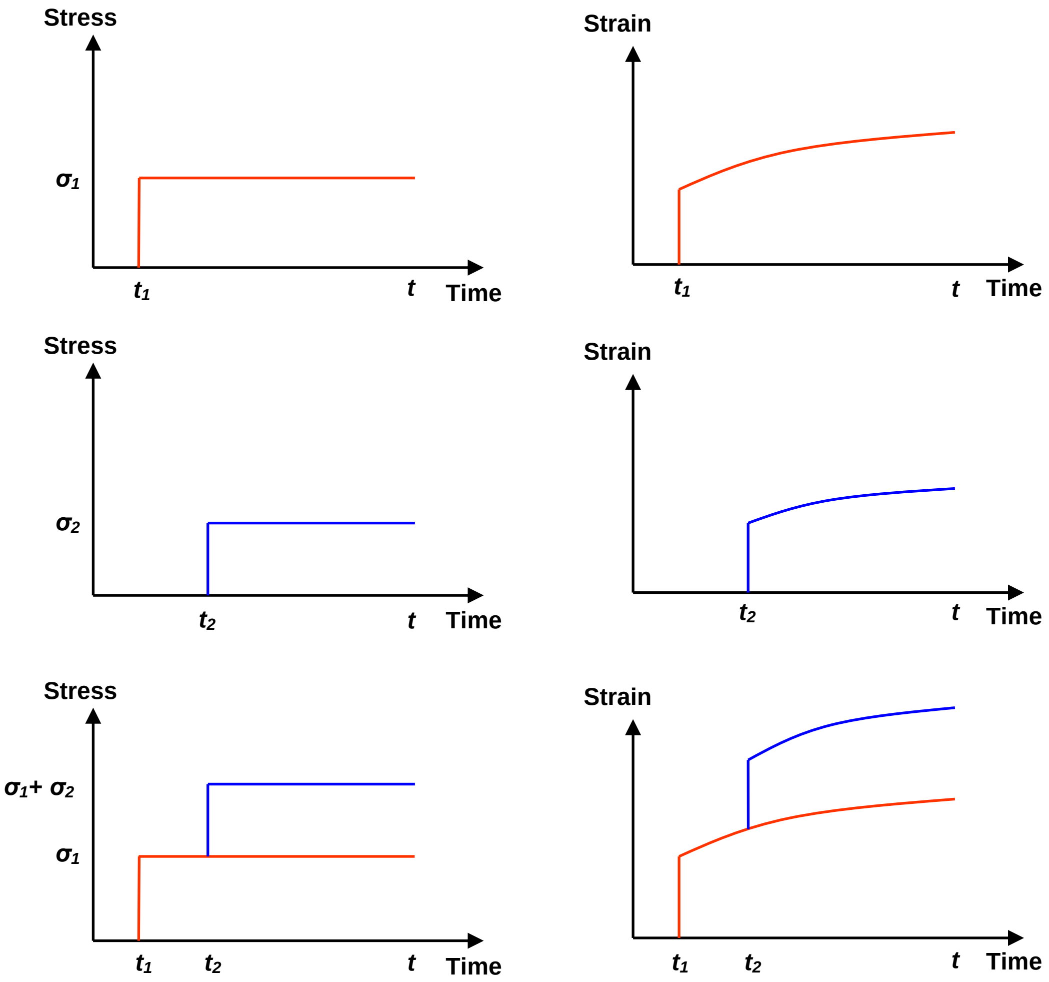

Figure 3.24: *Principle of superposition for creep strain*

3.2.1.4.3 Creep Models

To date substantial efforts have been made to model the creep behavior of concrete. Several examples of the creep models found in the literatures are listed as follows (ACI, 1983; Bažant and Panula, 1978; Bažant and Chern, 1985; CEB-FIP, 1993; Emborg, 1989).

ACI Model describes:

$$J(t,t_0) = \frac{1}{E_0}\left(1 + \frac{(t-t_0)^{0.6}}{10+(t-t_0)^{0.6}} \cdot \varphi_\infty(t_0)\right) \quad \text{(Eq. 3.20)}$$

where, $\varphi_\infty(t_0) = 2.35\kappa'_1\kappa'_2\kappa'_3\kappa'_4\kappa'_5\kappa'_6\kappa'_7$; and κ'_1 to κ'_7 are the factors related with environmental humidity, minimum thickness, and mixture properties.

Bažant and Panula's Model is well known as Double-Power Law, and it is described as:

$$J(t,t_0) = \frac{1}{E_0} + \frac{\varphi_1}{E_0}\left(t_0^{-m} + \zeta\right)\left(t-t_0\right)^n \quad \text{(Eq. 3.21)}$$

The Triple-Power Law suggested by Bažant and Chern can be expressed as follows:

$$J(t,t_0) = \frac{1}{E_0} + \frac{\varphi_1}{E_0}\left(t_0^{-m} + \zeta\right)\left[\left(t-t_0\right)^n - B(t,t_0,n)\right] \quad \text{(Eq. 3.22)}$$

where, E_0, m, n, and ζ are the material-related parameters.

The creep model for CEB-FIP Model Code 90 can be expressed as follows:

$$J(t,t_0) = \frac{1+\phi(t,t_0)}{E_c(t_0)} \quad \text{(Eq. 3.23)}$$

in which,

$$\phi(t,t_0) = \phi_0\beta_c(t-t_0) \quad \text{(Eq. 3.24)}$$

$$\phi_0 = \phi_{RH}\,\beta(f_{cm})\,\beta(t_0) \tag{Eq. 3.25}$$

with,

$$\phi_{RH} = 1 + \frac{1-(RH/100)}{0.46(h_0/h_{ref})} \tag{Eq. 3.26}$$

where, RH is the relative humidity, %; $h_0 = 2A_c/u$ with A_c is the area in contact with the atmosphere of the cross-section of the considered member; and u is the perimeter in contact with the atmosphere of the cross-section of the considered member.

$$\beta(f_{cm}) = \frac{5.3}{(f_{cm}/f_{cm0})^{0.5}} \tag{Eq. 3.27}$$

where, $f_{cm} = f_{ck}$ + 8 MPa; f_{cm0} = 10 MPa; and f_{ck} is the characteristic compressive strength at 28-day, MPa.

$$\beta(t_0) = \frac{1}{0.1 + {t_0}^{0.2}} \tag{Eq. 3.28}$$

where, t_0 is the age at loading.

Emborg used two additional terms over the Triple-Power Law to improve the early-age creep characteristics:

$$J(t,t_0) = \frac{1}{E_0} + \frac{\varphi_1}{E_0}\left({t_0}^{-m} + \zeta\right)\left[(t-t_0)^n - B(t,t_0,n)\right] + \frac{G(t_0)}{E_0} + \frac{H(t,t_0)}{E_0} \tag{Eq. 3.29}$$

where, $G(t_0)$ considers the strong age-dependent instantaneous deformation; and $H(t,t_0)$ considers the increase of the early-age creep at the load application.

3.2.2 Experimental Methods to Measure Restrained Stress in Concrete

Currently, the following three laboratory testing techniques are the most widely used to evaluate the cracking tendency and stress development in early-age concretes.

3.2.2.1 Ring Test

To determine the cracking tendency of early-age concrete, a laboratory testing method per AASHTO PP 34-99 is commonly used (AASHTO, 2006). This testing method utilizes the ring concrete specimen cast surrounding a rigid steel ring. Strain gages mounted onto the surface of the steel ring measures the elastic strain of the steel ring as the surrounding concrete shrinks. This technique determines the time-to-cracking of concrete by detecting the time of sudden strain change. This testing procedure only measures the time of crack initiation; stress developments in the concrete specimen cannot be measured. Figure 3.25 shows the testing apparatus for the ring test.

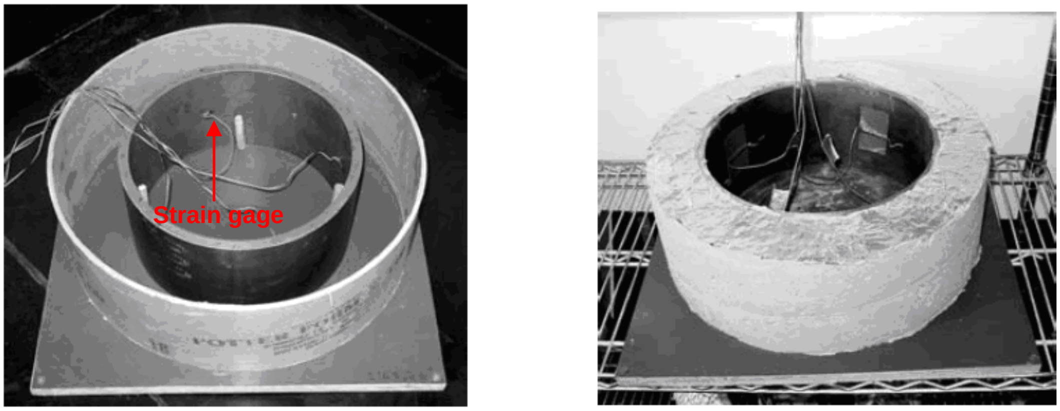

Figure 3.25: *Apparatus for ring test*

3.2.2.2 Cracking Frame

The cracking frame (or rigid cracking frame) is the device used to simulate the restrained condition and to measure the early-age restrained stress evolution in concrete in a passive manner, invented by Springenshmid, Breitenbücher, and Nischer in 1970s (Mangold, 1998). This testing device is mainly composed of two solid crossheads, insulated formwork equipped with a water circulating computer controller, and constraining longitudinal invar steels. The design details of the rigid cracking frame are described in Figure 3.26.

The measurement of early-age stress development using a rigid cracking is made in accordance with the following sequences:

1) Fresh concrete is cast into the thermally insulated formwork located between two rigid crossheads.

2) A desired temperature history is imposed to the specimen using a computer controller. As the medium for the temperature control, the water circulating through copper tubing installed around the concrete specimen is used.

3) At the same time, the strain gages mounted onto the constraining invar steels continuously measure the small elastic strain of invar steels caused by the volume changes of the concrete specimen.

4) Based the force-deformation relationship, calculate the force applied in the invar steels. Then, evaluate the force in the concrete specimen using the force equilibrium condition between the concrete specimen and invar steel.

(a) Rigid cracking frame

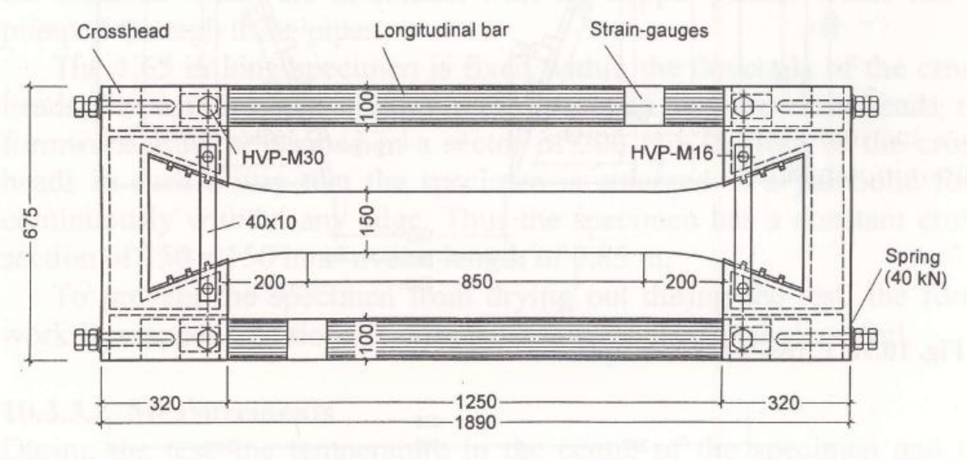

(b) Design of rigid cracking frame (Springenschmid, 1998)

Figure 3.26: *Rigid cracking frame*

3.2.2.3 Temperature-Stress Testing Machine

The temperature-stress testing machine (TSTM) operates in a similar manner with the rigid cracking frame. While both crossheads of a rigid cracking frame are restrained by the axial stiffness of constraining invar steels, the TSTM is designed to allow the adjustment of distance between two crossheads using a closed-loop system, i.e. one crosshead is fixed and the other crosshead is adjustable. Due to such difference in the operation principle, it is generally known that the cracking frame is a passive testing device while the TSTM is an active testing device.

Once fresh concrete is placed in the insulated formwork, a deformation of concrete specimen under the desired temperature history is continuously measured by linear variable displacement transducers (LVDT) with a sensitivity of 0.03937 mil (0.0001 mm). Once the deformation of concrete specimen reaches 0.3937 mil (0.001 mm), the adjustable cross head is pulled back to the initial position using a step motor. This closed-loop operation system makes the degree of restraint of concrete specimen maintain 100 % over the testing period. Meanwhile, the pulling force induced by the step motor is successively recorded by the load cell mounted on the main axis of the machine so that the stress development in the concrete specimen can be measured. Figure 3.27 shows the design and configuration, and the typical measured response from the TSTM.

In addition to the early-age stress development, many other types of testing for material property characterization can be conducted with the TSTM: elastic modulus evolution of concrete, CTE evolution in hardening concrete, developments of tensile strength and failure strain, and compressive and tensile creep measurements.

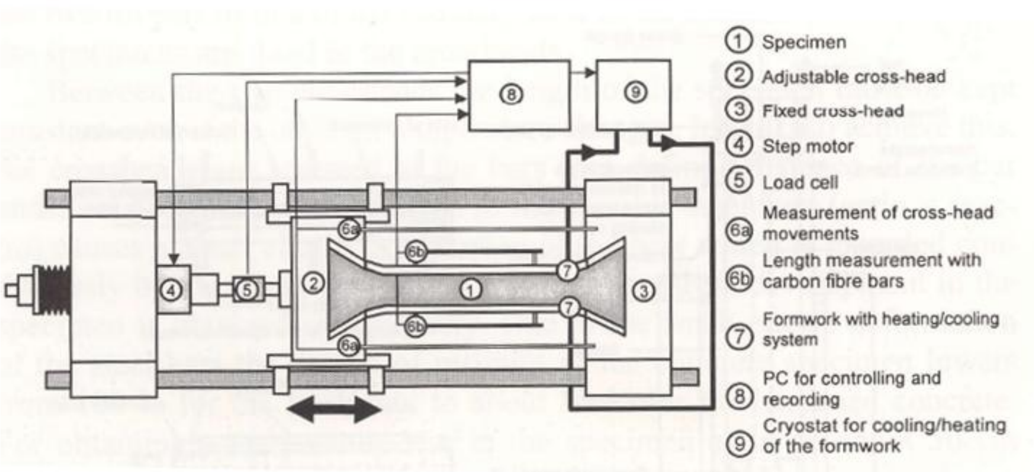

(a) Design of TSTM (Mangold, 1998)

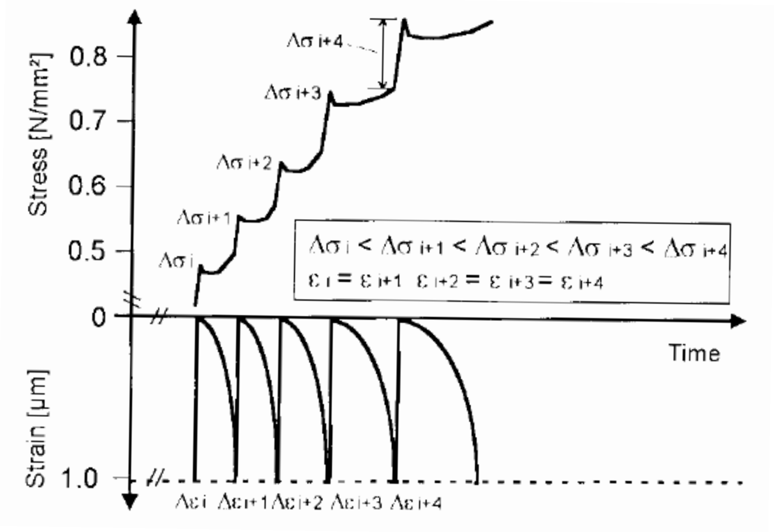

(b) Typical measured response of TSTM (Mangold, 1998)

Figure 3.27: *Temperature-stress Testing Machine*

3.2.2.4 Stressmeter

The stressmeter is a device which is designed to directly monitor the stress development in cast-in-place concrete due to volume changes, considering a modulus development and viscoelastic behavior. The stressmeter is generally composed of a porous tube, a load cell with a steel grip, and anchors. Concrete is directly placed inside the tube, and the steel grip anchors restrain the inner concrete as it moves due to temperature and moisture variations. Then, the load cell anchored to the concrete inside the tube continuously measures the stresses arise in the inner concrete specimen (it actually measures the strain of the material, elastic modulus of which is exactly known).

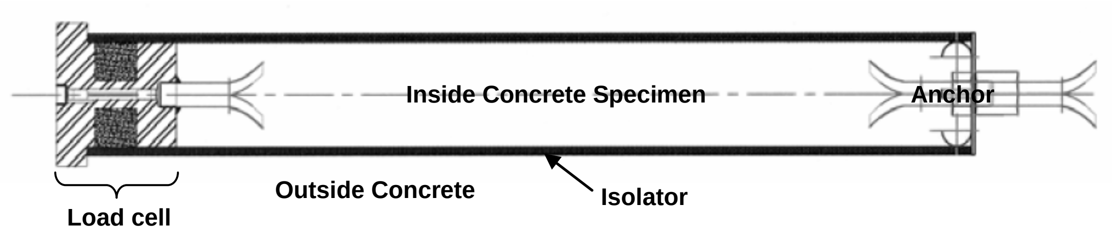

(a) Design of stressmeter (figure courtesy: Geokon)

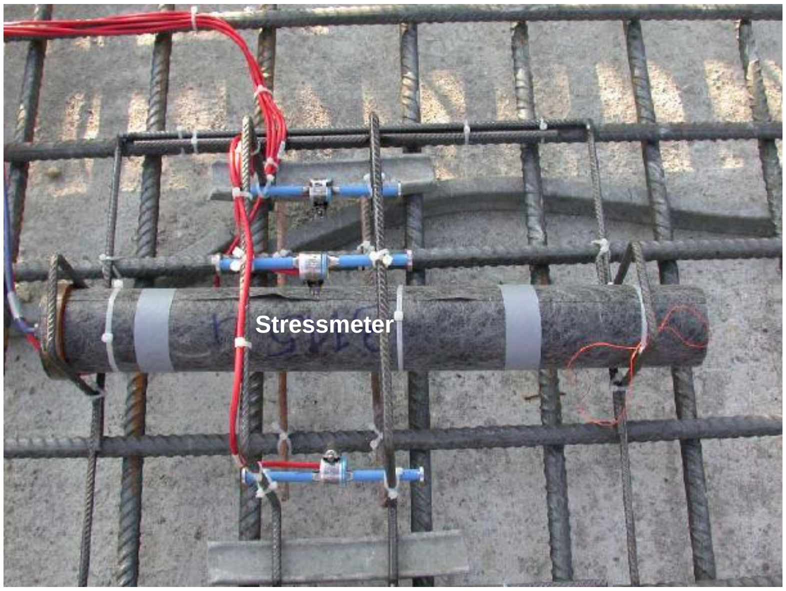

(a) Stressmeter installation (photo courtesy: Geokon)

Figure 3.28: *Stressmeter*

Chapter 4: Field Experimental Programs

4.1 OVERVIEW OF FIELD TESTING SITES

A series of field experiments was conducted in four different PCC pavement construction projects. The primary objective of the field testing was to evaluate the early-age and later-age behavior and structural responses of PCC pavements subjected to environmental loadings, i.e., temperature and RH variations.

Among the four testing sections, two were placed in Austin (Austin-A and Austin-B), Texas in September 2003 and May 2007, and the other two testing sections were constructed in Fort Worth and Hillsboro, Texas in September 2006 and February 2009, respectively.

The Austin-A and Fort Worth sections were newly constructed CRCP with different thicknesses. The Austin-B section was a 6-in.-thick full-scale bonded concrete overlay placed over the existing asphalt pavement (whitetopping). It was a controlled test section constructed at the J. J. Pickle Research Campus at the University of Texas at Austin. The Hillsboro section was a special designed PCC pavement to improve the response of the concrete against the external loads, i.e., post-tensioned prestressed concrete pavement (PTCP). The test section was located on the interstate highway 35 (IH-35) northbound outermost lane. In the Hillsboro project, concrete was placed between transverse armor joints 300 ft. apart. Before the concrete placement, steel tendons and bars were placed at the preselected locations. After the concrete sets, post-tensioning was applied at two separate times in the longitudinal direction in order to introduce precompression to the PCC slab. The first and second longitudinal post-tensionings were applied at the equivalent ages of 0.58 and 3.08 days, respectively. About 6.5 day after the concrete placement, 96,000 lbf of post-tensioning force was applied in the transverse direction as well.

The detailed information of the test sites is summarized in Table 4.1 and Figure 4.1.

Table 4.1: *Detailed information of testing sites*

	Austin-A	Fort Worth	Austin-B	Hillsboro
Location	US-183, Austin, TX	SH-114B, Fort Worth, TX	Pickle Research Campus at University of Texas at Austin, Austin, TX	I-35, Hillsboro, TX
Date of construction	Sep. 25th, 2003	Sep. 19th, 2006	May 3rd, 2007	Feb. 23rd, 2009
Type of structure	CRCP[a]	CRCP[a]	Whitetopping	PTCP[b]
Dimensions	24 ft. wide; and 11 in. thick	24 ft. wide; and 8 in. thick	18 ft. long; 18 ft. wide; and 6 in. thick	300 ft. long; 35 ft. wide; and 9 in. thick

[a] Continuously reinforced concrete pavements

[a] Post-tensioned concrete pavements

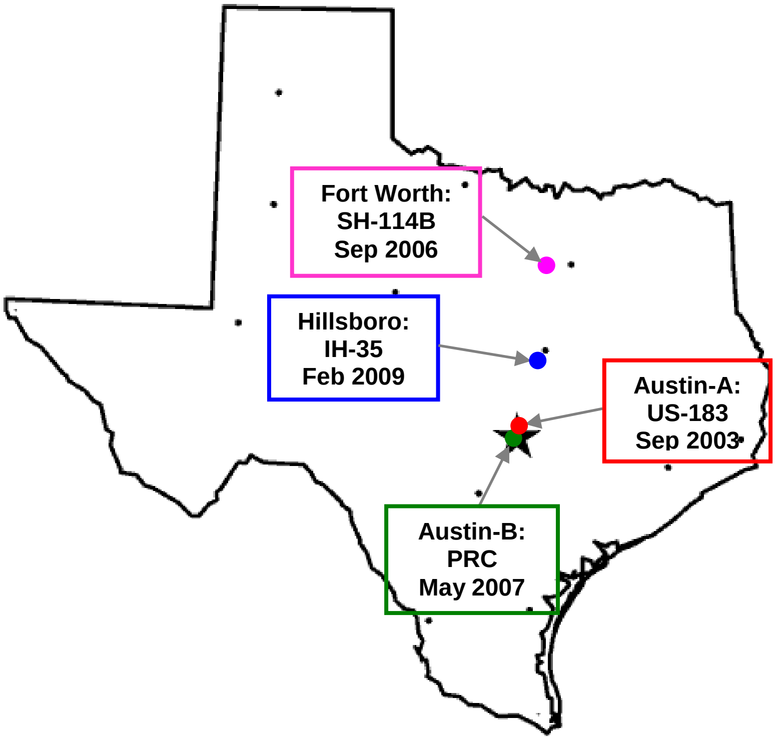

Figure 4.1: *Field test sections in the state of Texas*

4.2 MATERIAL PROPERTIES

The concrete mixtures used in all test sections were the Class P concretes, typically used in concrete paving in Texas. The water-to-cement ratio for all the concretes was 0.45 except for the Austin-A section, which was 0.50.

The Austin-A section used limestone as coarse aggregate and 27% of cement was replaced by Class F fly ash. In the Fort Worth section, concrete with 4.75-sacks of cementitious material with 20% of Class F fly ash replacement by weight was used. The type of cement incorporated into the mixture was Type I/II portland cement. For coarse aggregate, limestone with a maximum size of 1.5 in. was used. The mixture used in the Austin-B section included 5-sacks of Type I/II portland cement with no supplementary cementing material (SCM). The coarse aggregate was limestone with a 1.0 in. maximum size. The concrete mixture for the Hillsboro section had a total of 5.5-sacks of cementitious materials with 25 % replaced by Class F fly ash. Siliceous river gravel with a maximum size of 1.25 in. was used as coarse aggregate.

The mixture proportions and material properties of the concretes are summarized in Table 4.2.

Table 4.2: *Mixture proportion of materials used in the field tests*

	Unit	Austin-A	Fort Worth	Austin-B	Hillsboro
Cement (Type I/II)	lb/yd^3	329	335	470	419
Fly ash (Class F)	lb/yd^3	121	112	-	105
Water	lb/yd^3	226	202	212	236
Coarse aggregate	Type max. size, in. lb/yd^3	Limestone - 1814	Limestone 1.5 2042	Limestone 1.0 1998	SRG[a] 1.25 1986
Fine aggregate	max. size, in. lb/yd^3	- 1330	- 1252	0.19 1301	0.19 1177
Air-entraining agent	fl oz/yd^3	-	4	1.2	8.0
Water reducing admixture	fl oz/yd^3	-	16	18.8	37.0
w/cm	-	0.50	0.45	0.45	0.45
Air content	%	5.0	4.5	5.0	4.5
Slump	in.	-	1.3	1.75	1.5
28-day compressive strength	psi	-	5365	4972	6798
28-day elastic modulus	10^6 psi	-	5.84	5.51	6.21

[a]Siliceous river gravel

4.3 FIELD INSTRUMENTATION

As previously explained with Eq. 3.19, the measured total strain consists of four independent strain components. They include: elastic strain, creep strain, shrinkage strain, and thermal strain, and these components are additively related. To investigate the contribution of each strain component on the time-dependent behavior and structural response of PCC pavements, the following testing setups were employed in the field experiments.

4.3.1 Total Strain and Temperature Measurements in Concrete

In order to measure the behavior and structural response of in-situ PCC pavement in-situ, it is essential to measure the strain histories of concrete elements right after concrete placement. The vibrating wire strain gages (VWSG) (Model 4200; Geokon) were used to measure the variations in concrete strain. Figure 4.2 (a) shows a set of the VWSGs installed in the field. In order to monitor the overall behavior of PCC pavements under environmental loadings, the VWSGs were installed at different depths: 1 in. below the top surface, mid-depth, and 1 in. above the bottom surface of the slab. Because each VWSG had a built-in thermostat inside the gage body, concrete temperatures at the gage locations could be simultaneously monitored with VWSGs.

Figure 4.2: *VWSGs installed at top, middle, and bottom of PCC pavement*

4.3.2 Relative Humidity Measurements in Concrete

To examine the contribution of drying shrinkage and swelling effects on the behavior and response of PCC pavements, capacitive type RH sensors were also installed at different depth as shown in Figure 4.2 (b). The requirements for the gages in accurately measuring local RH along the various depths in concrete pavements were: 1) small enough to monitor the localized RH variations at various depths, and 2) achieving rapid RH equilibrium in the system to promptly react to the ambient humidity changes.

After evaluating various RH measurement systems, it was determined that the RH measurement system developed by University of Illinois at Urbana-Champaign (Grasley and Lange, 2004) met the above requirements and was selected for the field testing. This system utilizes a capacitive type RH measurement sensor, called SHT75 developed by CMOSens® (Figure 4.3). The performance specifications of the SHT75 are described in Table 4.3.

Even though the SHT75 provides the users with the above advantages, it is prone to malfunctions if it is in a direct contact with water. This issue was resolved by capping the sensor with a plastic tube and special engineered fabric acting as a semi-permeable membrane that prevents direct water infiltration into the tube but allows vapor exchange. Figure 4.4 shows the RH sensors pre-installed at various depths before concrete is placed. It is clearly seen that the RH sensors were treated with the plastic tube and the special fabric.

***Figure 4.3**: SHT75 for internal RH measurement*
(figure courtesy: sensirion.com)

Table 4.3: *Performance specifications of SHT75*

Parameter	Conditions	Min.	Typ.	Max.	Units
Humidity					
Resolution		0.5	0.03	0.03	%RH
		8	12	12	bit
Repeatability			±0.1		%RH
Accuracy Uncertainty	linearlized	±1.8		±3.5	%RH
Interchangeability			fully interchangeable		
Nonlinearity	raw data		±3		%RH
	linearlized		<<1		%RH
Range		0		100	%RH
Response time	1/e (63%) at 25℃, 1m/s air	6	8	10	
Hysteresis			±1		%RH
Long term stability	typical		<0.5		%RH/yr
Temperature					
Resolution		0.04	0.01	0.01	℃
		0.07	0.02	0.02	℉
		12	12	14	bit
Repeatability			±0.1		℃
			±0.2		℉
Accuracy		±0.3		±3	℃
Range		-40		123.8	℉
Response time	1/e (63%)	5		30	s

***Figure 4.4**: RH sensors installed at various depths of PCC pavement*

Figure 4.5 presents the example of RH readings obtained from the proposed testing setup. The data shows the variations in RH monitored at five different depths – surface, 0.5 in., 1 in., 2 in., and 6 in. – during the first 30 days after concrete placement. The daily fluctuation of RH is due to the changes of concrete temperature. It is noted that as the measurement depth increases, the RH levels become higher, as expected.

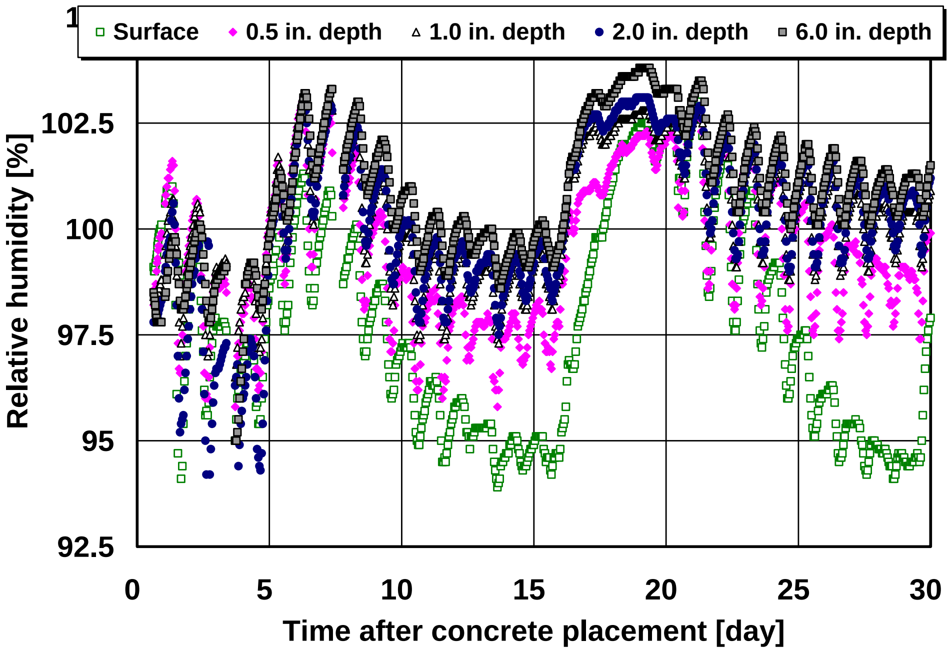

***Figure 4.5**: Typical measured RH data measured from RH sensors*

4.3.3 Stress-Independent Strain Measurements in Concrete

As will be discussed in detail in the following chapter, measuring the stress-independent strain components – thermal strain and drying shrinkage strain – of concrete was essential to evaluate the time-dependent behavior of PCC pavement responses subjected to temperature and moisture changes. In case of high-performance concrete which typically has a low water-cement ratio, the autogenous shrinkage can be pronounced and needs to be considered. In the scope of this experimental program, however, it was assumed that the effect of autogenous shrinkage is quite minimal since the water-cement ratio of the concretes used in the testing was as high as 0.45 to 0.50.

To measure the development of thermal and shrinkage strain, the specially designed devices called “non-stress cylinder (NC)” (Choi and Won, 2010) was employed in the field testing. The NC was designed to perform in such a way that the concrete inside the NC is separated from the surrounding concrete so that the concrete inside the

NC can move without any influence of external restraint such as base friction and restraint from an adjacent structure.

Two different types of NC were used to isolate the thermal strains and drying shrinkage strains from the total strains in the concrete. The first one is named “impervious non-stress cylinder (INC)”. It is designed not to allow the moisture exchange with the surrounding concrete, and the total strain measured from the concrete inside the INC represents only thermal strain at the depth of installation. On the other hand, the other one, called “porous non-stress cylinder (PNC)”, has a sufficient number of holes around its surface to allow moisture exchange between the concrete inside the PNC and surrounding concrete, and the strain measured in the inner concrete of the PNC is stress-independent strain, i.e., thermal strain plus drying shrinkage strain, at the depth of installation. By subtracting the strains measured by INC from those measured by PNC, the drying shrinkage strain can be estimated. Figures 4.5 (a) and (b) respectively show the INC and PNC placed in the field.

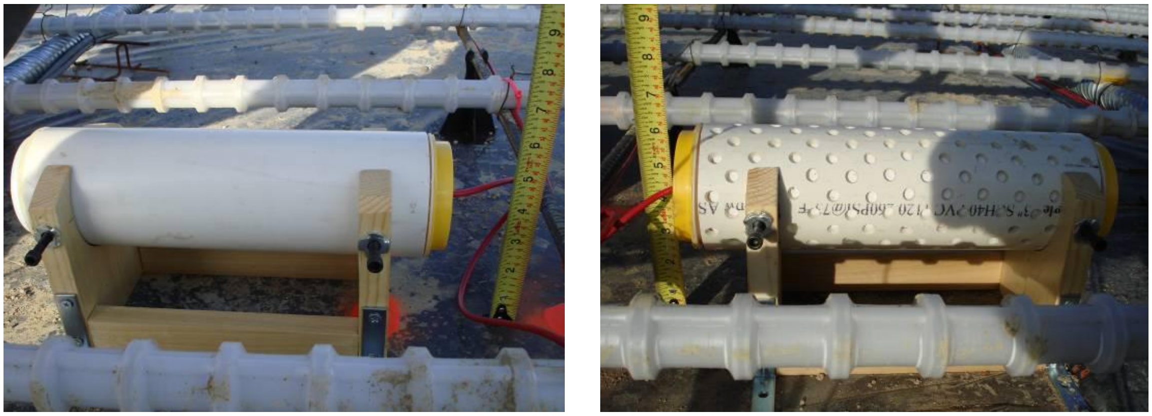

(a) Impervious non-stress cylinder (b) Porous non-stress cylinder

(c) Non-stress cylinders placed in the field

Figure 4.6*: Non-stress cylinders*

The dimensions of the NC adopted in the testing were 3 in. (diameter) x 9.5 in. (length). A hollow polyvinyl chloride (PVC) slip was used as a body of the NC and both ends of the PVC slip were capped with plastic caps. On the inner side of each plastic cap, a piece of Styrofoam® was attached to allow the volume expansion of the concrete inside the NC without restraints, ensuring stress-free condition in concrete. Also, a single layer of soft fabric was glued onto the inner surface of the NC body to alleviate the friction between concrete and NC as well as the radial pressure of concrete. To measure the strain of the concrete inside the NC, an embedment type VWSG with 6 in. of effective gage length was placed at the center of the specimen in the longitudinal direction. The resolution of the used VWSG was 1.0 x 10^{-6} in./in., which is precise enough to be implemented in the experiments. Further detailed information regarding NC and its validation works are given in the literature (Choi and Won, 2010).

Figure 4.7 shows the typical stress-independent strain data measured from the INC and PNC, and the drying shrinkage strain computed from their difference.

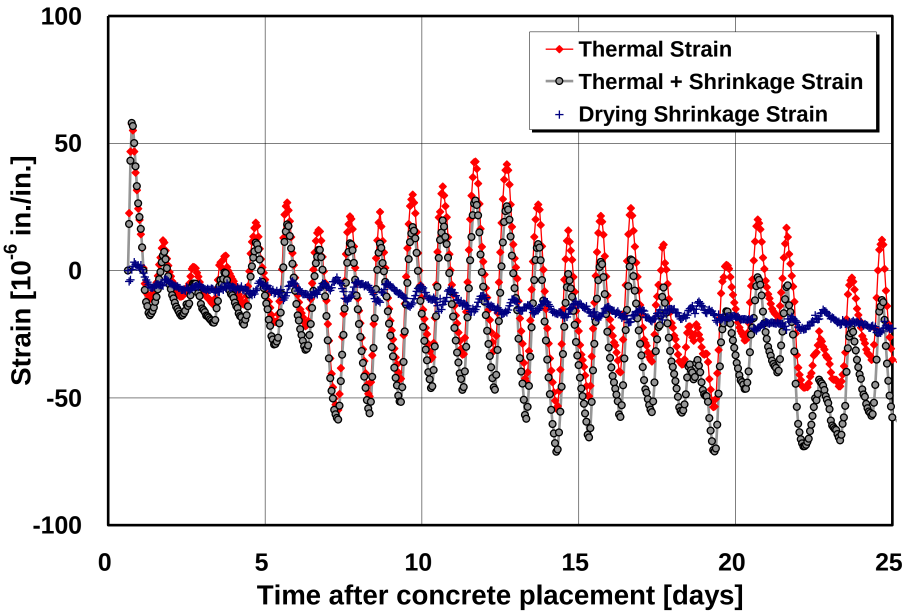

(a) Typical measurements from NC

***Figure 4.7**: Typical measured strain components measured from testing setup*

4.4 SUMMARY

To measure the total strain, thermal strain, and drying shrinkage strain at the depths of interest, specially designed non-stress devices were employed in the field testing. Along with the direct measurement of strain components, temperature and internal RH variations at various depths were also monitored to evaluate the stress-independent strain at other depths. Table 4.4 summarizes the field instrumentation employed in each field test section.

Table 4.4: *Summary of field instrumentation*

	Austin-A	Fort Worth	Austin-B	Hillsboro
Total strain	√	√	√	√
PNC		√	√	√
INC	†	√	√	√
Temperature	√	√	√	√
RH			√	√
Stressmeter			√	

† Free thermal strain was measured with a separate specimen.

Also, Figures 4.8 and 4.9 present the overall testing setup instrumented in the field and the design details of the proposed non-stress apparatus, respectively.

Figure 4.8*: Overall field testing setup*

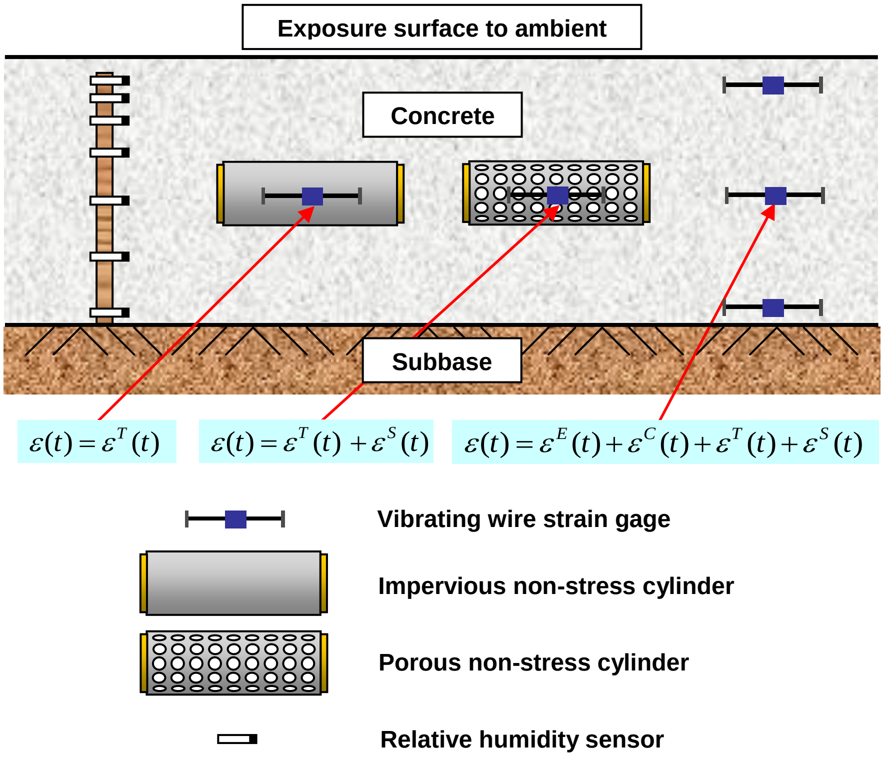

(a) Field testing setup

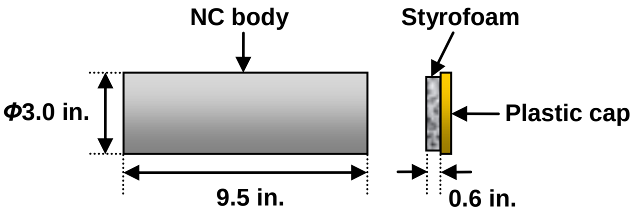

(b) Design details of INC

Figure 4.9*: Conceptual illustration of field testing setup and design details of non-stress device*

Chapter 5: In-Situ Evaluation of Zero-Stress Temperature

This chapter primarily deals with the experimental and data analysis methods to evaluate the early-age stress developments in portland cement concrete (PCC) pavement. Once the early-age stress history is determined, a zero-stress temperature (ZST) is estimated. The ZST thus determined is compared with the predicted ZST values obtained from the existing models to verify the accuracy of the current the models. Also, the findings from this chapter are used as the basic information to develop a more advanced ZST predictive model.

5.1 DATA INTERPRETATION

5.1.1 Determination of Final Setting

Final setting of concrete denotes the origin in which fresh concrete begins to gain mechanical properties and thus to carry stresses (Neville, 1995). A penetration resistance standard procedure, ASTM C 403 (ASTM, 2008), is most commonly used to determine the setting time of cement-based materials.

In this study, however, a more practical method developed by Glisic and Simon (2000) was used to estimate the actual structural setting time of concrete. The fundamental principle of this method is to find the point where a VWSG and concrete exhibit composite behavior based on the measured raw VWSG readings. Because concrete prior to setting barely resists the thermal dilation of a VWSG, the measured strain by the VWSG tends to change in proportion to the variation of concrete temperature. Once the concrete reaches the final setting, however, the thermal movement of the VWSG is restrained by surrounding concrete and thus starts to move in an opposite direction with concrete temperature.

Figures 5.1 (a) and (b) show the temperature and raw strain readings collected from Fort Worth and Hillsboro test sections, respectively.

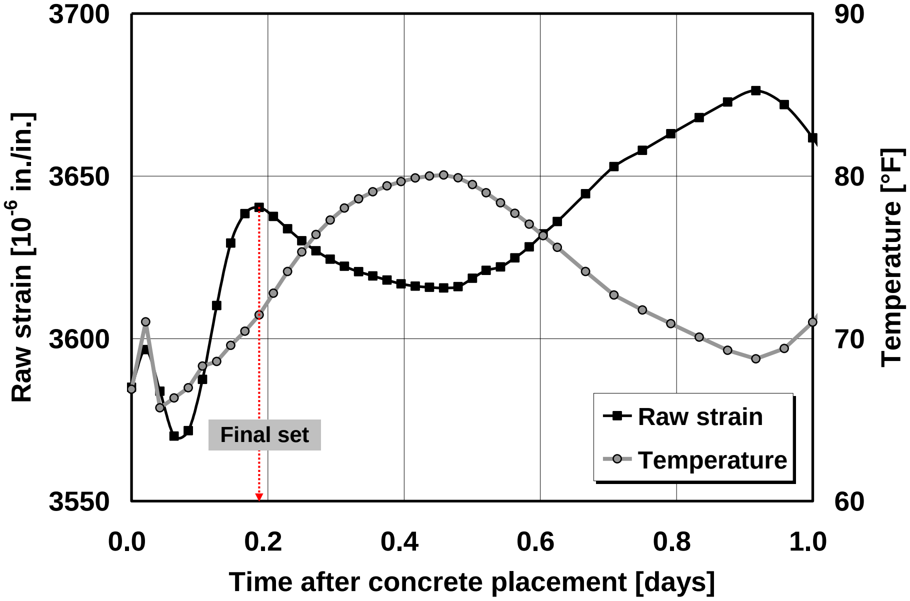

(a) Setting time estimated for Forth Worth test section

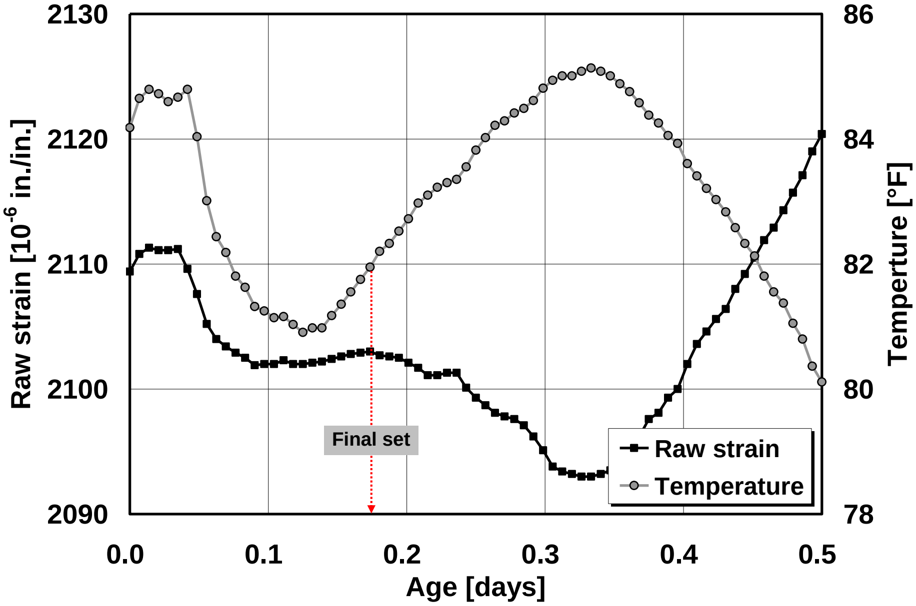

(b) Setting time estimated for Hillsboro test section

Figure 5.1*: Determination of structural setting time*

It is noted that the measured raw strain starts to change in opposite to the variation of concrete temperature about 0.194 days and 0.139 days after concrete placement. Those points were defined as the final setting time of the cast-in-place concrete element. Once the final setting time is determined, a temperature calibration was conducted using the following equation to remove the thermal effect from the raw strain measurements.

$$\varepsilon = (R_1 - R_0)B + (T_1 - T_0)\alpha_G \quad \text{(Eq. 5.1)}$$

where, ε is the temperature-corrected total strain; R_1 and R_0 are the final and initial raw readings from a vibrating wire strain gage, respectively, 10^{-6} in./in.; B is the batch calibration coefficient; T_1 and T_0 is the final and initial temperature readings, respectively, °F; and α_G is the thermal coefficient of a vibrating wire strain gage, 10^{-6} in./in./˚F.

To verify the acceptance of the employed method, the setting time obtained from the employed method was compared with the setting time obtained from the standard penetration resistance test. For this purpose, the data collected in the Forth Worth section was used. Based on the periodic penetration resistance measurements after concrete placement, the follow equation for the fitting curve was derived (Kim and Won, 2007):

$$t_S = \frac{\log(0.7154 \cdot R)}{0.01147} \quad \text{(Eq. 5.2)}$$

in which, t_S is the final setting time, min.; and R is the penetration resistance, psi.

Using Eq. 5.2, it was identified that the final setting time, when the penetration resistance reaches 4000 psi as specified in ASTM C403, is 301 minutes, which quite well agrees with the final setting time estimated by the employed method, 279 minutes.

5.1.2 Identification of Strain Components

5.1.2.1 Evaluation of Stress-Independent Strain History

To measure each strain component of concrete in the field, VWSGs, INC, and PNC were employed in the test sections. While the VWSGs were installed at the top, middle, and bottom of the pavements, the NCs were placed only at the mid-depth due to the size limitation. Because the method implemented in the field experimental program was only valid for presenting the strain history at the depth where NCs are placed, the thermal and shrinkage strains at the top and bottom could not be directly measured. Thus, the simple relations presented in Eqs. 3.6 and 3.13 were used to estimate the thermal and shrinkage strain histories based on the measured temperature and RH variations.

The CTE for Eq. 3.6 was determined by the slope of the linear regression between temperature and strain (Won, 2005) collected from the INC. Because the CTE of concrete is not constant but varies with age (Kada et al., 2004), internal RH level (Meyers, 1950; Grasley and Lange, 2007; Sellevold and Bjøntegaard, 2006; Yeon et al., 2009), and heating/cooling phases (Emborg, 1989), the CTE averaged for the entire testing period was chosen for thermal strain evaluations.

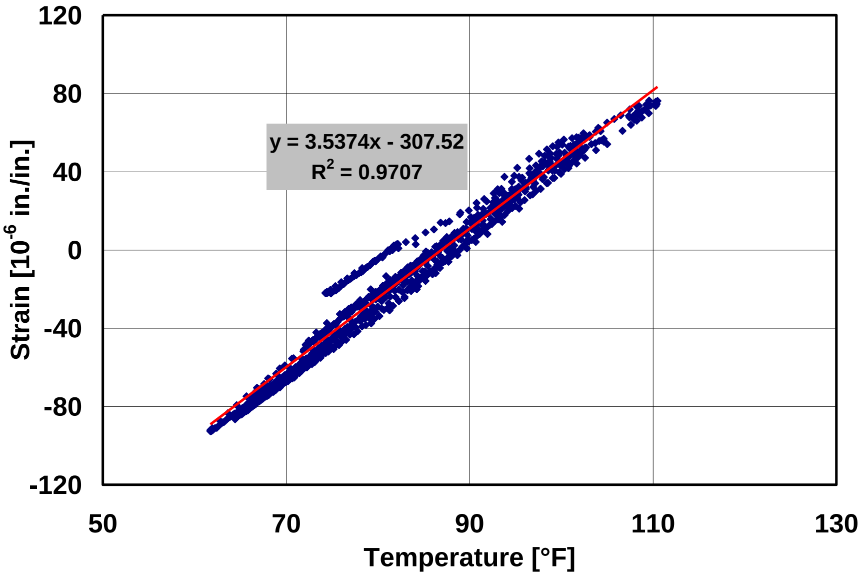

Figure 5.2: *Determination of coefficient of thermal expansion*

To determine the hygral shrinkage coefficient of concrete for Eq. 3.13, a separate prismatic specimen was fabricated using the same concrete material used in the actual constructions. The schematic of the specimen was shown in Figure 3.15. The specimen was equipped with RH sensors at different depths to monitor the changes of RH in the cross-section with time. Also, a VWSG was placed in the longitudinal direction at the center of the cross-section to measure the corresponding sectional average shrinkage strains. Figure 5.3 presents the specimen molds equipped with RH sensors for RH measurement (left) and vibrating wire strain gage for strain monitoring (right).

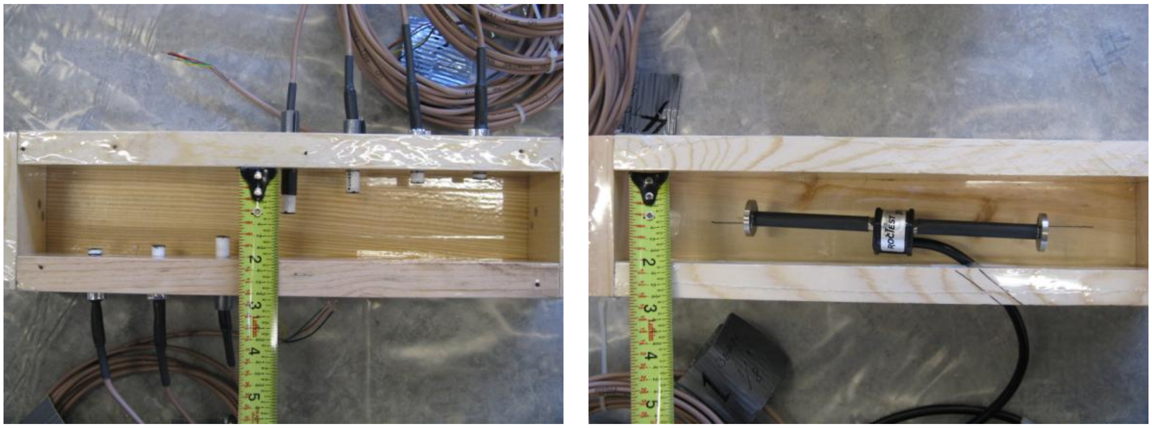

Figure 5.3: *Testing setup for hygral shrinkage coefficient measurement*

Once the specimens were cured for a few days, they were demolded and exposed to the controlled ambient temperature and RH (73 °F and 50 % RH) in a symmetric drying condition. Because of the poor diffusivity of concrete, a non-uniform but symmetric RH gradient distribution was obtained along the depth of the specimen as presented in Figure 5.4.

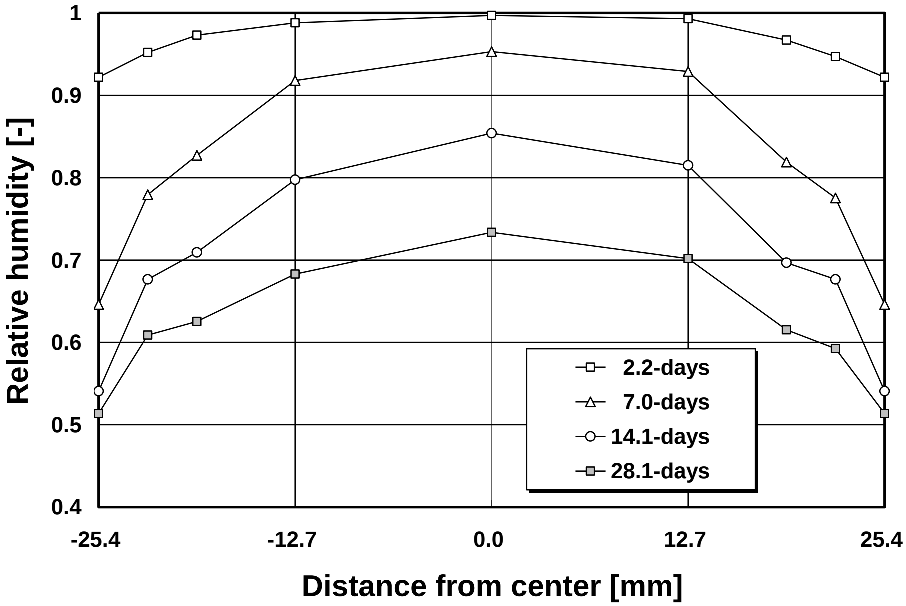

Figure 5.4: *Measurement of RH distribution over the cross-section* (Choi, 2010)

The obtained non-uniform RH distribution was converted to the sectional average RH value. The sectional average RH in the cross-section was calculated as follows (Choi and Won, 2010):

$$h_i^{avg} = \frac{1}{A}\int h_i(z)dA \qquad \text{(Eq. 5.3)}$$

where, h_i^{avg} is the sectional average RH; *A* is the total area of the cross-section; and $h_i(z)$ is the distribution of the RH in the section of interest.

Then, the sectional RH value was compared with the average drying shrinkage strain occurred in the cross-section as shown in Figure 5.5. The slope of the linear regression between RH and drying shrinkage strain was defined as the hygral shrinkage coefficient. It was found that the slope of the curve was not constant over the entire RH levels; from 100 % to about 95 % RH, the slope was slightly steeper than the slope at the lower RH levels because the concrete's modulus was quite low (Choi and Won, 2010).

For this reason, the hygral shrinkage coefficient was determined once the relationship between RH and shrinkage strain was stabilized as indicated in Figure 5.5 (b).

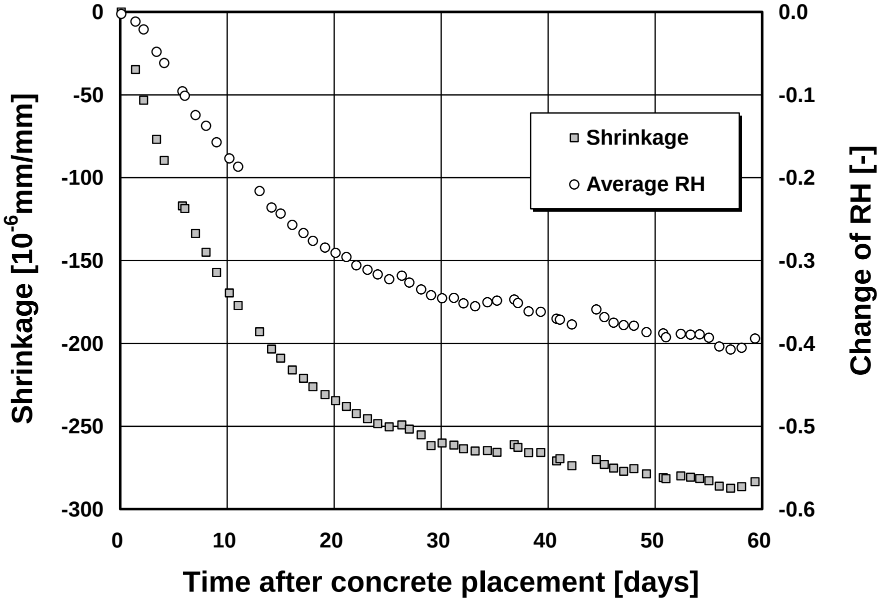

(a) Measurement of RH and shrinkage strain (Choi, 2010)

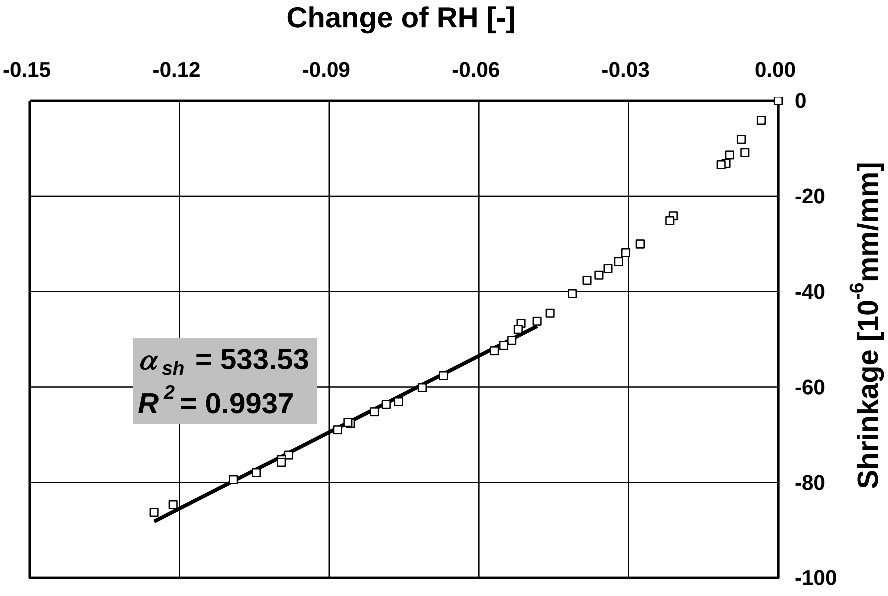

(b) Determination of hygral coefficient from prism specimen (Choi, 2010)

***Figure 5.5**: Determination of hygral shrinkage coefficient*

5.1.2.2 Evaluation of Stress-Dependent Strain History

Based on the identified stress-independent strain histories, the stress-dependent strain histories for each test section were calculated using Eq. 5.4 to evaluate the stress developments:

$$\varepsilon^{\sigma}(t) = \varepsilon(t) - \varepsilon^{0}(t) \qquad \text{(Eq. 5.4)}$$

where, $\varepsilon^{\sigma}(t)$ is the stress-dependent strain; $\varepsilon(t)$ is the total strain; and $\varepsilon^{0}(t)$ is the stress-independent strain.

Figure 5.6 presents the total strain, stress-independent strain, and stress-dependent stress evaluated in the Fort Worth CRCP section. As expected, it was observed that the actual movement (total strain) of CRCP was quite small, less than 20 microstrain, prior to the occurrence of transverse cracking. This is because the uncracked CRCP is long enough to have high friction with the underlying layer. On the other hand, it was found that the stress-independent strain measured by the NC more fluctuated than the total strain because it was completely separated from the surroundings. The difference between the actual and free strain is the stress-dependent strain, which results in restrained stress developments in the CRCP.

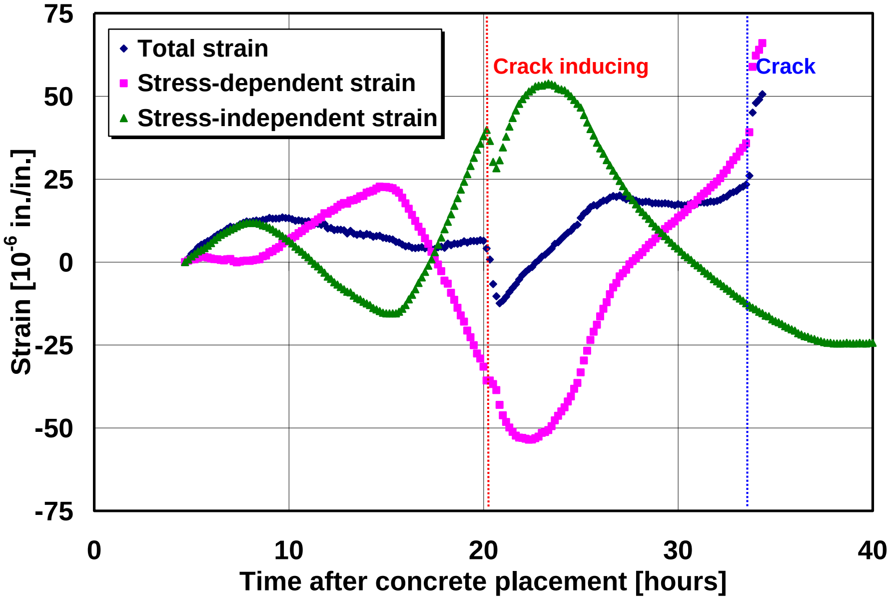

(a) Strain components measured at 1 in. below the top surface

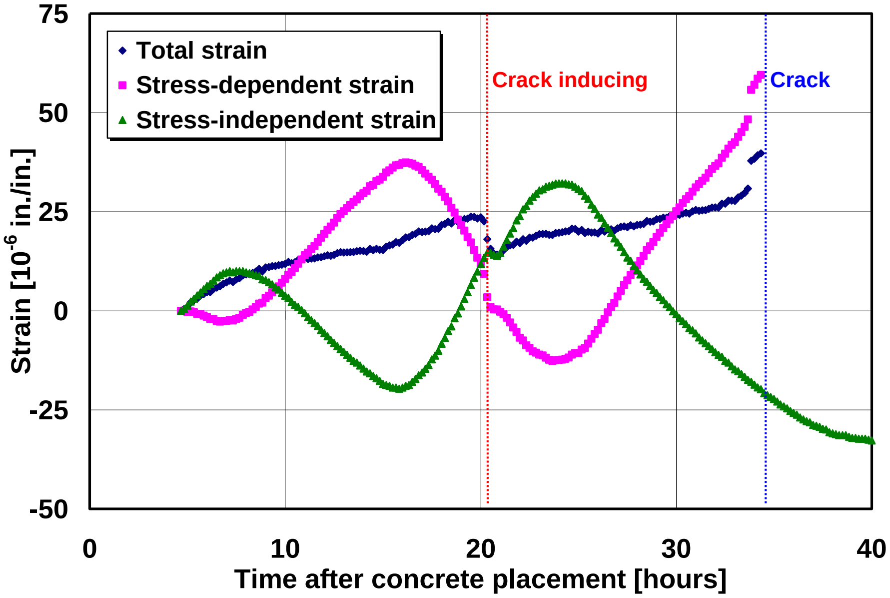

(b) Strain components measured at mid-depth

Figure 5.6: *Strain histories measured in Fort Worth section*

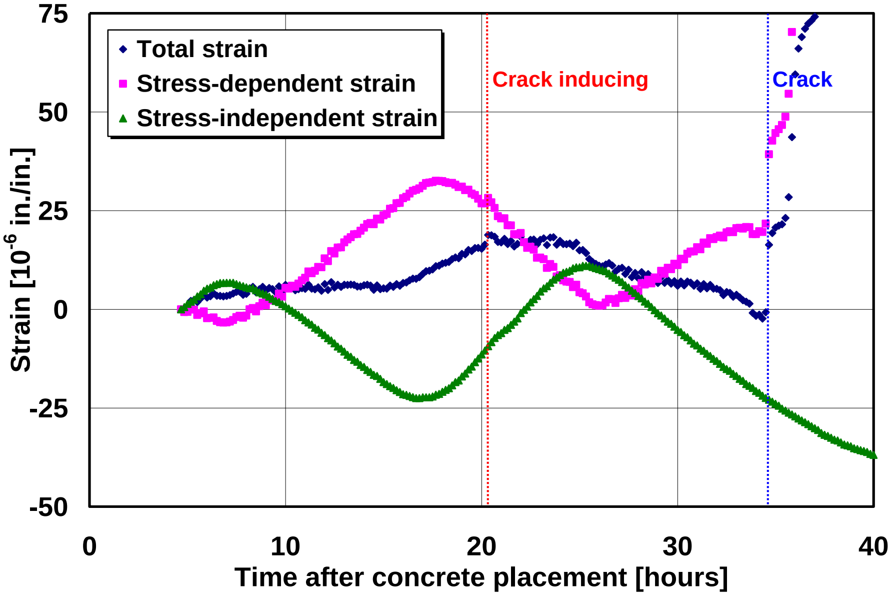

(c) Strain components measured at 1 in. above the bottom surface

***Figure 5.6 (cont.)**: Strain histories measured in Fort Worth section*

Figure 5.7 presents the data collected from the Austin-B section; as described previously, the Austin-B section is the 18-ft. long, 18-ft. wide, and 6-in. thick bonded concrete overlay slab placed over an existing asphalt pavement. The result showed that the variation of the total strain was almost similar to that of the stress-independent strain. This is because a very weak external restraint is applied to the slab due to the relatively small slab dimensions. This behavior resulted in a small amount stress-dependent strain development in the concrete element, up to 30 microstrain at 15 days after concrete placement. Also, it is interesting to note that the drying shrinkage strain, estimated by the difference between the stress-independent strain and thermal strain, continued to develop, as expected.

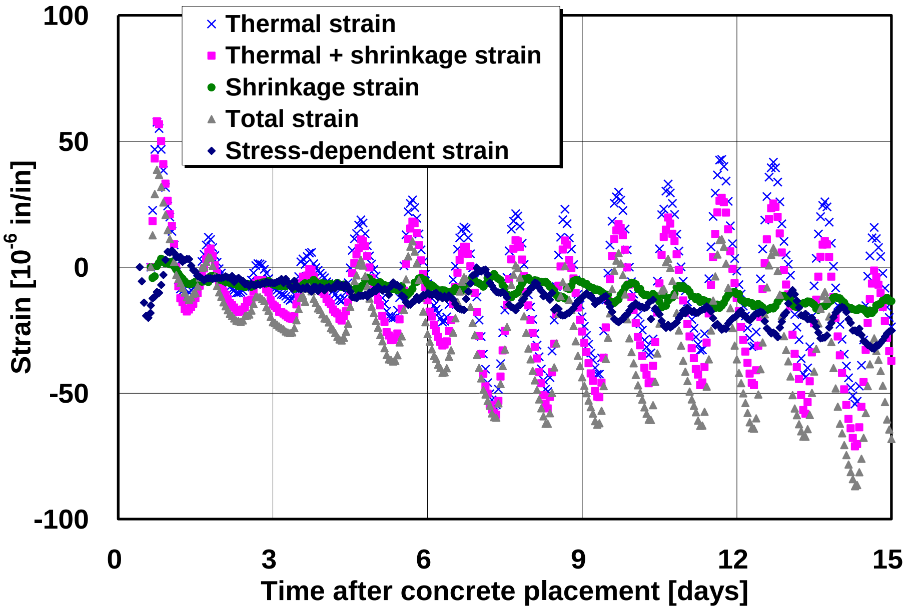

***Figure 5.7**: Strain histories measured in Austin-B project*

Figure 5.8 displays the strain histories obtained from the Hillsboro test section, a 9 in. thick and 300 ft. long post-tensioned prestressed concrete pavement. It is found that the total strain fluctuations due to environmental loading were quite significant over the measurement period. This is because the degree of restraint of the concrete slab was too small as the PTCP uses a single layer of polyethylene sheet placed underneath the concrete slab to reduce the loss of post-tensioning force. In addition, there were negligible restraints from tendons, since they were discontinuous at transverse joints. Also, it is noted that the twice post-tensionings applied at the equivalent ages of 0.58 and 3.08-day made the stress-dependent strain continue to develop in the compression side throughout the overall monitoring period.

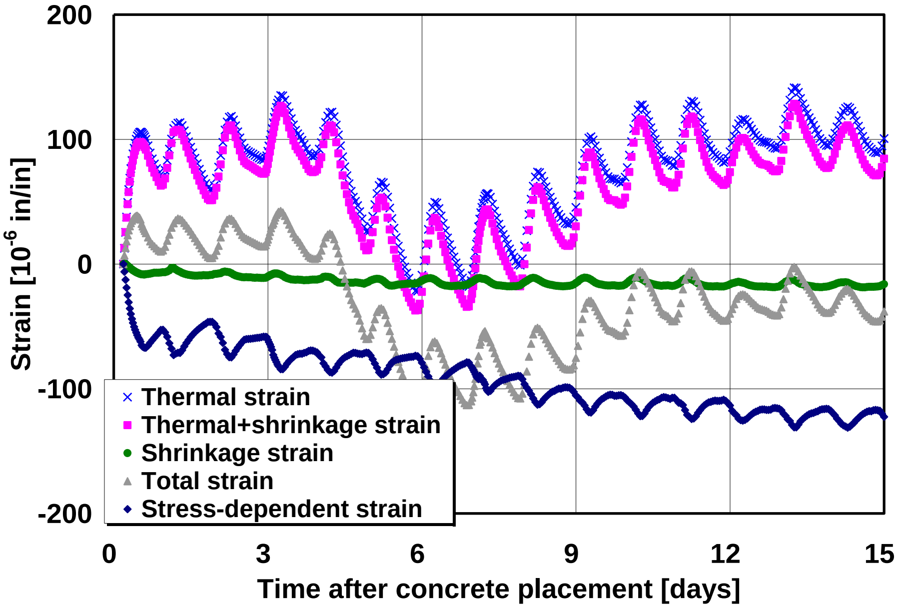

Figure 5.8: *Strain histories measured in Hillsboro project*

5.2 ANALYSIS OF STRESS HISTORY BASED ON MEASURED STRAIN HISTORY

5.2.1 Concept of Stress Calculation

When a concrete member is subjected to environmental loading such as temperature and moisture changes, volume changes take place. If these volume changes are not externally restrained and if no temperature and moisture gradient exists in the concrete member (Case 1 of Figure 5.9), the strain will be equal to the sum of thermal strain and drying shrinkage strain. In this case, no stress will arise in the member since the strain does not include any of the stress-dependent strain components – elastic and creep strain. On the other hand, if the concrete member is fully or partially restrained without any temperature and moisture gradients (Case 2 of Figure 5.9), stresses will arise because the concrete cannot be at the position where it originally was ($\varepsilon^0(t)$). Thus, the strain discrepancy between the $\varepsilon^0(t)$ and $\varepsilon(t)$ causes the stress in the concrete member coupled with its mechanical properties.

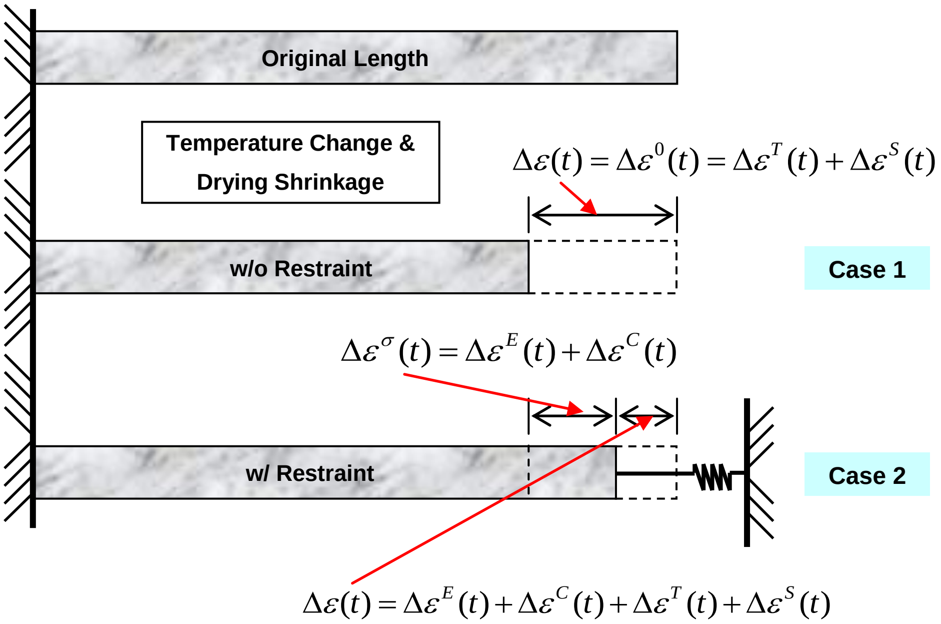

***Figure* 5.9:** *Effect of restraint conditions on strain and stress*

5.2.2 Stress-Strain Constitutive Relation in Aging Viscoelastic Material

With a known stress-dependent strain history, the stress evolution due to elastic and creep strain can be calculated based on the principle of superposition. The basic mathematical formulation can be expressed as Eq. 5.5. Again, the actual strain measured in a concrete element is the total strain, and the stress-dependent strain can be determined by subtracting the stress-independent strain from the total strain. The terms in the square bracket of Eq. 5.5 indicates the stress-dependent strain.

$$\begin{aligned} \sigma(t) &= \int_0^t R(t,t')[d\varepsilon(t') - d\varepsilon^0(t')] \\ &= \int_0^t R(t,t')\, d\varepsilon^\sigma(t') \end{aligned} \qquad \text{(Eq. 5.5)}$$

where, $\sigma(t)$ is the stress history; and $R(t,t')$ is the relaxation function which describes the stress at time t due to a stress-dependent strain increment $d\varepsilon^\sigma(t')$ imposed at time t'.

Eq. 5.5 indicates that each stress increment induced by the small stress-dependent strain increment $d\varepsilon^{\sigma}(t')$ becomes $R(t,t')\ d\varepsilon^{\sigma}(t')$, and summing all of these stress increments over the age will result in the actual stress development, which includes stress relaxation effects.

5.2.3 Numerical Calculation of Stress History

Several approaches have been introduced to calculate the time-dependent stresses based on the measured strain histories, i.e. effective modulus method, age-adjusted effective modulus method, increment method, or step-by-step method (Bažant, 1972a; Bažant, 1972b; Bažant and Cedolin, 1991; Ghali et al., 2002). In this study, the step-by-step numerical method was used to solve the stress-strain relation because it accurately evaluates the stress history subject to a varying strain history even in aging concretes, considering stress relaxation due to creep (Bažant, 1972a). For prompt and accurate calculation of the step-by-step numerical formulation, the calculating algorithm was programmed with the Visual Fortran 6 and run throughout the analysis period. Figure 5.10 schematically shows how the step-by-step method works for the stress history evaluation.

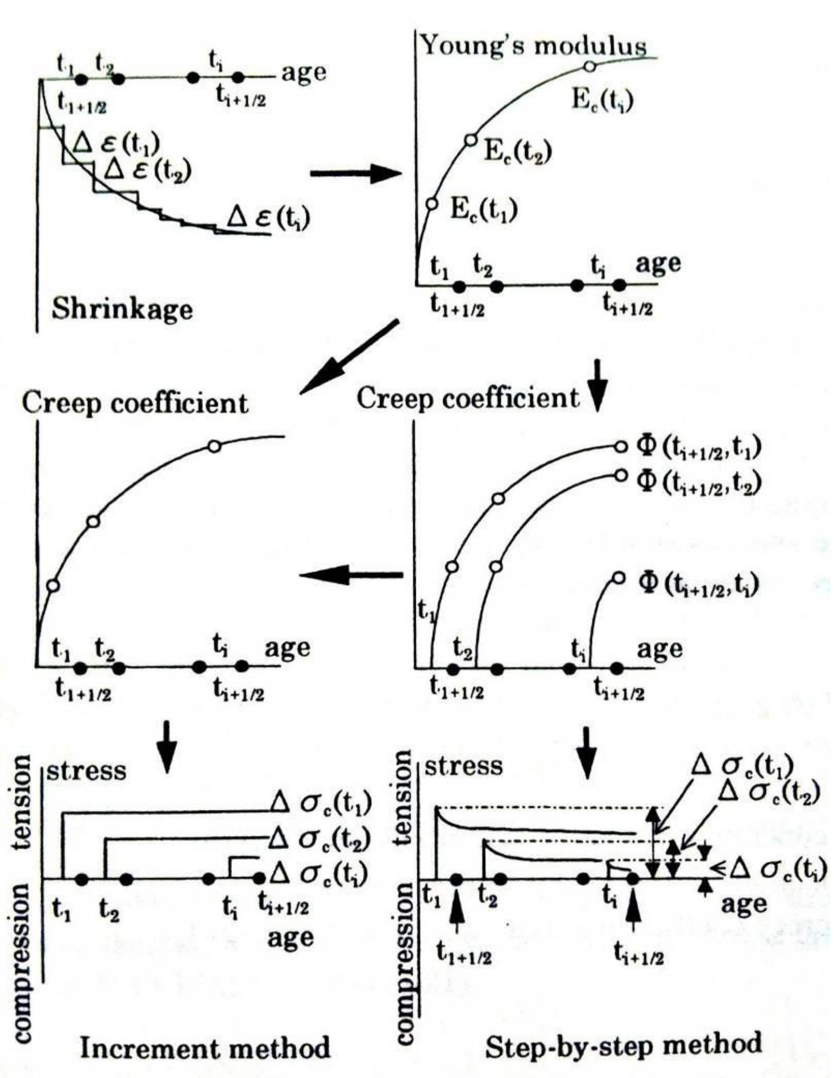

Figure 5.10: *Concept of stress calculation using step-by-step method*
(Tazawa, 1999)

The total strain in time t due to the applied stresses and stress-independent deformations can be expressed as follows (Ghali et al., 2002):

$$\varepsilon(t) = \sigma(t_o)\frac{1+\varphi(t,t_0)}{E(t_0)} + \int_0^{\Delta\sigma(t)} \frac{\varphi(t,t')}{E(t')}\,d\sigma(t') + \varepsilon^0(t,t_0) \qquad \text{(Eq. 5.6)}$$

in which, t_0 and t are the concrete ages at initial loading and when the strain is considered, days; $\sigma(t_o)$ is the initial stress due to initial loading at t_0, psi; $\varphi(t,t')$ is the creep coefficient in time t due to loading at age t'; $E(t')$ is the elastic modulus of concrete at age t', psi; $d\sigma_c(t')$ is the stress increment applied at age t', psi; and $\varepsilon^0(t,t_0)$ is the stress-independent strain occurred between ages t_0 and t, 10^{-6} in./in..

If Eq. 5.6 is introduced into the form of the step-by-step method by dividing the period of interest $(t - t_0)$ into short intervals, the strain at the end of j^{th} interval can be written as follows:

$$\varepsilon(t_{i+1/2}) = \sum_{j=1}^{i}\left((\Delta\sigma)_j \frac{1+\varphi(t_{i+1/2},t_j)}{E(t_j)}\right) + \varepsilon^0(t_{i+1/2},t_0) \qquad \text{(Eq. 5.7)}$$

where, $t_{j-1/2}$, t_j, and $t_{j+1/2}$ are the instant at the start, the middle, and the end of the jth interval, respectively.

To find the stress increment in each interval, Eq. 5.7 can be altered by extracting the last term out of the summation:

$$\varepsilon(t_{i+1/2}) = (\Delta\sigma)_i \frac{1+\varphi(t_{i+1/2},t_i)}{E(t_i)} + \sum_{j=1}^{i-1}\left((\Delta\sigma)_j \frac{1+\varphi(t_{i+1/2},t_j)}{E(t_j)}\right) + \varepsilon^0(t_{i+1/2},t_0) \qquad \text{(Eq. 5.8)}$$

Rewrite the Eq. 5.8 in terms of $(\Delta\sigma)_i$, then the stress increment at i^{th} interval becomes:

$$(\Delta\sigma)_i = \frac{E(t_i)}{1+\varphi(t_{i+1/2},t_i)}\left[\varepsilon(t_{i+1/2}) - \varepsilon^0(t_{i+1/2},t_0) - \sum_{j=1}^{i-1}\left((\Delta\sigma)_j \frac{1+\varphi(t_{i+1/2},t_j)}{E(t_j)}\right)\right] \qquad \text{(Eq. 5.9)}$$

As previously mentioned in Chapter 3, various mathematical models for estimating the creep coefficient of concrete have been suggested. In this study, the basic creep model suggested by CEB-FIP Model Code 90 (CEB, 1993) was employed to estimate the creep coefficient. It was assumed that the creep coefficient in compression and in tension is identical because little information has been available on the tensile creep behaviors. Once the stress increments at each step were calculated using Eq. 5.9, the stress history was determined by summing each stress increment:

$$\sigma(t_{i+\frac{1}{2}}) = \sum_{j=1}^{i} (\Delta\sigma)_j \qquad \text{(Eq. 5.10)}$$

5.3 VALIDATION OF PROPOSED FIELD INSTRUMENTATION AND ANALYSIS METHOD

In order to validate the testing set-up employed in this field experimental program, a validation was performed using the data obtained from the Austin-B section by comparing the stress measured from a stressmeter with the stress calculated based on measured strain histories. The stressmeter is a device which is designed to directly monitor the stress development in concrete due to stress-independent volume changes, considering actual modulus development and viscoelastic behavior. To identify the actual stress development in concrete, a stressmeter was placed at a 4.5-in. depth from the slab surface. Additionally, VWSGs and NCs were installed at the same depth with the stressmeter to measure the total strain and stress-independent strains, respectively. Figure 5.11 shows the testing setup installed in the Austin-B project. With the obtained strain readings from the slab and the concrete inside the embedded NCs, the stress history of the bonded overlay slab was evaluated using the step-by-step numerical method.

Figures 5.12 (a) and (b) respectively show the measured temperature profile and corresponding stress history at 4.5 in. depth for the first 25 days, obtained from both evaluation methods, i.e. the direct stress measurement with stressmeter and the calculated stress using strain-based approach. It is noted that the stress history evaluated with the viscoealstic analysis was quite similar to the reference stress development measured by the stressmeter, even though some difference was observed in the first 3 days. The difference at very early-age might be due to the relatively low modulus of young concrete compared to the high gage stiffness. At other ages, it is also observed that the stress evaluated by strain-based approach resulted in slightly higher daily stress fluctuations than the use of stressmeter. It may be explained by the contribution of the delayed deformation and time-dependent variation of CTE. This issue will be addressed in detail in the following chapter. Despite the above limitations, the result obtained from strain-based approach showed a quite good agreement with the reference measurements when the creep effect was considered.

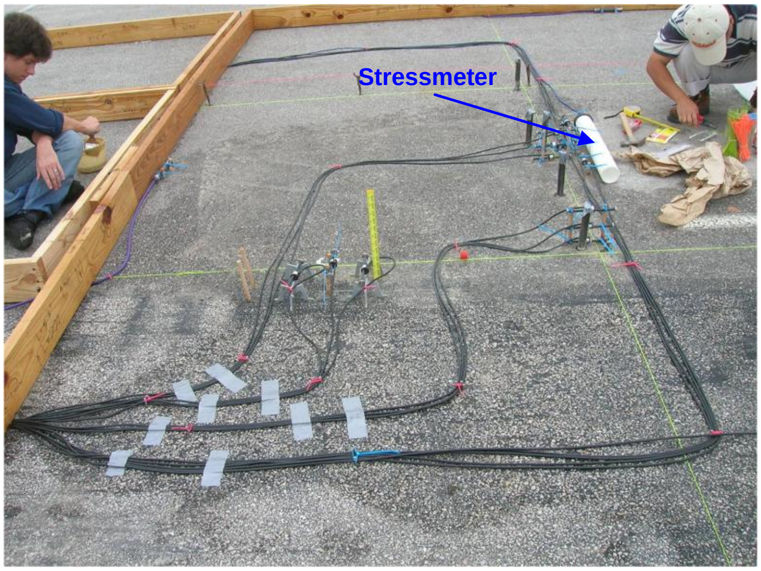

(a) Testing setup for Austin-B project

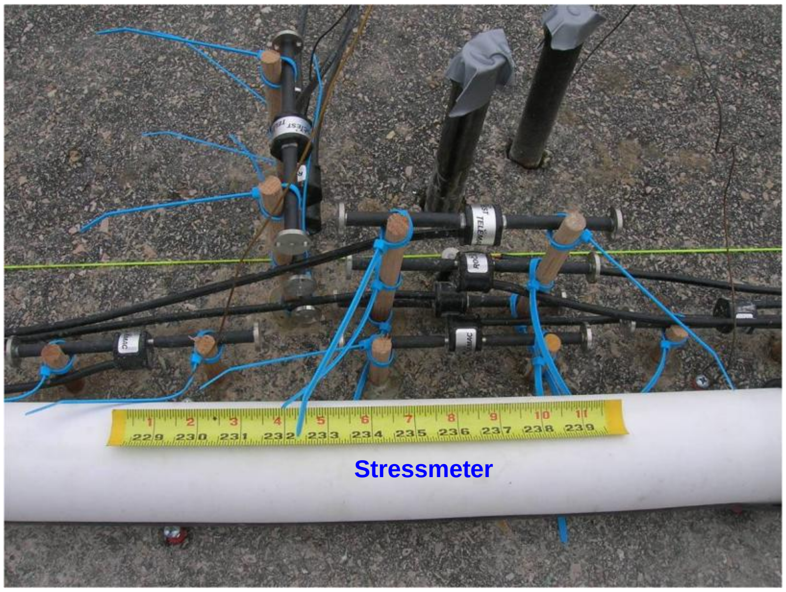

(b) Stressmeter and VWSGs for Austin-B project

Figure 5.11: *Testing setup for Austin-B project*

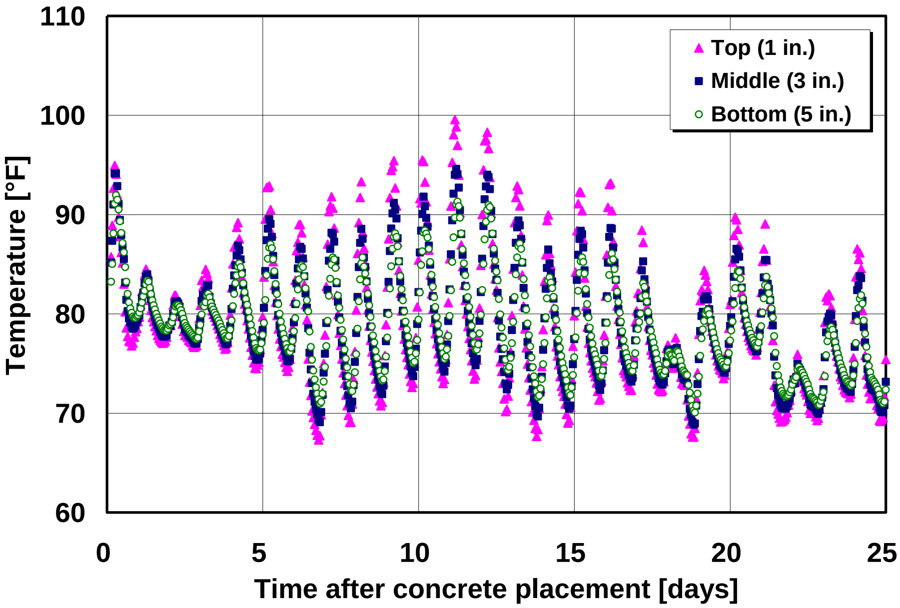

(a) Temperature measured at different depth for initial 25 days

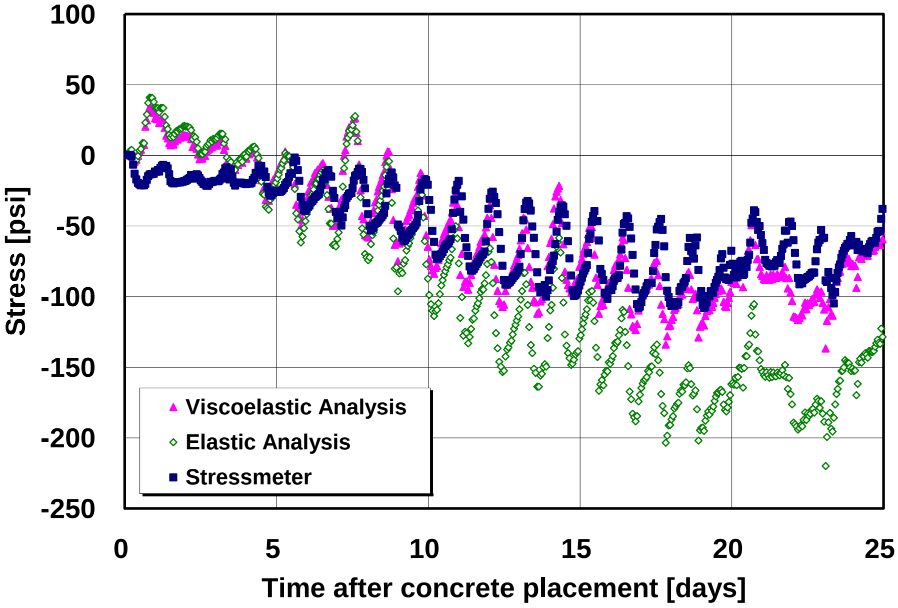

(b) Stresses evaluated from stressmeter and strain-based approach

Figure 5.12: *Validation of proposed method using reference data obtained from stressmeter*

5.4 EVALUATION OF EARLY-AGE STRESS DEVELOPMENT AND ZERO-STRESS TEMPERATURE

Figure 5.13 shows the measured early-age stress development and zero-stress temperature (point) for each of the projects. In order to check the validity of the ZST prediction model suggested by MEPDG, the ZST values determined for each test section were compared with those predicted in accordance with Eq. 3.1. Also, the reduction factor, R_d, was calculated using Eq. 3.2 to compare with the previous work by Schindler. The measured and predicted ZST and their percentage difference are summarized in Table 5.1 and Figure 5.14. Also, the calculated reduction ratio for each project is presented in the table. As can be seen in the table, about 7 °F to 25 °F differences are observed between the measured and predicted ZST values. Specifically in the Hillsboro project, the percent difference was as high as 24.5 °F, which is quite substantial. As for the reduction ratio, the values were nearly 100 % for all the projects, which means that the ZST was very close to the maximum temperature.

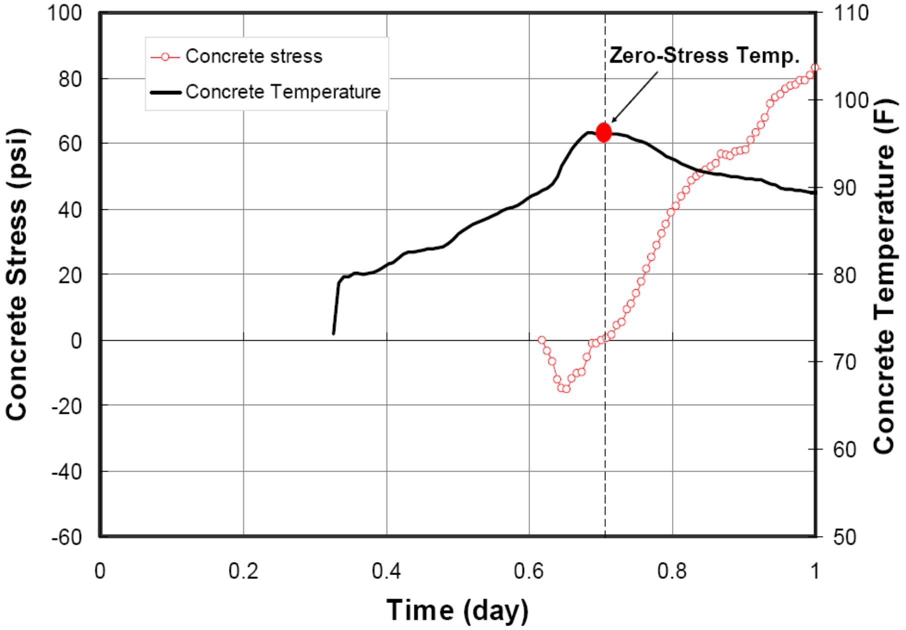

(a) Austin-A project (top) (Nam, 2005)

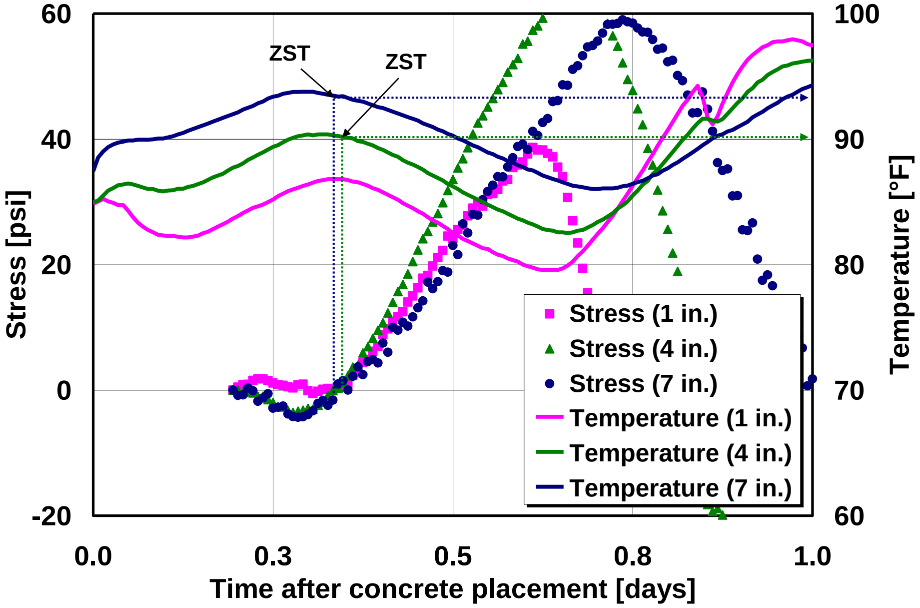

(b) Fort Worth project (top, middle, and bottom)

Figure 5.13: *Early-age stress development and ZST evaluation*

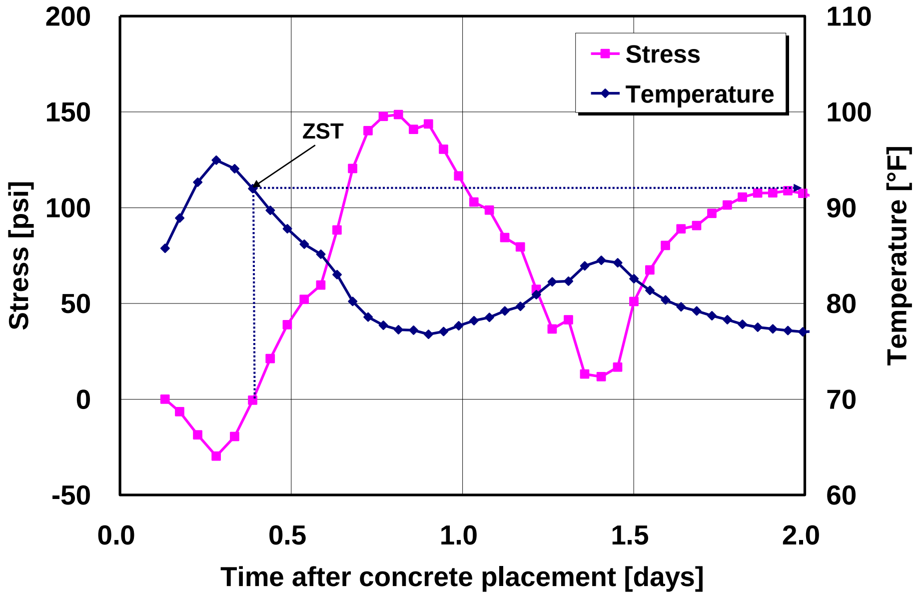

(c) Austin-B project (top)

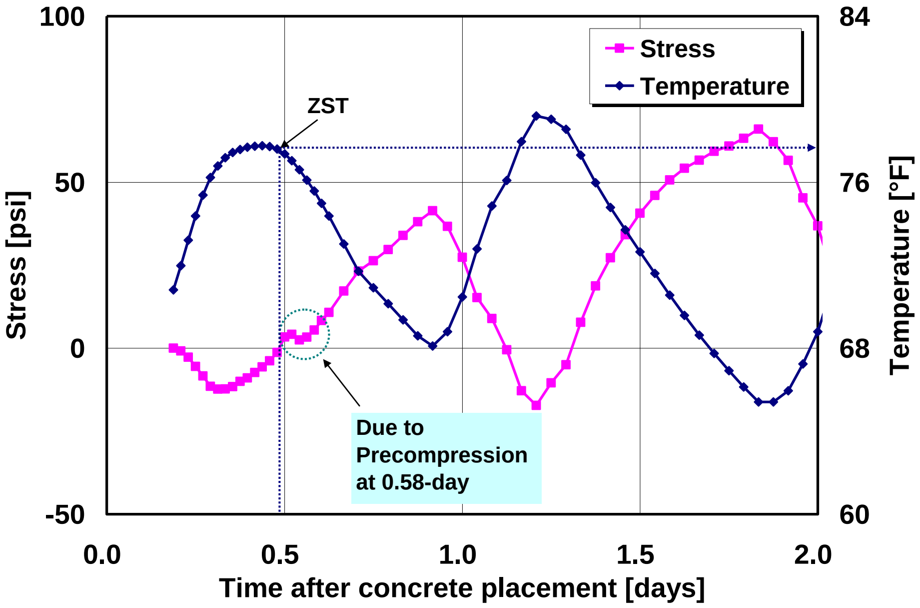

(d) Hillsboro project (bottom)

Figure 5.13 (cont.): *Early-age stress development and ZST evaluation*

Table 5.1: *Summary of the measured and predicted ZST for each project*

	Austin-A	Fort Worth	Austin-B	Hillsboro
CC (lb/yd^3)	450	446.5	470	482
MMT (°F)	78	76	76	75
Predicted ZST (°F)	103.9	101.3	102.6	102.1
Measured ZST (°F)	96.6	90.3 (M)/ 93.3 (B)	92.0	77.6
Difference (%)	7.0	10.9 (M)/ 7.9 (B)	10.3	24.0
R_d (%)	99.8	99.9 (M)/ 99.2 (B)	96.9	99.7

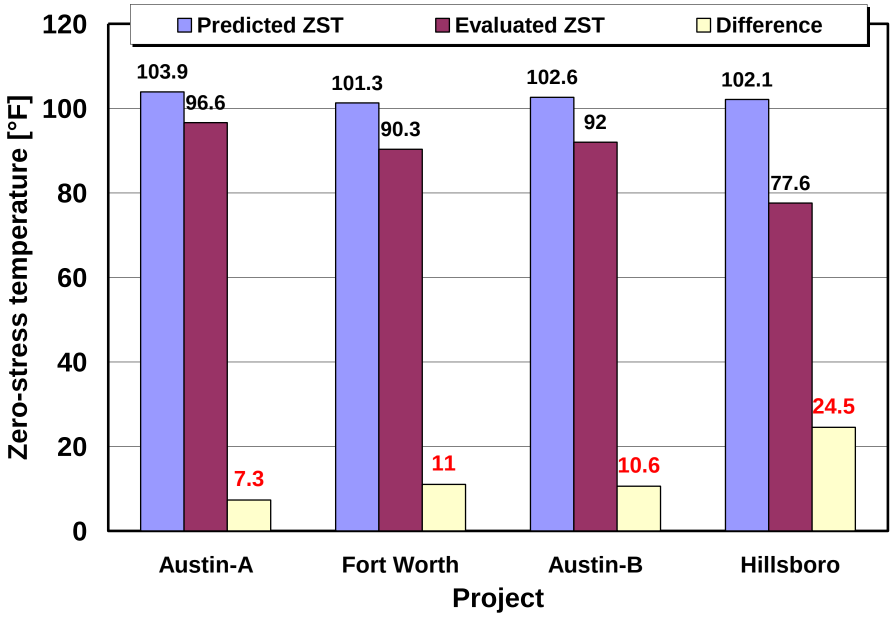

Figure 5.14: *Comparison of measured and predicted ZST for each project*

5.5 SUMMARY

This chapter focused on the in-situ evaluation of early-age concrete stress developments in continuously reinforced concrete pavements (CRCP), bonded overlay slab, and post-tensioned concrete pavement (PTCP) in order to find a zero-stress temperature (ZST). Since the strain measured directly from a concrete element contains both stress-dependent strain and stress-independent strain, primary research efforts have been made to identify the stress-dependent strain history out of the total strain. For this purpose, non-stress cylinders (NC) which are specially designed to measure the strain-dependent strain component were employed.

With the identified strain history, a stress history was calculated with a step-by-step numerical method considering a time-dependent behavior – creep and relaxation – of concrete. The reference stress data monitored with a stressmeter validated the proposed experimental and stress analysis methodologies.

To evaluate the reliability of the current ZST prediction model, the ZST evaluated with the field experiment was compared with the ZST estimated with the current model. The result showed that about 7 °F to 25 °F difference existed between the measured and predicted ZST values, and this finding suggests a need for a more realistic and accurate model development.

Chapter 6: In-Situ Measurement of Coefficient of Thermal Expansion in Hardening Concrete and Its Effect on Early-Age Stress Development

The coefficient of thermal expansion (CTE) has a substantial effect on early-age cracking tendency and post-cracking behavior of concrete structures. In this chapter, a time-dependent variation of CTE in hardening concrete is examined based on a series of field experiments. A non-stress cylinder (NC) was employed in the field structure to measure the in-situ free thermal strain development. To examine the effect of the time-dependent variations of CTE on early-age thermal stress build-up, the study presented in this chapter quantitatively investigated the difference in thermal stress development between the case when the CTE is constant and the case when the CTE varies throughout the measurement period.

6.1 INTRODUCTION

When concrete is placed in the field, it experiences significant volume changes, especially at early-age, due to variations in temperature and internal RH (Springenschmid 1995; Springenschmid, 1998). It is well known that autogenous shrinkage can be significant in cement-based materials with a low water-to-cement ratio such as HPC. Among the factors related to the volume changes in concrete such as thermal, drying shrinkage, and autogenous deformations, the thermal effect can be dominant in determination of the early-age cracking potential in concrete structures due to heat of hydration of portland cement and its dissipation, coupled with rapid evolution of concrete's mechanical properties (Breitenbücher, 1990; Emborg, 1989; Springenschmid, 1995; Springenschmid, 1998).

As has been reviewed throughout the literature studies in Chapter 3, it is recognized that various parameters affect the CTE of cement-based systems. They include internal RH, age of concrete, temperature, heating and cooling paths, and specimen shape. In this chapter, an experimental approach to evaluate the time-dependent variation of CTE in hardening concrete was carried out based on a series of in-situ free thermal deformation measurements using NC (Choi and Won, 2010). Furthermore, the effect of time-dependent variations of CTE, which may contribute to the early-age thermal stress build-up, in turn, cracking potential of concrete structures, was investigated. It is expected that such an in-situ approach will provide more practical and useful information to comprehensively understand the time-dependent behavior of concrete structures subjected to environmental loading and thus will be helpful to develop more reliable designs of concrete structures.

6.2 EXPERIMENTAL PROGRAM

6.2.1 Testing Sites and Materials

A series of field experiments was conducted in three different construction sections: Fort Worth section, Austin-B section, and Hillsboro section. The detailed information of testing sites and used materials are summarized in Tables 4.1 and 4.2, respectively.

6.2.2 Experimental Method

As described in Chapter 3 with Eq. 3.13, the measured total strain consists of four independent strain components, i.e., elastic strain, creep strain, shrinkage strain, and thermal strain, and these components are additively related.

To separate the thermal strain from the measured total strain, INC was employed in the field testing. As explained in Chapter 4, the INC was designed to perform in such a way that the concrete inside the INC is separated from the surrounding concrete so that the concrete inside the INC can move without any influence of external restraint such as base friction and restraint from an adjacent structure. Since the INC is designed not to allow the moisture exchange with the surrounding concrete, the free strain measured from the concrete inside the INC represents only thermal strain at the depth of installation.

The proposed test apparatus was implemented in the field experiments to measure the in-situ free thermal strain development. Figure 6.1 shows the actual field instrumentation of INC in the Hillsboro project. As can be seen in the figure, the INC was placed at the mid-depth of the slab prior to concrete placement. As previously described, a VWSG was installed at the center of the cross-section of INC in the longitudinal direction to monitor the free thermal strain variations in the concrete inside the INC.

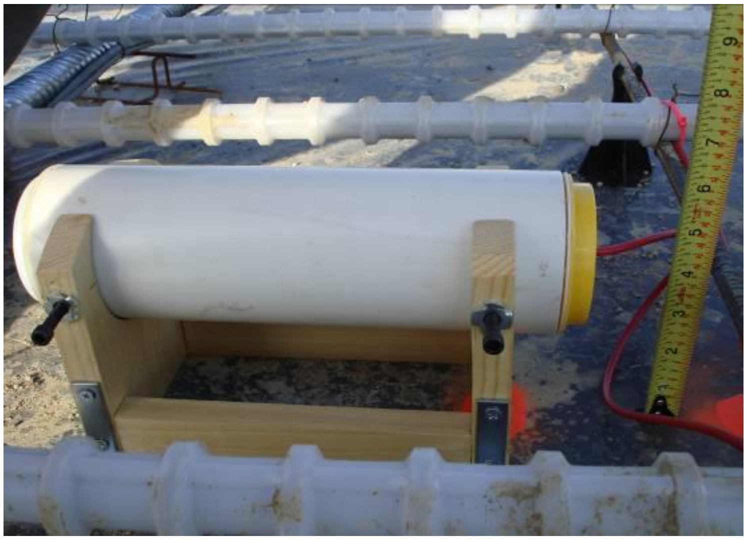

***Figure 6.1**: Field testing setup for free thermal strain measurement with INC*

Along with the strain, a temperature development of the concrete inside the INC was simultaneously measured using a built-in thermostat of the VWSG. For a thermal stress calculation, total strain was also measured at the same depth with the INC by installing an additional VWSG. To monitor the temperature profile in the testing slab, three temperature sensors were embedded at different depths, i.e., 1 in. below the top surface, mid-depth, and 1 in. above the bottom surface. Figure 6.2 illustrates the testing setup of INC, temperature sensor, and VWSG implemented in the field testing, and Figure 6.3 shows the typical relationship between the temperature and corresponding free thermal strain measured by the proposed testing setup.

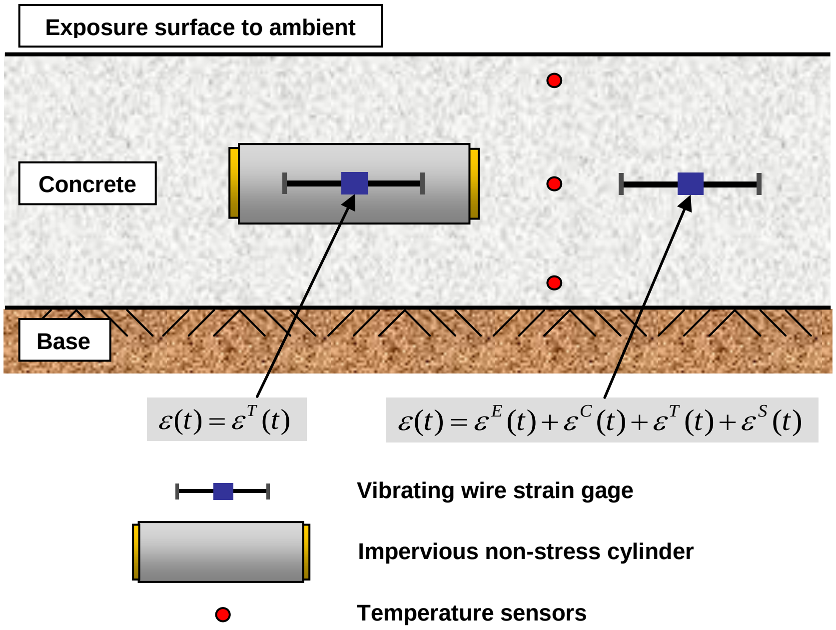

***Figure 6.2**: Field testing setup*

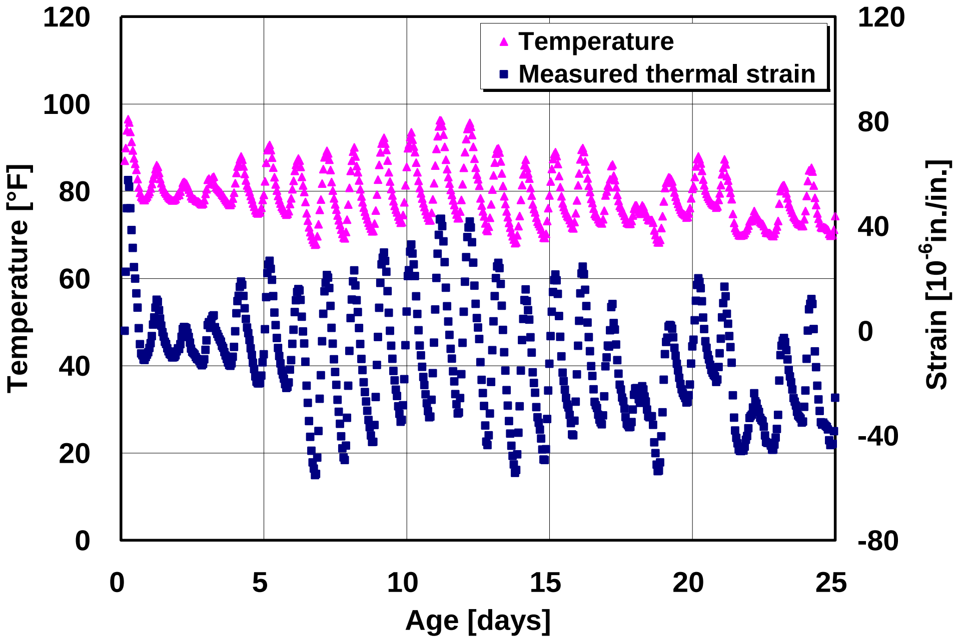

***Figure 6.3**: Typical measured temperature and corresponding free thermal strain using INC*

6.2.3 General Discussions on the Proposed Method

Previous research studies on characterization of thermal volume changes were mainly performed on cement paste or mortar (Choktaweekarn and Tangtermsirikul 2009; Grasley and Lange 2007; Loser et al. 2010; Maruyama and Teramoto 2011; Meyers 1950; Sabri and Illston 1982). There are several advantages of using cement paste or mortar as testing materials.

First, the cross-sectional dimensions of a specimen can be appreciably reduced because cement paste and mortar do not incorporate coarse aggregates into the mixture. As the specimen has a small cross-section, it will take a shorter period to achieve thermal equilibrium throughout the specimen. Especially, when air is used as a medium for temperature control of the specimen, selection of the small cross-section is essential to have the specimen prompt thermal equilibrium. It is because air has a low heat capacity. In the previous research works, diverse cross-sectional thicknesses from 0.4 in. to 1.25 in. were employed in the testing to address the thermal equilibrium issue.

Also, the specimen with a small cross-section can minimize the influence of internal restraint, which results from a nonlinear thermal gradient, on the length change measurements. If a nonlinear thermal gradient exists in the cross-section of a specimen, an addition strain component – a self-equilibrium strain – could take place due to the plane assumption (Ghali et al. 2002), making the accurate measurements of free thermal deformation quite difficult.

Moreover, the use of cement paste or mortar can produce a more homogeneous bulk structure, which enables the more precise and accurate measurements of temperature and strain of the specimen than the use of concrete which is quite heterogeneous because of the random dispersion of various sized aggregates in the hydrated matrix.

Despite the above benefits of using cement paste or mortar, a cylindrical concrete specimen was used in this study to ensure the practicality and applicability of the experimental work. The circular cross-section with 3 in. diameter of NC was relatively large compared to the cross-sectional dimensions of the specimens employed in the previous studies but was chosen based on the maximum size of coarse aggregate incorporated into the mixtures. It is based on the general belief that the diameter of cross-section has to be at least two to three times larger than the maximum aggregate size in order to accurately measure the realistic and reasonable behavior as a concrete material. Since the cross-sectional dimensions were comparatively large, a slight thermal gradient existed along the depth of the specimen. The maximum positive and negative thermal gradients between the top and bottom of the concrete specimen recorded throughout the measurement period ranged from 4.37 to 6.69 °F and -3.87 to -5.24 °F, respectively. These were small enough to prevent the occurrence of an error in axial length change measurements. Figure 6.4 shows the maximum negative and positive temperature gradient inside the INC measured from the Hillsboro project, which is 9 in. thick.

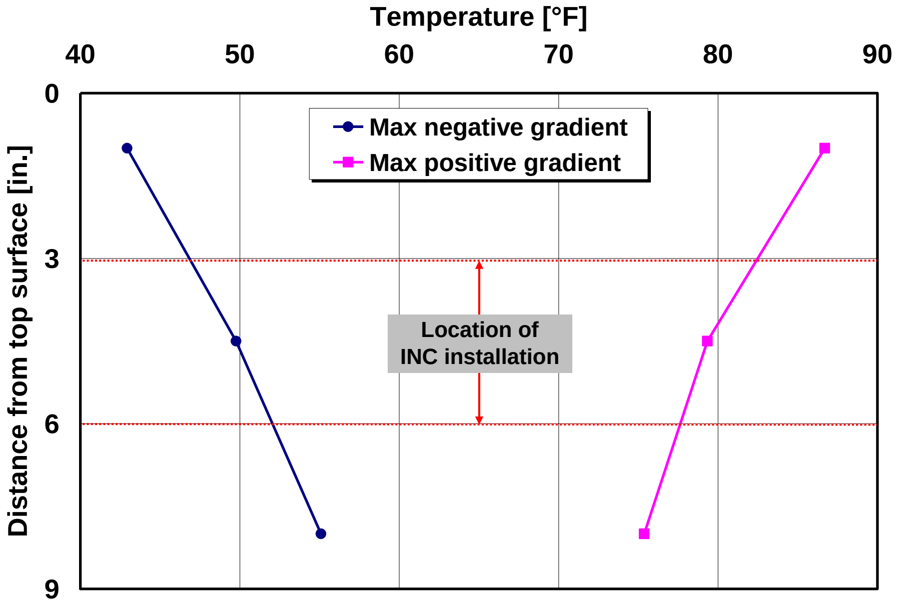

***Figure 6.4**: Temperature distribution through depth at maximum negative and positive temperature gradient inside INC measured in Hillsboro section*

6.3 ANALYSIS OF EXPERIMENTAL RESULTS AND DISCUSSIONS

6.3.1 Thermal Strain Measurement and Determination of CTE

The temperature and corresponding thermal strain developments in the concrete element inside the INC since its final setting was measured using the embedded VWSG. Figure 6.5 displays the experimental data of temperature and thermal strain collected in each test section. Only first 7-day results were presented herein because the CTE is nearly stabilized after this period. As seen in the results, the trend of measured temperature and thermal strain variations was quite similar as expected.

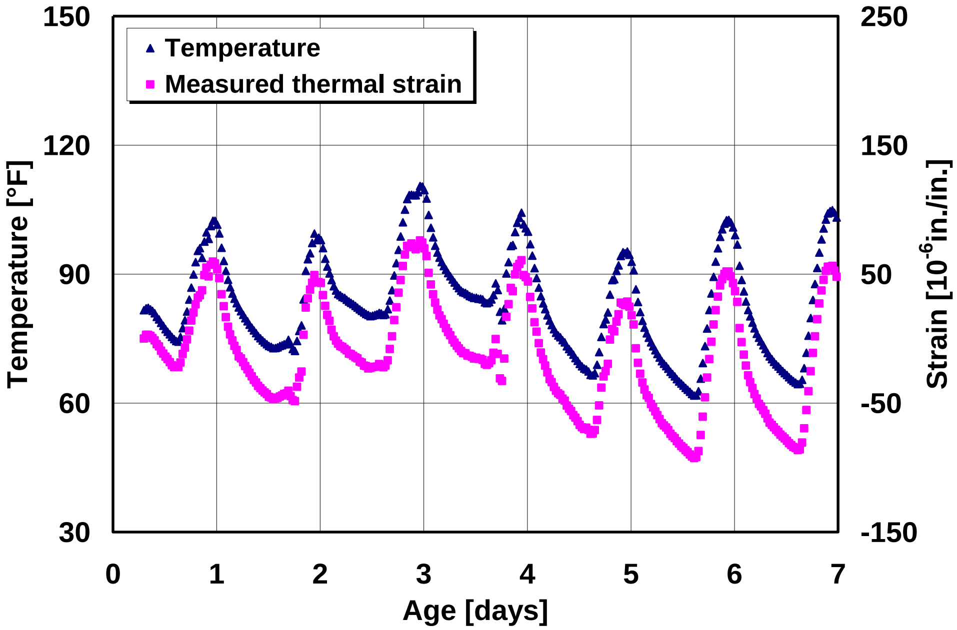

(a) Fort Worth section

***Figure 6.5**: Temperature and corresponding thermal strain measurements*

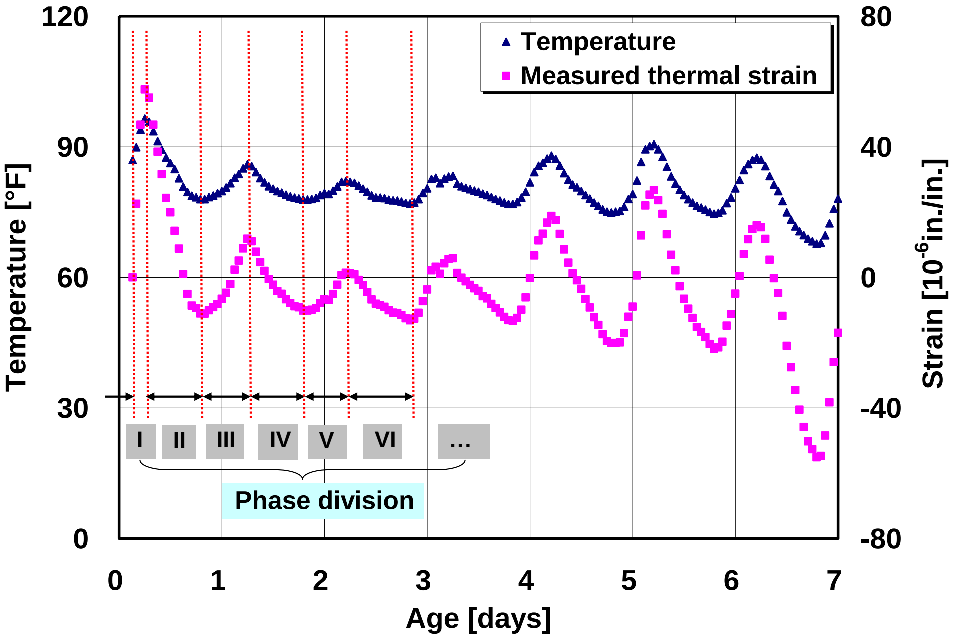

(b) Austin-B section

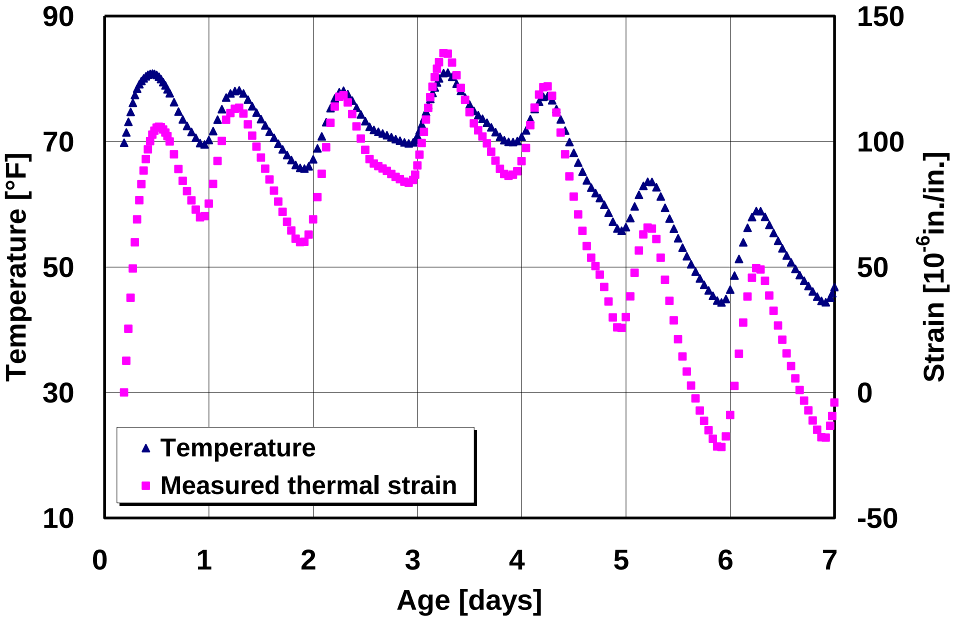

(c) Hillsboro section

Figure 6.5 (cont.): *Temperature and corresponding thermal strain measurements*

In order to determine the time-dependent evolution of CTE in the tested concretes, the measured temperature and thermal strain developments were divided into several phases, with ascending or descending branches, as indicated in Figure 6.5 (b). Subsequently, the CTE at each phase was determined as shown in Figure 6.6; a linear fitting curve was plotted based on the temperature and corresponding strain measurements of that phase, and the slope of the linear fitting curve, when the coefficient of determination, R^2, is closed to 1.0, was defined as the CTE (Won, 2005). Figure 6.6 represents the determination of CTE in the selected phases using the data collected in Hillsboro section. It is of importance to note that the CTE values are not constant over time, rather vary depending on the age of the concrete.

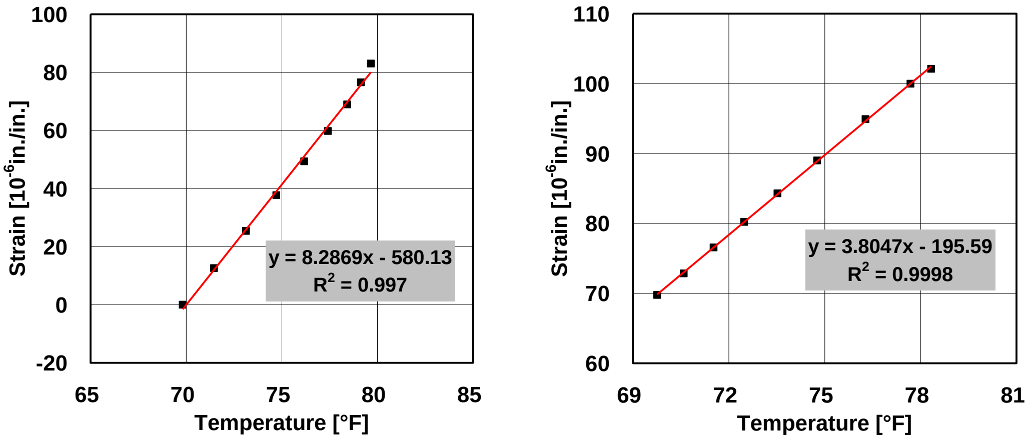

(a) 0.19-day to 0.52-day (b) 0.52-day to 0.92-day

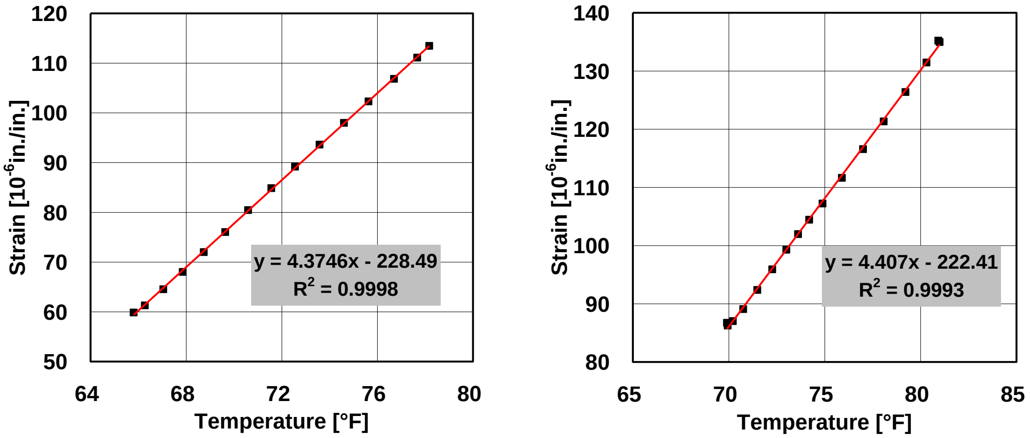

(c) 1.29-day to 1.88-day (d) 3.25-day to 3.92-day

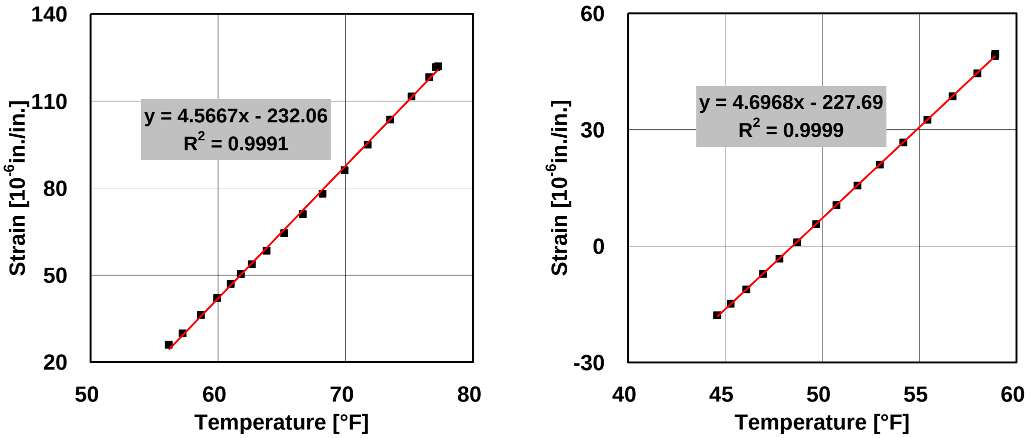

(e) 4.21-day to 4.92-day (f) 6.25-day to 6.88-day

Figure 6.6*: Determination of CTE for selected phases in Hillsboro section*

Figure 6.7 shows the variations of CTE over concrete age calculated on the basis of the measured temperature and thermal strain. The age of concrete presented along the x-axis was defined as the mid-age of each measurement period.

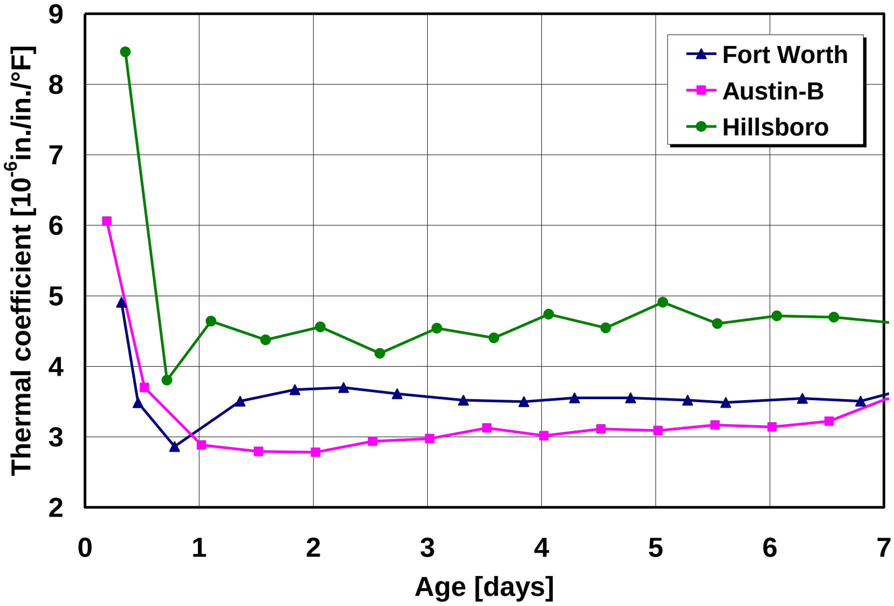

Figure 6.7: *Evolution of time-dependent CTE measured in all test sections*

The results from all the testing sections showed the strong time dependency of CTE in early-age concrete. It is interesting to note that the CTE right after the final setting is approximately twice higher than that in the later age. This finding may be attributed to the large amount of free bulk water absorbed in the concrete at very early-age (Kada et al., 2002) because water, which has a significantly greater linear CTE of 115 x 10^{-6} in./in./°F at 73 °F, dominates the thermal volume changes of early-age concrete. After the initial sudden drop of CTE, it is seen that the CTE starts to slightly increase for a certain period of time and then stabilizes. This is probably because some amount of free water was consumed for further hydration of cement particles. It is recognized that the partially saturated porous material results in a larger vapor pressure difference under the temperature variation than the fully saturated one, which causes a larger volume change per unit temperature difference (Sellevold and Bjøntegaard, 2006).

Even though the trend of the results presented in Figure 6.7 was quite similar, some discrepancy in absolute value was found because of the difference in material properties. It is noted that the later-age CTE of the Hillsboro section is approximately 33% higher than that of the Fort Worth and Austin-B sections. This is because the concrete mixture for the Hillsboro section used siliceous river gravel as coarse aggregate which typically has a higher CTE and elastic modulus while the Fort Worth and Austin-B sections used limestone. Also, a slight difference in CTE was found between the mixtures for the Fort Worth and Austin-B sections due probably to the effect of fly ash that was only incorporated into the mixture for the Fort Worth section.

6.3.2 Effect of Time-Dependent CTE Variation on Early-Age Stress

As investigated in the previous subsection, the CTE of concrete varies significantly during early-age hydration. In many previous mechanistic (Nam et al. 2006; and Richardson et al. 2010) and numerical (Amin et al. 2009; De Schutter 2002; Sheibany and Ghaemian 2006; Yuan and Wan 2002) studies on thermal strain and stress analyses, however, a fixed CTE value was normally used, assuming that the CTE of hardening concrete is independent of concrete age.

To evaluate the effect of time-dependent CTE on early-age thermal stress build-up, the difference in thermal stress development between two individual cases, i.e., one with the assumption of constant CTE and the other with CTE varying over time, was examined. The thermal stress difference between those cases is induced by their thermal strain difference plus modulus and creep developments. In order to calculate the thermal stress difference, the thermal strain developments for each case were identified first, followed by their difference computed. For identification of the thermal strain development subjected to the varying CTE, the free thermal strain data measured with the INC were directly used because the data already include the influence of the time-dependent CTE. To estimate the thermal strain development with the assumption of the constant CTE, Eq. 3.6 was used with the mean CTE value during the measurement period and the measured concrete temperature history.

The mean CTE value used in the thermal strain estimation was determined based on the linear regression between the temperature and thermal strain measured in the first 7 days after the final setting of concrete, as indicated in Figure 6.8. By averaging the CTE in terms of the entire measurement period, the influence of autogenous deformation that might exist in the strain measurement by INC could be internally compensated during the post-processing of data analysis.

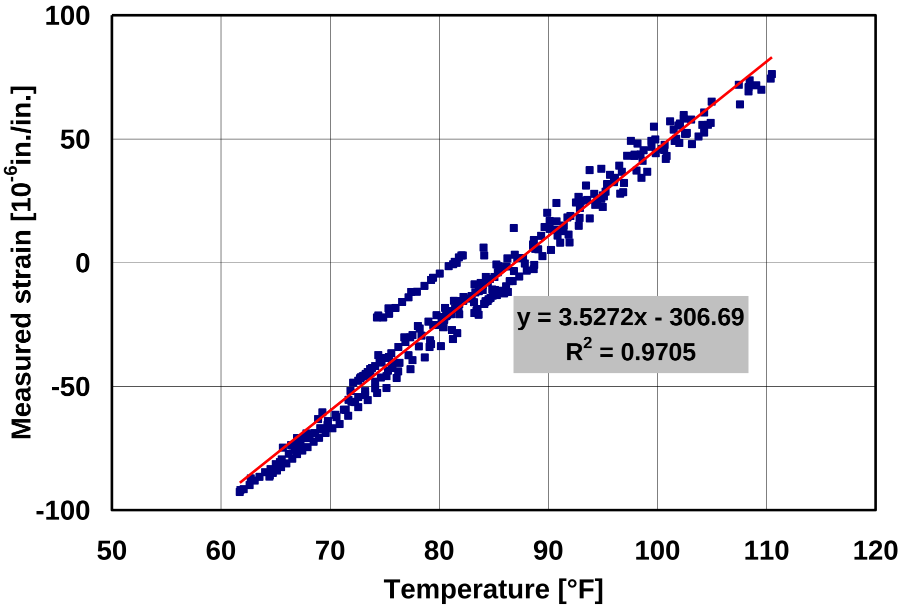

Figure 6.8: *Determination of mean CTE for Fort Worth project*

Figure 6.9 displays the developments of thermal strains, one directly measured by the INC and the other estimated by the mean CTE. Their difference, which causes the difference in thermal stress development between those cases, is also presented.

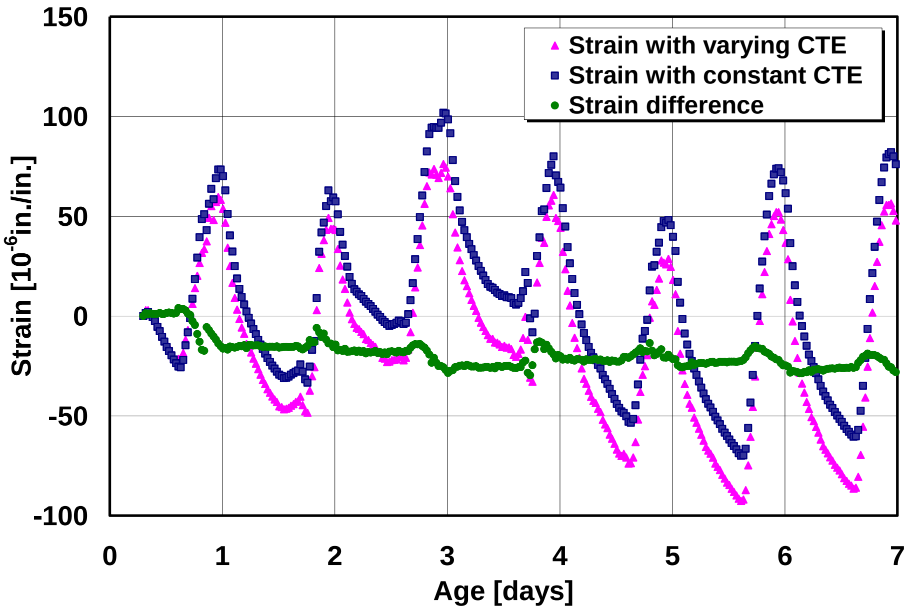

(a) Fort Worth section

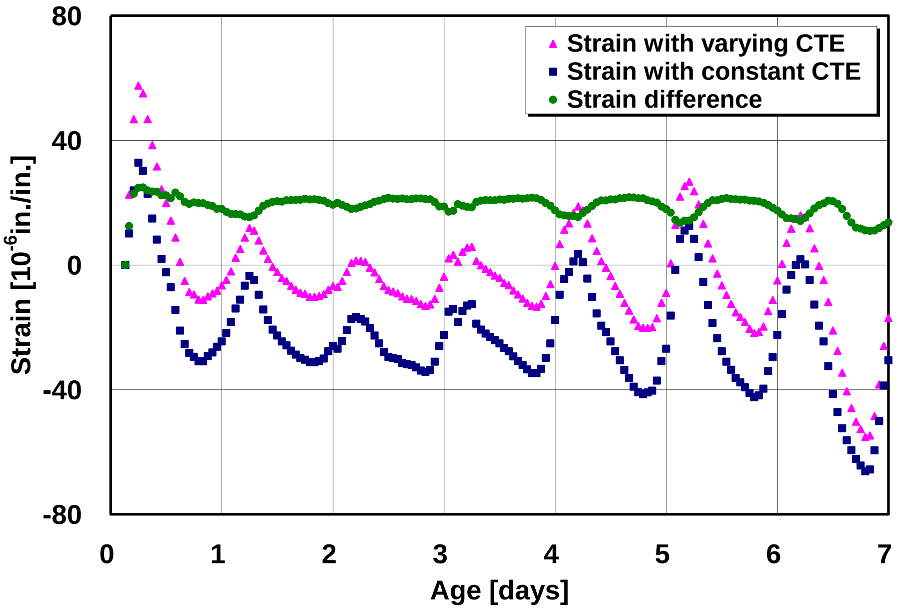

(b) Austin-B section

Figure 6.9: *Presentation of measured thermal strain, estimated thermal strain with mean CTE, and their difference*

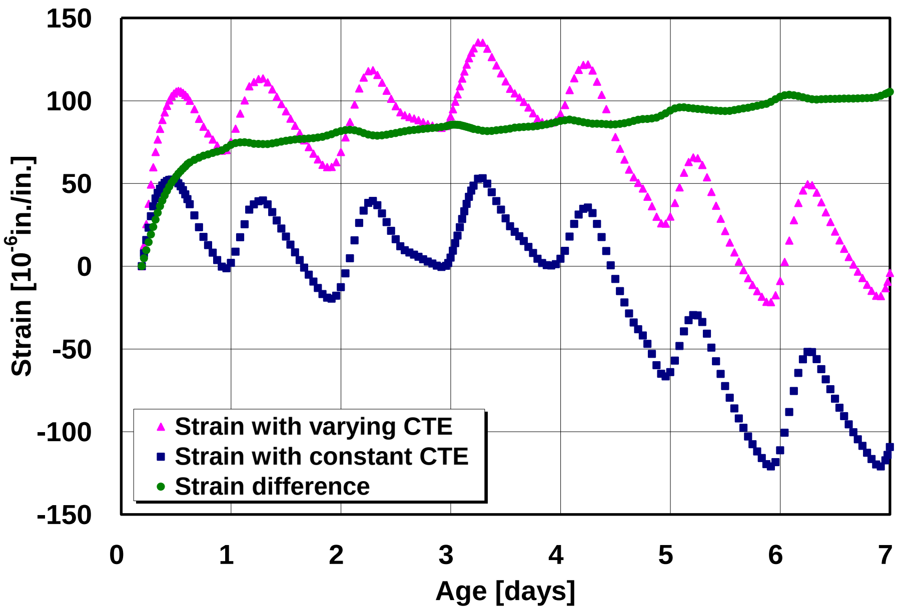

(c) Hillsboro section

Figure 6.9 (cont.): *Presentation of measured thermal strain, estimated thermal strain with mean CTE, and their difference*

It was found from the results that approximately 20 to 75 x 10^{-6} in./in. of thermal strain difference was developed during the first day after concrete placement. This was because the CTE of concrete considerably varied within the first few hours after the final setting as revealed by the foregoing investigation. The results also show that the thermal strain differences are maintained for the rest of the measurement period.

In order to evaluate the difference in thermal stress development induced by the prescribed thermal strain difference history, the present study adopted the step-by-step numerical method (Bažant, 1972a; and Ghali et al., 2002). The formulation of the step-by-step method is previously given through Eqs. 5.5 to 5.10.

Using the equations, developments of stress difference in each test section were determined based on the identified strain difference histories as shown in Figure 6.10.

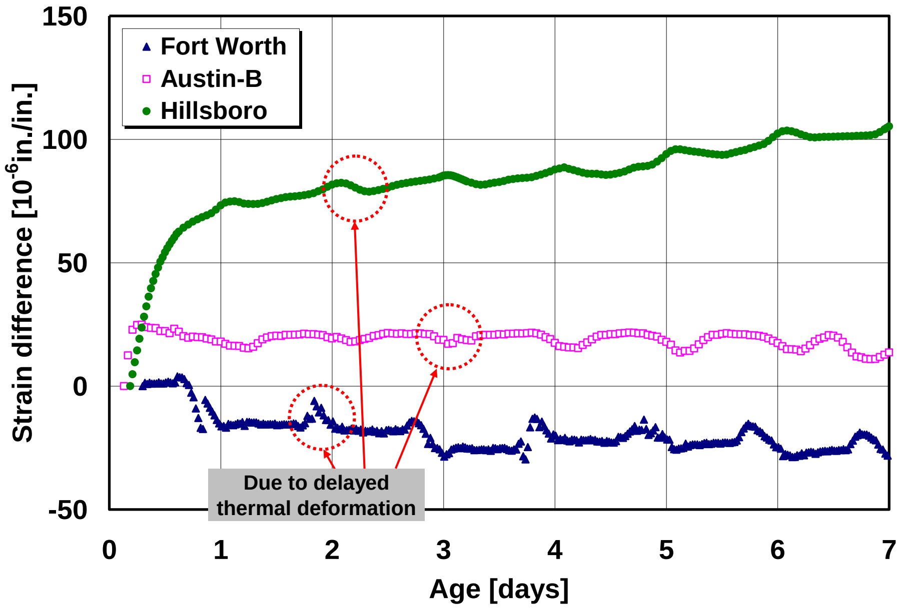

(a) Strain differences

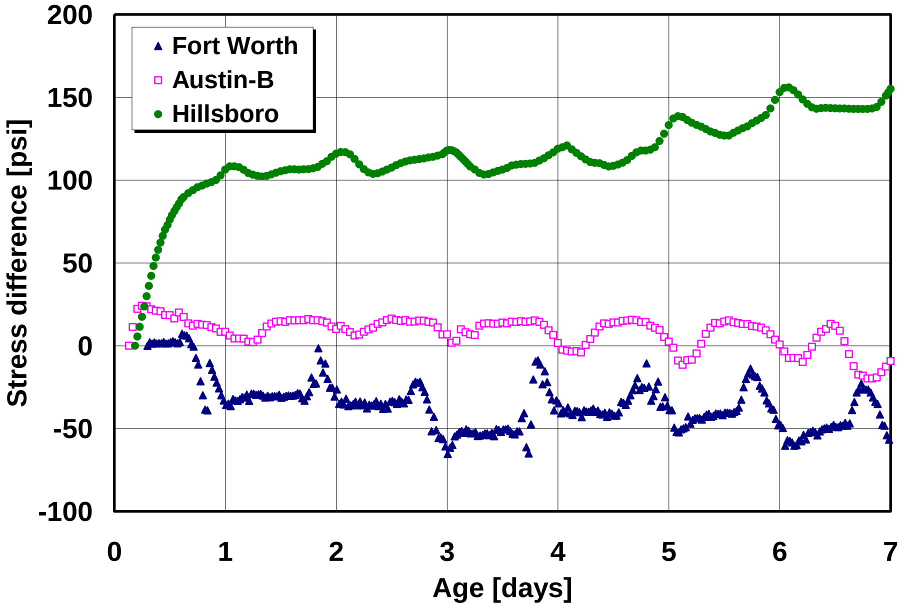

(b) Stress differences

Figure 6.10: *Developments of thermal strain and stress differences in all test section*

The results show about -70 to 120 psi of stress differences in the first 3 days after concrete placement. This fact indicates that the selection of correct CTE values at early ages is quite important in order to accurately predict the early-age cracking potential. It is also revealed from the results that the effect of time-dependent CTE may be extended to the later-age, which implies that the later-age behavior of a concrete member may be also affected by the time-dependent change of CTE at early ages.

6.3.3 Discussions on the Experimental Results

It was verified from the experimental results that the CTE of concrete is age-dependent. Further investigation also revealed that the age-dependence of CTE could significantly affect the early-age thermal stress development of cast-in-place concrete. Except the effect of time-dependent variation of CTE, however, other effects may be involved in the results presented in Figures 6.10 (a) and (b).

As indicated in Figure 6.10 (a), the strain difference curve tended to sharply fluctuate around the temperature inflection points. This effect, in turn, yielded considerable variations in stress difference development in the vicinity of every temperature inflection point as presented in Fig. 6.10 (b). This phenomenon appears to result from the delayed thermal deformation induced by moisture redistribution in the concrete specimen during and after the temperature changes.

Figure 6.11 shows the hysteresis loop in the temperature-strain curve observed in the actual field measurements, which provides the evidence of delayed thermal deformation effect. It is found that the slope of the temperature-strain curve –a CTE– significantly varied around the temperature inflection points due to the delayed deformation effect, which ultimately led to the repetitive fluctuations in the strain and stress curves.

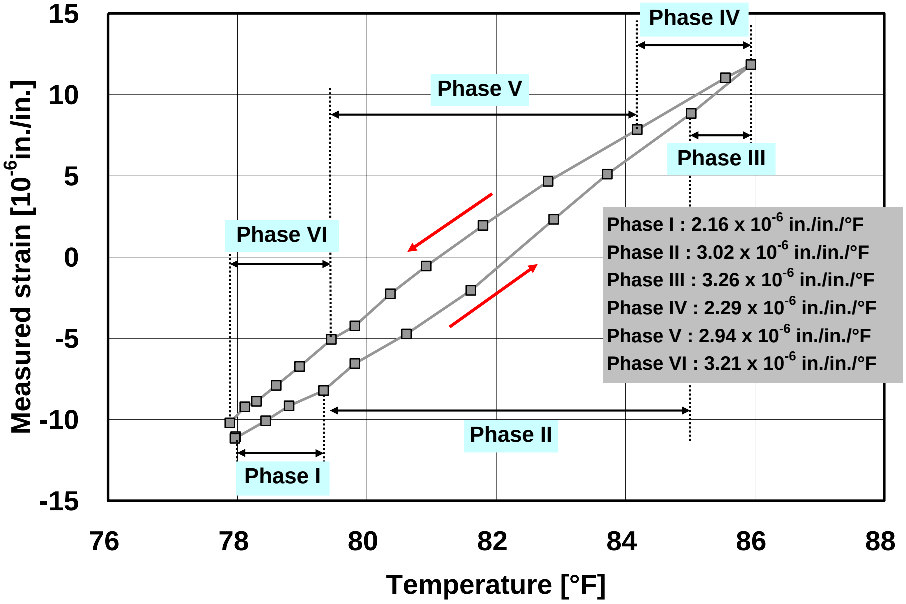

Figure 6.11: *Hysteresis loop in temperature-strain curve measured in Austin-B section*

The measured strain from the INC may be affected by autogenous deformations, which considerably occur in the cementitious systems with a low water-to-cement ratio such as HPC or UHPC. In this study, however, it was assumed that the effect of autogenous deformation is quite minimal because: 1) a water-to-cement ratio of the concretes used in this study was 0.45, 2) the mixtures for the Fort Worth and Hillsboro sections incorporated 20 % to 25 % fly ash, which may reduce the autogenous deformation (Tazawa, 1999); and 3) the CTE was calculated based on the short-term measurements. Even though it was assumed that the influence of autogenous deformation is almost negligible, a slight self-desiccation might have occurred during the testing period. The autogenous deformation not only induces an additional stress-independent volume change in concrete but also may cause the variation in thermal strain history, coupled with the internal RH drop in concrete. As aforementioned, reduction in internal RH will increase the CTE of concrete until the internal RH level reaches around 70%, and this effect might have caused the additional strain differences.

Other than the probable effects described above, a slight temperature differential imposed to the concrete specimen inside the INC also might have influenced on the determination of CTE and, in turn, have affected the early-age thermal stress developments.

6.4 CASE STUDIES

6.4.1 Effect on Early-Age Cracking Tendency

The early-age stress development calculated with the varying CTE was compared with the one calculated with the estimated mean CTE in order to identify the impact of time-dependent CTE on the early-age thermal stress development and cracking tendency of concrete structures. The time-dependent stress development was computed using the step-by-step numerical method based on the in-situ total and thermal strain measurements. Elastic modulus evolution and creep behavior were also considered using the model code suggested by CEB-FIP. Drying shrinkage was not taken into account for the stress calculation because 1) a proper amount of curing compound was applied onto the drying surface in accordance with the specification to ensure water retention, 2) the stress evaluation was performed at the mid-depth of the slab, which is far enough from the drying surface, and 3) only data for the first 1.5 days was presented, which is too short to initiate significant moisture loss.

Fig. 6.12 shows the measured temperature profile and calculated longitudinal time-dependent stress developments for both varying and constant CTE cases in the Forth Worth section, a 9 in. thick CRCP structure. As indicated in the result, the testing section cracked at the age of 1.44 days due to the restrained volume changes.

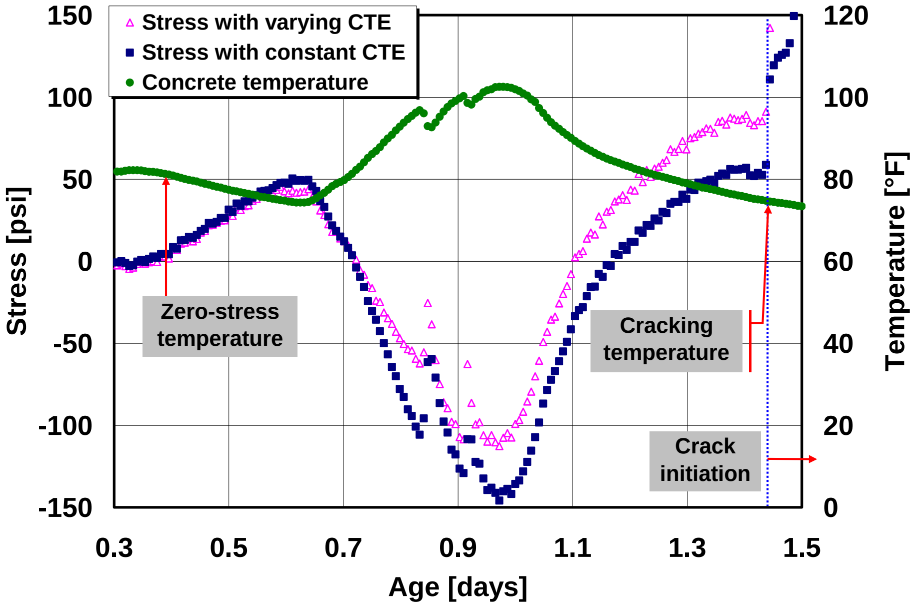

Figure 6.12: *Early-age thermal stress development for varying and constant CTE cases*

As shown in Figure 6.12, some difference in early-age stress development was noted between both cases. This difference is most likely due to the combined effect of the time-dependent variation of CTE and delayed thermal deformation occurred during the measurement period. It was observed that the stress values at crack initiation differed about 36 % even though the zero-stress temperature was almost identical in both cases; the cracking stress was 91 psi for the varying CTE case while 58 psi for the constant CTE. This example case study indicates that the effect of time-dependent CTE is non-negligible, rather may be of great importance for an accurate assessment of early-age cracking tendency of cast-in-place concrete structures.

6.4.2 Effect on Later-Age Behavior

Figure 6.13 displays the temperature and stress evolutions evaluated in the Austin-B section, a 6-in.-thick concrete slab placed over an existing asphalt pavement. This testing section was not cracked during the measurement period since the stress mostly developed in the compression side.

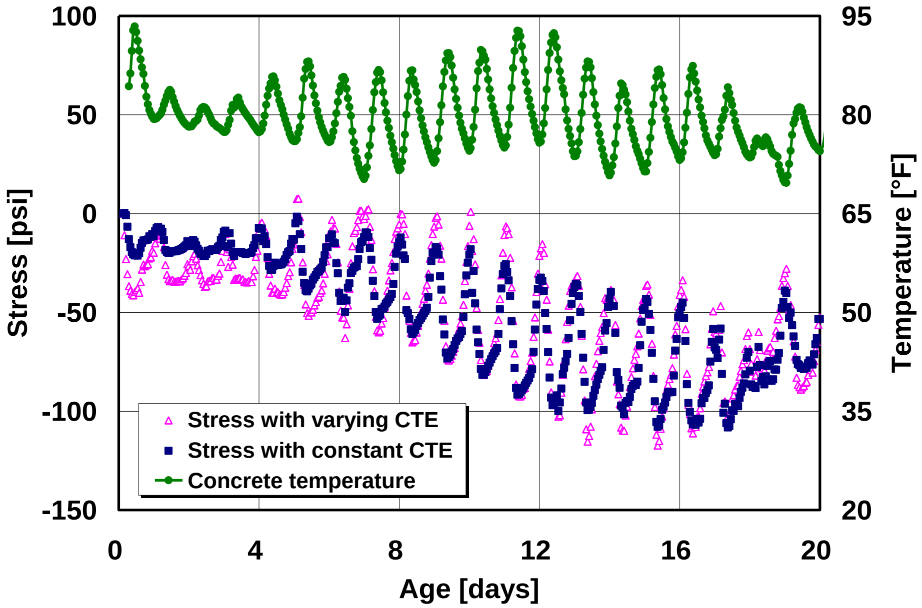

***Figure 6.13:** Later-age behavior for varying and constant CTE cases*

At early-ages between 0 and 5 days, it is observed that the stress calculated with the varying CTE experienced about twice high compressive stress than the case calculated with the constant CTE. This is because the actual CTE right after the final setting was significantly greater than the mean CTE value as identified in the experimental result. This finding again implies that the early-age cracking risk of cast-in-place concrete structures quite depends on the time-dependent CTE of the concrete. After this period, the stress intensity starts to decrease closer to the stress calculated with the constant CTE although the strain difference between both cases is still maintained as shown in Figure 6.10 (a). This result appears to stem from the creep effect. Also, it was revealed that the amplitude of daily stress fluctuations was slightly different between both cases due probably to the effects of the delayed thermal deformation and continuous slight changes of CTE in the case of the varying CTE.

6.5 SUMMARY

In order to accurately predict the thermal stress developments in cast-in-place concrete structures, characterization of the coefficient of thermal expansion (CTE) is quite important because the instantaneous thermal stress increment is proportional to the CTE of concrete. An experimental study was conducted to investigate the time-dependent variation of CTE in hardening concrete in a series of field tests. An in-situ test method using non-stress cylinder (NC) was implemented to determine time-dependent CTE. Also, the effect of time-dependent CTE on early-age thermal stress build-up was quantitatively evaluated by computing the difference in thermal stress development between two different cases, i.e., one calculated with the mean CTE and the other calculated with the varying CTE.

The findings presented in this chapter can be summarized as follows:

1. The results from the field testing showed that the CTE in hardening concrete is age-dependent, which agrees with the previous research studies. The CTE at the time of final setting was about twice as high as that in the stabilized stage. After the sudden decrease of CTE in the initial stage, the CTE began to slightly increase for a certain period of time and then stabilized.

2. The results from the numerical investigation revealed that the age-dependent characteristic of CTE, compared with constant CTE, could increase the early-age thermal stresses and cracking potential of cast-in-place concrete. The result of the case study showed that the stress values at crack initiation differed about 37 % between the constant CTE and varying CTE cases although the zero-stress temperature was nearly identical.

3. The delayed thermal deformation induced by moisture redistribution in concrete during and after the temperature changes could affect the early and later-age stress developments in concrete structures, especially around the temperature inflection points.

Chapter 7: Effect of Creep and Built-in-Curling on Stress History

Adequate evaluation of stresses in concrete is of great importance to ensure well-performing and long-lasting portland cement concrete (PCC) pavements. In this chapter, effects of creep and built-in curling (BIC) on the long-term stress history of PCC pavements were primarily investigated based on a series of field instrumentations and various analysis methods. For accurate and realistic evaluation of stress-independent strains in-situ, non-stress cylinders (NC) were employed. To investigate the effect of creep on stress history, stresses of PCC pavements were evaluated in both viscoelastic analysis and elastic analysis, and then the analysis results were compared with each other to examine the effect of stress relaxation on stress developments. Furthermore, a variation of BIC stresses is also investigated in this chapter based on the field measured data.

7.1 INTRODUCTION

When PCC pavements are placed in the field, the PCC pavements undergo volume changes due to variations in temperature and moisture (Beyer, 1949; Sargand et al., 2005; Westergaard, 1927). The restrained volume changes cause development of stresses in a pavement system, and cracking may occur if the developed stresses exceed the strength of concrete (Bazánt, 1982; Springenschmid, 1995). In CRCP, the cracks are not always harmful to the long-term performance of CRCP as long as the cracks are kept tight (ERES, 2004). However, it has been reported that the cracking may increase the potential risk of major distresses in CRCP such as punchout and spalling (ERES, 2004; Won, 2009; Won et al., 2011). Because the cracking potential, which may affect the long-term performance of PCC pavements, is closely related to the stress field in the pavement, it is quite important to be able to accurately estimate the development of stresses in the pavement structure.

In current rigid pavement design and analysis considerations (ERES, 2004; Huang, 2004), several assumptions are typically made when the stresses induced by environmental loads are evaluated. They include: (1) the material is completely elastic,

(2) certain material properties such as CTE are not time-dependent, (3) the setting temperature is uniform along the depth of the PCC layer, and (4) the PCC slab is effectively restrained by subbase friction. Yet, the assumptions made in the current design and analysis may not be valid in that: (1) concrete is a viscoelastic material, (2) the mechanical properties of concrete significantly vary as the cement hydrates, especially at early ages, (3) the actual setting temperature is non-uniform along the depth of the slab, and (4) the slab is not fully restrained; rather, the field investigations (Choi and Won, 2009; Wu and McCullough, 1992) showed that the slab moves to some degree.

It is well known that creep develops in the concrete structures which experience temperature variations and drying shrinkage (Ghali et al., 2004; Springenschmid, 1995; Springenschmid, 1998). Because the PCC pavement system cast in the field is affected by the environmental loads whose loading rate is substantially lower than that of traffic loading, the stress history of PCC pavements could be significantly influenced by the viscoelastic behavior of concrete, especially at early ages. However, until recently, the effect of creep on long-term stress development has not been considered in the design and analysis procedures for PCC pavements.

Moreover, in the current rigid pavement design and analysis procedures (ERES, 2004; Huang, 2004), the behaviors of PCC pavements are evaluated under the assumption that the setting temperature is constant along the depth. When the PCC pavement is cast in the field, however, each concrete element experiences different temperature history due to the slow rate of environmental interaction and thus a non-uniform setting temperature gradient is formed in the pavement. This non-uniform setting temperature gradient is termed a “built-in curling (BIC)” (Beckemeyer et al., 2002; Rao and Roesler, 2005; Yu et al., 1998) in the rigid pavement design and analysis. It is reported that the RH gradient at setting may also contribute to the BIC. However, the laboratory testing revealed that no significant RH differential occurs at the age of setting as long as the proper amount of curing compound is applied in accordance with the specification (TxDOT, 2004). This issue will be addressed in the following chapter.

There have been several research studies on the effects of BIC on the behavior and response of PCC pavements. Yu et al. (1998) evaluated the relationship between BIC and critical wheel load stresses to predict the cracking performance of jointed concrete pavements (JCP). They used the finite element program, ILSL2, which operates on the basis of a linear elastic theory. The analysis results showed that the critical stress at slab corner increases as the BIC increases while the critical stress at slab edge decreases as the BIC increases. Rao and Roesler (2005) theoretically defined the "effective BIC" considering the combined effects of temperature, shrinkage, and creep. They validated the proposed theoretical concept through the experimental and analytical studies. Beckemeyer et al. (2002) quantified the amount of BIC in JCP sections with different base types.

While the previous research studies were quite insightful for the characterization of the BIC effects, the studies were mainly limited to the investigation of instant structural response due to wheel loading, especially in JCP sections. Their research efforts did not directly identify the effects of BIC on long-term structural responses of PCC pavements due to environmental loads. This chapter primarily investigated the effects of creep and BIC on the long-term stress history of PCC pavements to provide adequate criteria for stress-related design inputs. To identify the creep effect, field data sets were analyzed into two different methods, i.e., elastic analysis and viscoelastic analysis. The results from two methods were compared each other, and then the creep effect was quantified in terms of the stress relaxation over time.

In addition, the effect of BIC on stress history was also investigated. In order to quantify the BIC effect, the difference between the actual setting temperature gradient and sectional averaged temperature was determined first, followed by the variation in time-dependent stress induced by the temperature difference. It is expected that the present approach will allow more realistic and accurate evaluation of the stresses developing in PCC pavements and, in turn, will be helpful in providing the advanced PCC pavement design procedures.

7.2 EXPERIMENTAL PROGRAMS

To evaluate the development of stresses in PCC pavements, the field experimental data obtained from two different construction sections, i.e. Austin-B and Hillsboro was used. The details of the testing sites and mixture proportions of the concrete materials are summarized in Tables 4.1 and 4.2, respectively.

All the testing setup, testing sequences, data interpretation, and analysis schemes were identical to the methods described in Chapters 4 and 5.

7.3 ANALYSIS OF EXPERIMENTAL RESULTS AND DISCUSSIONS

7.3.1 Effect of Creep on Long-Term Stresses

7.3.1.1 Results from Austin-B Project

Figure 7.1 (a) displays the selected strain history of Austin-B project, which were evaluated at 3 in. below the surface. The stress caused by the strain history was evaluated in two different methods, i.e. elastic analysis and viscoelastic analysis (Figure 7.1 (b)). The result would indicate how the creep effect plays a role on stress histories. The green marks indicate the stress relaxation over time, estimated by the difference of stress between elastic analysis and viscoelastic analysis. It was noted that the relaxation significantly develops over time although only about 25 microstrain of drying shrinkage occurred in the first 25 days. At the 25th day after concrete placement, the stress evaluated from viscoealstic analysis was only about 40% of that from elastic analysis, which means about 60% of stress was relieved due to creep.

Commonly, it has been believed that the creep does not substantially affect the stress history caused by cyclic temperature variations because the creep effects are internally compensated every cycle. Based on the observation, however, it may be concluded that the relaxation effect is not negligible; rather, it may be important especially when the trend of entire stress history is biased. If the structural design of PCC pavements is solely based on the elastic theory as the current procedure is, the stress-related design inputs might be overestimated, which may lead to overly conservative PCC pavements designs.

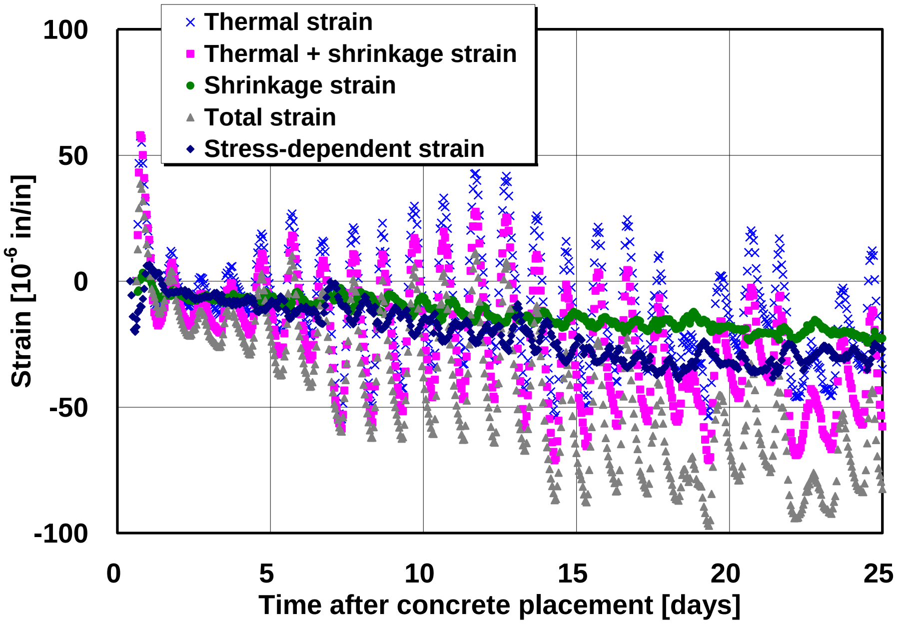

(a) Strain history evaluated at mid-depth in Austin-B section

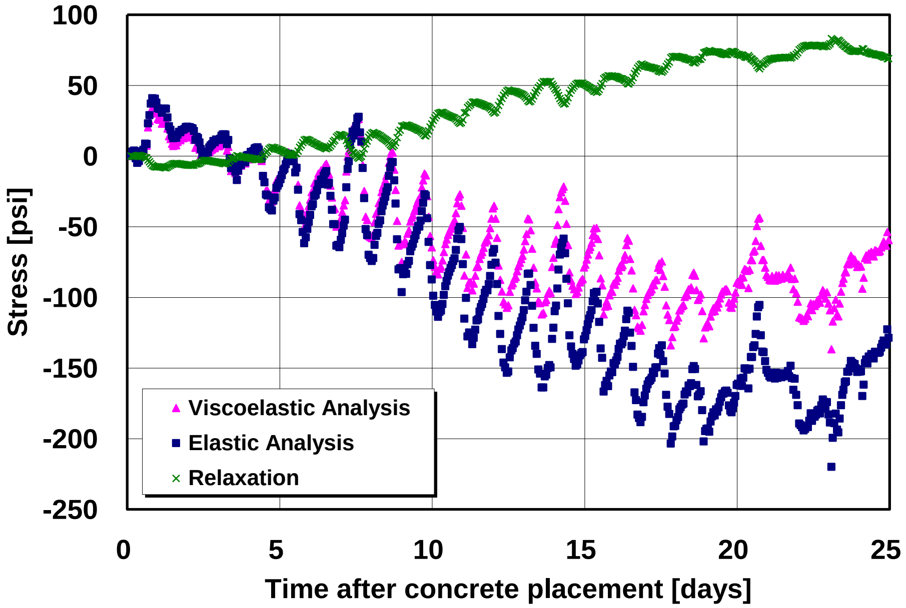

(b) Stress history evaluated at mid-depth in Austin-B section

Figure 7.1: *Strain and stress history measured in Austin-B section*

7.3.1.2 Results from Hillsboro Project

Figures 7.2 (a) and (b) presents the measured temperature and strain profiles for the first 25 days after the concrete placement, respectively. It was noted that the trend of strain histories were nearly proportional to the temperature variations as anticipated. Also, about 20 microstrains of drying shrinkage was observed at the mid-depth at the age of 25 days, which is a quite small amount. Figures 7.2 (c) and (d) respectively show the corresponding stress histories evaluated at the mid-depth in longitudinal direction and at the bottom in transverse direction. To ascertain post-tensioning effect, the data collected from the longitudinal VWSG located 23 in. away from the transverse armor joint and the only VWSG installed in transverse direction were selected and presented. The sudden stress changes were detected in both directions at the times of post-tensioning applications, as expected.

The results showed that the direction of stress relaxation significantly depends on the preceding stress history. In the transverse direction, as seen in Figure 7.2 (c), it was noted that the stress headed to the tension side first, and then the stress history turned to the compression side when the post-tensioning was applied. Subsequently, the direction of stress reversed to the tension side again due to the huge temperature drop at the ages of 16th and 17th day. It was clearly seen that the stress relaxation develops in the same direction as the stress proceeds at a quite rapid rate. As the consequence of continuous changes in stress application directions, the results from elastic analysis and viscoelastic analysis became identical due to the complete compensation of relaxation component at the days of twelve, sixteen, and twenty. On the other hand, the result from the longitudinal measurement showed that the stress and relaxation continuously develops to the compression side due to the twice applied post-tensioning at early-ages. Because the location of measurement was very close to the transverse armor joint which has a quite low frictional resistance with the underlying subbase, an enormous amount of precompression was detected when the second post-tensioning was applied (3.08 days in equivalent age). After 25 days after the concrete placement, about 50 % of stress was relieved as noted in Figure 7.2 (d). Based on the experimental results, it may be concluded that the creep effect is path-dependent, which is very sensitive to the preceding stress histories.

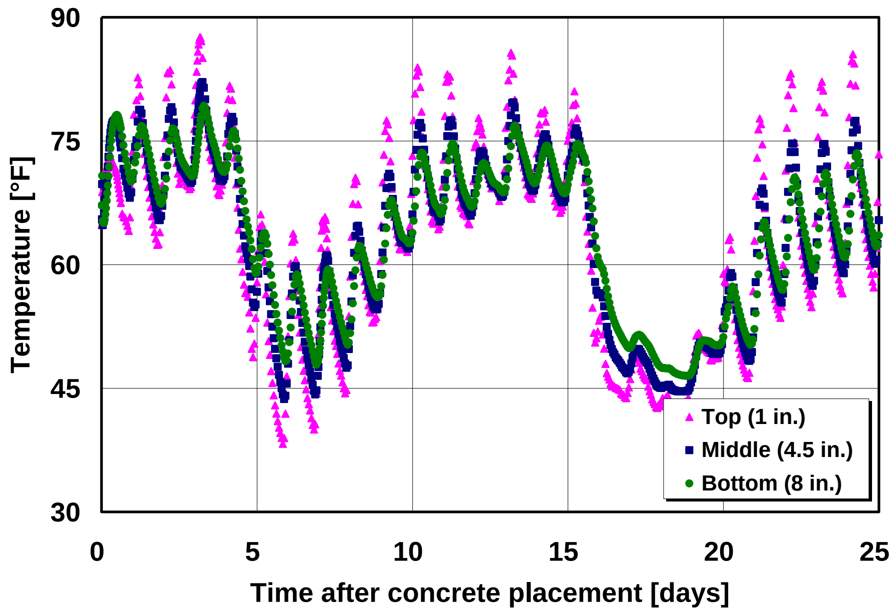

(a) Temperature measured at different depths for first 25 days

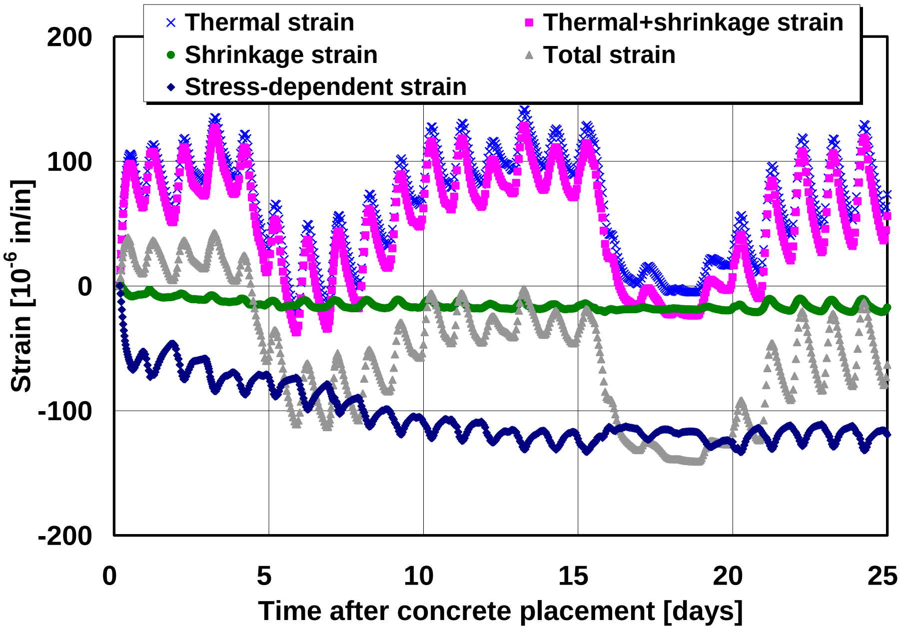

(b) Measured strain histories at the mid-depth for first 25 days

Figure 7.2: *Temperature, strains, and stresses evaluated in Hillsboro project*

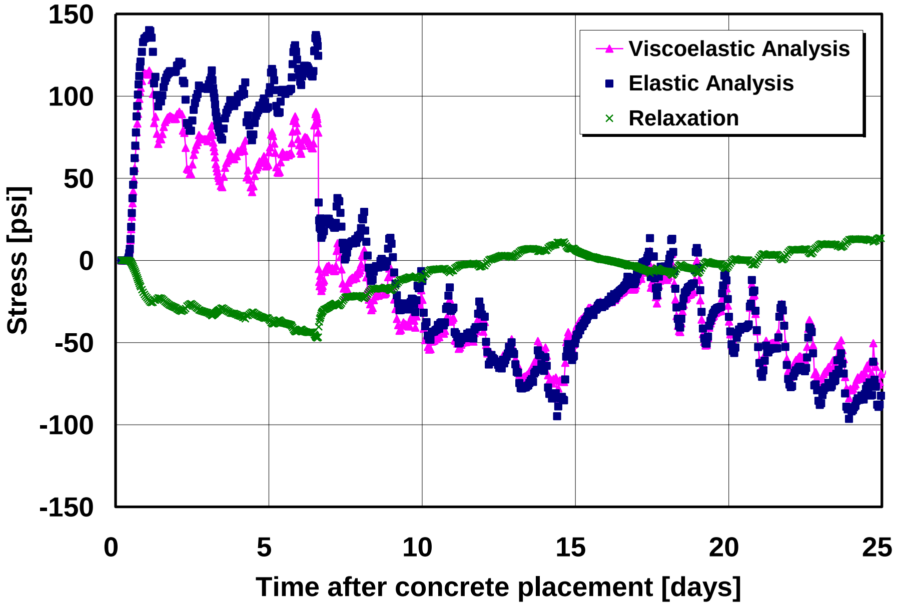

(c) Stress and relaxation evaluated at 8 in. depth in transverse direction (transverse center)

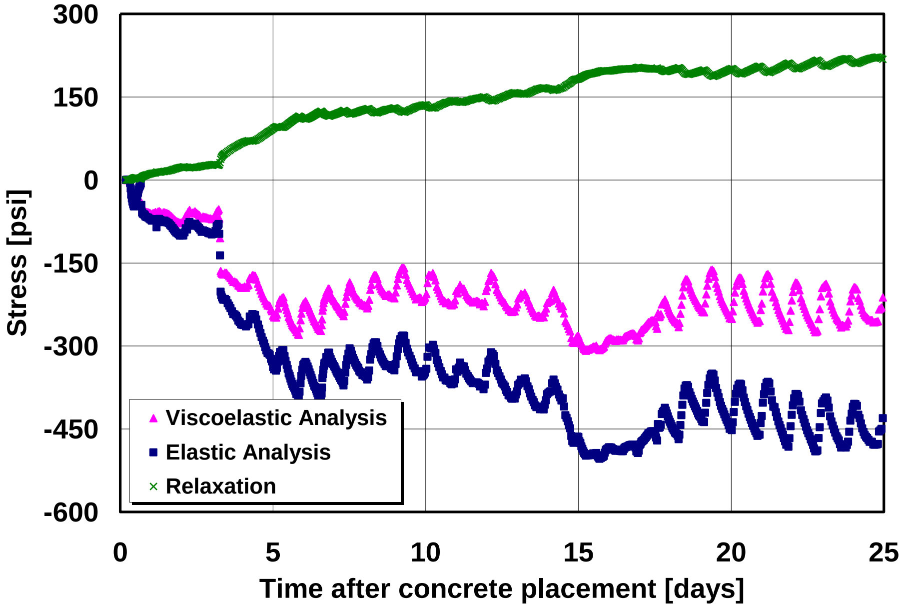

(d) Stress and relaxation history evaluated at mid-depth in longitudinal direction (23 in. away from transverse armor joint)

Figure 7.2 (cont.): *Temperature, strains, and stresses evaluated in Hillsboro project*

7.3.2 Effect of Built-in-Curling on Long-Term Stress

It has been stated that additional stresses can be developed in PCC pavements due to the non-uniform setting temperature gradient. In reality, many previous field experimental data showed that there was a definite non-linear setting temperature gradient along the depth of a slab while the RH gradient at setting is quite little. In order to investigate the effect of BIC on long-term residual stress field, the variation of stresses due to BIC (hereinafter, referred to as "BIC stress") was evaluated based on the field measured data set. Here, the BIC stress is defined as the stress induced by the temperature difference between the actual setting temperature gradient and sectional averaged setting temperature as indicated in Figure 7.3 (a).

Figure 7.3 (a) presents the actual setting temperatures measured at the top, middle, and bottom of the slab. The actual setting temperature gradient regressed in a second-order polynomial and the sectional average setting temperature calculated based on the obtained regression equation were also indicated. The sectional average setting temperature was calculated using Eq. 5.3.

About 5.9 °F of non-linear BIC gradient was found along the depth of the slab. To examine the variation of BIC stress over time, two independent thermal strain histories were identified first, using the concrete temperature history and the measured CTE: one based on the actual setting temperature and the other based on the average setting temperature. Subsequently, these independent thermal strain histories were subtracted from the measured total strain history to determine the stress-dependent strain histories. Using the obtained stress-dependent strain histories for both separate cases, the stress histories were evaluated using the step-by-step numerical method in both elastic and viscoelastic approaches. Figure 7.3 (b) shows the result from viscoelastic analysis which was evaluated at the bottom in transverse direction. It was noted that the BIC stress keeps diminishing over time, from -17.5 psi to -5.9 psi in 25 days. As anticipated, on the other hand, the BIC stress did not change at all when elastic analysis was performed since the creep effect was not taken into account. The same approach was conducted in terms of the top and middle in transverse direction. The results showed the exactly same trend as indicated in Figure 7.2 (c). The relaxation of BIC stresses seems to stem from the initially sustained thermal strain due to the reference temperature difference.

Based on the investigations, it may be concluded that the long-term residual stress might not be significantly affected by BIC due to the gradual relaxation of BIC stresses, no matter which one becomes the reference temperature for stress evaluation. Also, the early-age characteristics of concrete, such as a large amount of creep and a low modulus, could be the other reasons to keep the BIC stresses not significant.

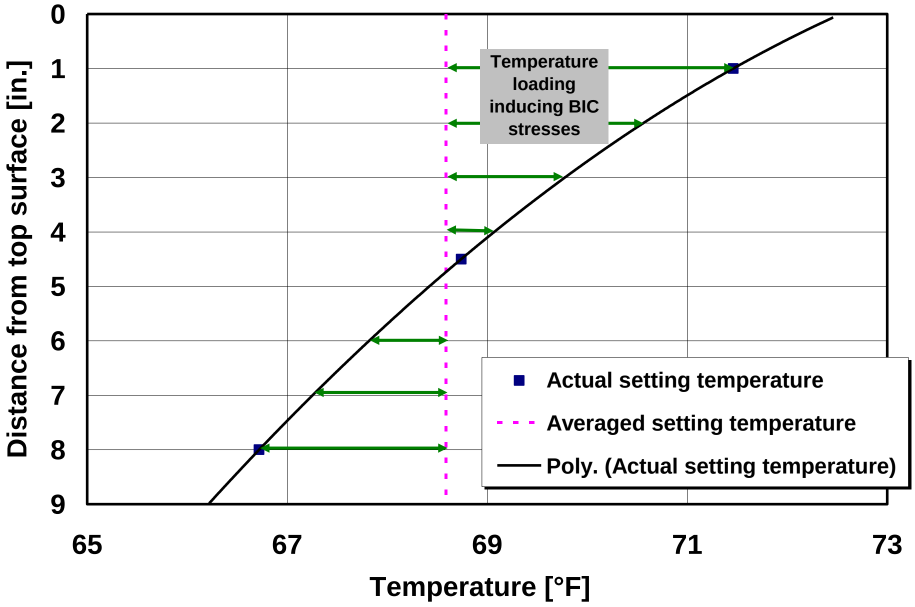

(a) BIC and averaged setting temperature

Figure 7.3: *BIC and relaxation of BIC stresses over time*

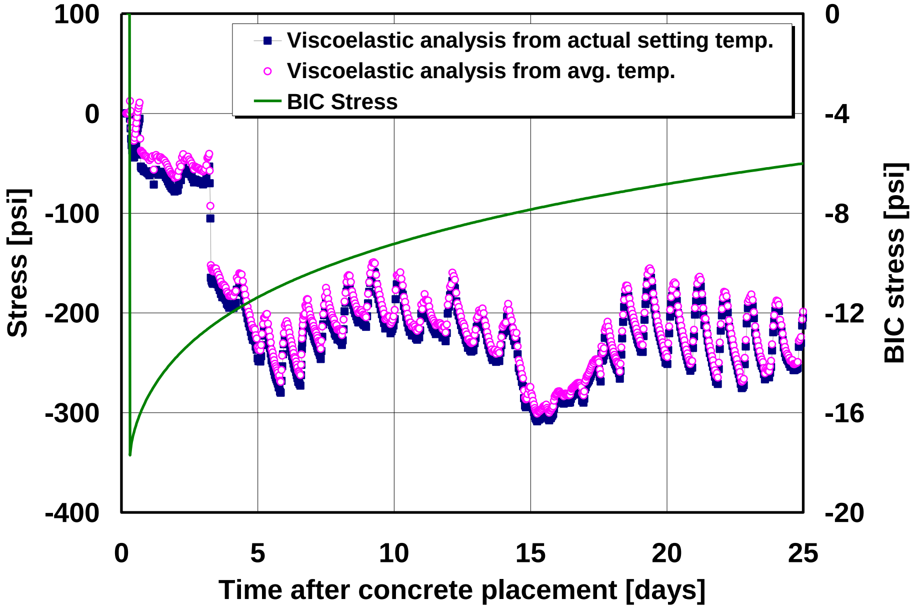

(b) Relaxation of BIC stress over time evaluated at 8 in. depth in transverse direction

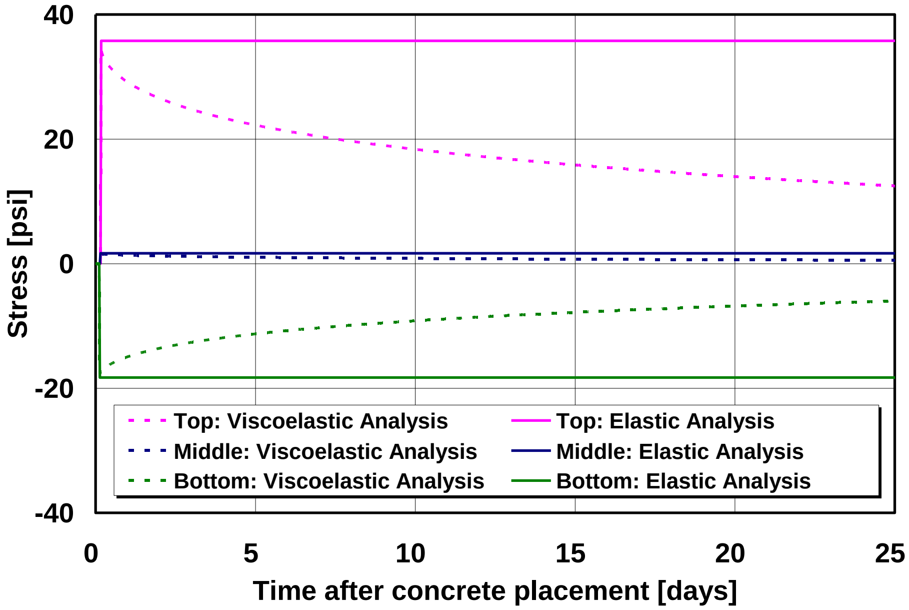

(c) Variation of BIC stresses over time evaluated at top, middle, and bottom

Figure 7.3 (cont.): *BIC and relaxation of BIC stresses over time*

7.4 SUMMARY

Adequate evaluation of stresses in concrete is important for the development of reasonable PCC pavement design procedures, which will increase the potential for well-performing and long-lasting PCC pavements. In this study, the effects of creep and built-in-curling (BIC) on the restrained stress history of portland cement concrete (PCC) pavements subjected to environmental loading were primarily investigated based on the field instrumentations. The investigations were conducted in two different test sections located in Austin and Hillsboro in Texas. In order to complete the stress analysis, stress-independent strain histories were measured with the non-stress cylinders (NC). The identified stress-independent strain was subtracted from the measured total strain to estimate the mechanical strain, which was induced by stresses. Subsequently, the obtained mechanical strain was converted to stress based on the strain-stress constitutive relation. To solve the constitutive strain-stress relation, the step-by-step numerical method was used.

The findings from the analysis can be summarized as follows:

1. The stress relaxation due to creep is not negligible; rather it might be important in the design and analysis of PCC pavements. The experimental results showed about 50 % to 60 % of stress relaxation due to creep at the age of 25 days, which is quite substantial.

2. The creep effect is path-dependent, which is very sensitive to the preceding stress histories.

3. The early-age stress developments are affected by an actual setting temperature gradient. This indicates that the accurate zero-stress temperature (ZST) evaluation should be based on the consideration of BIC.

4. The long-term residual stress might not be significantly affected by BIC due to the following reasons:
    a. The gradual relaxation of BIC stresses, no matter which one becomes the reference temperature for stress evaluation.
    b. The large amount of creep in early-age concrete.
    c. The low modulus of early-age concrete.

Based on the findings described in this chapter, it is recommended that stress-related inputs for PCC pavements design need to be developed considering the creep effect. It is because the current design procedures are solely based on the elastic theory, which may lead to overestimation of stresses. It is also advisable to consider aging effects for more accurate evaluation of long-term stresses. Application of the age-adjusted effective modulus method could be one of the most practical ways incorporating both creep and aging effects in the stress analysis.

Chapter 8: Development of Numerical Model and Its Validation

Throughout this chapter, numerical models for temperature and corresponding thermal stress evolutions in early-age concrete are proposed. These models will be ultimately used for developing a zero-stress temperature (ZST) prediction model in the following chapter. For reasonable modeling, theoretical backgrounds for numerical modeling are thoroughly reviewed first, followed by the discussions on the numerical models developed based on the adequate considerations of boundary conditions. Once the temperature and thermal stress prediction models are established, the numerical models are validated with the field measured data presented in Chapter 4.

8.1 MODELING CONSIDERATIONS

For realistic numerical assessments of temperature and thermal stress developments in early-age CRCP, a sound understanding of the actual CRCP behavior is required. To achieve the knowledge on the actual behavior, a preliminary laboratory experiment and field observation were conducted.

8.1.1 Effect of RH on Early-Age Stress Development

A number of previous research studies described that variations in temperature and internal RH affect the development of early-age stress in concrete structures. However, the experimental results showed that the contribution of RH on the stress developments was not as significant as the literatures addressed while the effect of temperature was substantial. The reason for this could be due to the moisture retention effect of curing compound that is typically applied to the concrete surface after a paver forms the concrete slab (Figure 8.1). To verify the effect of curing compound on the RH variation in early-age concrete, a separate laboratory experiment was conducted.

Figure 8.1: *Application of curing compound over PCC pavement surface*

8.1.1.1 Experimental Program

A total of three levels of curing compound application rates, 90, 270, and 360 ft^2/gal., and two reference conditions, no curing and sealed, was selected for the testing. Figure 8.2 shows the testing setup for specimen fabrication. The dimensions of the specimens were 2 in. (width) x 2 in. (height) x 12 in. (length), and two RH sensors were installed at two different depths from the exposure surface, 0.2 in and 0.5 in., to measure the moisture condition of the specimens.

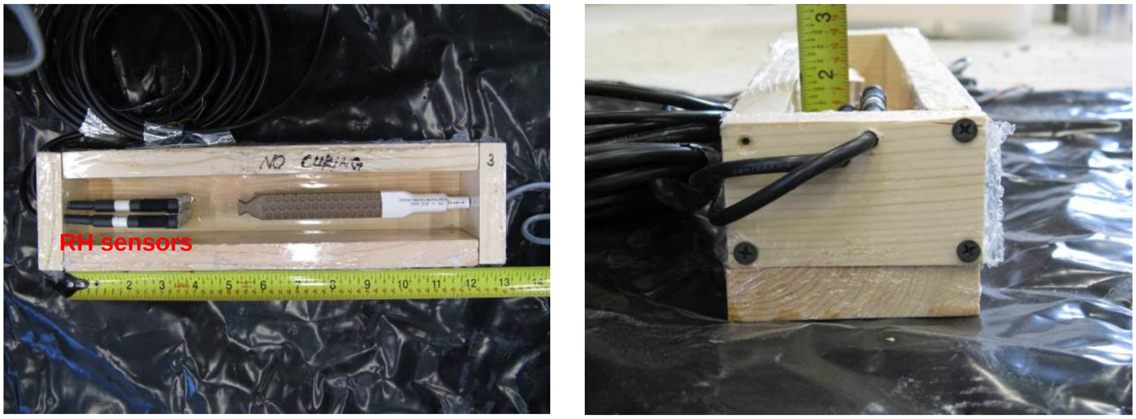

Figure 8.2: *Fabrication of specimen*

The concrete material used was Class P concrete typically used in concrete paving in Texas. As soon as the concrete material was mixed, it was placed into the specimen molds equipped with the RH sensors at the preselected locations as seen in Figure 8.3 (a). When most of the bleeding water was evaporated (Figure 8.3 (b)), curing compound was applied onto the exposure surface of the specimen using a fine sprayer as shown in Figure 8.3 (c). To control the application rate, the area that was covered by a unit volume of curing compound, and the weight of specimen before and after the curing compound application were measured using a scale. The measured weight difference was converted to the curing compound volume with a known specific gravity of curing compound. When the exposure surface of the specimens was covered with each target amount of curing compound, they were stored in the environmental chamber simulating harsh ambient conditions, i.e. 113 °F and 40 % ambient RH, and the variations of RH in concrete specimens after the final setting were monitored using the embedded RH sensors. The reference specimens – no curing and sealed – were also stored in the environmental chamber and their internal RH was measured every hour.

Figure 8.3: *Fabrication of specimen*

8.1.1.2 Results and Discussions

Figures 8.4 (a) and (b) present the variations of RH over time measured in the specimens. As expected, as the amount of curing compound application rate increased, the less RH drop took place at both investigated depths. Also, it is interesting to note that the role of curing compound in water retention is quite significant; regardless of the amount of curing compound applied, the use of curing compound remarkably reduced the early-age moisture loss.

Because the current TxDOT specification (TxDOT, 2004) requires double applications with each application rate not to exceed 180 ft^2/gal, which is equivalent to a maximum 90 ft^2/gal of curing compound, the variation of RH when the application rate of 90 ft^2/gal was investigated. It is noted that the RH drop around one day after setting, at which the ZST is typically formed, was quite small; the RH drop was less than 3 % at 0.2 in. depth and was negligible at 0.5 in. depth.

Based on these findings, it could be a reasonable conclusion that the contribution of RH in early-age stress developments is quite minimal when the appropriate amount of curing compound is applied. For this reason, the stress development due to drying shrinkage is not considered in the scope of this numerical study.

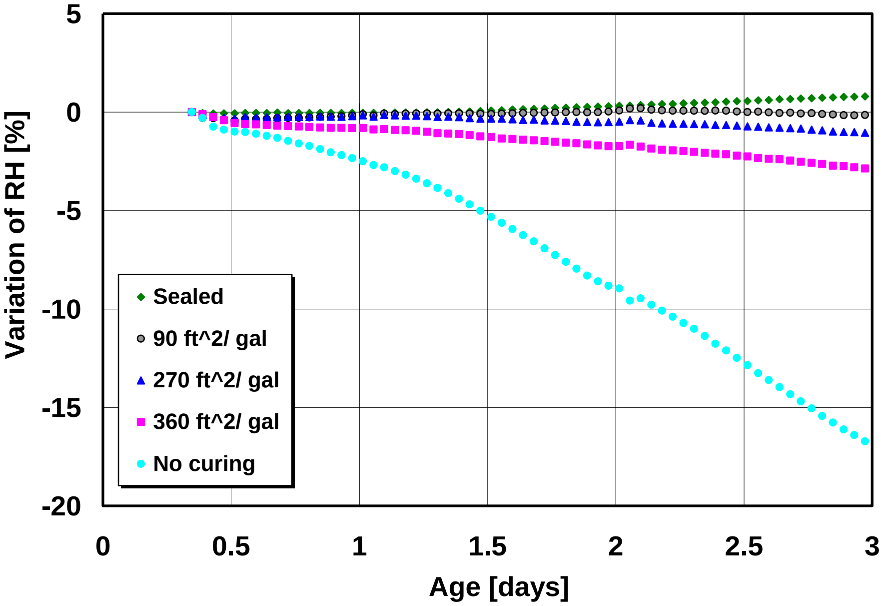

(a) RH variations in 0.5 in. depth

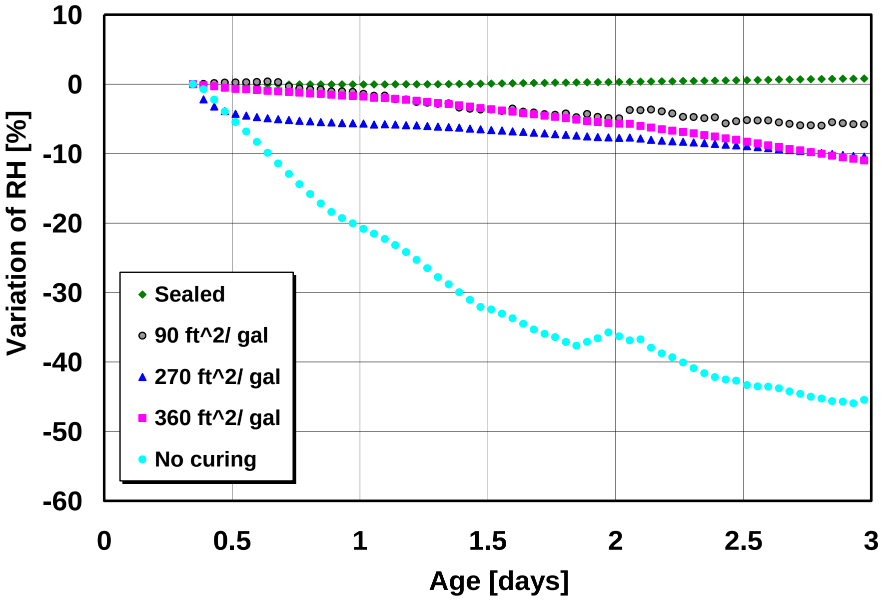

(b) RH variations in 0.2 in. depth

Figure 8.4: *Variations of RH over time*

8.1.2 Boundary Conditions of CRCP

For accurate stress analysis, it is important to adequately determine the boundary conditions of the modeled section. To recognize the actual behavior of early-age CRCP, the experimental data obtained from the Fort Worth project were used.

Figure 8.5 shows the strain gage setup implemented in the field testing (Fort Worth project). To monitor the longitudinal movement of CRCP prior to cracking and after cracking, a set of strain gages was embedded at the top, middle, and bottom of the pavement along the longitudinal direction prior to concrete placement, and a crack inducer was installed at the center of the strain gages to make an artificial transverse crack at the desired position. Figure 8.6 indicates the total strain data measured from those strain gages. As can be seen in the gage readings, the CRCP before transverse cracking showed little variation in total strain. This indicates that the CRCP prior to transverse cracking is nearly fully restrained along the longitudinal direction.

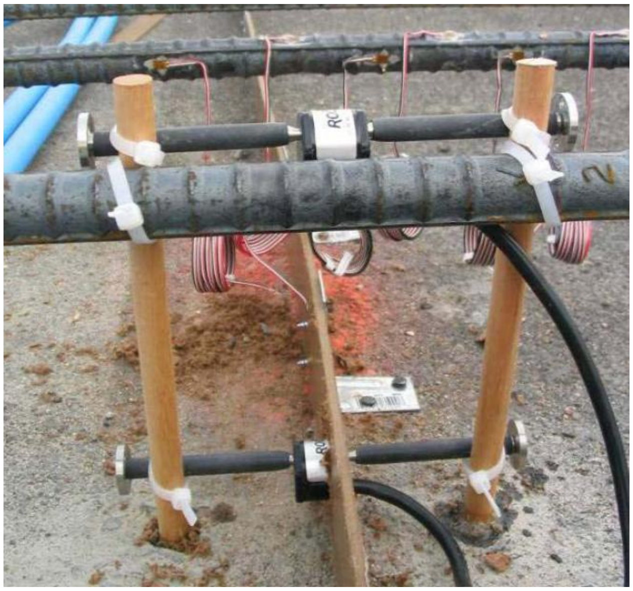

Figure 8.5: *Installation of vibrating wire strain gages with crack inducer* (Nam, 2005)

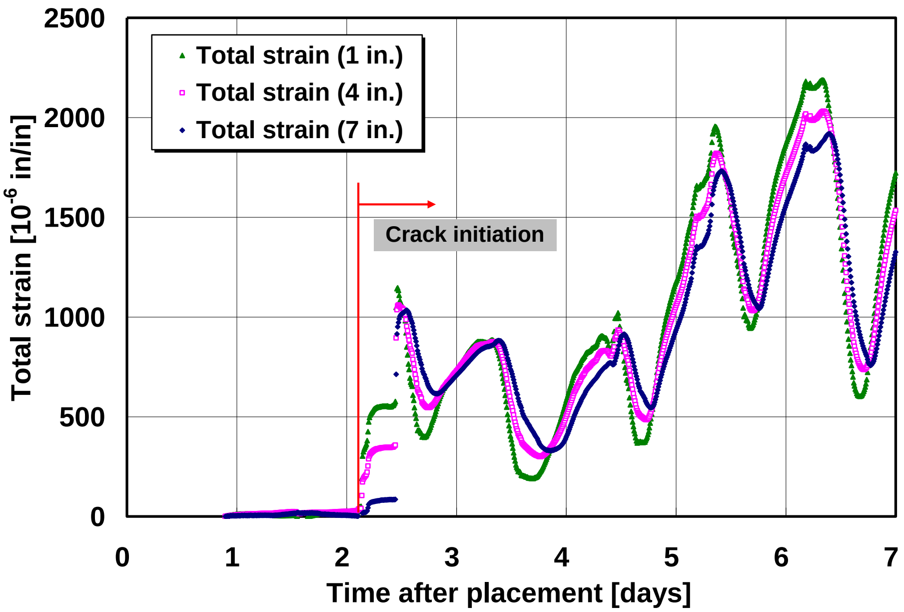

Figure 8.6: *Total strain measurement across transverse crack*

In the cracked CRCP section, steel plays a role in the post cracking behavior because bond-slip occurs at the interface between steel reinforcement and surrounding concrete. In the non-cracked CRCP, however, steel will ave little influence on the stress development of concrete since no bond-slip arises. Thus, the steel reinforcement is not considered in the stress prediction modeling of this study. For the same reason, the frictional stress-slip relationship between the concrete slab and underlying subbase layer is not taken into account.

8.2 MATHEMATICAL MODELS FOR HEAT TRANSFER

8.2.1 Heat Transfer

As shown in Figure 8.7, the temperature development of early-age PCC pavement is affected by various factors including short-wave solar radiation emitted by the sun, long-wave thermal irradiation emitted by the structure itself, reflection, thermal convection, geometry, and material properties such as hydration heat of portland cement and thermal conductivity.

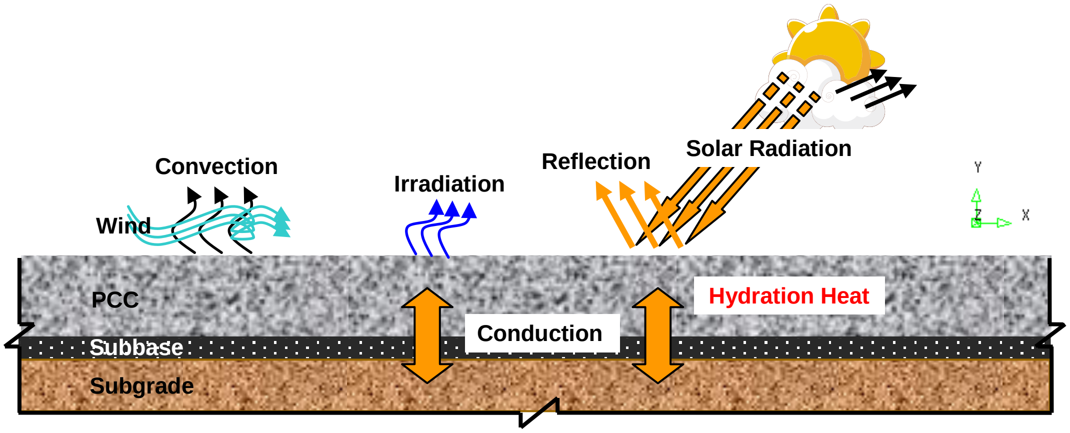

Figure 8.7: *Thermal interactions of PCC pavement with surrounding environment*

The temperature at any point within the boundary of the body and time can be determined by the transient heat transfer analysis, which is governed by the Fourier's law of flow (Lienhard IV and Lienhard V, 2000):

$$\nabla \cdot (k \nabla T) + \dot{Q} = \rho c_p \dot{T} \qquad \text{(Eq. 8.1)}$$

where, $\dot{Q}$ is the rate of internal heat generation due to cement hydration; T is the temperature; k is the thermal conductivity of concrete; ρ is the density; and c_p is the specific heat.

The above thermodynamic equation can be rewritten in a two-dimensional form as follows:

$$\frac{\partial}{\partial x}\left(k_x \frac{\partial T}{\partial x}\right) + \frac{\partial}{\partial y}\left(k_y \frac{\partial T}{\partial y}\right) + q = \rho c_p \frac{\partial T}{\partial t} \qquad \text{(Eq. 8.2)}$$

where, $k = k_x = k_y$ is the thermal conductivity for a isotropic material; and q is the rate of heat generation per unit volume.

The isotropic material assumption simplifies Eq. 8.2 as follows:

$$k\left(\frac{\partial^2 T}{\partial x^2}+\frac{\partial^2 T}{\partial y^2}\right)+q=\rho c_p \frac{\partial T}{\partial t} \tag{Eq. 8.3}$$

Two types of boundary conditions are related with Eq. 8.3. The first boundary condition is that the temperature along the boundary is known. The second boundary condition is the energy transfer through the boundary (Wang and Dilger, 1995). The second boundary condition for typical engineering structures which allow a heat flow through the boundaries can be written as follows:

$$k\left(\frac{\partial T}{\partial x}n_x+\frac{\partial T}{\partial y}n_y\right)+q_b=0 \tag{Eq. 8.4}$$

where, n_x and n_y are the direction cosines of the unit outward normal to the boundary surfaces; and q_b is the rate of boundary heat energy transfer with environment per unit area.

8.2.2 Environmental Interactions

The rate of heat energy transfer with environment, q_b, is the sum of the heat energy transfer due to convection, solar radiation, and thermal irradiation (Cengel, 2002):

$$q_b = q_c + q_s + q_r \tag{Eq. 8.4}$$

where, q_c, q_s, and q_r are the heat energy transfer with environment due to convection, solar radiation, and thermal irradiation, respectively.

The convection heat transfer caused by the temperature difference between the PCC pavement surface and ambient can be expressed by Newton's Law (Lienhard IV and Lienhard V, 2000):

$$q_c = h_c (T_s - T_a) \quad \text{(Eq. 8.5)}$$

where, h_c is the convection heat transfer coefficient; T_s is the surface temperature of PCC pavement; and T_a is the ambient temperature.

Herein, h_c is typically expressed as a function of wind speed. In this study, the following convection coefficient estimation models were used (Schindler, 2002):

$$h_c = 20+14 \cdot v \text{ (KJ/m}^2\text{/hr/°C)} \qquad \text{If } v \leq 5 \text{ m/s} \qquad \text{(Eq. 8.6)}$$

$$h_c = 25.6 \cdot v^{0.78} \text{ (KJ/m}^2\text{/hr/°C)} \qquad \text{If } v > 5 \text{ m/s} \qquad \text{(Eq. 8.7)}$$

where, v is the wind velocity, m/s.

If there are formworks or any other insulation layers covering the pavement, the overall convection heat transfer coefficient can be determined using Eq. 8.8 (Schindler, 2002).

$$h_c = \left(\frac{d_1}{k_1} + \frac{d_2}{k_2} + \frac{d_3}{k_3} + \frac{d_n}{k_n} \right)^{-1} \quad \text{(Eq. 8.8)}$$

where, d_n is the thickness of n successive layers; and k_n is the thermal conductivity of n successive layers.

Short-wave solar radiation is the heat flux absorbed by the PCC pavement surface and is influenced by many factors such as the time of the day or year, the latitude, and cloudiness (Chapman, 1982). To consider the solar absorption, the following equation can be used (Schindler, 2002).

$$q_s = \beta_s \cdot I_f \cdot q_{solar} \qquad \text{(Eq. 8.9)}$$

where, β_s is the solar radiation absorptivity; I_f is the intensity factor to account for angle of the sun during a day; and q_{solar} is the instantaneous solar radiation.

The typical solar absorptivity for grey PCC surface ranges from 0.5 to 0.6. However, the solar absorptivity for PCC pavement covered with white curing compound can be reduced to 0.1 to 0.35 (Schinder, 2002).

The heat exchange due to the long-wave thermal irradiation between the PCC pavement surface and ambient can be estimated by the Stefan-Boltzman Law (Cengel, 2002):

$$q_r = \varepsilon \cdot \sigma(T_s^{\ 4} - T_a^{\ 4}) \qquad \text{(Eq. 8.10)}$$

where, ε is the emissivity coefficient, which relates the radiation of the PCC pavement surface to that of a perfect radiator at the same temperature; and σ is the Stefan-Boltzman constant.

8.3 TEMPERATURE PREDICTION

8.3.1 Finite Element Discretization and Thermal Properties

Concrete temperature at early-age is affected by the significant amount of hydration heat of portland cement and thermal interactions with the surroundings as described in Figure 8.7. To estimate the temperature development in the concrete elements, a numerical analysis was performed using DIANA v. 8.1.2, the commercial finite element analysis package developed by TNO (TNO, 2003).

Figure 8.8 shows the two-dimensional finite element meshes adopted in this study for temperature prediction. For reasonable estimation of temperature, three different layers, i.e., concrete layer, hot mixed asphalt subbase layer, and stabilized subgrade layer, were modeled with the two-dimensional flow elements (CQ8HT). The dimensions of the modeled concrete layer, subbase layer, and subgrade layer were 5 ft. (length) x 6 to 14 in. (thickness), 5 ft. (length) x 4 in. (thickness), and 5 ft. (length) x 5 ft. (thickness), respectively. It was verified that the selected finite element mesh size showed a good convergence in the analysis results.

To model the thermal convection to ambient, the boundary line elements (B2HT) were used along the top surface of the concrete layer. As the material related thermal properties for concrete and underlying layers, adiabatic temperature rise, thermal conductivity, and thermal capacitance were considered. Also, the heat sources from environment such as short-wave radiation emitted from the sun, long-wave irradiation emitted by the structure itself, and ambient temperature were taken into account. The heat exchange due to atmosphere convection was considered as well.

Since the initial temperature of the underlying layers, i.e., asphalt subbase and subgrade, influences the early-age temperature development of the concrete layer, the initial temperature distribution prior to concrete placement was estimated using the numerical analysis. Figure 8.9 shows the example of temperature distribution variation in the underlying layers due to changes in daily air temperature and solar radiation during summer.

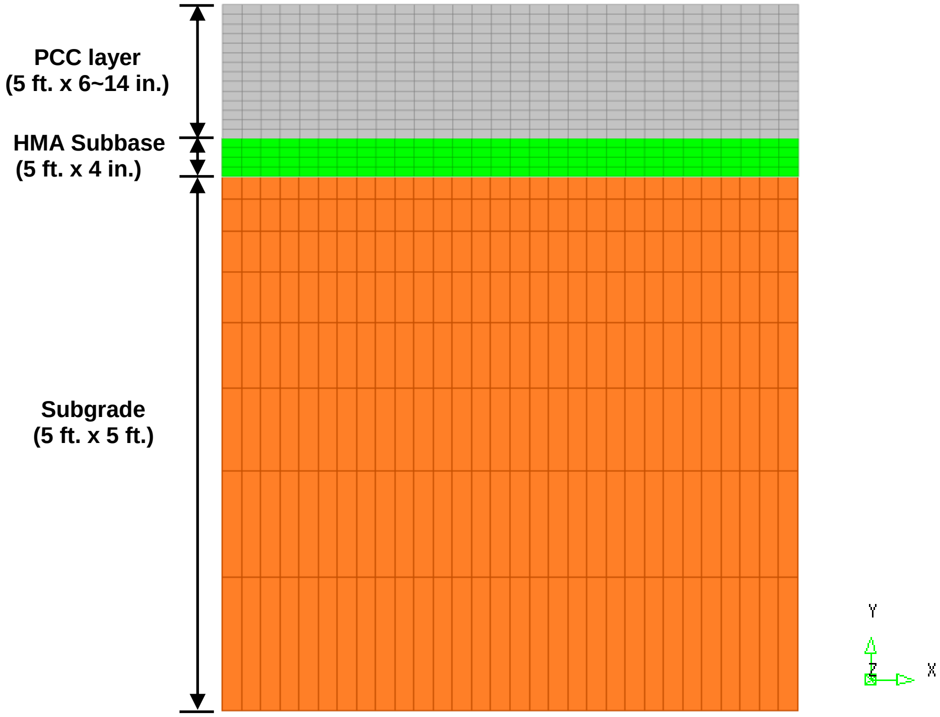

Figure 8.8: *Finite element mesh for temperature analysis*

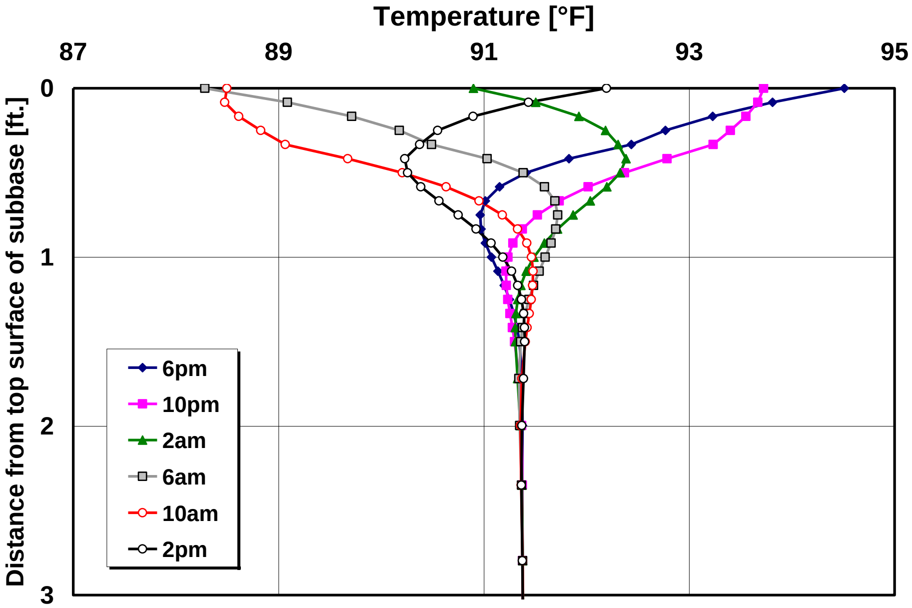

Figure 8.9: *Variation of temperature distribution in underlying layers*

8.3.2 Validation of Proposed Temperature Prediction Model

To validate the developed temperature prediction model above, the field measured temperature history obtained from the Fort Worth project was compared with the temperature history predicted by the model. Table 8.1 summarizes the default input parameters used in the heat transfer analysis. The material-related input parameters were not tested values but were appropriately assumed within the typical ranges, understanding the properties of the materials and environmental conditions at the time of field monitoring.

Figure 8.12 presents the measured and predicted temperature histories at 1 in. below the top, mid-depth, and 1 in. above the bottom of the pavement for the first 36 hours after concrete's final setting. As shown in the result, the predicted and measured temperature profiles quite well agreed each other, which indicate that the developed temperature prediction model was appropriate.

Table 8.1: *Default thermal input parameters used in numerical analysis* (Ali, 2010)

Parameters	Concrete	Subbase	Subgrade
Thermal conductivity (W/m ℃)	2.70	1.38	3.32
Thermal capacitance (kJ/m^3 ℃)	2,360	2,180	2,350
Density (kg/m^3)	2,445	2,370	2,340
Convection coefficient (W/m^2 ℃)	15.3		
Ambient temperature	See Figure 8.10		
Solar radiation	See Figure 8.11		

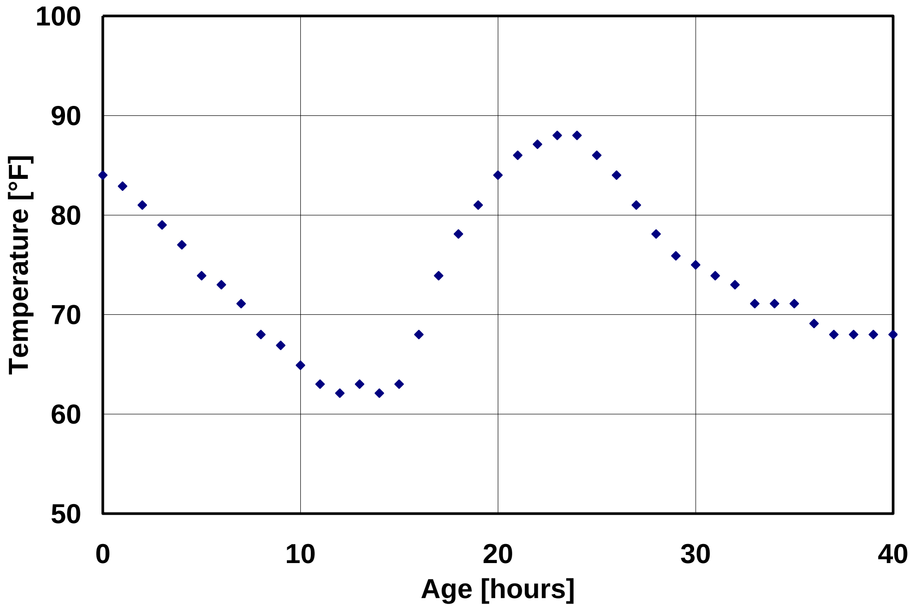

Figure 8.10: *Ambient temperature input used in numerical analysis*

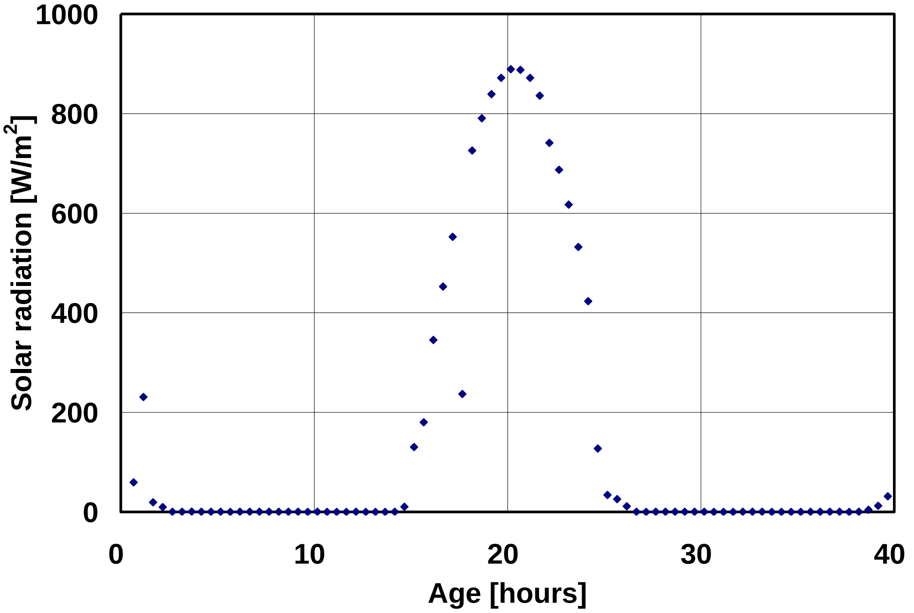

Figure 8.11: *Solar radiation input used in numerical analysis*

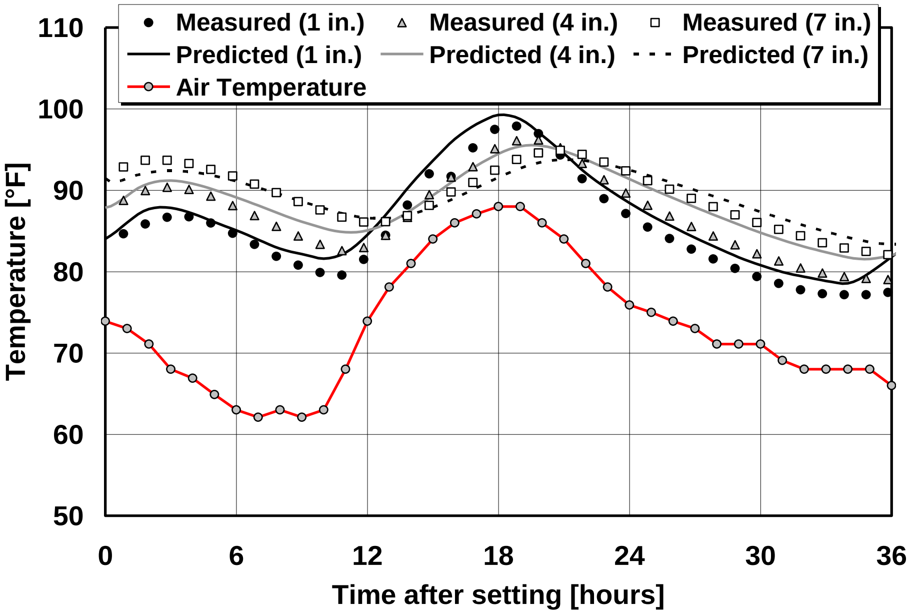

Figure 8.12: *Measured and predicted temperature profile in Fort Worth project*

The additional validation work was performed with the temperature data collected from Belton project, a 13-in.-thick CRCP with double mat steel reinforcement. It was constructed on I-35 northbound near Belton, TX in October 2009. The concrete temperature was measured at the top 1in., mid-depth, and bottom 1in. In this project, the environmental factors – solar radiation and air temperature – were not collected and the estimated values were used, which resulted in a slight difference in the measured and predicted temperature histories. However, the results showed fairly good agreement as shown in Figure 8.13.

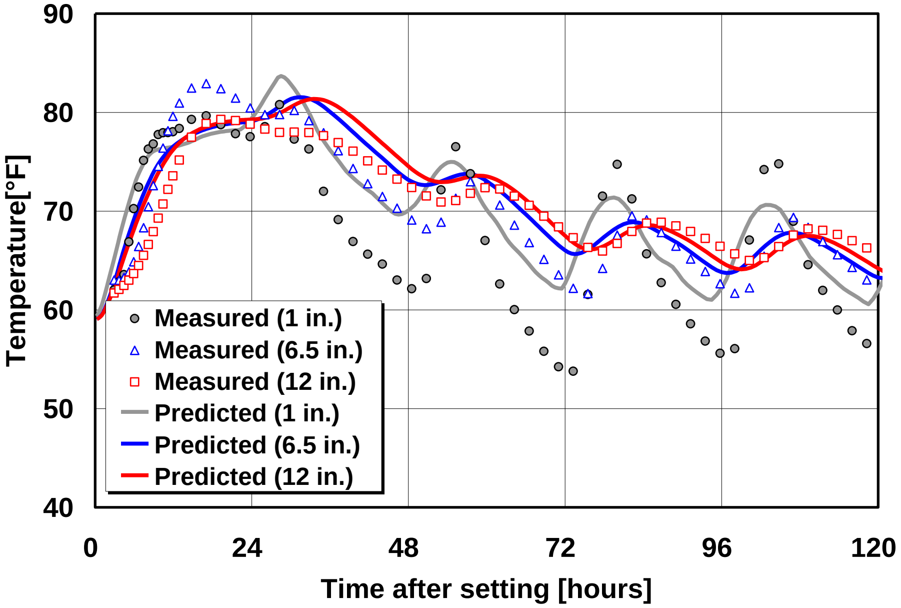

Figure 8.13: *Measured and predicted temperature profile in Belton project*

8.4 THERMAL STRESS PREDICTION

8.4.1 Finite Element Discretization and Material Properties

The DIANA software package offers the heatflow-stress staggered analysis. Using this type of analysis, the temperature distribution in the modeled section at each predetermined time step is evaluated first, and the corresponding time-dependent stress is calculated.

To accurately estimate the concrete stresses due to restrained thermal volume changes, eight-node quadrilateral plane strain elements (CQ16E) were used for mesh presentation of concrete. The subbase and subgrade layers were also modeled with the eight-node quadrilateral plane strain elements. The finite element meshing was same with the one used in the temperature prediction model shown in Figure 8.8. As described in the previous subchapter with the field measured evidence, it was considered that the modeled section is fully restrained along the longitudinal direction.

To account for the material properties of early-age concrete, which significantly vary as the degree of hydration develops, various models have been suggested to model the evolution of material properties to date. In this study, CEB-FIP Model Code 1990 provided by DIANA was used to present the material properties of hydrating concrete such as modulus development and creep. The basic inputs to initiate the model code were the 28-day compressive strength and elastic modulus, ambient RH and temperature, age at the birth of the element, type of cement, and notional size of the member. In the actual analysis algorithm, the creep model was automatically considered as the equivalent relaxation function with the Maxwell-chain elements.

The mathematical model for elastic modulus development presented in CEB-FIP Model Code 1990 can be written as follows (CEB, 1993):

$$E_c(t) = \beta_E(t) \cdot E_c(28) \qquad \text{(Eq. 8.11)}$$

with,

$$\beta_E(t) = \sqrt{\beta_{cc}(t)} \qquad \text{(Eq. 8.12)}$$

$$E_c(28) = 21{,}500\left[(f_{ck} + \Delta f)/f_{cm0}\right]^{1/3} \qquad \text{(Eq. 8.13)}$$

$$\beta_{cc}(t) = \exp(s(1 - \sqrt{28/t_T}) \qquad \text{(Eq. 8.14)}$$

where, s is the cement factor: 0.2 for rapid cement, 0.25 for normal cement, 0.38 for slow cement; t is the equivalent age, days; f_{ck} is the characteristic compressive strength at 28-day, MPa; Δf is 8 MPa; f_{cm0} is 10 MPa; and t_T is the concrete age adjusted for temperature (equivalent age).

t_T can be mathematically expressed as follows:

$$t_T = \sum_{i=1}^{n}\left[\Delta t_i \exp\left(13.65 - \frac{4000}{273 + T(\Delta t_i)}\right)\right] \qquad \text{(Eq. 8.15)}$$

where, Δt_i is the number of days where a temperature $T(\Delta t_i)$ degree Celsius prevails.

For the prediction of autogenous shrinkage, one of the important elements causing volume changes in cement-based material, the JSCE model originally suggested by Tazawa (1999) was adopted. Besides, the basic physical properties of concrete and underlying layers such as density, Poisson's ratio, and CTE were considered.

The age-dependent CTE and setting temperature differential were not considered in the numerical analysis scheme due to a lack of available information.

8.4.2 Validation of Proposed Stress Prediction Model

To evaluate the validity of the theoretical modeling developed above, the stress predicted by the model was directly compared with the field evaluated stresses. The field measurement scheme was well described in Chapters 4 and 5 of this dissertation. The field measurements obtained from the Fort Worth project was used for the comparison.

Figure 8.14 shows the measured and predicted stress histories for the first 36 hours after the final setting of concrete. It is noted that transverse cracking occurred at the strain gage location about 29 hours after the final setting. Prior to the transverse cracking, the result showed that the measured and predicted stress histories at each depth showed favorable agreements, as indicated in Figure 8.15.

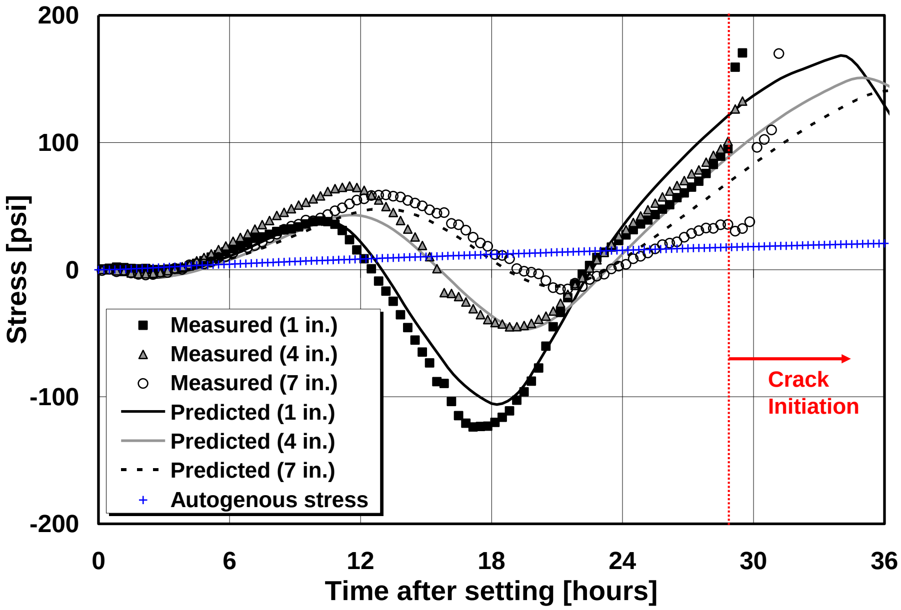

Figure 8.14: *Measured and predicted stress profiles in Fort Worth project*

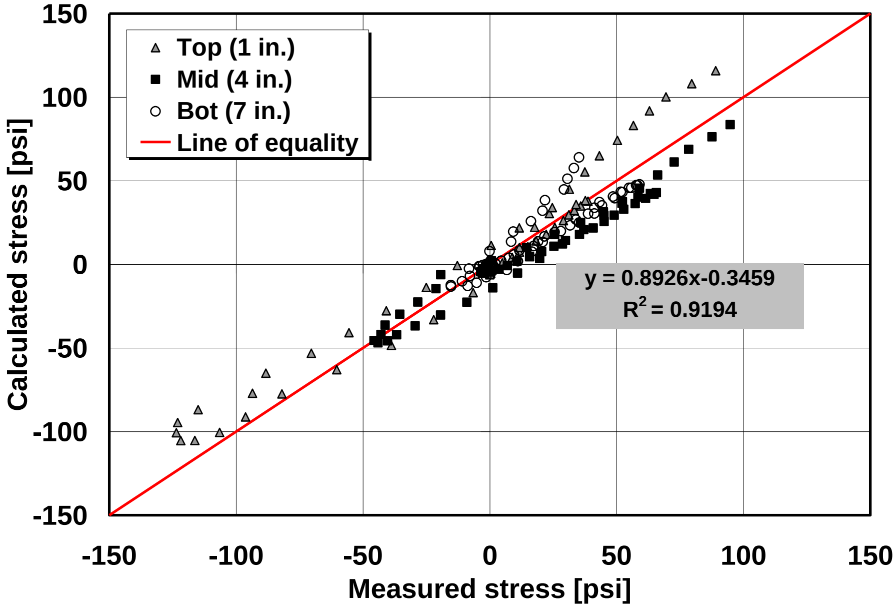

Figure 8.15: *Measured stress vs. predicted stress in Fort Worth Project*

8.5 SUMMARY

Throughout this chapter, theoretical models for temperature and corresponding thermal stress predictions were proposed. For reasonable modeling, underlying theories on temperature and time-dependent stress analyses were thoroughly reviewed first, and the numerical models were established based on the sound understanding of actual continuously reinforced concrete pavement (CRCP) behavior. By comparing the results obtained from the numerical analysis with the measured field data sets, the developed theoretical models were validated to be quite appropriate to implement in the further parametric numerical investigations for developing a zero-stress temperature (ZST) predictive model.

Chapter 9: Development of Zero-Stress Temperature Predictive Model

Through Chapter 8, the proposed theoretical models were validated by comparing the analysis results with the field experimental results. In this chapter, a parametric study is performed using the developed temperature and thermal stress models in terms of predetermined analysis parameters. The result of parametric study is statistically analyzed using a multivariate regression analysis to provide a zero-stress temperature (ZST) prediction model.

9.1 PARAMETRIC INVESTIGATION

9.1.1 Analysis Parameters

As described previously, the early-age concrete stress development is affected by the complex interactions of numerous factors during the hardening process. To develop a reasonable ZST prediction model, the major influencing parameters on the early-age stress development were evaluated first based on the preliminary study, and the factorial experiment was determined. Table 9.1 summarizes the analysis parameters adopted in the parametric study.

Table 9.1: *Summary of analysis parameters*

Thermal Parameters			Stress Parameters	
Geometric	Thickness		Material	Modulus of Elasticity[a]
Material	Cementitious Content			
	Water-Cement Ratio			
	Thermal Conductivity[a]			
	Thermal Capacitance[a]			
Environmental	Time of Day of Placement	Daytime		Coefficient of Thermal Expansion[a]
		Nighttime		
	Season of Placement	Summer		
		Winter		
	Wind Velocity	Thermal Convection		
	Solar Radiation	Summer		
		Winter		

[a] These parameters depend on the type of coarse aggregates

Since one of the primary objectives of this study is to investigate the early-age behavior of CRCP structures used in Texas, the material properties used in the numerical analysis were those of typical Class P concretes or closely related materials.

As the hydration heat and autogenous shrinkage-related material parameters, cementitous content and water-to-cement ratio were considered. The chemical composition and fineness of cement, and the type and chemical properties of SCMs were fixed to those of typical Type I portland cement and typical Class F fly ash used in Texas, respectively. The aggregate type has effects on the material properties such as modulus of elasticity, thermal conductivity, thermal capacitance, and CTE. In this study, two different types of aggregates – crushed limestone (LS) and siliceous river gravel (SRG) – that are widely used in concrete pavement applications in Texas were chosen. Also, the environmental parameters such as time of placement, season of placement, wind speed, and intensity of solar radiation emitted by the sun were considered for the parametric analysis. To investigate the effect of slab dimensions, the slab thicknesses of 6, 8, 10, 12, and 14 in. were investigated in this study. Table 9.2 shows the factorial experiment used in the numerical simulations.

Table 9.2: *Factorial experiment*

<table>
<tr><th>Parameters</th><th colspan="60">Levels</th></tr>
<tr><td>Thickness</td><td colspan="12">6 in.</td><td colspan="12">8 in.</td><td colspan="12">10 in.</td><td colspan="12">12 in.</td><td colspan="12">14 in.</td></tr>
<tr><td>Placement Season & Solar Radiation[a]</td><td colspan="30">Summer</td><td colspan="30">Winter</td></tr>
<tr><td>Time of Day of Placement</td><td colspan="30">Daytime[b]</td><td colspan="30">Nighttime[c]</td></tr>
<tr><td>Type of Coarse Aggregate</td><td colspan="30">Limestone</td><td colspan="30">Siliceous River Gravel</td></tr>
<tr><td>Cementitious Content</td><td colspan="20">4-sack (376 lbs/yd^3)</td><td colspan="20">5-sack (470 lbs/yd^3)</td><td colspan="20">6-sack (564 lbs/yd^3)</td></tr>
<tr><td>Water-Cementitious Ratio</td><td colspan="20">0.4</td><td colspan="20">0.45</td><td colspan="20">0.5</td></tr>
<tr><td>Wind Velocity</td><td colspan="15">0 mph</td><td colspan="15">4.5 mph</td><td colspan="15">9.0 mph</td><td colspan="15">13.5 mph</td></tr>
</table>

[a] Solar radiation input was sinusoidally assumed considering seasonal characteristic as shown in Figure 9.1

[b] For summer cases, daytime indicates noon. For winter cases, daytime indicates 1pm

[c] For summer cases, nighttime indicates 2am. For winter cases, nighttime indicates 1am

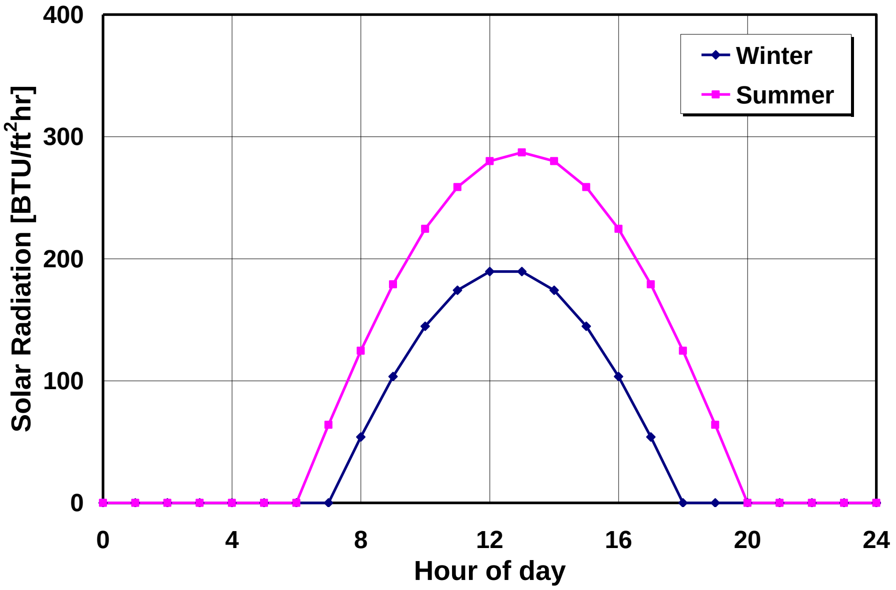

Figure 9.1: *Solar radiation inputs used for parametric study*

9.1.2 Material Properties for Parametric Study

9.1.2.1 Cement Properties

As will be discussed later, the heat of hydration and autogenous shrinkage predictive models involves the chemical composition and physical property of portland cement as the input variables. The properties of portland cement used in the parametric study are summarized in Table 9.3.

Table 9.3: *Typical chemical composition of ASTM Type I to V portland cements* (Mindess et al., 2003)

	Type I	Type II	Type III	Type IV	Type V
C_3S	55	55	55	42	55
C_2S	18	19	17	32	22
C_3A	10	6	10	4	4
C_4AF	8	11	8	15	12
SO_3	6	5	6	4	4
FreeCaO	0.8	0.6	1.3	0.3	0.4
MgO	2.4	3	2.6	2.7	1.6
Fineness (Blaine, m^2/kg)	365	375	550	340	380

9.1.2.2 Heat of Hydration

The sophisticated heat of hydration model for cementitious materials was developed under the TxDOT Research Project 0-1700 (Schindler, 2002). In order to predict the heat of hydration for various analysis cases, this heat of hydration model was used in the parametric study. The heat of hydration can be estimated using the following main models:

$$H_{cem} = 500 p_{C_3S} + 260 p_{C_2S} + 866 p_{C_3A} + 420 p_{C_4AF} + 624 p_{SO_3} + 1186 p_{FreeCaO} + 850 p_{MgO} \qquad \text{(Eq. 9.1)}$$

$$H_u = H_{cem} \cdot p_{cem} + 461 \cdot p_{SLAG} + 1800 \cdot p_{FA-CaO} \cdot p_{FA} \qquad \text{(Eq. 9.2)}$$

$$H_T = H_u \cdot C_c \tag{Eq. 9.3}$$

$$\alpha(t_e) = \alpha_u \cdot \exp\left(-\left[\frac{\tau}{t_e} \right]^{\beta} \right) \tag{Eq. 9.4}$$

$$\alpha_u = \frac{1.031 \cdot w/cm}{0.194 + w/cm} + 0.50 \cdot p_{FA} + 0.30 \cdot p_{SLAG} \leq 1.0 \tag{Eq. 9.5}$$

$$\tau = 66.78 \cdot p_{C_3A}{}^{-0.154} \cdot p_{C_3S}{}^{-0.401} \cdot Blaine^{-0.804} \cdot p_{SO_3}{}^{-0.758} \cdot \exp(2.187 \cdot p_{SLAG} + 9.50 \cdot p_{FA} \cdot p_{FA-CaO}) \tag{Eq. 9.6}$$

$$\beta = 181.4 \cdot p_{C_3A}{}^{0.146} \cdot p_{C_3S}{}^{0.227} \cdot Blaine^{-0.535} \cdot p_{SO_3}{}^{0.558} \cdot \exp(-0.647 \cdot p_{SLAG}) \tag{Eq. 9.7}$$

$$H(t_e) = H_T \cdot \alpha(t_e) \tag{Eq. 9.8}$$

where, H_{cem} is the total heat of hydration of the cement; the p_i is the weight ratio of i^{th} component; H_u is the ultimate heat of hydration; C_c is the cementitious content; H_T is the $\alpha(t_e)$ is the degree of hydration at equivalent age at t_e; α_u is the ultimate degree of hydration; τ is the hydration time parameter; β is the hydration shape parameter; *w/cm* is the water-to-cementitious ratio; *Blaine* is the Blaine value (specific surface area); and $H(t_e)$ is the cumulative heat of hydration at equivalent age t_e.

9.1.2.3 Autogenous Shrinkage

For autogenous shrinkage prediction for each of the analytical cases, Japan Society of Civil Engineers (JSCE) Model suggested Miyazawa and Tazawa (Tazawa, 1999) was used; recall Eq. 3.12. Because the original JSCE model does not include the effect of SCM, the improved autogenous shrinkage model suggested by Yan et al. (2007)

was used. Yan et al. added the term describing the effect of SCM in addition to the basic formula seen in Eq. 3.12.

$$\alpha = (1 - 2.8x_{FA}^2) \qquad \text{for fly ash concrete} \qquad \text{(Eq. 9.9)}$$

$$\alpha = (1 - 2.5x_{SL}^2) \qquad \text{for slag concrete} \qquad \text{(Eq. 9.10)}$$

$$\alpha = (1 + 1.3x_{SF} - 3x_{SF}^2) \qquad \text{for silica fume concrete} \qquad \text{(Eq. 9.11)}$$

where, x_{FA}, x_{SL}, and x_{SF} are the replacement ratio of cement by fly ash, slag, and silica fume, respectively.

9.1.2.4 Mechanical, Physical, and Thermal Properties of Concrete

The mechanical, physical, and thermal properties of concrete largely depend on the type of coarse aggregate used. As aforementioned, two different types of coarse aggregate – LS and SRG – widely used in the paving applications in Texas were investigated. The various properties affected by the coarse aggregate type and their values used in the numerical parametric study are listed in Table 9.3

Table 9.4: *Typical aggregate properties* (Ali, 2010)

	Limestone	Siliceous River Gravel
Density (lbs/ft^3)	152.5	149.5
Conductivity (cal./hr/ft./°F)	392	523
Capacitance (cal./ft^3/°F)	8,847	8,667
CTE (x 10^{-6}/°F)	4	6
28-day Elastic Modulus (x 10^{6}psi)	4	6
28-day Compressive Strength (psi)	4,000	6,000

To investigate the effect of cementitious content on the compressive strength, the experimental data sets presented in Mindess et al. (2003) and Mehta and Monteiro (2006) were used (Figure 9.2). Based on this information and Eq. (9.12) (ACI, 2008), the relationship between the cementitious content and elastic modulus was also established.

$$E_c = 57{,}000\sqrt{f_c^{'}} \qquad \text{(Eq. 9.12)}$$

where, E_c is the elastic modulus of concrete stressed to a working stress level, psi; and $f_c^{'}$ is the compressive strength of concrete, psi.

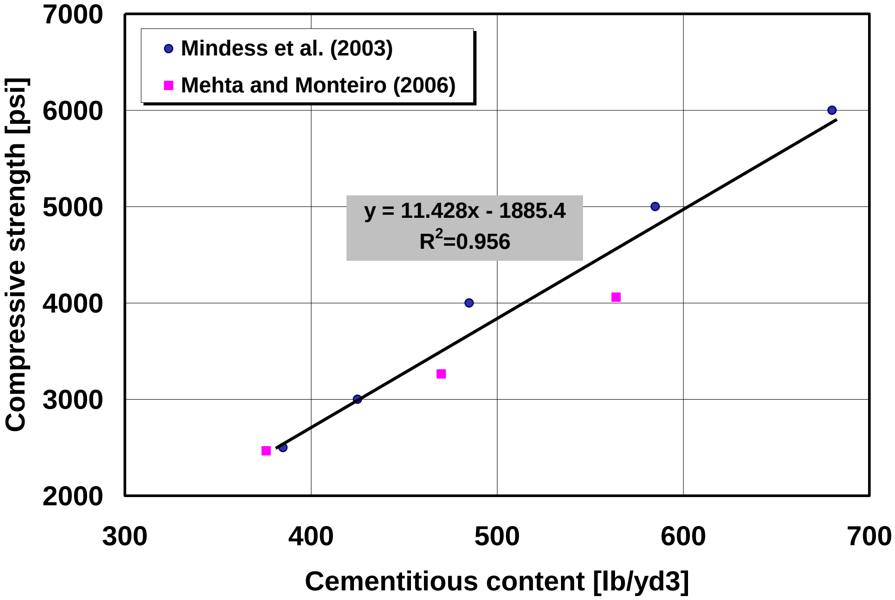

Figure 9.2: *Effect of cementitious content on compressive strength*
(Mindess et al.,2003; Mehta and Monteiro, 2006)

Furthermore, it is well known that the water-to-cement ratio has a substantial effect on the mechanical property development (Mehta and Monteiro, 2006; Neville, 1996; Mindess et al., 2003). Because the relationship between the water-to-cement ratio and mechanical properties can significantly vary depending on various factors such as mixture proportions, curing condition, and properties of used materials, etc., there was no standard relationship available for the parametric investigation. In this study, the correlations suggested by Popovics and Ujhelyi (1998) were employed. Figure 9.3 displays the relative relationships between water-to-cement ratio and various mechanical properties of concrete adopted in this study.

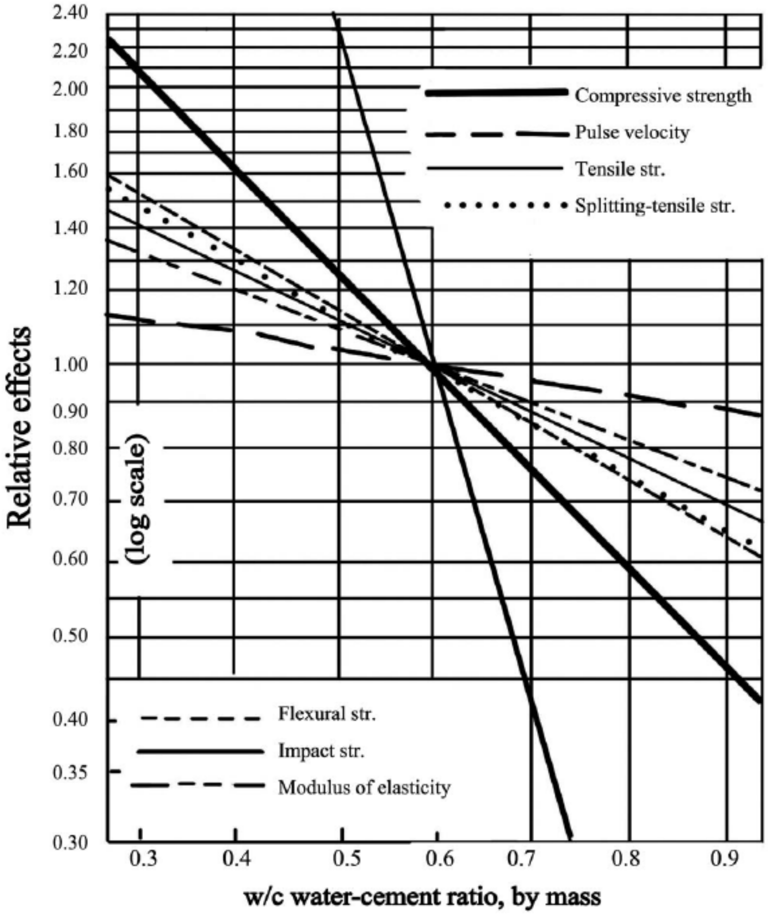

Figure 9.3: *Effect water-to-cement ratio on various mechanical properties*
(Popovics and Ujhelyi, 1998)

9.1.3 Presentation of Parametric Study Results

A parametric study was performed using the developed theoretical models to investigate the impact of each parameter on the temperature and corresponding thermal stress developments.

9.1.3.1 Effect of Concrete Slab Thickness

Figure 9.4 presents the effect of slab thickness on the temperature and thermal stress developments. The other variables were fixed as follows: daytime placement, LS, 5-sack of cementitious material, 0.45 of water-to-cement ratio, summer placement, 4.5 mph of wind speed, and mid-depth.

The result shows that the overall temperature histories during the analysis period become higher as the slab thickness increases. This is because the total amount of heat generation increases as the dimensions of concrete slab becomes larger. The trend of stress developments was different for each case; the thicker slab resulted in higher maximum compressive stress, thus took longer time the compressive stress is completely relieved, which delayed the time of ZST formation. Also, it is found that the absolute ZST increases as the slab thickness increases.

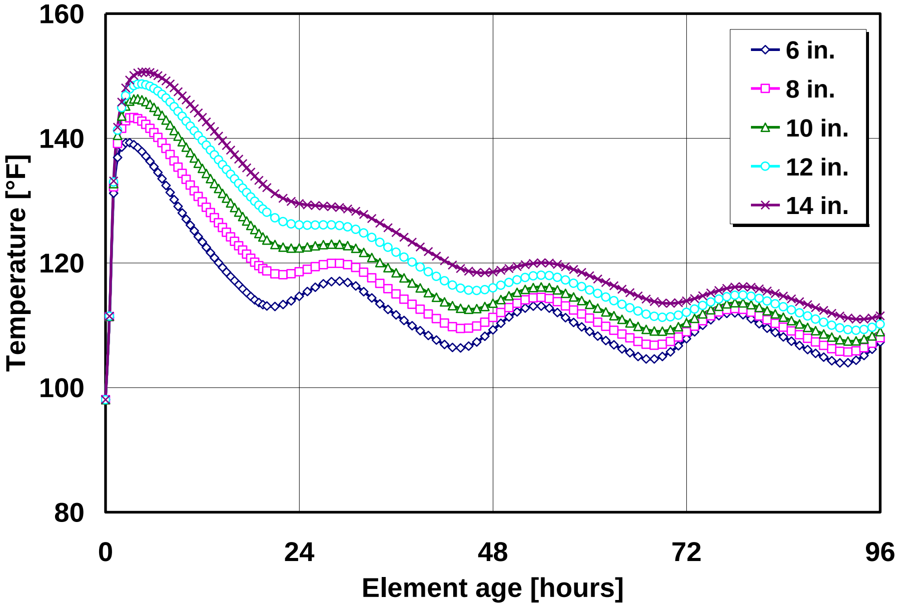

(a) Concrete temperature development

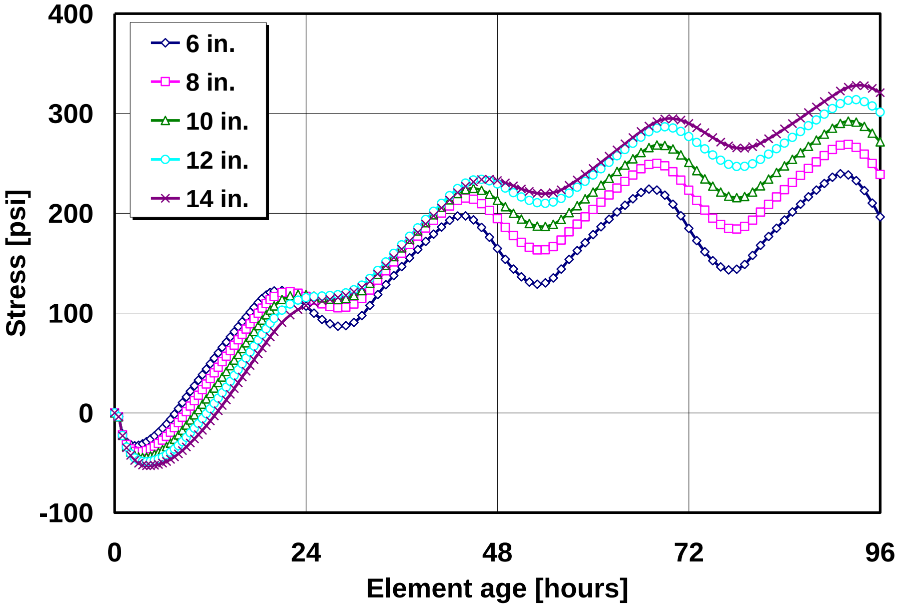

(b) Concrete stress development

Figure 9.4: *Effect of thickness on temperature and stress development*

The impact of wind speed on temperature and stress developments is displayed in Figure 9.5. The other variables were fixed as follows: 6 in. of slab thickness, daytime placement, LS coarse aggregate, 5-sack cement factor, 0.45 of water-to-cement ratio, summer placement, and mid-depth.

The result shows that as the wind speed increases, the maximum temperature becomes lower. In addition, it is noted that the wind speed affects the rate of early-age heat dissipation. This is because the wind speed determines the convection heat transfer coefficient which determines the rate of heat energy transfer, along with the temperature difference between the concrete slab surface and ambient (recall Eq. 8.5). As expected, the higher the wind speed is, the earlier the ZST is formed since the PCC pavement loses the compressive stress more rapidly.

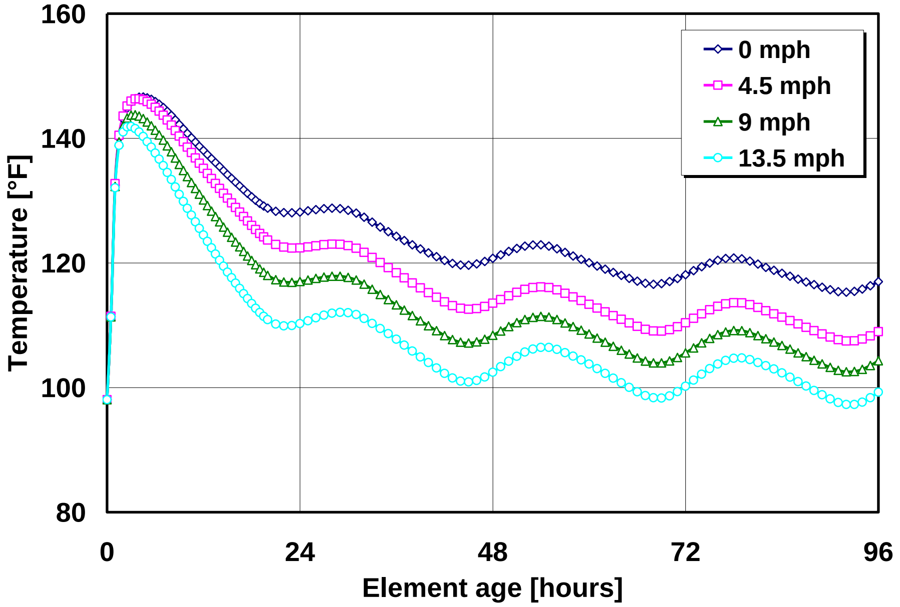

(a) Concrete temperature development

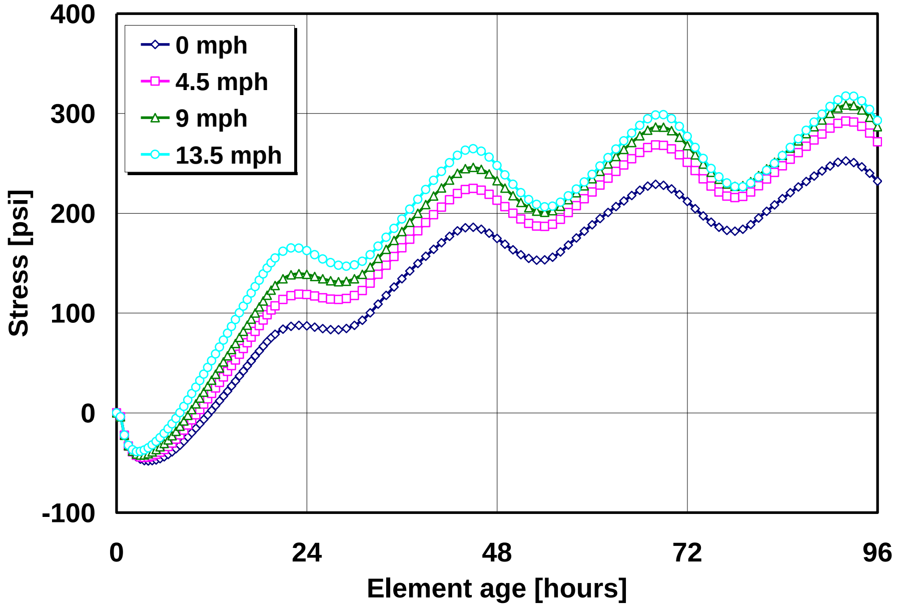

(b) Concrete stress development

Figure 9.5: *Effect of wind speed on temperature and stress development*

Figure 9.6 shows the effect of placement season. The other variables were set to 6 in. of slab thickness, daytime placement, LS coarse aggregate, 5-sack cement factor, 0.45 of water-to-cement ratio, 4.5 mph of wind speed, and mid-depth.

The result shows that the summer placement has a higher and steeper temperature rise during the first few hours compared to the winter placement. This is because both cases are exposed to different temperature history; in the context of DIANA, the quantity of the heat production is presented as a function of temperature history and degree of reaction (TNO, 2003). In the heat of hydration of analysis, the momentary heat production rate q can be defined as follows:

$$q(r,T) = \alpha \cdot q_r(r) \cdot q_T(T) \qquad \text{(Eq. 9.13)}$$

where, α is the maximum value of the heat production rate, $q_r(r)$ is the degree of reaction-dependent heat production, and $q_T(T)$ is the temperature-dependent heat production.

Also, the difference in stress development between both cases is found. This is because, as previously described, CEB-FIP Model Code 1990 was used to present the modulus development for stress evaluation. In this model code, the Arrhenius type equivalent age relation is adopted to consider the temperature influence on the modulus development.

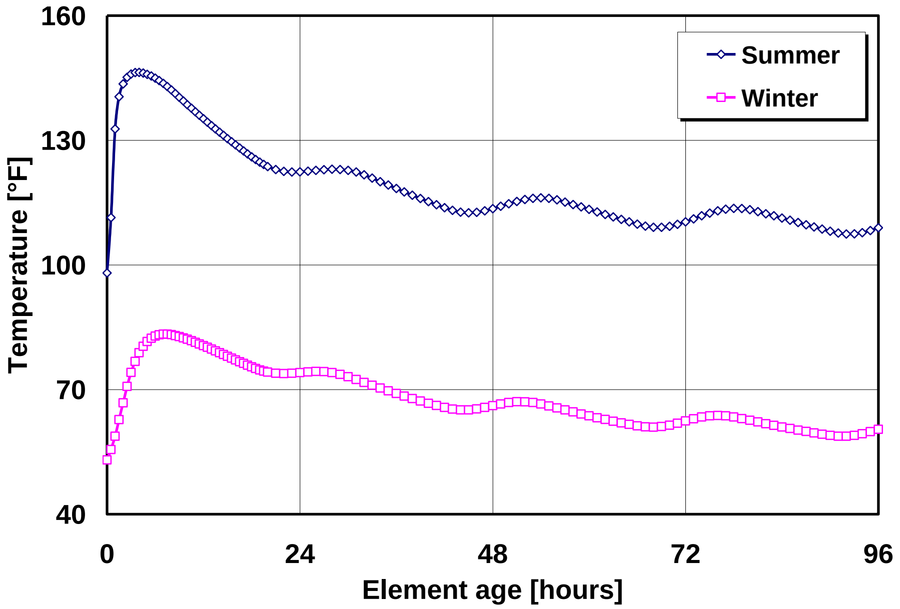

(a) Concrete temperature development

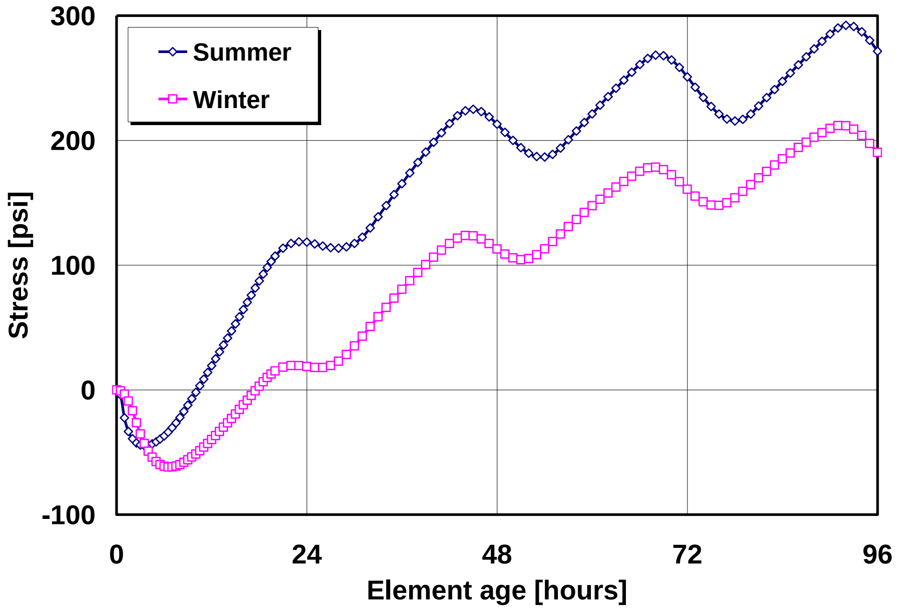

(b) Concrete stress development

Figure 9.6: *Effect of placement season on temperature and stress development*

In Figure 9.7, the influence of water-cement ratio is presented. The other variables were fixed as follows: 6 in. of slab thickness, daytime placement, LS coarse aggregate, 5-sack of cementitious material, summer placement, 4.5 mph of wind speed, and mid-depth.

The result presents that the 0.5 water-to-cement ratio case undergoes overall a slightly higher temperature history because the ultimate adiabatic temperature rise tends to increase as the water-cement ratio increases. Except for the very early-age stage, the temperature histories were quite similar each other as they achieve the thermal equilibrium with the ambient.

In the stress history, however, significant differences were found among the cases, as can be seen in Figure 9.7 (b). This is due to the effect of water-to-cement ratio on the development of mechanical properties of concrete. It is reported by numerous previous research studies (Mindess et al., 2003; Neville, 1996; Mehta and Monteiro, 2006) that the mechanical properties of concrete sensitively vary depending on the water-to-cement ratio of the mixture; as the water-to-cement ratio increases, the 28-day mechanical properties – strength and moduli – tends to decrease.

Furthermore, the autogenous shrinkage may contribute to the difference in stress history because the substantial difference in autogenous shrinkage is typically found as the water-to-cement ratio varies.

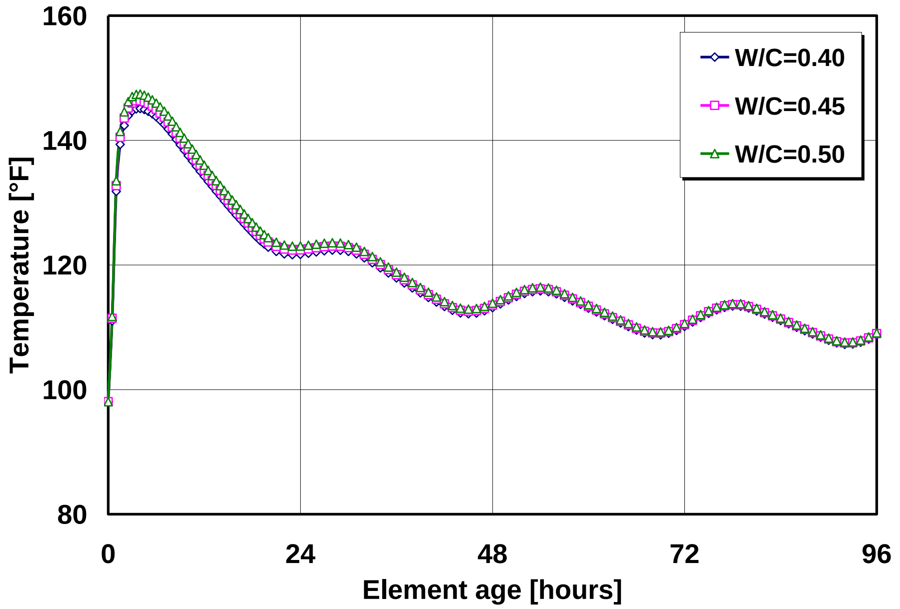

(a) Concrete temperature development

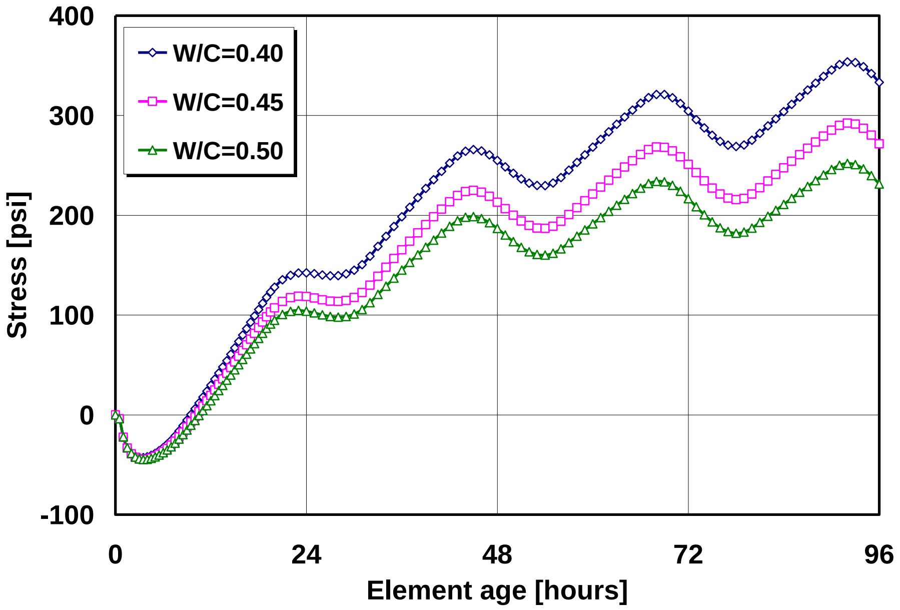

(b) Concrete stress development

Figure 9.7: *Effect of water-cement ratio on temperature and stress development*

The influence of coarse aggregate type on the temperature and stress evolutions is presented in Figure 9.8. The fixed parameters were: 6 in. of slab thickness, daytime placement, 5-sack of cementitious material, 0.45 of water-to-cementitious ratio, summer placement, 4.5 mph of wind speed, and mid-depth.

The temperature development was almost identical but a little difference was observed at early ages. This slight difference seems to arise from the discrepancy in thermal capacitance between those coarse aggregate types. However, when it comes to the stress histories, there was a huge difference between the LS and SRG concretes. This is because SRG concretes tend to have a 150% higher CTE and elastic modulus than the concrete incorporating LS. In reality, many field condition surveys performed under the TxDOT Research Project 0-6274 revealed that the CRCP incorporating SRG typically has shorter crack spacing at early-age than the one incorporating LS, which implies that the SRG concrete tends to have a higher residual stress level than the LS concrete.

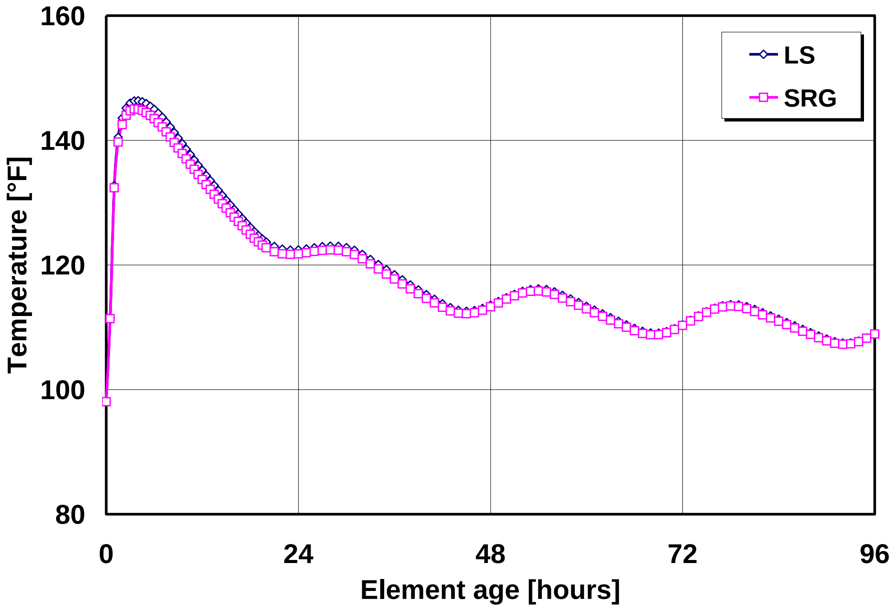

(a) Concrete temperature development

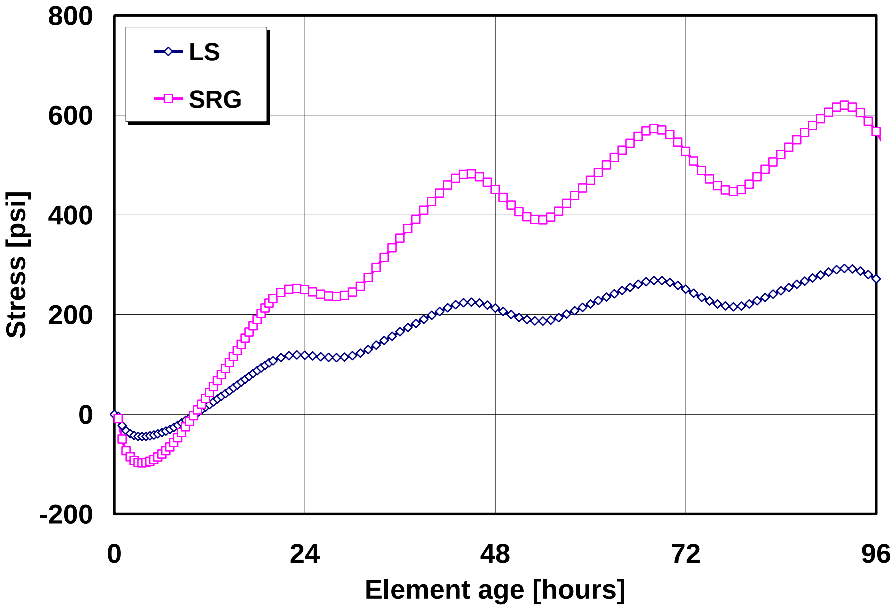

(b) Concrete stress development

Figure 9.8: *Effect of aggregate type on temperature and stress development*

The effect of cement content on stress and temperature developments was investigated based on the numerical simulation. The variables except for cement content were as follows: 6 in. of slab thickness, daytime placement, LS concrete, 0.45 of water-to-cementitious ratio, summer placement, 4.5 mph of wind speed, and mid-depth.

It was identified from the analysis results that the maximum temperature becomes higher as the cementitious content increases. This is because the total heat generation per unit volume increases as the concrete mixture incorporates more amount of portland cement.

As presented in Figure 9.9 (b), there were significant differences in their stress development histories. The reason for these differences seems to arise from their temperature-dependent mechanical property evolution as well as their temperature history differences.

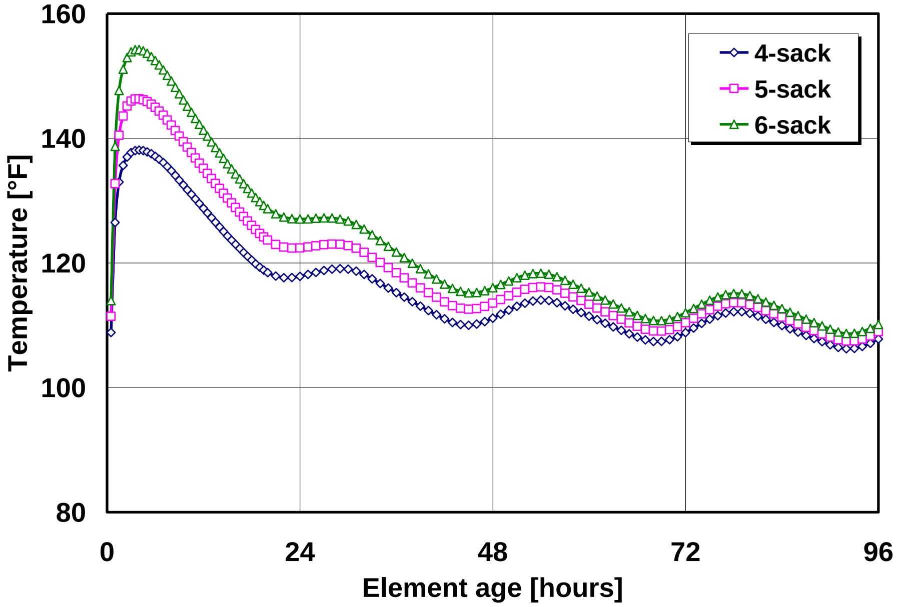

(a) Concrete temperature development

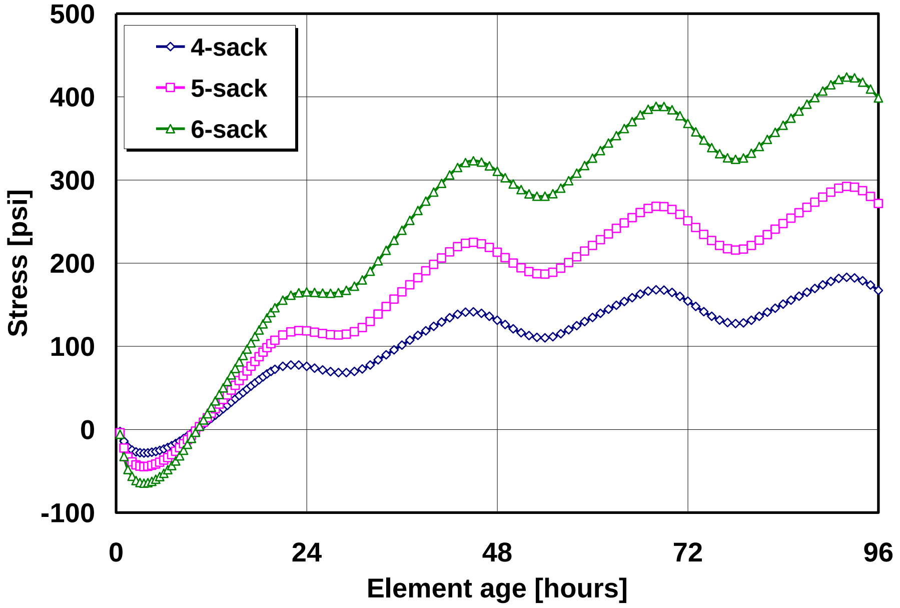

(b) Concrete stress development

Figure 9.9: *Effect of cement content on temperature and stress development*

The effect of time of placement of a day on the stress and temperature evolutions is shown in Figure 9.10. The other parameters were: 6 in. of slab thickness, LS concrete, 5-sack of cementitious material, 0.45 of water-to-cementitious ratio, summer placement, 4.5 mph of wind speed, and mid-depth.

As can be seen in the simulation results, the concrete temperature histories at early-age were significantly influenced by the placement time of a day. This is because concretes placed at different times of the day are subjected to the different air temperature history and solar radiation history (in turn, the rate of heat of hydration). Also, the difference in initial temperature of concrete and sub-layers can affect the evolution of early-age concrete temperature. As indicated in Figure 9.10 (a), it is of great importance to note that the time of placement of a day significantly affects the formation of ZST.

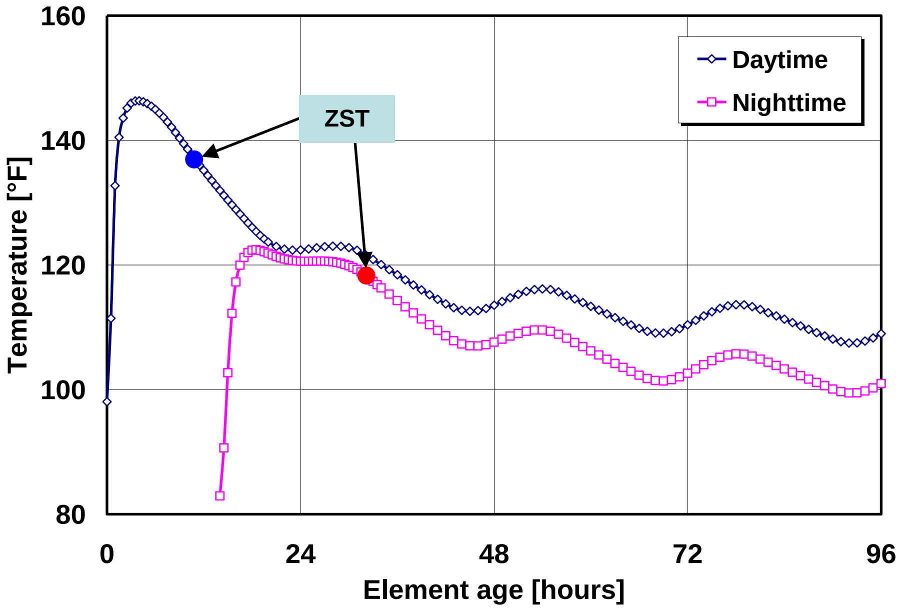

(a) Concrete temperature development

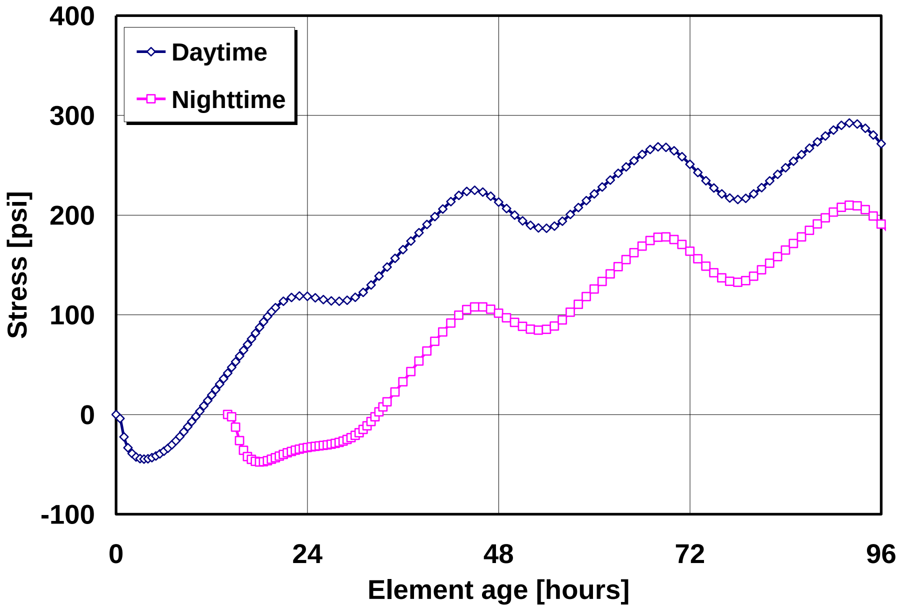

(b) Concrete stress development

Figure 9.10: *Effect of time of placement on temperature and stress development*

To examine the effect of concrete placement time of a day on the concrete temperature, stress, and the formation of ZST in more detail, the concrete temperature and corresponding stress histories were evaluated every four hour of a day using the developed numerical models. For the summer placement analysis cases, midnight, 4 am, 8 am, noon, 4 pm, and 8 pm were selected as the times of concrete placement while the winter cases included 1 am, 5 am, 9 am, 1 pm, 5 pm, and 9 pm as the concrete casting times.

Figures 9.11 and 9.12 present the results obtained from the numerical simulations. The results indicate that the placement time has substantial effects on the temperature and stress evolutions during the first few days after concrete placement. Especially in the case of temperature, up to 33 °F of maximum temperature difference was recorded. Accordingly, it is noted that the corresponding ZST significantly varies even in the same day placements as seen in Figure 9.13. For the summer and winter placement cases, up to 30 °F and 17.5 °F of ZST differences were found, respectively.

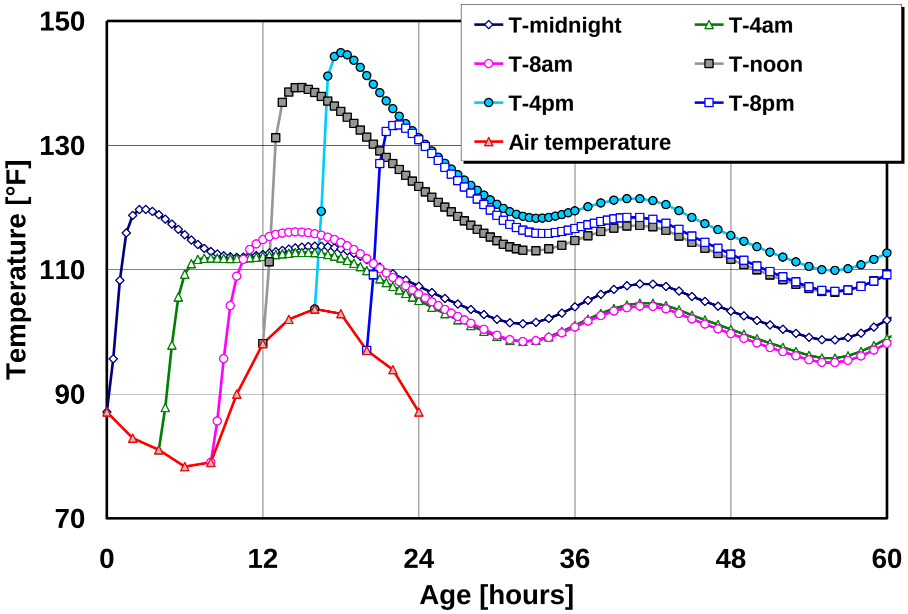

(a) Concrete temperature development

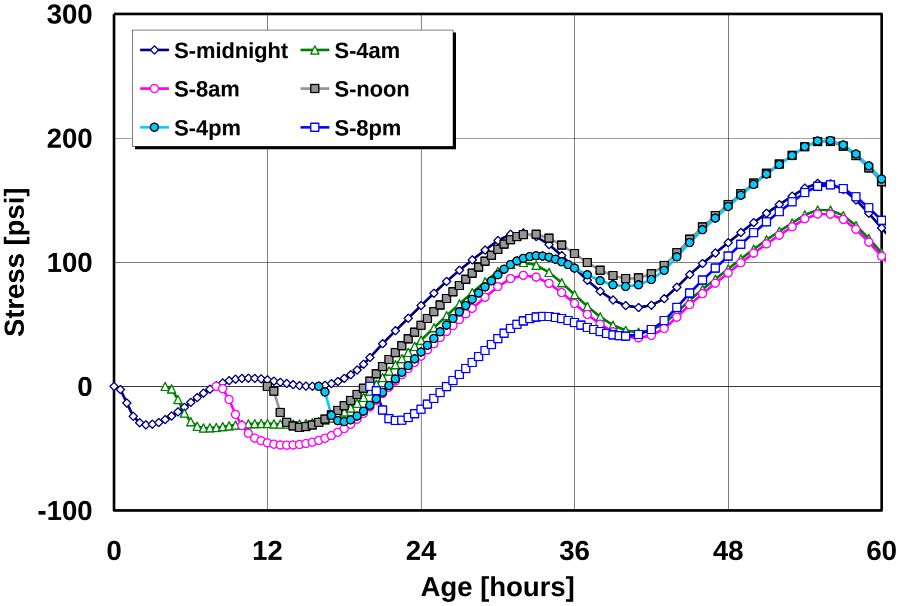

(b) Concrete stress development

Figure 9.11: *Effect of time of placement (summer placement)*

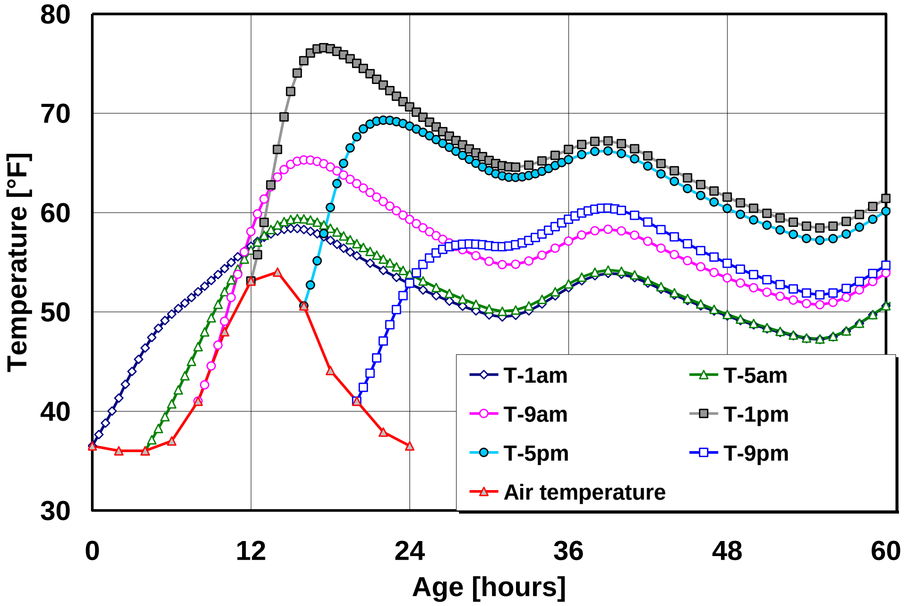

(a) Concrete temperature development

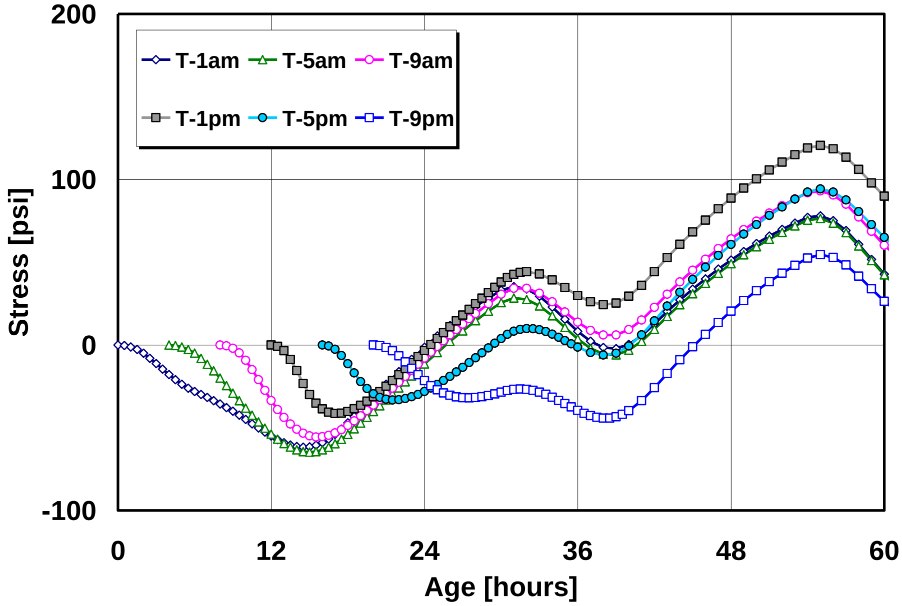

(b) Concrete stress development

Figure 9.12: *Effect of time of placement (winter placement)*

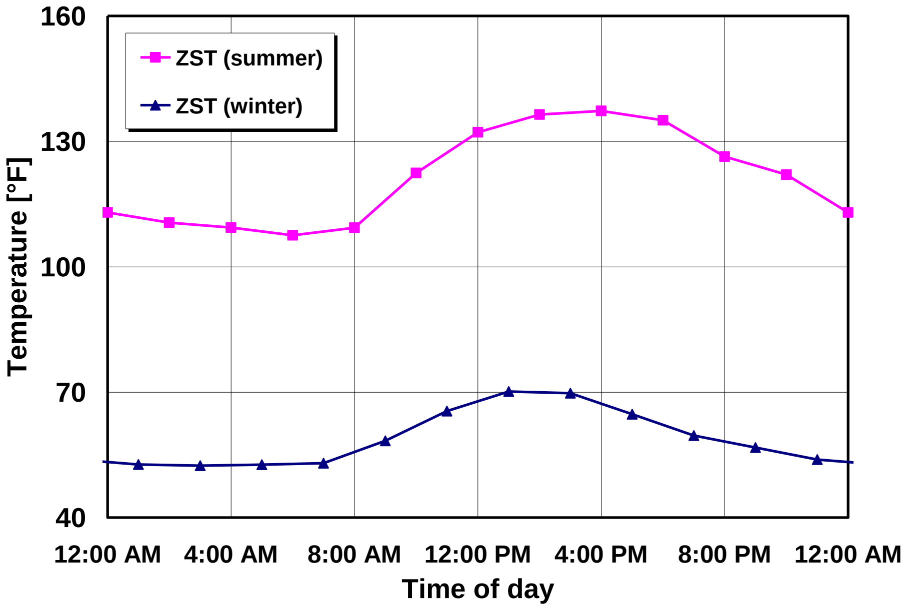

Figure 9.13: *Effect of placement time on ZST*

9.2 QUANTIFICATION OF ZERO-STRESS TEMPERATURE

To develop the ZST predictive model based on the results of parametric study, a basic form of the quantification indicator was derived using the mechanistic relations. Figure 9.14 illustrates the typical temperature development in a concrete element. T_s, T_{max}, and T_z indicate the setting temperature, maximum temperature, and ZST, respectively.

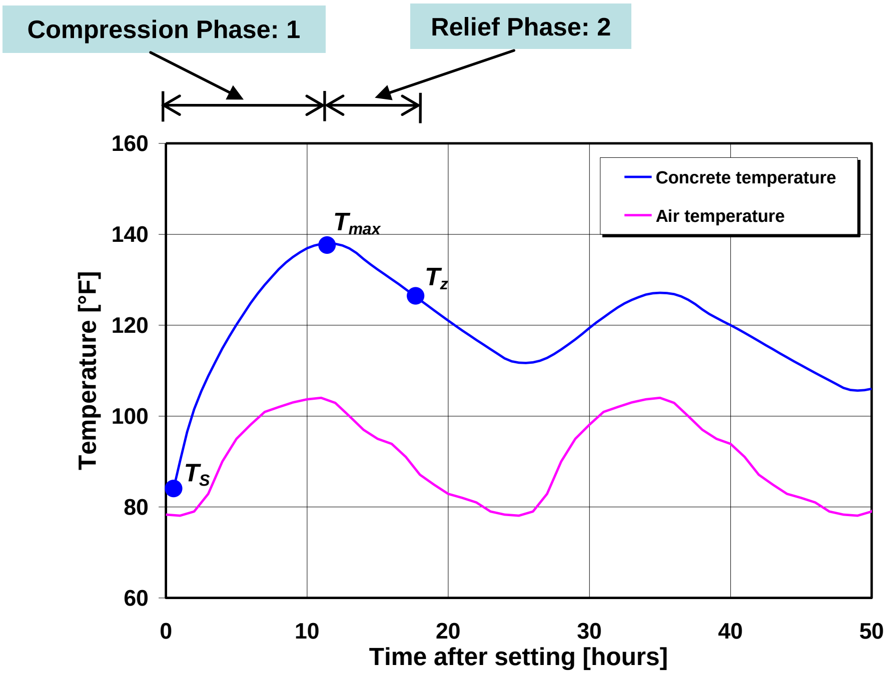

Figure 9.14: *Typical temperature development in concrete element*

During the temperature rise from T_s to T_{max}, compressive stress will be developed. Subsequently, the developed compressive stress will be completely relieved as the concrete temperature drops from T_{max} to T_z along with the concrete's rapid stiffness evolution. The stress build-ups during those phases can be mechanistically expressed as Eqs. 9.13 and 9.14, respectively.

$$\sigma_{c,1} = \frac{E_{c,1}}{(1+\phi_1)} \cdot \alpha_{c,1} \cdot (T_s - T_{\max}) \cdot R_{D,1} \qquad \text{(Eq. 9.13)}$$

$$\sigma_{c,2} = \frac{E_{c,2}}{(1+\phi_2)} \cdot \alpha_{c,2} \cdot (T_{\max} - T_z) \cdot R_{D,2} \qquad \text{(Eq. 9.14)}$$

To achieve the zero residual stress, the sum of Eqs. 9.13 and 9.14 should be zero:

$$\frac{E_{c,1}}{(1+\phi_1)}\cdot\alpha_{c,1}\cdot(T_s-T_{\max})\cdot R_{D,1}+\frac{E_{c,2}}{(1+\phi_2)}\cdot\alpha_{c,2}\cdot(T_{\max}-T_z)\cdot R_{D,2}=0 \qquad \text{(Eq. 9.15)}$$

Rewrite the Eq. 9.15 in terms of T_z, than the following equation is obtained:

$$T_z=T_{\max}-(T_{\max}-T_s)\cdot\frac{E_{c,1}}{E_{c,2}}\cdot\frac{\alpha_{c,1}}{\alpha_{c,2}}\cdot\frac{(1+\phi_2)}{(1+\phi_1)}\cdot\frac{R_{D,1}}{R_{D,2}} \qquad \text{(Eq. 9.16)}$$

where, $E_{c,i},\alpha_{c,i},\phi_i,\text{and}\, R_{D,i}$ are the "characteristic" elastic modulus, coefficient of thermal expansion, creep coefficient, and degree of restraint, respectively.

All these variables are not constant but continue to vary during the compression and relief phases, which make the equation hard to solve mechanistically. Thus, so-called "C-value" was introduced in this study to conveniently quantify the correlation of these variables. If Eq. 9.16 is rewritten in terms of the C-value, Eq. 9.17 is ultimately derived:

$$C=\frac{T_{\max}-T_z}{T_{\max}-T_s} \qquad \text{(Eq. 9.17)}$$

As can be understood from Eq. 9.17, the C-value indicates the ratio of the temperature variation during the relief phase to the temperature variation during the compression phase. If the quantification model for C-value is developed, the ZST will be determined once the maximum and setting temperatures of a project are known (in Fahrenheit), which is quite simple to implement in actual practices.

Figure 9.15 shows the example of ZST quantification with C-value. Also, Figure 9.16 displays the representative cases showing the effect of each variable on the C-value. The legends presented in Figure 9.16 indicate (in order): thickness, [in.] – time of placement of a day, [D: daytime, N: nighttime] – type of coarse aggregate, [LS: limestone, SRG: siliceous river gravel] – cementitious material content, [sack] – water-to-cement ratio, [-] – season of placement [S: summer, W: winter] – wind speed, [mph].

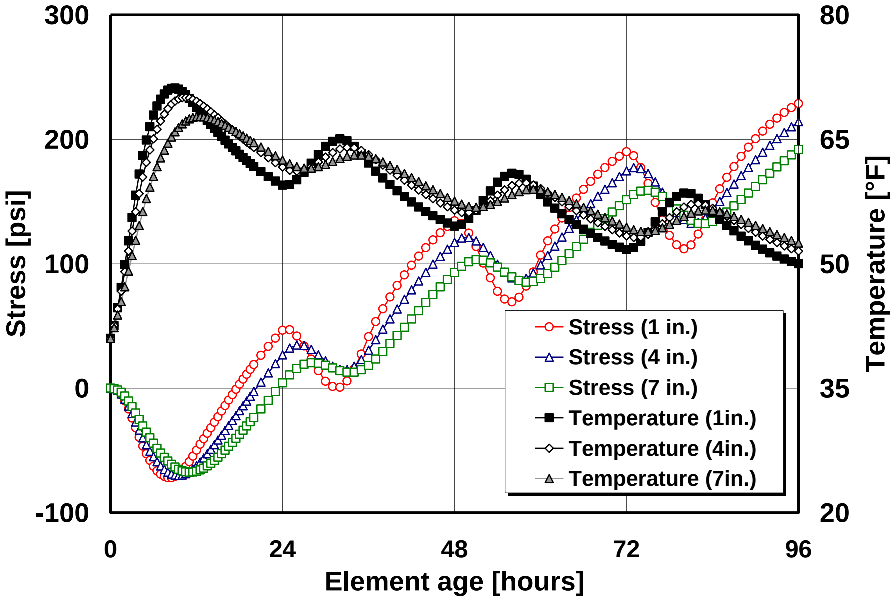

	Top	Mid	Bot
T_s (°F)	38.0	38.0	38.0
T_{max} (°F)	71.2	70.0	67.7
T_z (°F)	63.5	63.8	62.8
C-value (-)	0.30	0.24	0.20

Figure 9.15: *Example of ZST quantification with C-value*

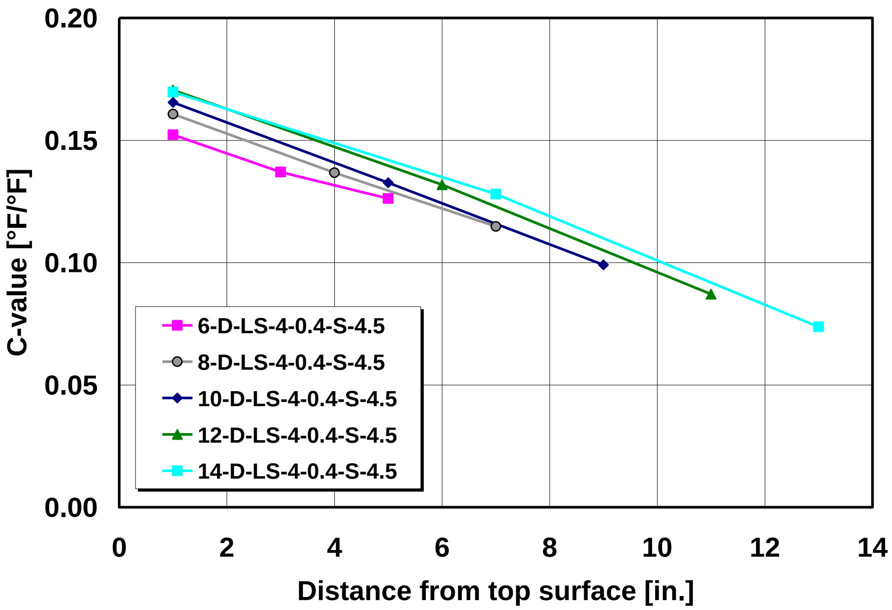

(a) Effect of thickness

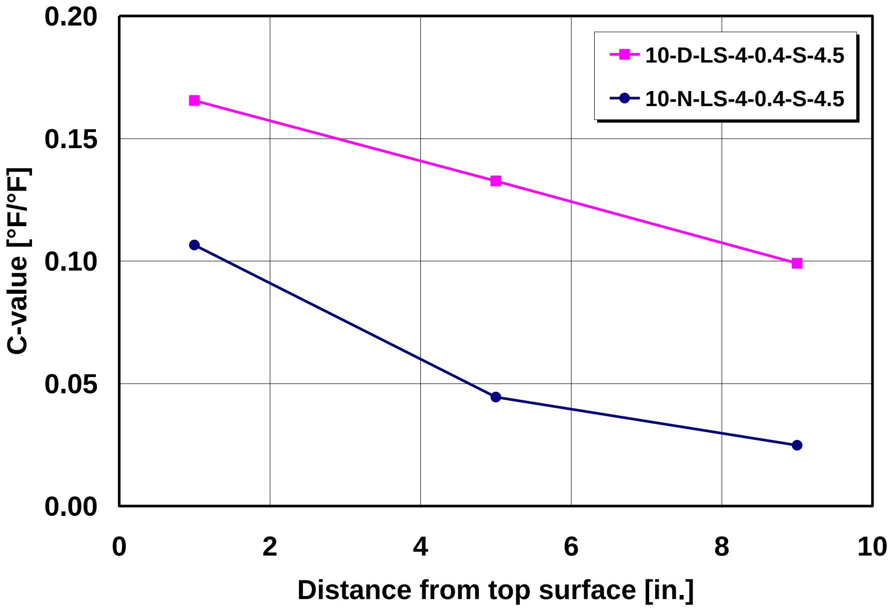

(b) Effect of placement time of day

Figure 9.16: *Effect of each variable on C-value*

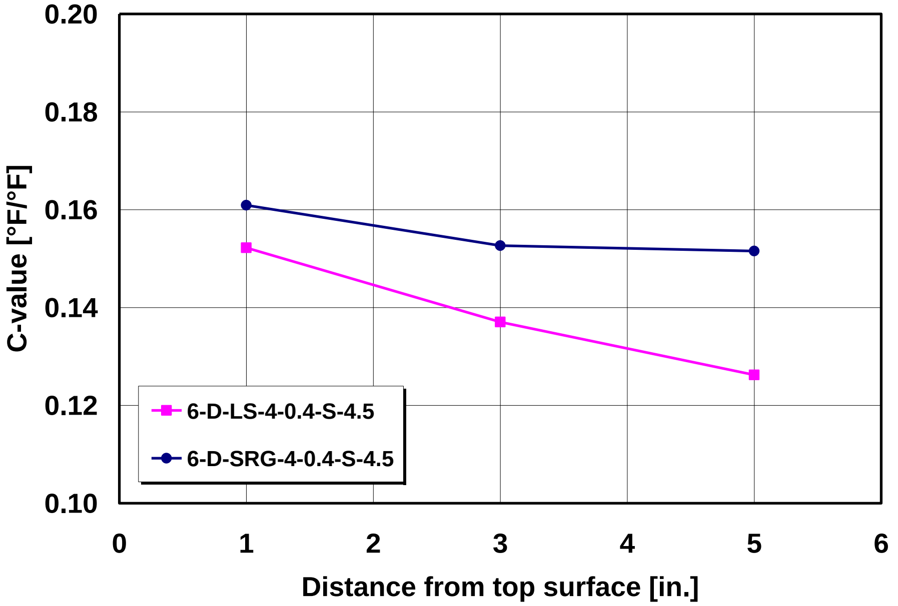

(c) Effect of coarse aggregate type

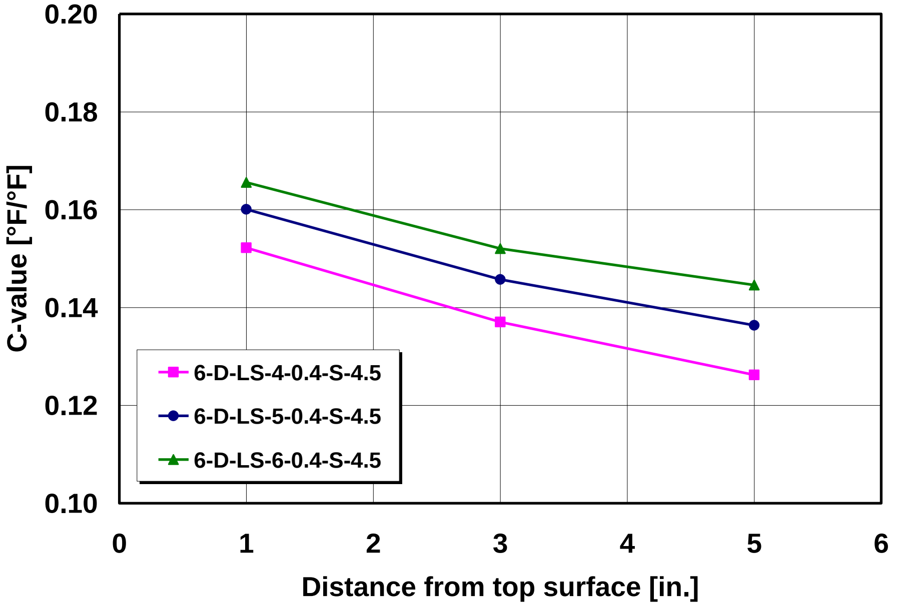

(d) Effect of cementitious content

Figure 9.16 (cont.): *Effect of each variable on C-value*

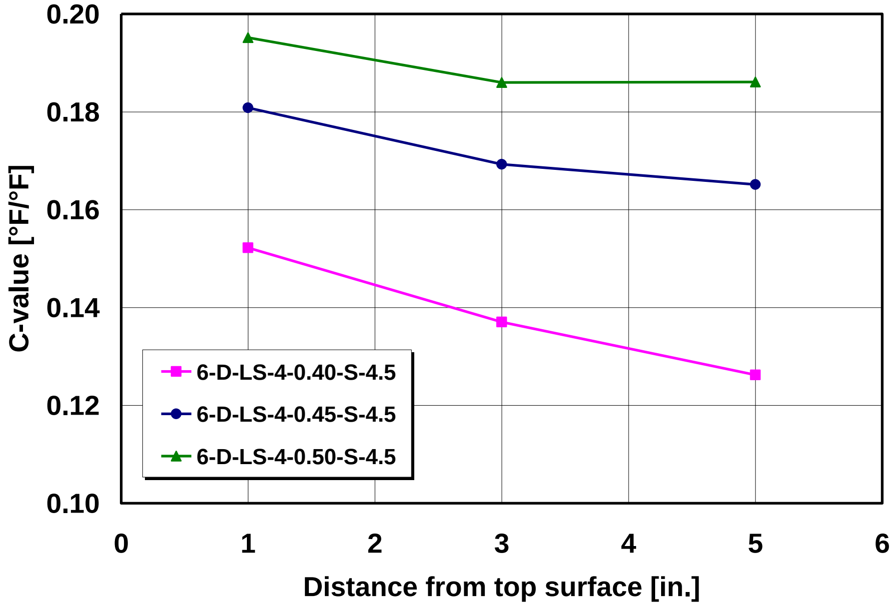

(e) Effect of water-to-cement ratio

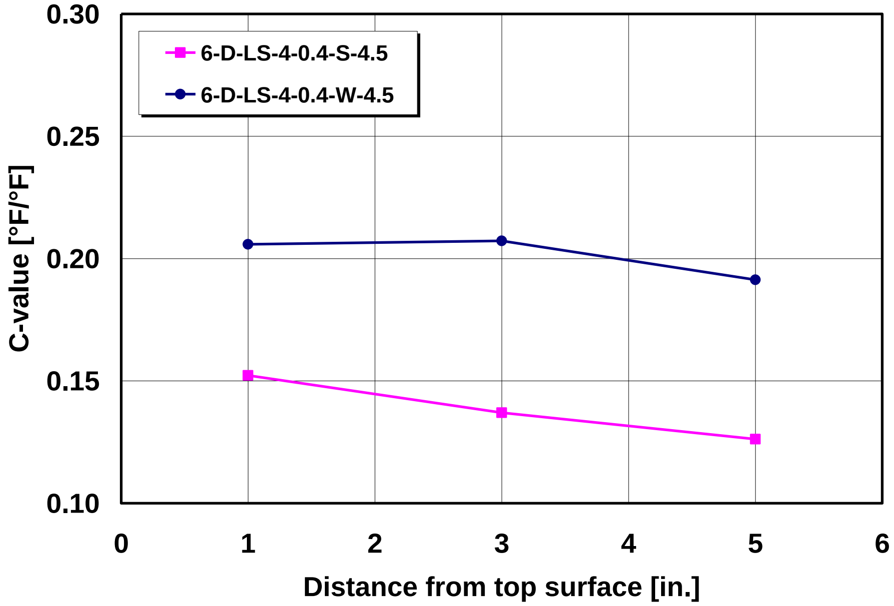

(f) Effect of placement season

Figure 9.16 (cont.): *Effect of each variable on C-value*

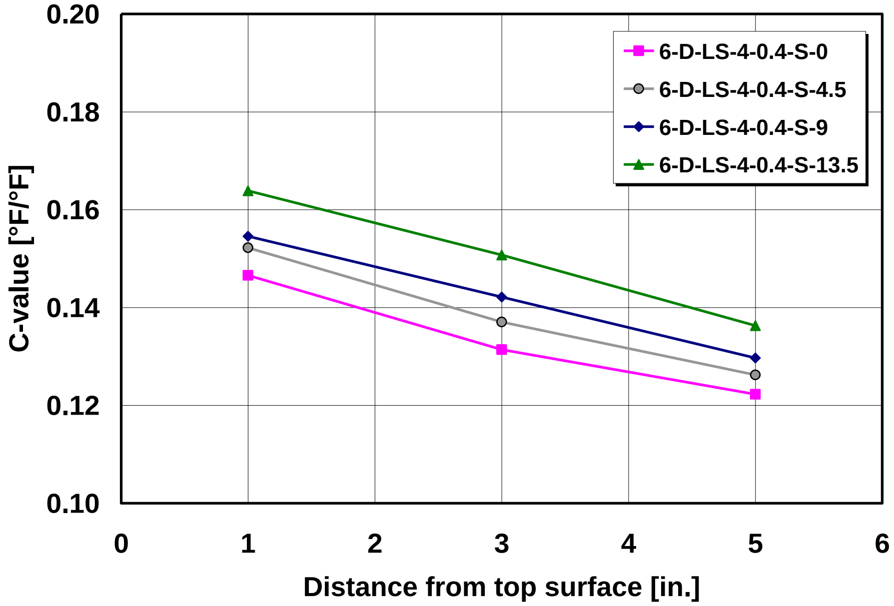

(g) Effect of wind speed

Figure 9.16 (cont.): *Effect of each variable on C-value*

9.3 REGRESSION ANALYSIS

9.3.1 Analysis Methods

To develop C-value predictive model (in turn, ZST predictive model), the C-value was evaluated for all the variable categories. Then, the multivariate linear regression analysis was performed utilizing the SPSS v. 16.00, commercial statistic analysis software, in terms of all the variable categories. A total of 1,440 analysis cases were investigated considering the factorial experiment shown in Table 9.2. To increase the acceptability of the C-value predictive model, the multivariate regression analysis was performed by dividing the 1,440 analysis cases into 24 different groups. The regression analysis groups are shown in Table 9.5.

Table 9.5: *Groups for regression analysis*

Group	Fixed Variables [a]	Group	Fixed Variables [a]	Group	Fixed Variables [a]
1	D-LS-S-T	9	D-SRG-S-B	17	N-LS-W-M
2	D-LS-S-M	10	D-SRG-W-T	18	N-LS-W-B
3	D-LS-S-B	11	D-SRG-W-M	19	N-SRG-S-T
4	D-LS-W-T	12	D-SRG-W-B	20	N-SRG-S-M
5	D-LS-W-M	13	N-LS-S-T	21	N-SRG-S-B
6	D-LS-W-B	14	N-LS-S-M	22	N-SRG-W-T
7	D-SRG-S-T	15	N-LS-S-B	23	N-SRG-W-M
8	D-SRG-S-M	16	N-LS-W-T	24	N-SRG-W-B

[a] indicates (in order): time of placement of a day – coarse aggregate type – placement season – depth, [T: 1 in. below top surface, M: mid-depth, B: 1 in. above bottom surface

In the multivariate regression analysis, the dependent variable was set to C-value while the independent variables were slab thickness, cementitious content, water-to-cement ratio, and wind speed for each analysis group.

9.3.2 Multivariate Regression Model for C-Value Prediction

Since the regression equations derived based on the linear combination of the original variable terms yielded a low coefficient of determination (R^2), higher degree variable terms and their combination terms were added to increase the R^2 value of the derived regression equations. The basic form of the regression equations can be written as follows:

$$\begin{aligned} C = {} & \beta_0 + \beta_1 \cdot TH + \beta_2 \cdot CC + \beta_3 \cdot WC + \beta_4 \cdot WS + \beta_5 \cdot WS^2 + \beta_6 \cdot TH \cdot CC \\ & + \beta_7 \cdot TH \cdot WC + \beta_8 \cdot CC \cdot WC + \beta_9 \cdot CC \cdot WS + \beta_{10} \cdot WC \cdot WS \\ & + \beta_{11} \cdot WS \cdot TH + \beta_{12} \cdot TH^3 + \beta_{13} \cdot CC^3 + \beta_{14} \cdot WC^3 + \beta_{15} \cdot WS^3 \end{aligned} \quad \text{(Eq. 9.18)}$$

where, β_i is the unstandardized coefficients for i^{th} variable term; *TH* is the thickness, in.; *CC* is the cementitious material content, sack; *WC* is the water-to-cement ratio, -; and *WS* is the wind speed, mph.

Tables 9.6, 9.7, and 9.8 summarize the unstandardized coefficients for each variable term obtained from the multivariate linear regression analysis using SPSS v. 16.00. By replacing the unstandardized coefficients into Eq. 9.18, the predictive models for C-value can be derived. Also, R^2, which explains the goodness of fit of the regression equation, was presented in the table. Since the R^2 tends to increase as the number of independent variables increases, herein, the adjusted-R^2 was suggested. As the adjusted-R^2 is closer to 1.0, the independent variables can explain the dependent variable more strongly. For most cases, the significance levels were less than 0.05, which indicates that the models were statistically quite confident.

Table 9.6: *C-value regression results (top)*

Location	Coarse Aggregate	Season	Time	Unstandardized coefficient	R^2
Top	Limestone	Summer	Day	β_0 =-0.461; β_1 =0.007; β_2 =0.031; β_3 =1.626; β_4 =0.01; β_5 =0; β_6 =0; β_7 =0; β_8 =-0.052; β_9 =0; β_{10} =0.01; β_{11} =0; β_{12} =-8.010E-6; β_{13} =-2.445E-5; β_{14} =-1.655; β_{15} =4.520E-6	0.990
			Night	β_0 =-0.519; β_1 =0.014; β_2 =-0.01; β_3 =1.826; β_4 =0.005; β_5 =-1.203E-5; β_6 =-0.003; β_7 =0.006; β_8 =-0.025; β_9 =0.001; β_{10} =-0.004; β_{11} =-0.001; β_{12} =-3.514E-5; β_{13} =0.001; β_{14} =-1.936; β_{15} =1.199E-5	0.748
		Winter	Day	β_0 =-0.862; β_1 =-0.006; β_2 =0.06; β_3 =3.019; β_4 =0.006; β_5 =-0.001; β_6 =0; β_7 =-0.011; β_8 =-0.109; β_9 =0; β_{10} =0.009; β_{11} =0.001; β_{12} =-5.856E-6; β_{13} =-4.21E-5; β_{14} =-2.757; β_{15} =4.252E-6	0.963
			Night	β_0 =-0.85; β_1 =-0.004; β_2 =0.028; β_3 =3.187; β_4 =0.003; β_5 =0; β_6 =0.001; β_7 =-0.026; β_8 =-0.074; β_9 =0; β_{10} =0.01; β_{11} =0.001; β_{12} =-1.614E-6; β_{13} =1.557E-5; β_{14} =-2.869;β_{15} =2.071E-6	0.938
	Siliceous River Gravel	Summer	Day	β_0 =-0.303; β_1 =0.007; β_2 =0.023; β_3 =1.197; β_4 =0.002; β_5 =-8.002E-5; β_6 =0; β_7 =-0.001; β_8 =-0.04; β_9 =0; β_{10} =0.001; β_{11} =0; β_{12} =-7.258E-6; β_{13} =-1.834E-5; β_{14} =-1.20; β_{15} =2.706E-6	0.991
			Night	β_0 =-0.264; β_1 =0.012; β_2 =-0.024; β_3 =1.218; β_4 =0.004; β_5 =-1.522E-5; β_6 =-0.003; β_7 =0.006; β_8 =-0.003; β_9 =0.001; β_{10} =-0.005; β_{11} =0; β_{12} =3.082E-5; β_{13} =0.001; β_{14} =-1.375; β_{15} =1.326E-5	0.723
		Winter	Day	β_0 =-0.525; β_1 =-0.009; β_2 =0.037; β_3 =2.217; β_4 =0.008; β_5 =0; β_6 =0; β_7 =-0.006; β_8 =-0.066; β_9 =0; β_{10} =0.003; β_{11} =0.001; β_{12} =-1.352E-6; β_{13} =-3.499E-5; β_{14} =-2.114; β_{15} =3.287E-5	0.968
			Night	β_0 =-0.429; β_1 =-0.005; β_2 =0.005; β_3 =2.207; β_4 =0.007; β_5 =0; β_6 =0.001; β_7 =-0.014; β_8 =-0.041; β_9 =0; β_{10} =-6.617E-6; β_{11} =0.001; β_{12} =-4.75E-6; β_{13} =-4.779E-5; β_{14} =-1.938; β_{15} =1.728E-5	0.943

Table 9.7: *C-value regression results (middle)*

Location	Coarse Aggregate	Season	Time	Unstandardized coefficient	R^2
Middle	Limestone	Summer	Day	β_0 =-0.524; β_1 =0; β_2 =0.037; β_3 =1.843; β_4 =0.01; β_5 =0; β_6 =0; β_7 =0; β_8 =-0.065; β_9 =0; β_{10} =0; β_{11} =8.74E-5; β_{12} =-2.137E-6; β_{13} =-4.278E-5; β_{14} =-1.805; β_{15} =9.179E-6	0.997
			Night	β_0 =-0.929; β_1 =0.009; β_2 =0.074; β_3 =2.270; β_4 =0.009; β_5 =-8.821E-5; β_6 =-0.002; β_7 =0.002; β_8 =-0.081; β_9 =0.001; β_{10} =-0.015; β_{11} =0; β_{12} =6.068E-6; β_{13} =0; β_{14} =-1.958; β_{15} =2.838E-5	0.927
		Winter	Day	β_0 =-0.868; β_1 =-0.005; β_2 =0.055; β_3 =3.037; β_4 =0.008; β_5 =-0.001; β_6 =0; β_7 =-0.013; β_8 =-0.093; β_9 =0; β_{10} =0.008; β_{11} =0.001; β_{12} =8.108E-7; β_{13} =-7.094E-5; β_{14} =-2.833; β_{15} =4.179E-5	0.984
			Night	β_0 =-0.941; β_1 =-0.01; β_2 =0.036; β_3 =3.461; β_4 =0.003; β_5 =0; β_6 =0.002; β_7 =-0.024; β_8 =-0.085; β_9 =0; β_{10} =0.009; β_{11} =0; β_{12} =1.457E-5; β_{13} =-6.015E-5; β_{14} =-3.058; β_{15} =7.152E-6	0.951
	Siliceous River Gravel	Summer	Day	β_0 =-0.303; β_1 =0; β_2 =0.026; β_3 =1.344; β_4 =0.001; β_5 =0; β_6 =0; β_7 =0; β_8 =-0.047; β_9 =0; β_{10} =0; β_{11} =7.350E-5; β_{12} =-2.93E-6; β_{13} =-3.111E-5; β_{14} =-1.326; β_{15} =8.144E-6	0.996
			Night	β_0 =-0.696; β_1 =0.009; β_2 =0.059; β_3 =1.795; β_4 =0; β_5 =-4.690E-5; β_6 =-0.002; β_7 =0; β_8 =-0.063; β_9 =0.002; β_{10} =-0.006; β_{11} =0; β_{12} =6.211E-6; β_{13} =9.819E-5; β_{14} =-1.615;β_{15} =2.282E-5	0.919
		Winter	Day	β_0 =-0.535; β_1 =-0.009; β_2 =0.035; β_3 =2.268; β_4 =0.011; β_5 =-0.001; β_6 =0; β_7 =-0.007; β_8 =-0.068; β_9 =0; β_{10} =0.001; β_{11} =0; β_{12} =-4.177E-6; β_{13} =-7.771E-5; β_{14} =-2.112; β_{15} =3.99E-5	0.981
			Night	β_0 =-0.613; β_1 =-0.018; β_2 =0.029; β_3 =2.636; β_4 =0.012; β_5 =0; β_6 =0.002; β_7 =-0.004; β_8 =-0.069; β_9 =-0.001; β_{10} =0; β_{11} =0; β_{12} =-1.371E-5; β_{13} =-6.998E-5; β_{14} =-2.421; β_{15} =2.715E-5	0.949

Table 9.8: *C-value regression results (bottom)*

Location	Coarse Aggregate	Season	Time	Unstandardized coefficient	R^2
Bottom	Limestone	Summer	Day	β_0=-0.618; β_1=-0.011; β_2=0.043; β_3=2.197; β_4=-1.113E-5; β_5=0; β_6=6.771E-5; β_7=0.01; β_8=-0.079; β_9=0; β_{10}=0; β_{11}=0; β_{12}=-2.290E-6; β_{13}=-5.373E-5; β_{14}=-2.21; β_{15}=9.449E-6	0.998
			Night	β_0=-0.771; β_1=0.002; β_2=0.057; β_3=1.909; β_4=0.004; β_5=0; β_6=-0.001; β_7=0.013; β_8=-0.063; β_9=0.002; β_{10}=-0.021; β_{11}=0; β_{12}=1.071E-7; β_{13}=0; β_{14}=-1.472; β_{15}=2.042E-5	0.935
		Winter	Day	β_0=-0.824; β_1=-0.017; β_2=0.052; β_3=2.986; β_4=0.009; β_5=-0.001; β_6=0.001; β_7=-0.002; β_8=-0.096; β_9=0; β_{10}=0.009; β_{11}=0; β_{12}=8.366E-6; β_{13}=-5.577E-5; β_{14}=-2.67; β_{15}=4.130E-5	0.984
			Night	β_0=-0.877; β_1=-0.024; β_2=0.033; β_3=3.223; β_4=0.003; β_5=0; β_6=0.002; β_7=-0.003; β_8=-0.065; β_9=-0.001; β_{10}=0.021; β_{11}=0; β_{12}=1.642E-5; β_{13}=0; β_{14}=-3.090; β_{15}=2.567E-5	0.956
	Siliceous River Gravel	Summer	Day	β_0=-0.398; β_1=-0.006; β_2=0.031; β_3=1.609; β_4=0; β_5=0; β_6=8.333E-6; β_7=0.007; β_8=-0.057; β_9=0; β_{10}=0; β_{11}=0; β_{12}=-6.971E-6; β_{13}=-3.5E-5; β_{14}=-1.65; β_{15}=8.606E-6	0.997
			Night	β_0=-0.61; β_1=0.001; β_2=0.044; β_3=1.765; β_4=-0.004; β_5=0; β_6=-0.001; β_7=0.012; β_8=-0.067; β_9=0.002; β_{10}=-0.007; β_{11}=0; β_{12}=2.579E-6; β_{13}=-7.922E-6; β_{14}=-1.578; β_{15}=2.021E-5	0.921
		Winter	Day	β_0=-0.589; β_1=-0.019; β_2=0.047; β_3=2.4; β_4=0.015; β_5=0; β_6=0.001; β_7=0.005; β_8=-0.083; β_9=0; β_{10}=-0.003; β_{11}=0; β_{12}=9.63E-6; β_{13}=-6.077E-5; β_{14}=-2.175; β_{15}=3.603E-5	0.977
			Night	β_0=-0.585; β_1=-0.037; β_2=0.022; β_3=2.73; β_4=0.009; β_5=0; β_6=0.003; β_7=0.018; β_8=-0.056; β_9=-0.001; β_{10}=0.005; β_{11}=0; β_{12}=2.114E-5; β_{13}=-9.887E-5; β_{14}=-2.924; β_{15}=1.814E-5	0.956

9.3.3 Verification of Proposed Models

In order to verify the general acceptance of the proposed regression models, the original data obtained from the parametric study were compared with the predicted values calculated with the proposed models. Figure 9.17 shows the representative case examples showing the effects of each variable: thickness, cementitious material content, water-to-cement ratio, and wind speed.

As can be seen in the figures, the C-values predicted with the proposed models showed quite good agreement with the original data sets obtained from the parametric study. This implies that the multivariate regression models proposed in this chapter were acceptable.

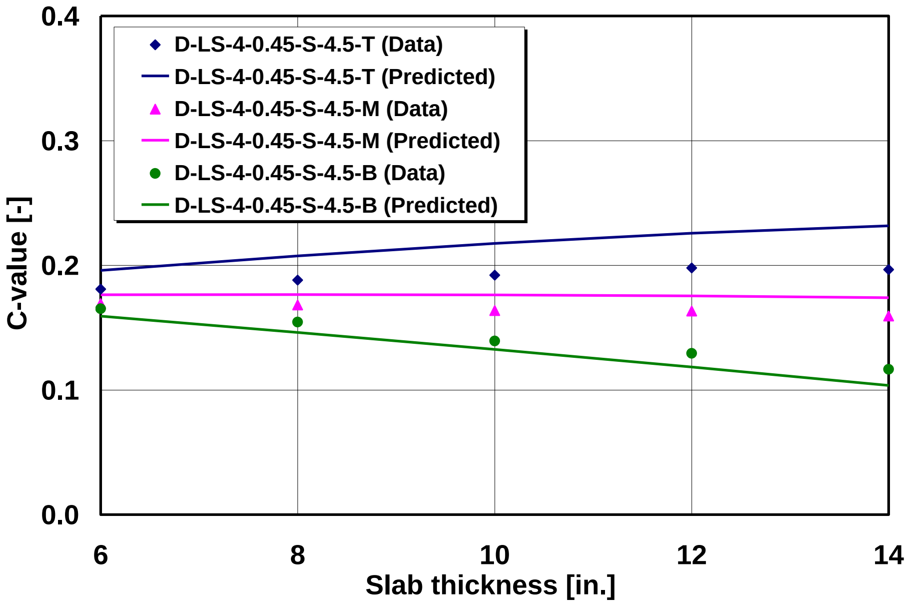

(a) Effect of thickness

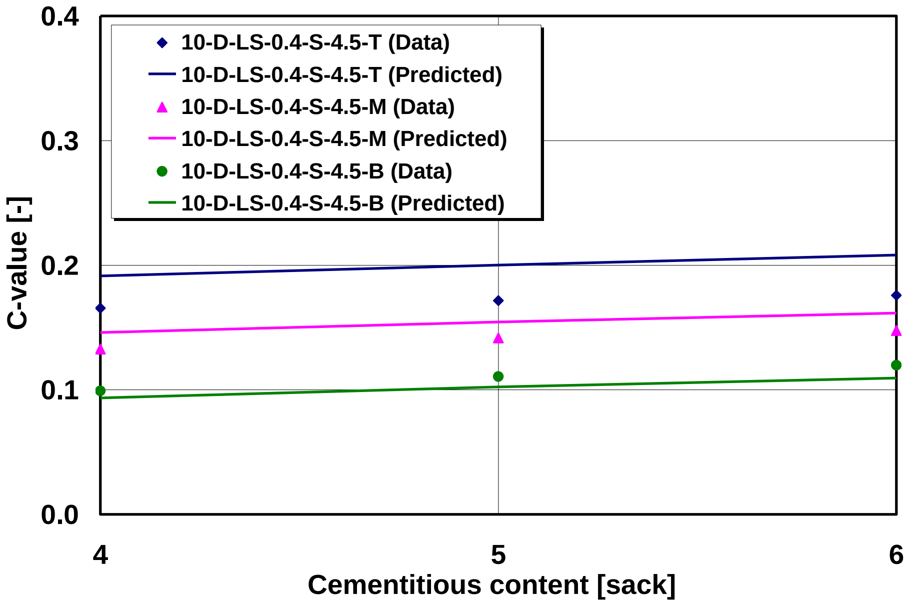

(b) Effect of cementitious content

Figure 9.17: *Comparison of original data with predicted value*

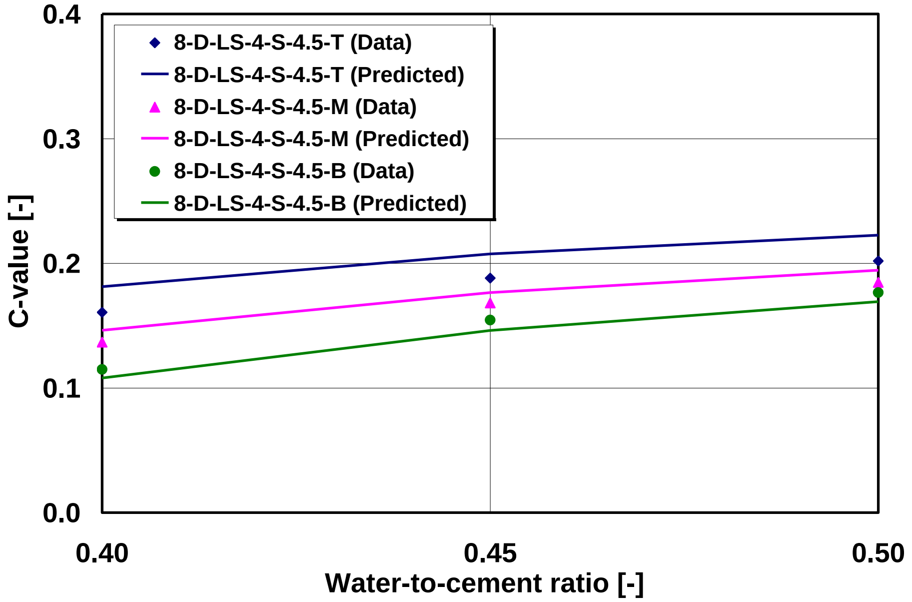

(c) Effect of water-to-cement ratio

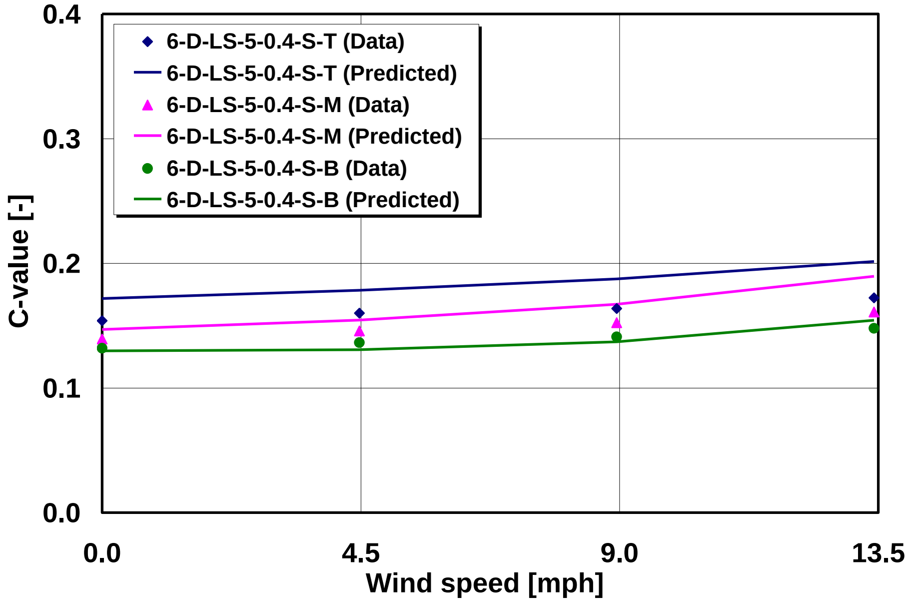

(d) Effect of wind speed

Figure 9.17 (Cont.): *Comparison of original data with predicted value*

Also, to investigate the validity of the proposed regression models, the prediction results obtained from the proposed regression models were compared with the measured

ZST values in the four test sections described in Table 5.1. Table 9.9 summarizes the actual setting temperature, maximum temperature, C-value obtained from the proposed models, and the predicted ZST values.

As seen in Figure 9.18, the measured ZST and the predicted ZST were quite similar each other, which resulted in only 0.2 °F to 1.7 °F differences. These differences were significantly smaller than the differences resulted from the comparison with the existing ZST prediction model, i.e. 7 °F to 25 °F, which is quite valid.

Table 9.9: *Estimation of ZST using the proposed regression models*

	Austin-A	Fort Worth (M)	Fort Worth (B)	Austin-B	Hillsboro
T_s (°F)	89.9	87.5	91.9	85.8	70.8
T_{max} (°F)	97.1	90.4	93.8	95.0	77.8
C-value (°F/°F)	0.30	0.18	0.15	0.26	0.23
T_z (°F)	94.9	89.9	93.5	92.6	76.2

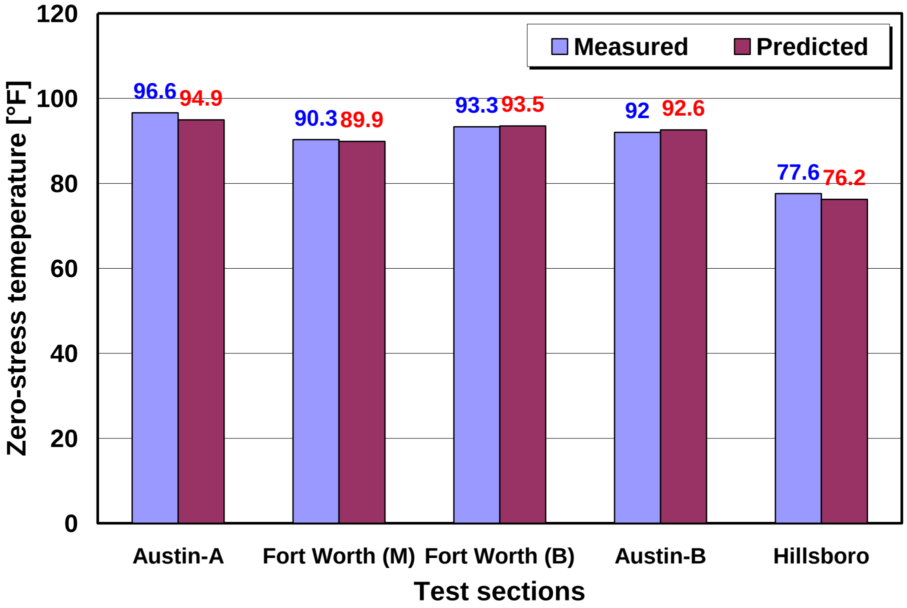

Figure 9.18: *Comparison of measured ZST with predicted ZST*

9.4 SUMMARY

In this chapter, the C-value predictive models (in turn, zero-stress temperature (ZST) predictive models) were proposed based on the multivariate linear regression analysis with support from the SPSS, commercial statistical analysis software. The data sets for the regression analysis were obtained from a parametric study using the finite element models proposed in Chapter 8.

The results from a total of 1,440 analysis cases were categorized into 24 groups, and the regression model for each group was proposed. For most cases, the coefficient of determination (well known as an R^2-value) was higher than 0.90 and the significance level was less than 0.01, which indicates that the proposed models were statistically confident.

To verify the general acceptance of the proposed regression models, the original data obtained from the parametric study were compared with the predicted values calculated with the proposed models. Also, the predicted results from the proposed models were compared with the actual measured ZST values to investigate the validity of the proposed regression models. The results quite well agreed each other, which indicates that the multivariate regression models proposed in this chapter were quite valid to implement in the codes of practice.

Chapter 10: Implication of ZST on Long-Term Performance of CRCP

This chapter explores the implications of zero-stress temperature (ZST) on the long-term performance of continuously reinforced concrete pavement (CRCP) structures. Since the experimental and numerical approaches shown in the former parts of this study tended to exhibit the localized behavior and response of CRCP, finding a direct relationship between the ZST formed at early-age and the overall long-term performance of CRCP was quite limited. In order to overcome this limitation, a series of field condition surveys was conducted in a total of seven CRCP sections recorded in TxDOT Research Projects 1700-2, 1244-3, and other available documents. Because the testing sections involved in these research projects have been in service for about 7 to 22 years, the data obtained from the field condition surveys is expected to provide meaningful and important information to examine the actual impact of ZST on the long-term behavior and performance of CRCP structures.

10. 1 SECTIONS FOR FIELD CONDITION SURVEY

To evaluate the long-term performance of CRCP in terms of various temperature conditions at the time of initial construction, field condition surveys were conducted. The survey sections were chosen meeting the following primary requirements to achieve the meaningful information:

1) The survey sections had to be at least 5 years old since constructed (and opened to traffic).

2) Initial temperature history and material conditions – the time of construction of a day, maximum concrete temperature at early-age, and material properties – should be known.

As a result, a total of seven different CRCP sections were selected for the field condition survey.

10.1.1 Sections for TxDOT Research Project 0-1700-2

A total of seven field testing sections are described in TxDOT Research Project Report 0-1700-2 (Schindler et al., 2002). Because of some limitations on the field location information and the accessibility to the sections, only two sections – one in Houston and the other in Dallas – were surveyed.

10.1.1.1 Houston FM 529 Section

The Houston section was 10-in.-thick CRCP located on the Farm-to-Market (FM) Road 529 between Ridgeberry Drive and Texas Highway 6. The section was the westbound inside lane which began from 350 ft. east of Ridgeberry Drive and ended 2,100 ft east of the beginning point. According to the field evidence, it seems that the paver moved from the west to east. Because of the large traffic intersection (Sommerall Drive) around 1,900 ft. away from the starting point, the rest of 200 ft. was not surveyed. Figure 10.1 and Figure 10.2 show the map and the photos of the field condition survey location, respectively.

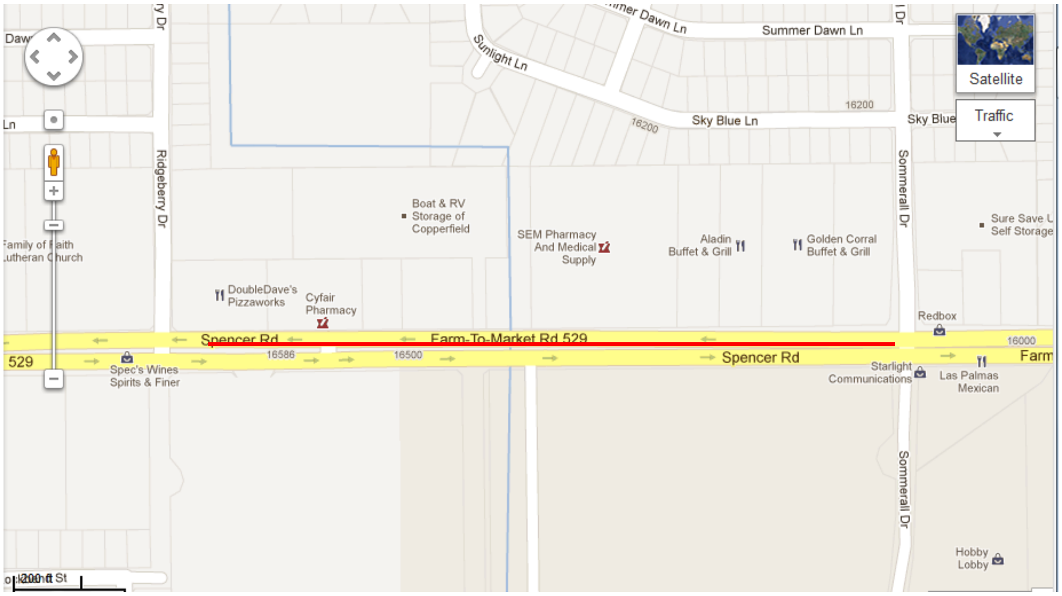

Figure 10.1: *Field survey location for Houston FM 529 section*

Figure 10.2: *Houston FM 529 section*

The Houston section was constructed on August 25th, 2000 and started concrete placement at 9:45 am. For concrete mixture, 6-sack cement with 35 % Class C fly ash was used. The coarse aggregate used was crushed limestone. Figure 10.3 shows the early-age temperature profile measured in the field. As can be seen in the temperature data, the maximum temperature at the first day after placement was about 113 °F, while the fresh concrete temperature was 90 °F.

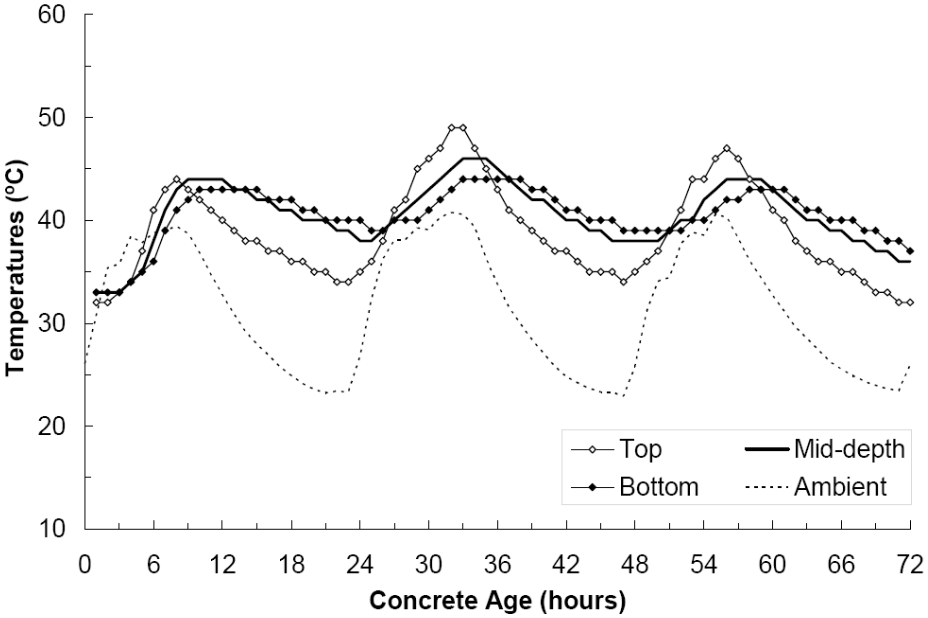

Figure 10.3: *Early-age temperature profile for Houston FM 529 section*
(Schindler et al., 2002)

10.1.1.2 Dallas IH-45 Section

The Dallas section was 13-in.-thick CRCP on IH-45 northbound inside lane. The section started 980 ft. south of the southern expansion joint of the Dowdy Ferry Road Bridge. According to the field evidence, the concrete was placed from the south to north. The length of the section was 510 ft. According to the final report, The Dallas section started to be constructed at 8:10 am on May 5th, 2000. For concrete mixture, 5.5-sack cementitious content with a 20 % replacement of Class F fly ash with 1.5-in. crushed limestone was used. Figure 10.4 and Figure 10.5 show the photos and the map of the field condition survey location, respectively.

Figure 10.4: *Dallas IH-45 section*

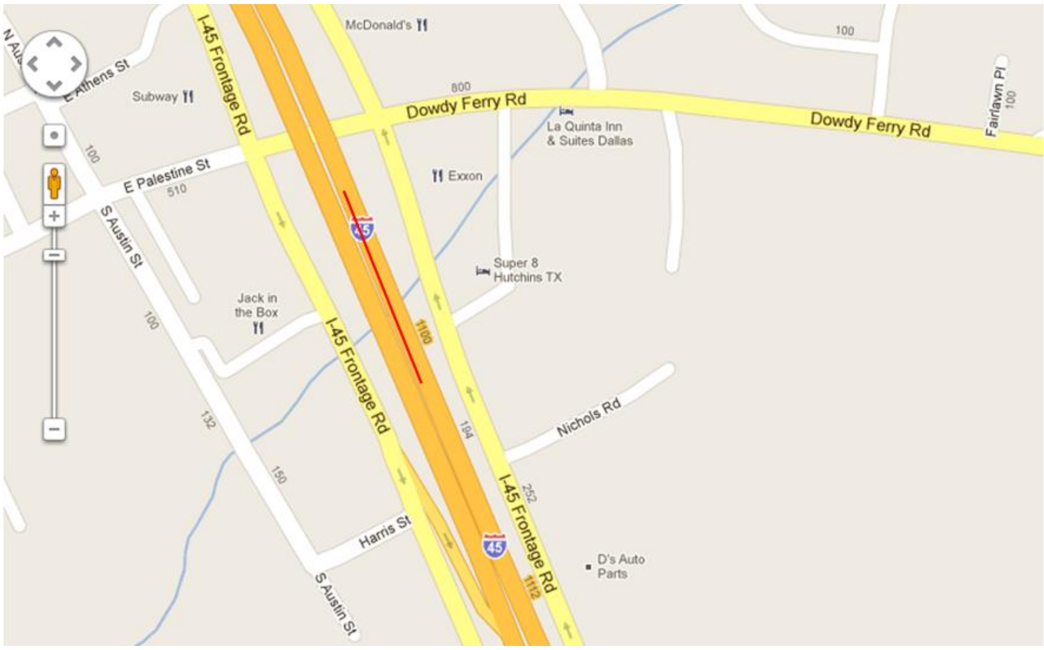

Figure 10.5: *Field survey location for Dallas IH-45 section*

Figure 10.6 shows the early-age concrete temperature development measured in the field section. As can be seen in the measured temperature data, the peak temperature at the first day after placement was about 102.2 °F, while the fresh concrete temperature was 72 °F.

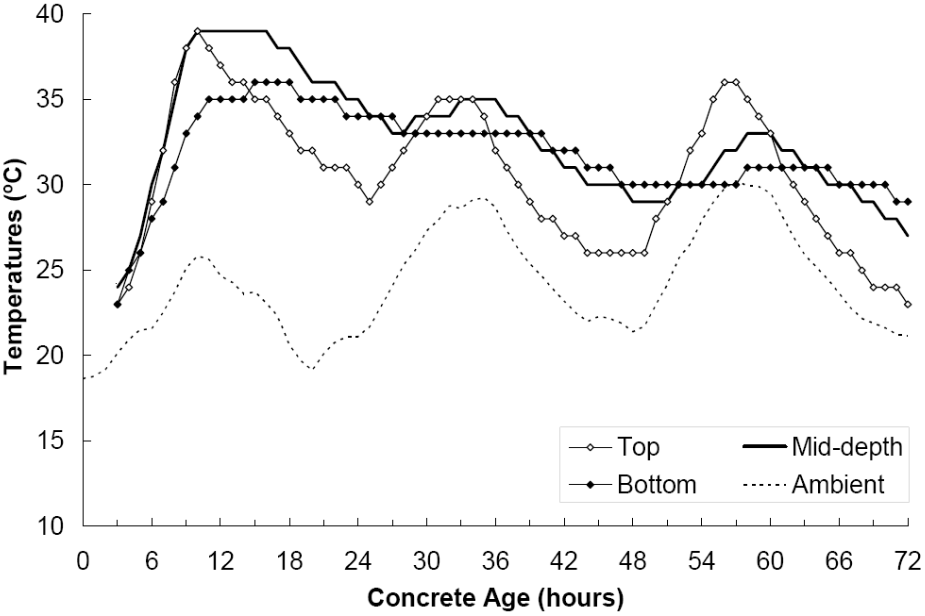

Figure 10.6: *Early-age temperature profile for Dallas IH-45 section* (Schindler et al., 2002)

10.1.2 Sections for TxDOT Research Project 1244-3

Under the TxDOT Research Project 0-1244, a total of four CRCP testing sections were constructed in Houston, TX (Suh et al., 1992). Among the four testing sections, two sections were asphalt overlaid. Thus, two experimental sections – one on the eastbound frontage road of Beltway (BW) 8 and the other on the northbound of IH-45 north Houston – were investigated. Both of them were constructed in late 1989 and early 1990, which have been in service for about 21 years. They were the oldest testing section available for the field condition surveys.

10.1.2.1 Houston BW 8 Section

The Houston BW 8 section was 10-in.-thick CRCP placed in the BW 8 east bound frontage road. The experimental variables were identical to the Houston IH-45 section to be described in the next subsection. The SRG section was constructed on November 24th, 1989 while the LS section was placed in the next day. Figure 10.7 illustrates the location map and design details of the testing section.

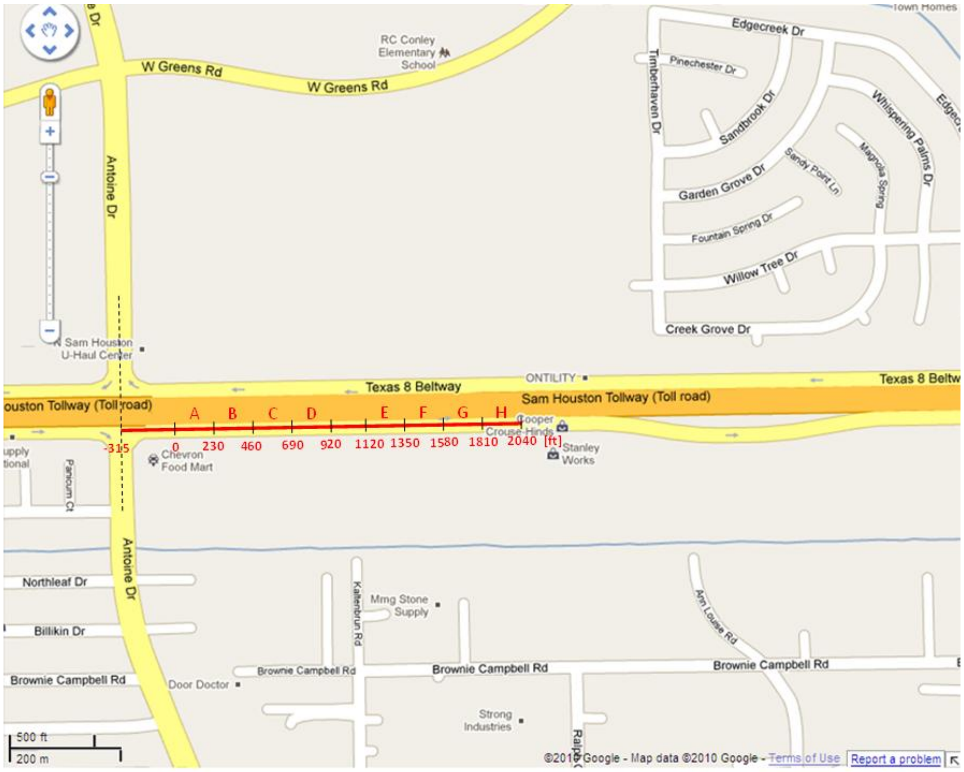

(a) Field survey location

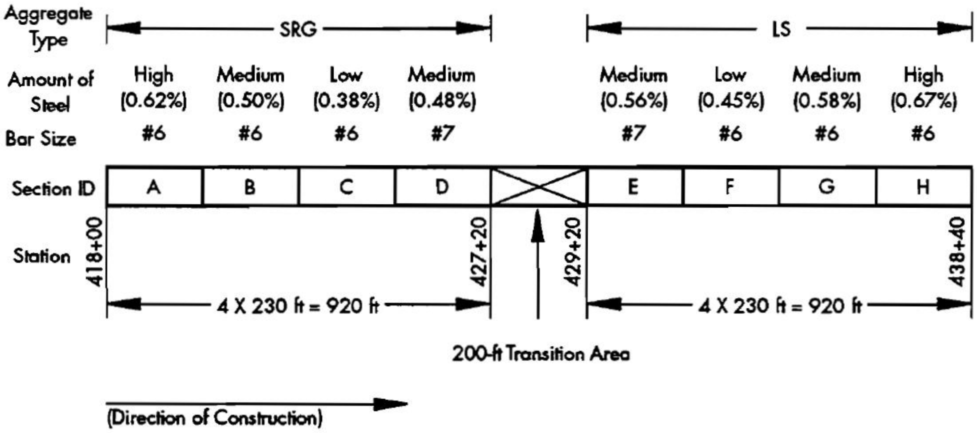

(b) Design details (Suh et al., 1992)

Figure 10.7: *Field survey location for Houston BW 8 section*

For concrete mixtures, 5.2-sack cement with a 25 % replacement of fly ash was used for the both SRG and LS sections. The water-to-cement ratio was 0.44 and 0.45 for the SRG section and LS section, respectively.

Figure 10.8 shows the concrete temperature developments measured in each subsection for the first 72 hours. Because each subsection was cast at different times of a day, the peak concrete temperature at the first day varied between 80 °F and 95 °F, while the fresh concrete temperature ranged from 65.4 °F to 71.0 °F.

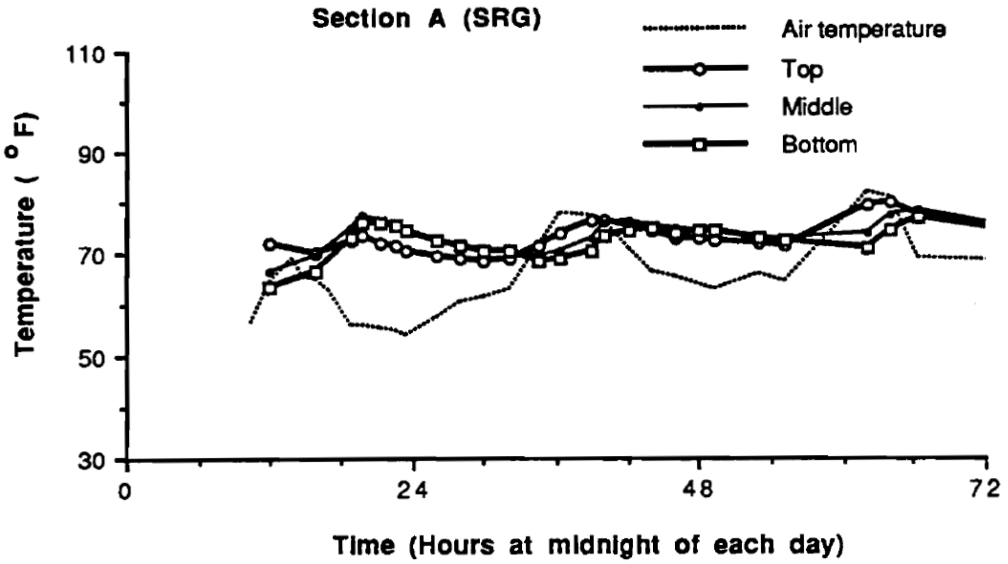

(a) Temperature profile for Subsection A

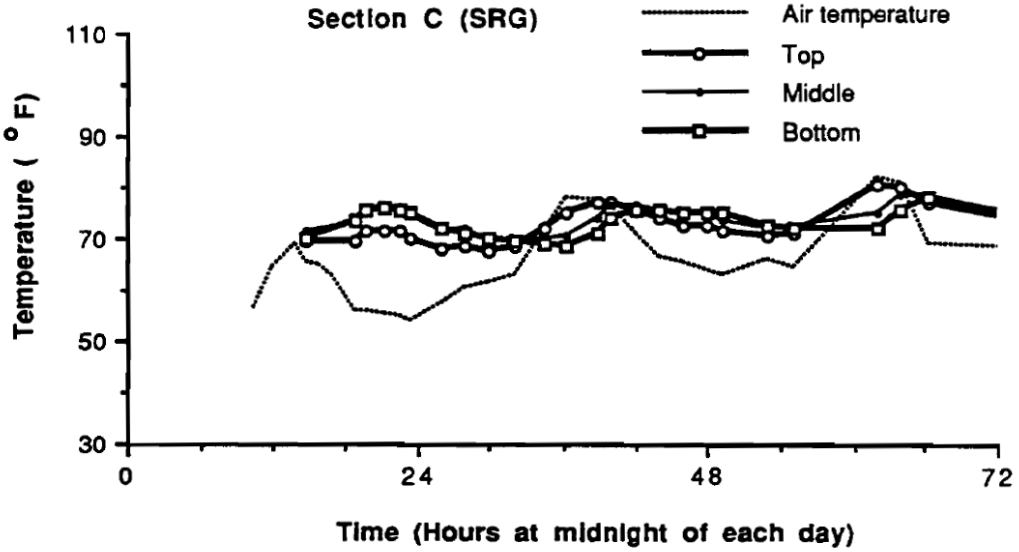

(b) Temperature profile for Subsection C

Figure 10.8: *Early-age temperature profiles for BW 8 section* (Suh et al., 1992)

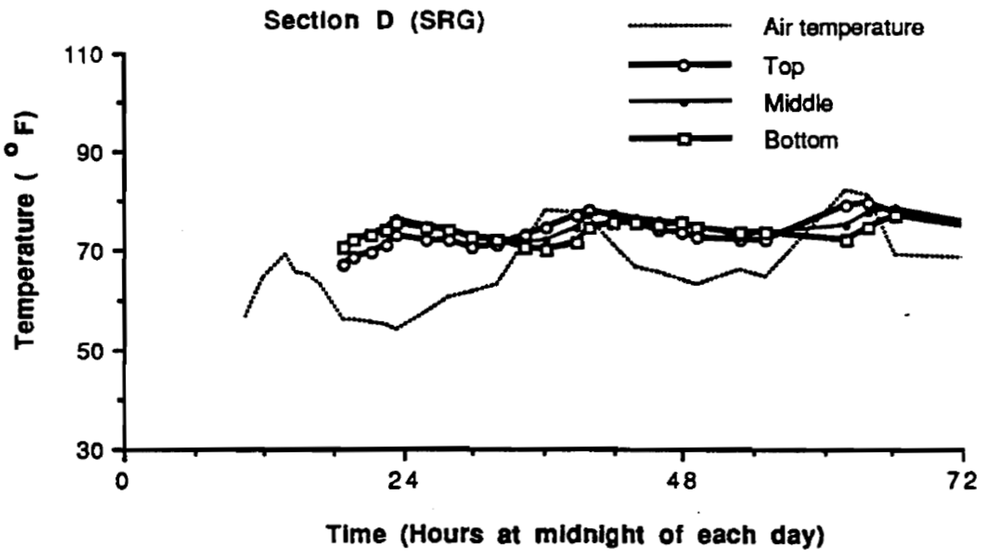

(c) Temperature profile for Subsection D

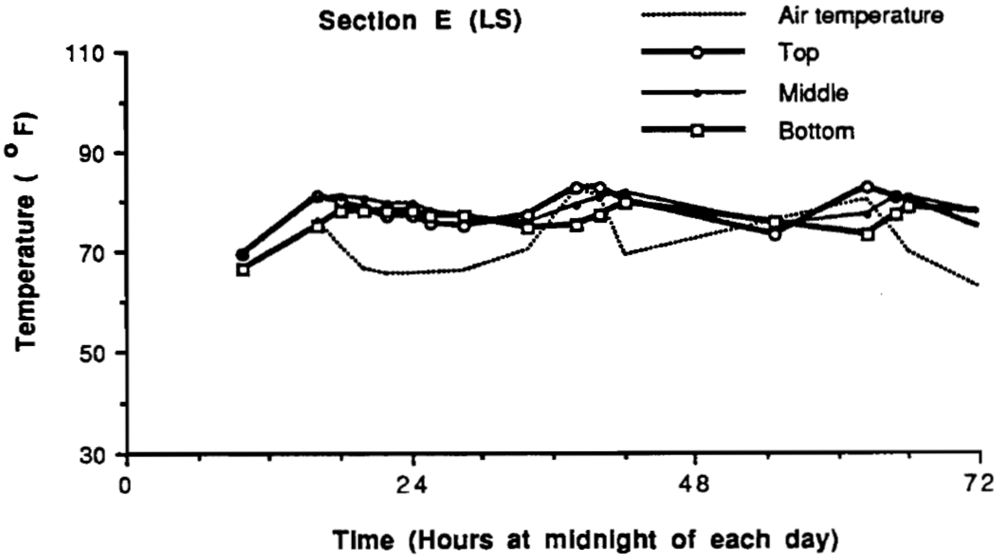

(d) Temperature profile for Subsection E

Figure 10.8 (cont.): *Early-age temperature profiles for BW 8 section*

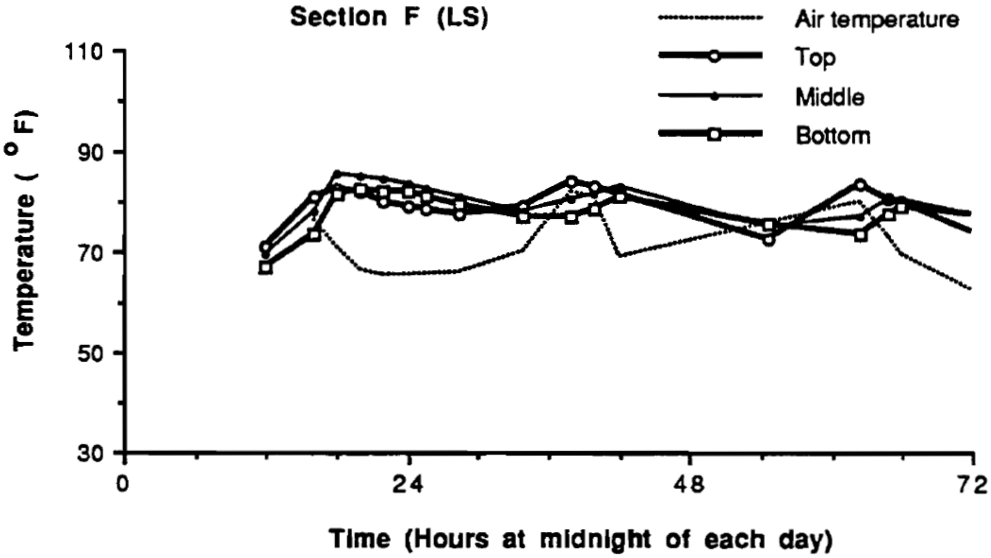

(e) Temperature profile for Subsection F

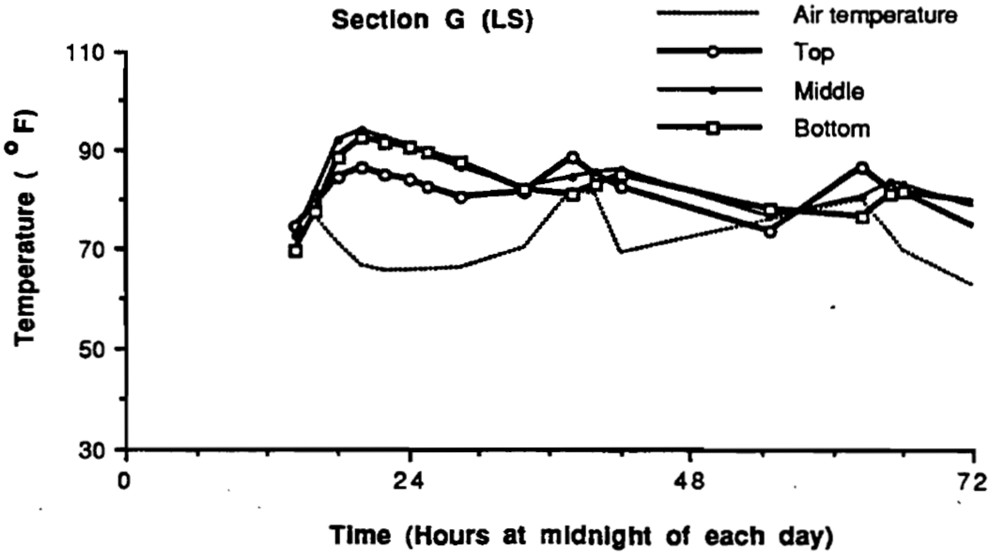

(f) Temperature profile for Subsection G

Figure 10.8 (cont.): *Early-age temperature profiles for BW 8 section*

10.1.2.2 Houston IH-45 Section

The Houston IH-45 section was 15 in. thick CRCP consisting a part of IH-45 northbound inside two lanes. The section was placed on January 14th and 21st, 1990. The total section length was 2,040 ft. In this testing section, eight different material and structural designs were employed for every 230 ft. The variables were 1) two different types of coarse aggregate, i.e., LS and SRG, and 2) four different levels of steel ratio from 0.38 % to 0.67 %. The 200 ft. between the LS and SRG section was a transition area. Figure 10.9 presents the location map and design details of the testing section.

For concrete material mixtures, a 5.7-sack cement factor with 30 % of fly ash, and a 5.3-sack cement factor and 25 % of fly ash were used for the SRG section and LS section, respectively. The water-to-cement ratio was 0.41 and 0.44 for the each of SRG and LS sections.

Figure 10.10 displays the early-age concrete temperature evolutions monitored in each subsection of the IH-45 test section. Since each subsection was placed at different times, the maximum concrete temperature at the first day varied between 80 °F and 88 °F, while the fresh concrete temperature ranged from 62.2 °F to 67.7 °F.

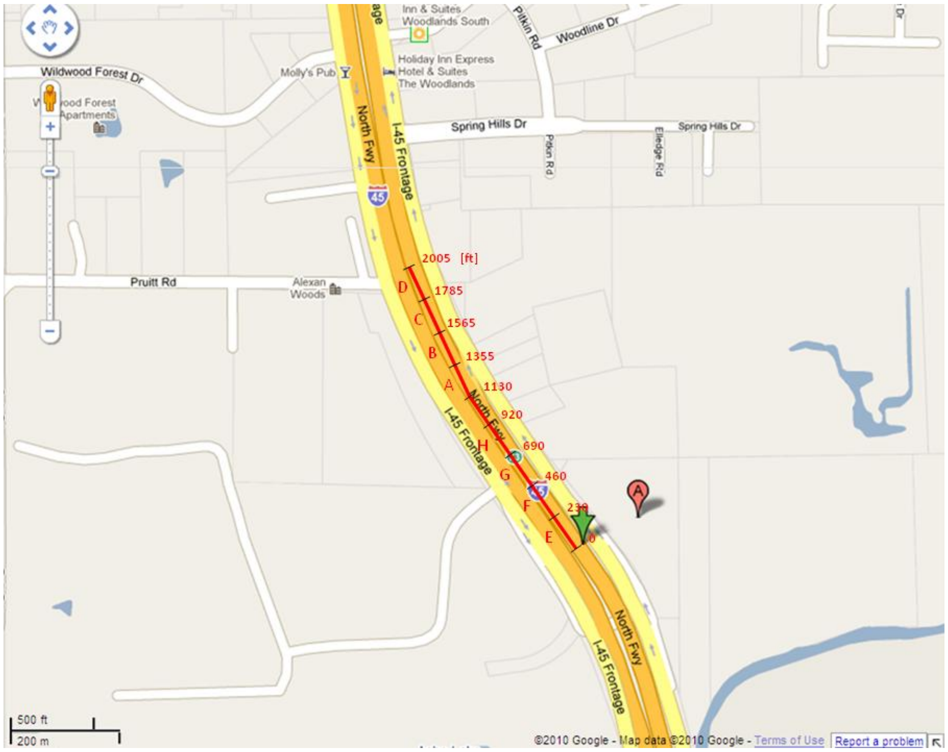

(a) Field survey location

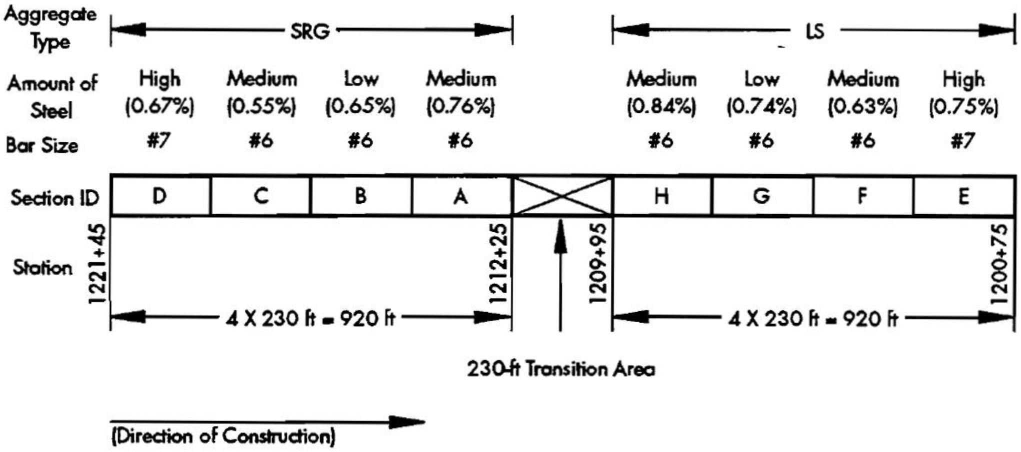

Aggregate Type	SRG					LS			
Amount of Steel	High (0.67%)	Medium (0.55%)	Low (0.65%)	Medium (0.76%)		Medium (0.84%)	Low (0.74%)	Medium (0.63%)	High (0.75%)
Bar Size	#7	#6	#6	#6		#6	#6	#6	#7
Section ID	D	C	B	A	⊠	H	G	F	E

(b) Design details (Suh et al., 1992)

Figure 10.9: *Field survey location for Houston IH-45 section*

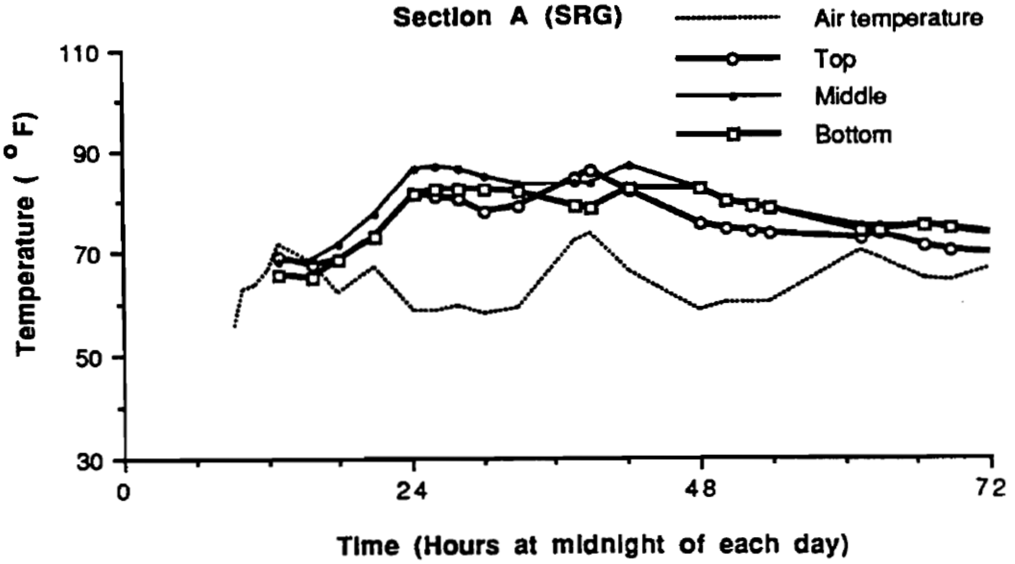

(a) Temperature profile for Subsection A

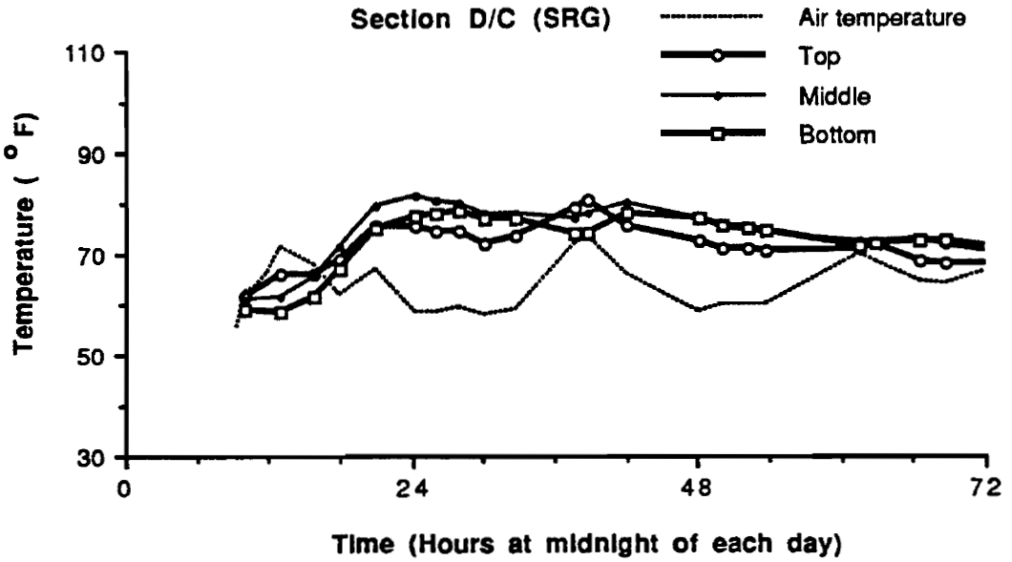

(b) Temperature profile for Subsection D/C

Figure 10.10: *Early-age temperature profiles for IH-45 section* (Suh et al., 1992)

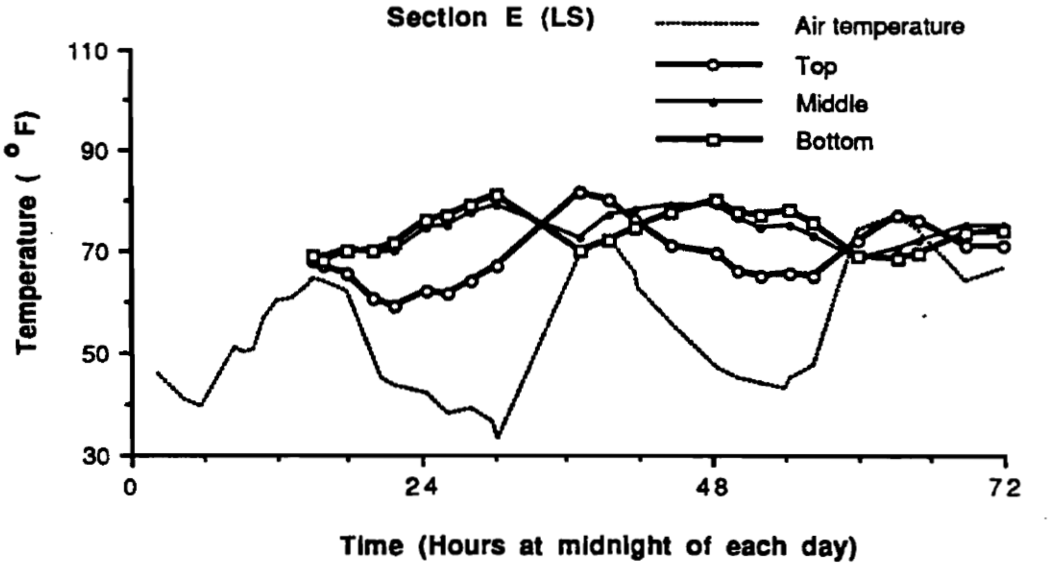

(c) Temperature profile for Subsection E

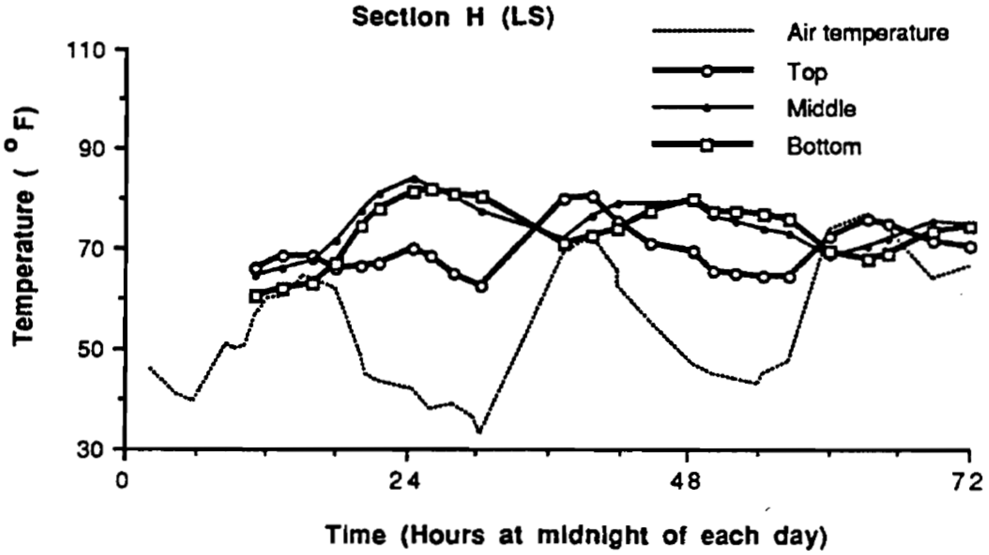

(b) Temperature profile for Subsection H

Figure 10.10 (cont.): *Early-age temperature profiles for IH-45 section*

10.1.3 Sections Conducted in 0-1700

To evaluate the early-age and the post-cracking behavior of CRCP structures, field instrumentation was carried out by Dr. Jeong-Hee Nam and the CTR research team in a total of seven CRCP sections in the state of Texas under TxDOT Research Project 0-1700 (Nam, 2005). Among the seven field testing sections, the field condition survey was conducted in two different sections near Houston, TX– Texas Spur 330 near Baytown and US-59 around Cleveland – and IH-10 near Van Horn, TX. All the sections were built in early 2000, which have been in service for about 10 years.

10.1.3.1 Baytown TX SPUR 330 Section

The Baytown TX SPUR 330 section was 13 in. thick CRCP located northwest of Baytown TX. The section was placed on the northbound inside main lane between Baker Road and Little Road at 7:30 am on July 26th, 2000. The total length of the section was 725 ft. Figure 10.11 illustrates the location map.

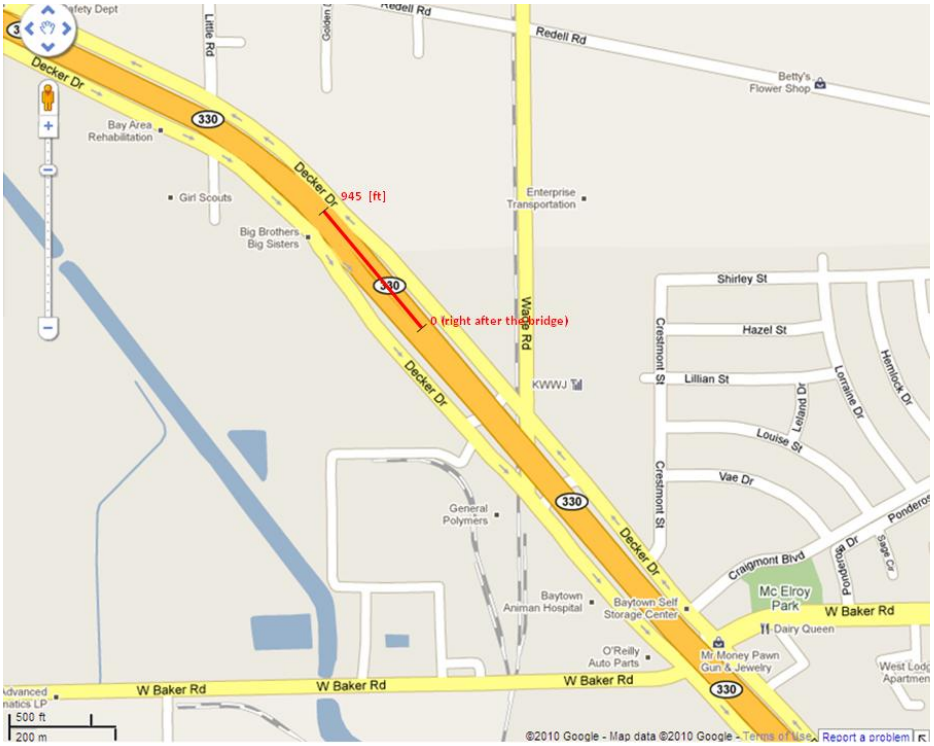

Figure 10.11: *Field survey location for Baytown TX SPUR 330 section*

The concrete material used in this section incorporated 5.2-sack cementitious material with 30 % of Class C fly ash replacement. The coarse aggregate type was crushed LS. The water-to-cement ratio of the mixture was 0.45.

Figure 10.6 displays the early-age concrete temperature evolutions monitored in the test section at the top 1 in., mid-depth, and bottom 1 in. The measured temperature data shows that the maximum concrete temperature at the first day was approximately 110 °F, while the fresh concrete temperature was about 80 °F.

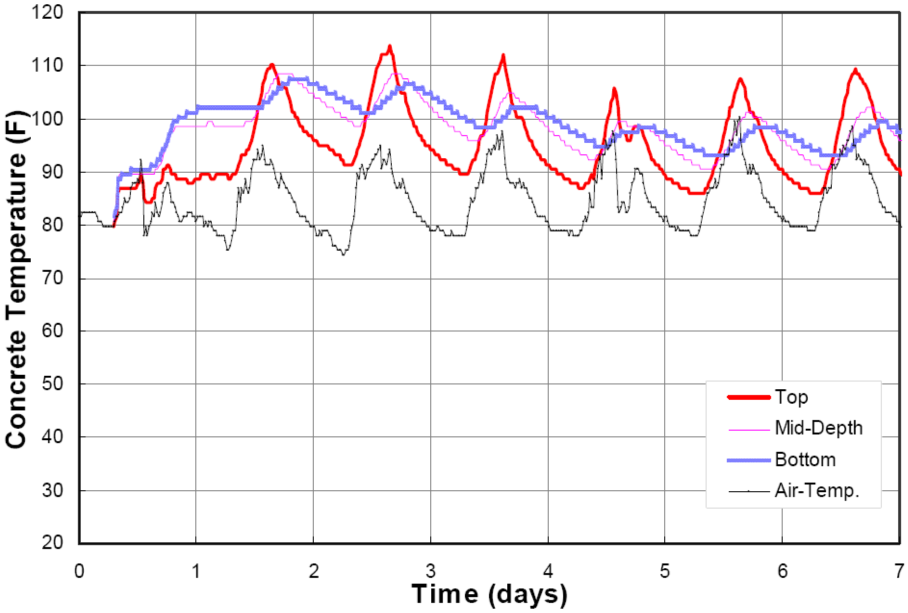

Figure 10.12: *Temperature history for Baytown TX SPUR 330 section* (Nam, 2005)

10.1.3.2 Cleveland US 59 Section

The Cleveland US 59 section was also 13 in. thick CRCP located in the Houston District south of Cleveland, TX. The section was a part of the US 59 northbound outside shoulder located between FM 2090 and Fosteria Road. The section began to be constructed at 9:00 am on July 20th, 2004. The total length of the section was 2360 ft. The detail of the field location is indicated in Figure 10.13.

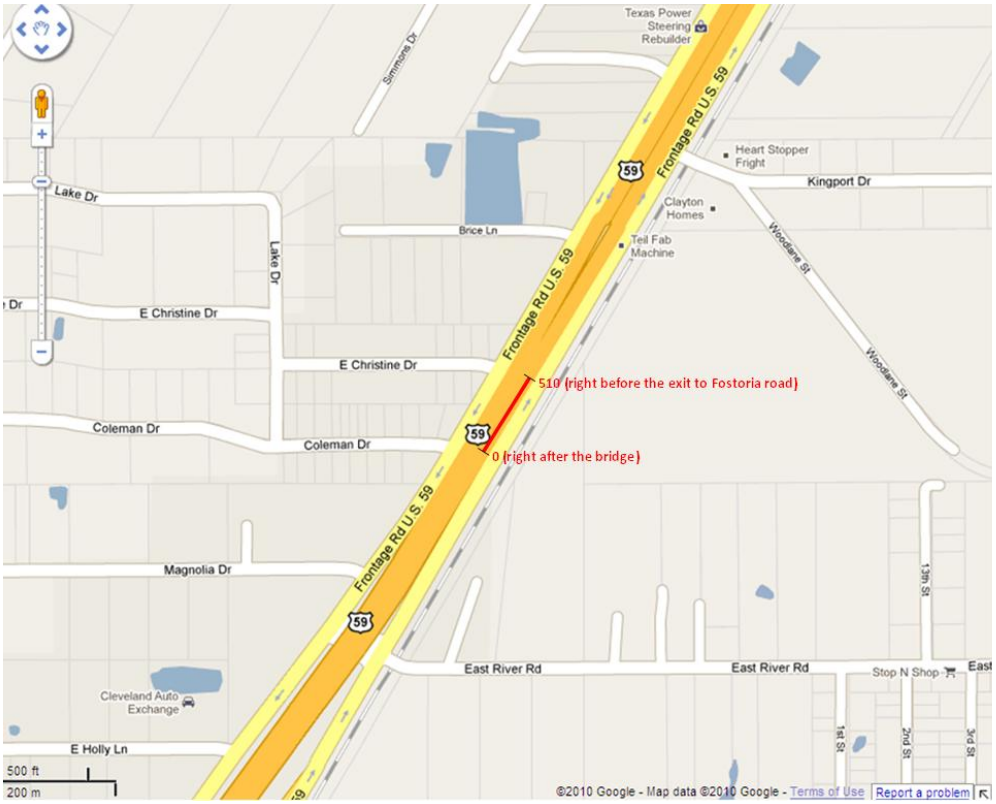

Figure 10.13: *Field survey location for Cleveland US 59 section*

The concrete material for this section used 5.25-sack cementitious material with 30 % of Class F fly ash replacement. The type of coarse aggregate was crushed LS. The water-to-cement ratio of the mixture was 0.44.

Figure 10.14 shows the early-age temperature history collected at the top 1 in., mid-depth, and bottom 1 in. of the test section. The measured temperature history presents that the maximum concrete temperature at the first day after concrete placement was approximately 110 °F, while the fresh concrete temperature was about 88 °F.

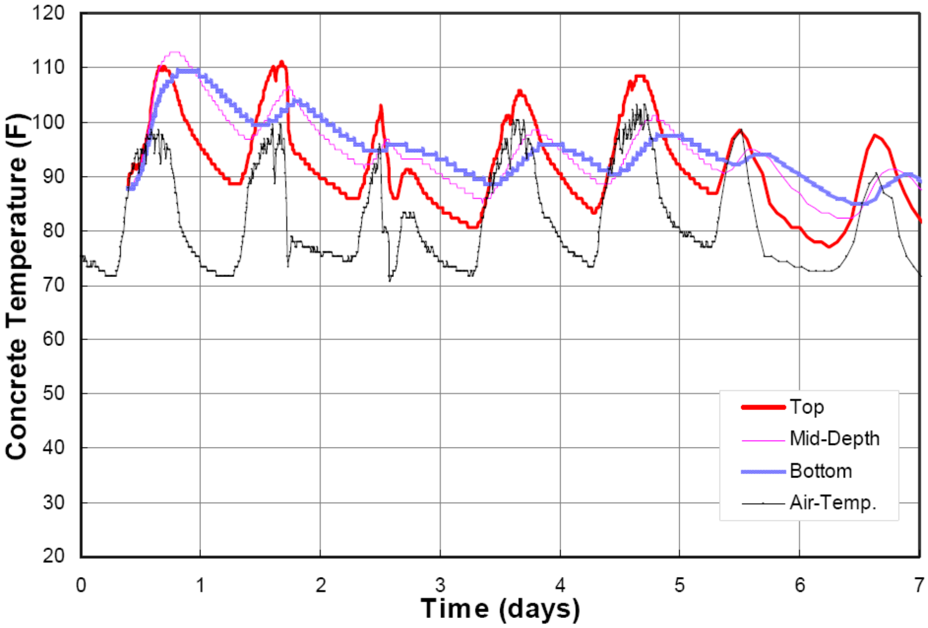

***Figure 10.14:** Temperature history for Cleveland US 59 section* (Nam, 2005)

10.1.3.3 Van Horn IH-10 Section

The Van Horn IH-10 section was 12 in. thick CRCP located around 15 miles west of Van Horn, TX. The section started 1,225 ft. before the mile post 125 on the westbound of IH-10 and extended 2,400 ft. from the section starting point. The section stared to be placed at 8:00 am on March 26th, 2003. Figure 10.15 shows the location map of the testing section.

The mixture used in this section incorporated 5-sack cement replaced with 50 % of slag. The type of coarse aggregate was crushed LS. The water-to-cement ratio of the used concrete was 0.50.

The early-age concrete temperature evolutions monitored in the test section are shown in Figure 10.16. The measured temperature data shows that the maximum concrete temperature at the first day was about 70 °F, while the fresh concrete temperature was about 65 °F.

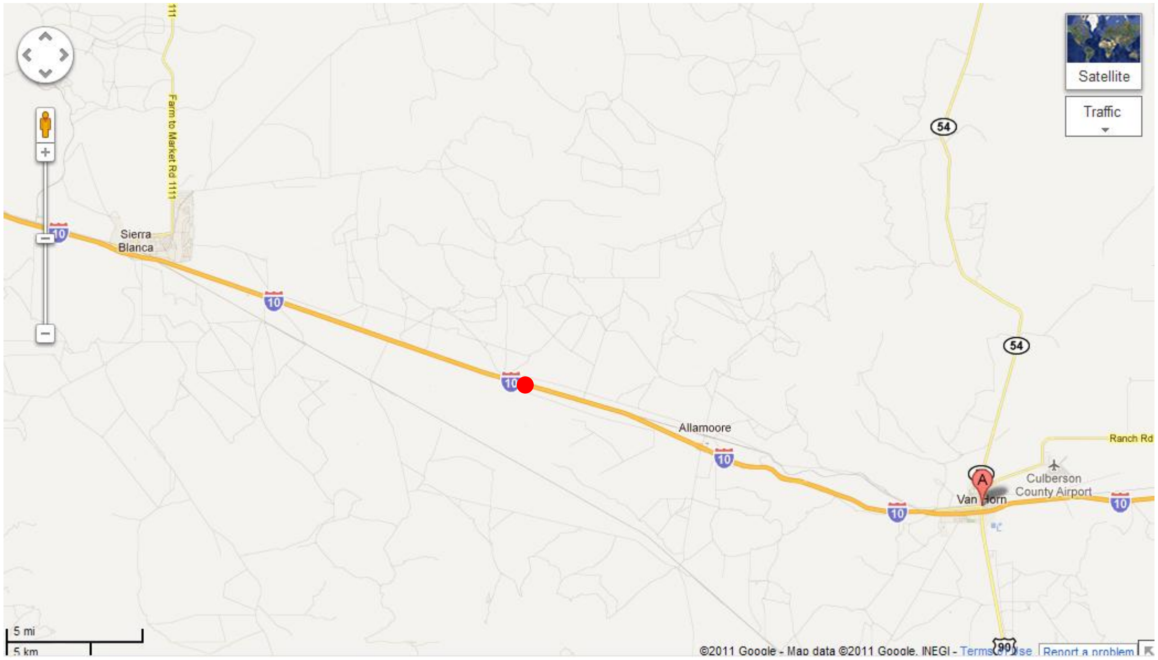

Figure 10.15: *Field survey location for Van Horn IH-10 section*

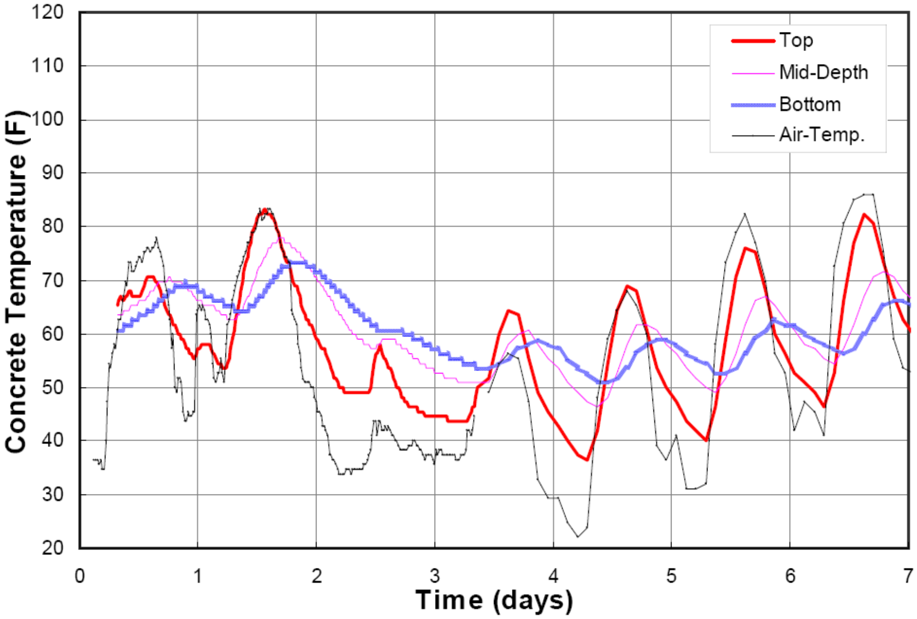

Figure 10.16: *Field survey location for Van Horn IH-10 section* (Nam, 2005)

10.2 MEASUREMENT ITEMS

10.2.1 Crack Spacing

As described in Chapter 2 along with the field observation result, CRCP undergoes transverse cracking at early-age due to (tensile) stress build-up induced by restrained volume changes. The volume changes at early-age are primarily caused by temperature variations, and the magnitude of early-age thermal (tensile) stress is in proportion to the temperature drop from the ZST (Breitenbucher, 1994; ERES, 2004). This fact indicates the ZST may influence on the transverse cracking pattern such as cracking spacing and crack width of CRCP structures. To examine the impact of ZST on the transverse cracking in CRCP, crack spacing was measured in each field testing section while a crack width was not investigated due to safety reasons.

10.2.2 Punchouts

As numerically investigated in Chapter 2, ZST may affect the potential for partial-depth punchout distress by increasing the level of the vertical concrete stress component at the transverse crack interface at the longitudinal steel depth. Also, according to the MEPDG developed per NCHRP 1-37A, the increased ZST can cause a larger transverse crack width and, in turn, can result in more number of full-depth punchouts in CRCP by degrading the LTE across the transverse cracks. To evaluate the effect of ZST on the punchout distress, the number of punchouts per lane mile was examined in the selected field sections.

10.2.3 Repairs

Once CRCP is deteriorated by punchout distress, they are diagnosed and then repaired. Depending on the extent of the distress, the repair method – full-depth repair, partial-depth repair – is properly chosen. Based on the assumption that those punchout distresses were associated with the high residual stress level in CRCP, the number of punchout repairs is also counted in each of the testing sections. The shallow patching for spalling repair was also investigated, but it will be regarded as a functional condition indicator since it has been reported that the spalling distress is not directly concerned with the ZST, rather is closely related with the material selection and the quality control issues.

10.3 RESULTS

10.3.1 Houston FM 529 Section

A field condition survey for the Houston FM 529 section was conducted on October 4th, 2011. Based on the given information and the ZST prediction model developed in Chapter 9, the ZST for this section was estimated as 108.9 °F at the top 1 in., 109.8 °F at the mid-depth, and 107.2 °F at the bottom 1 in.

Within the 1,875 ft. section, a total of 319 transverse cracks were found; the coordinate of the transverse cracks for all the sections are tabulated in Appendix A. The average crack spacing was 5.88 ft., and the standard deviation was 3.45 ft. Even though the section has been in service more than 11 years, there was no punchout, spalling or repair found. As can be seen in Figure 10.17, the cracks were generally tight. One thing noted is that the concrete around most of the transverse cracks was deteriorated by $CaCO_3$ produced by the reaction between $Ca(OH)_2$ and CO_2.

Figure 10.17: *Transverse cracks in Houston FM 529 section*

10.3.2 Dallas IH-45 Section

A field condition survey was performed in the Dallas IH-45 section on October 5th, 2011. Based on the given information on the material properties, geometric characteristic, environmental condition at the time of concrete placement, and measured concrete temperature history, the ZST for this section was predicted as 97.0 °F at the top, 98.4 °F at the mid-depth, and 94.5 °F at the bottom.

A total of 86 transverse cracks were found between the transverse construction joints 500 ft. apart. The collected data revealed that the average cracking spacing and standard deviation were 5.80 ft. and 2.89 ft., respectively. Similar to the FM 529 section, no punchout, spalling or repair was discovered in this 11 and a half years old CRCP section while the section mainly carries a lot of heavy traffic. Figure 10.18 shows the transverse crack condition in this section; the apparent crack width was very tight compared to the FM 529 section. Also, the concrete around the transverse cracks was less deteriorated by $CaCO_3$ as seen in the figure.

Figure 10.18: *Transverse cracks in Dallas IH-45 section*

10.3.3 Houston BW 8 Section

A field condition survey was conducted on the Houston BW 8 section on November 10th, 2010. As described in the previous subsection, this section was a special controlled section which consists of eight different subsections. Based on the general information provided by the 1244-3 report, the ZST for each subsection was predicted. The results are summarized in Table 10.3. Also, Table 10.4 shows the number of transverse cracks observed in each 230 ft. long subsection, and their average and standard deviation.

Table 10.1: *Estimated ZST in Houston BW 8 section* (unit: °F)

Section / Position	A (G[a]/0.62[b])	B (G /0.50)	C (G /0.38)	D (G /0.48)	E (L /0.56)	F (L /0.45)	G (L /0.58)	H (G /0.67)
Top	74.4	74.5	71.5	71.8	79.0	81.5	89.0	87.7
Middle	75.7	75.8	75.9	75.1	78.8	82.0	89.3	89.4
Bottom	74.9	74.5	76.0	76.2	76.1	80.8	84.0	84.9

[a] G: Siliceous river gravel; L: Limestone
[b] Steel ratio (%)

Table 10.2: *Results of transverse crack survey in Houston BW 8 section*

	A	B	C	D	E	F	G	H
# of Cracks	38	35	29	31	27	27	40	37
Average (ft.)	5.35	6.65	7.98	7.33	7.91	8.77	5.73	6.25
St. Dev. (ft.)	3.05	3.24	3.24	3.06	3.07	3.77	2.92	3.09

The finding from the SRG section shows that the crack spacing for each subsection is quite different while the subsections show a little difference in the ZST. This result seems to arise from the steel amount difference for each subsection. Figure 10.21 (a) show the relationship between the steel ratio and average transverse crack spacing found in the SRG section. It shows that the average crack spacing tends to significantly decrease as the steel ratio increases, as commonly believed.

The same trend was observed in the LS section except one outlier data point, i.e., data for subsection G. This outlier point gives a good implication to examine the effect of ZST on the transverse crack spacing when compared with the data from the subsection E; as can be seen Table 10.3, subsections E and G had about 10 °F of ZST difference while the steel ratio for both subsections were nearly same. The comparison result shows that this 10 °F of ZST difference resulted in about 28 % difference in the cracking spacing as indicated in Figure 10.21 (b). Based on this finding, it may be concluded that the ZST can have a substantial effect on the transverse crack spacing even in the later-age.

Also, another finding can be addressed in terms of the performance by comparing the pavement condition of both SRG and LS sections. In both sections, there was no punchout distress found, but there was a big difference in the surface condition caused by spalling distresses. Figure 10.22 displays the pavement condition in both SRG and LS sections. It clearly shows that the SRG section had a large portion of spalling repairs while the condition of the LS section was very fair and sound. Since it is stated that the spalling is not directly associated with the ZST, rather is related with the material selection and quality control issues, the comparison of spalling may not give a close correlation between the ZST and the performance. However, it is meaningful to see this finding to understand the impacts of the material selection and steel design on the long-term condition of CRCP structures.

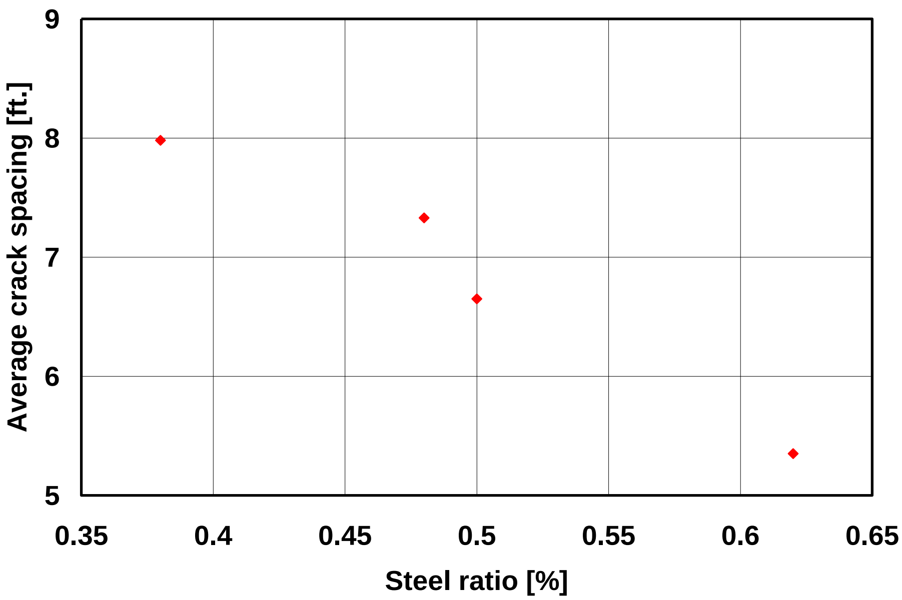

(a) SRG section

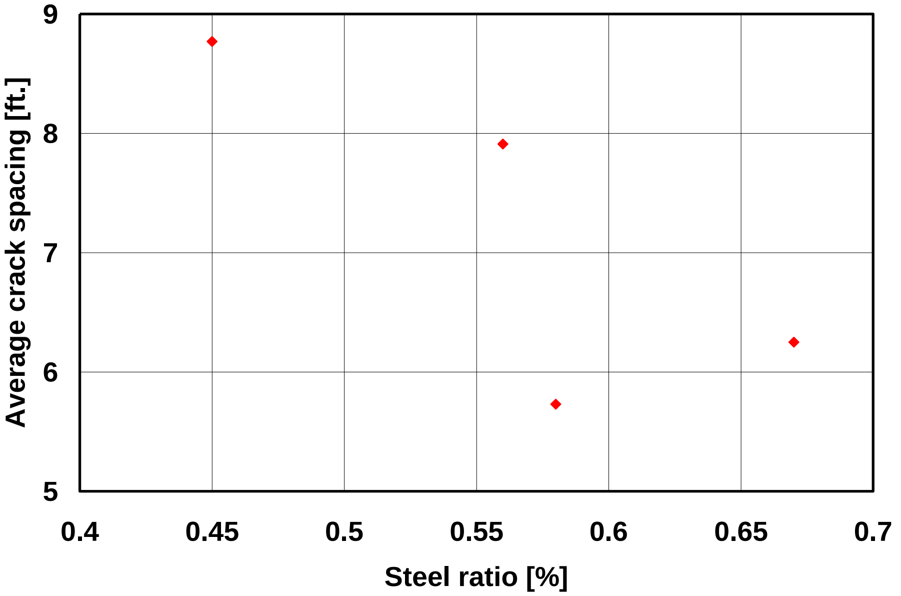

(b) LS section

Figure 10.19: *Transverse crack spacing vs. steel ratio in Houston BW 8 section*

(a) SRG section

(b) LS section

Figure 10.20: *Field condition survey in Houston BW 8 section*

10.3.4 Houston IH-45 section

A field condition survey for the Houston IH-45 section was carried out on November 10th, 2010. As with the Houston BW 8 section, this section was also a special treated CRCP section composed of eight subsections with the different experimental variables: four different levels of steel ratio and two different types of coarse aggregate. Based on the geometric, material, and temperature information described in the 1244-3 report, the ZST for each subsection was estimated using the proposed prediction model. Tables 10.3 and 10.4 respectively summarize the predicted ZST values for each subsection, and the number of transverse cracks found within each 230 ft. long subsection. Also, Table 4 includes the average crack spacing, standard deviation, and the number of spalling repairs in each subsection.

Table 10.3: *Estimated ZST in Houston IH 45 section* (unit: °F)

Section Position	A (G [a]/0.76[b])	B (G /0.65)	C (G /0.55)	D (G /0.67)	E (L /0.75)	F (L /0.63)	G (L /0.74)	H (G /0.84)
Top	80.6	79.8	78.9	78.9	78.9	79.5	69.4	69.3
Middle	84.3	79.2	74.1	74.1	77.9	77.9	80.9	80.8
Bottom	82.5	79.6	76.6	76.6	80.9	80.8	85.0	85.0

[a]G: Siliceous river gravel; L: Limestone
[b]Steel ratio (%)

Table 10.4: *Results of transverse crack survey in Houston IH 45 section*

	A	B	C	D	E	F	G	H
# of Cracks	51	58	47	54	61	45	58	58
Average (ft.)	4.30	3.68	4.62	4.11	3.69	5.01	3.92	3.98
St. Dev. (ft.)	2.56	2.29	2.35	2.10	1.98	3.50	2.39	2.47
# of Spalling Repairs	14	11	17	12	0	0	0	0

Figure 10.21 shows the correlation between the steel ratio and average transverse crack spacing evaluated in both SRG and LS sections. The results, as expected, showed that the average crack spacing tends to decrease as the steel ratio increases. The data points which did not follow the general trend seem to be caused by the influence of several other factors such as ZST, subbase friction, material properties, and quality control.

Also, it is of great importance to note that the SRG and LS sections showed the quite different long-term performance as the Houston BW 8 section did. Because both sections did not show any sign of punchout distress, the punchout-based performance comparison could not be made. However, the surface condition-based performance evaluation could be conducted by comparing the number of spalling repairs observed in each section. Figure 10.22 shows the general surface condition in both SRG and LS sections. As can be seen in the figure, a large number of spallings were developed only in the SRG section. Figure 10.23 presents the percentage of transverse cracks repaired due to spalling distresses in the SRG section. The result shows that approximately 25 % of transverse cracks experienced spalling in the SRG section whereas no spalling distress was observed in the LS section. This field survey finding agrees well with the condition survey results obtained from the BW 8 section. This again emphasizes the significance of material selection and quality control to ensure the longer-lasting and better-performing CRCP.

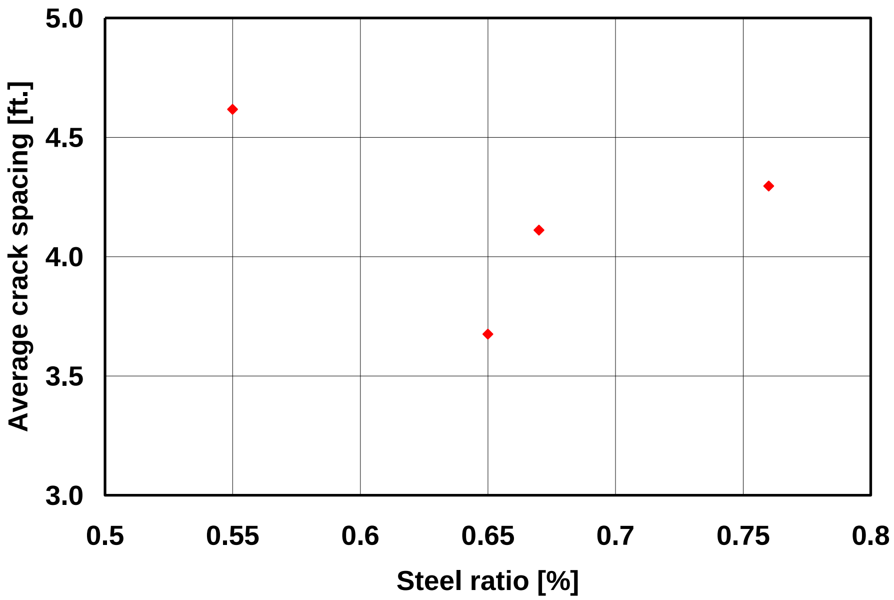

(a) SRG section

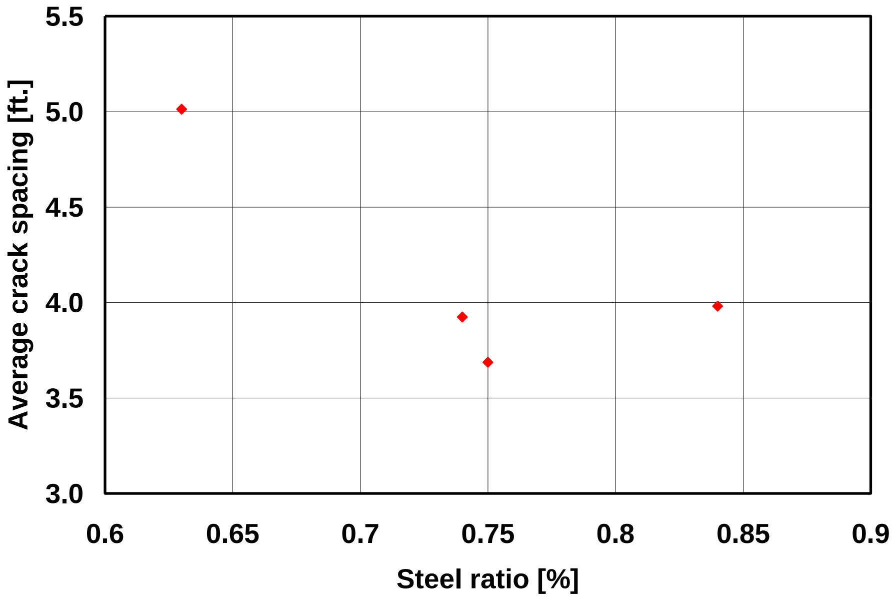

(b) LS section

Figure 10.21: *Transverse crack spacing vs. steel ratio in Houston IH 45 section*

(a) SRG section

(b) LS section

Figure 10.22: *Transverse cracks in Houston IH-45 section*

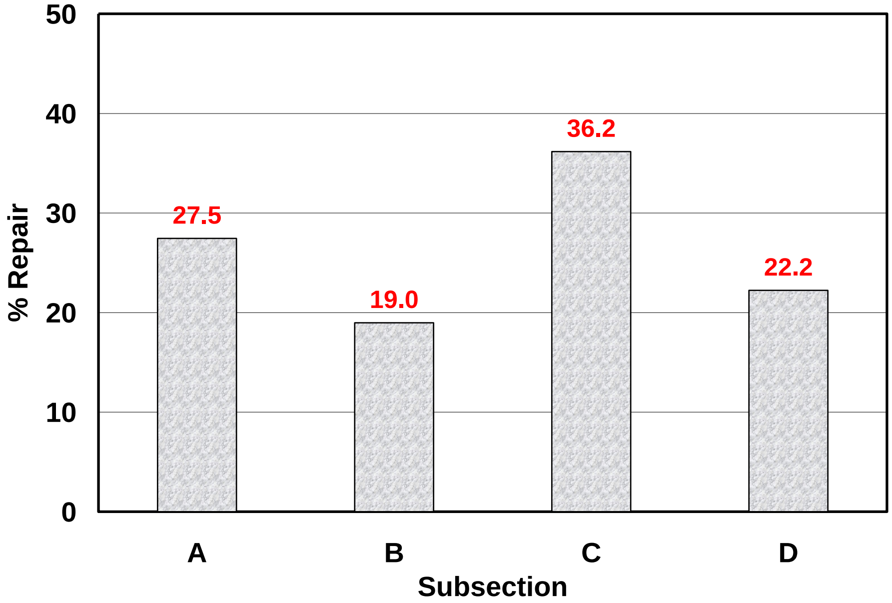

Figure 10.23: *Percentage of transverse cracking repair found in Houston IH-45*

10.3.5 Baytown SPUR 330 Section

A field condition survey was carried out under the database project (TxDOT Research Project 0-6274) on November 12th, 2010. Based on the measured temperature history at early-age and the material property information, the ZST for this section was predicted as follows: 104.1 °F at the 1 in. below top, 103.1 °F at the mid-depth, and 103.7 °F at 1 in. above the bottom.

The number of transverse cracks recorded in this 945 ft. long section was 92, and their average spacing and standard deviation were 10.0 ft. and 4.46 ft., respectively. In this section, no punchout, spalling, or repair was observed although the section has been opened to traffic more than 7 years. Figure 10.24 presents the transverse crack condition of the survey location. As can be seen in the figure, the surface crack width was relatively lager than the Houston FM-529 and Dallas IH-45 sections. Also, slight carbonation damage was observed around some transverse cracks.

11.12.2010 08:57

(a) Overview of section

11.12.2010 08:59

(b) Transverse cracks

Figure 10.24: *Field condition survey in Beltway SPUR 330 section*

10.3.6 Cleveland US 59 Section

A field condition survey was conducted in the Cleveland US 59 section located north of Houston on November 11th, 2010. Based on the given information and the ZST prediction model developed in Chapter 9, the following results were obtained: 105.6 °F at the top 1 in., 108.9 °F at the mid-depth, and 106.8 °F at the bottom 1 in.

A total of 80 transverse cracks were found in the 504 ft. long section. The average cracking spacing and standard deviation were 6.25 ft. and 3.04 ft., respectively. In this 7-year old CRCP section, there was no sign of punchout and spalling distresses, which indicates that the CRCP is very well-performing. Furthermore, the apparent transverse crack width was quite tight in general as shown in Figure 10.25.

Figure 10.25: *Transverse cracks in Cleveland US 59 section*

10.3.7 Van Horn IH-10 Section

A field condition survey was performed in the Van Horn IH-10 section on November 29th, 2010. It is interesting to note that the concrete material for this section incorporated 50 % of slag, which is different from the other sections included in the condition survey. With the given information, the ZST was roughly estimated because the developed ZST prediction model only covers Class P concrete. The estimated ZST values were: 69.4 °F at the top, 68.7 °F at the mid-depth, and 67.9 °F at the bottom.

During the survey, only a 500-ft. part out of total 2,400 ft. was investigated because of safety reasons. There were a total of 68 transverse cracks in the 500 ft. section. The average crack spacing and standard deviation were 7.36 ft. and 3.47 ft., respectively. Even though this CRCP section was winter-placed and has been in service for only eight-and-a-half years, a couple of spalling distresses were observed in the surveyed section. Also, the surface crack width was generally large. Figure 10.26 shows the transverse crack condition and the spalling distress found in the section.

(a) Transverse cracks

(a) Spalling distress

Figure 10.26: *Field condition survey for Van Horn IH-10 section*

10.4 DISCUSSIONS ON RESULTS

10.4.1 Transverse Crack Spacing

The current MEPDG states that the transverse crack spacing in CRCP is affected by equivalent temperature loading (ERES, 2004). This implies that the higher ZST could result in shorter crack spacing in CRCP. To examine the relationship between ZST and transverse crack spacing, the field data collected from the seven CRCP sections was analyzed. Figure 10.27 presents the result of the analysis. As can be seen, any clear tendency could not be found between the measured ZST and crack spacing since each section had different age, geometry, steel amount, material property, restraint condition, and environmental conditions. However, this finding at least indicates that the later-age transverse crack spacing might not be significantly influenced by the ZST level.

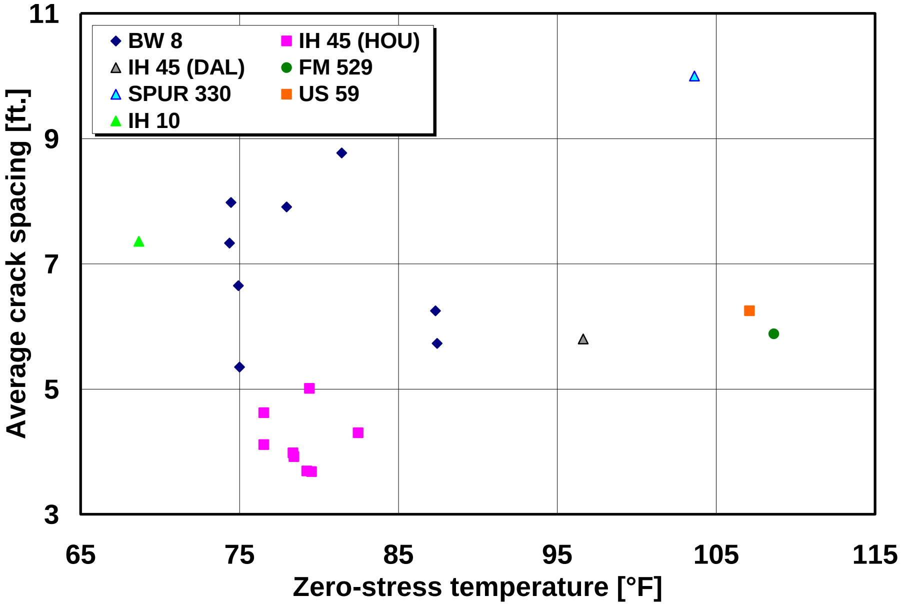

Figure 10.27: ZST vs. transverse crack spacing measured in seven CRCP sections

10.4.2 Punchout Distress

Since punchout is the only structural performance indicator associated with the temperature-related criteria in CRCP structures, the primary objective of this chapter was to investigate the effect of ZST on the occurrence of punchout distress based on the field condition surveys. As described in the previous subchapters, field condition surveys were performed in the seven selected CRCP sections. The ages of the surveyed sections ranged from about 7 years to 22 years old. While the relatively young sections – less than 10-year old sections – were too young to exhibit the punchout distress, it was expected that the 20-plus years old CRCP sections might show some indication of punchout distress in progress. Unfortunately, however, the field condition surveys revealed that no apparent punchout distress was developed even in the 10 and a half years old summer-placed CRCP section and the 21 years and 9 months old SRG CRCP section accommodating a large volume of heavy traffic on a daily basis.

This fact might support the finding from the TxDOT Research Project 0-5832 (Won et al., 2011). According to the TxDOT PMIS (pavement management information system) database, a total of 219 punchouts were recorded in the districts of Dallas, Fort Worth, Wichita Falls, and Childress as of 2009. However, the field surveys performed by the research team at Texas Tech University showed that the “true punchouts” caused by the structural deficiency were only about 33% (31 out of 95) of the recorded number of punchouts as shown in Figure 10.27. The rest of the punchouts recorded were identified as non-structural punchouts caused by material selection and construction quality control issues. This finding may indicate that the punchout distress due to temperature-related criteria may much less frequently occur than as has been stated by the previous research programs.

***Table 10.5:** Detailed classification of punchouts* (Won et al., 2011)

District	**Punchout**									
	PCH	**E-PCH**	**E-PCH-PTB**	**PCH-CJ**	**PCH-RJ**	**BS-PCW**	**Repair or Not Found**	**Not Investigated**	**Incorrect**	**TOTAL**
Dallas	10	8	2	7	8	6	9	19	15	84
Fort Worth	0	1	0	6	10	11	26	12	2	68
Wichita Falls	4	0	4	10	0	5	34	2	3	62
Childress	2	0	0	1	0	0	1	1	0	5
Sub Total	16	9	6	24	18	22	70	34	20	219
Ratio	**16.8%**	**9.5%**	**6.3%**	**25.3%**	**18.9%**	**23.2%**				

Note: PCH: punchout, E-PCH: edge punchout, E-PCH-PTB: edge punchout with poor tie bar, PCH-CJ: punchout at construction joint, PCH-RJ: punchout at repair joint, BS-PCW: big spalling with poor concrete work

10.4.3 Crack Width

Crack width is not classified as the direct performance indicator, but it has been described that the larger crack width may increase the potential of puchout distress (ERES, 2004). According to the NCHRP MEPDG, the crack width can be estimated using the equation as follows:

$$cw = Max\left(L \cdot \left(\varepsilon_{sh} + \alpha_{PCC} \Delta T_{\zeta} - \frac{c_2 f_{\sigma}}{E_{PCC}} \right) \cdot 1000 \cdot CC,\ 0.001 \right) \qquad \text{(Formerly Eq. 3.1)}$$

Again, the equation indicates that the crack width is in proportion to the temperature drop from the ZST, which means that the transverse crack width increases as the ZST increases. The equation also implies that the crack width becomes wider as the age of concrete increases because of the contribution of drying shrinkage. However, the field experiment performed by Kohler (2005) revealed that the crack width does not increase rather decrease as the pavement age increases as shown in Figure 10.28. It also shows that the crack width model in MEPDG significantly over-predicts the crack width. Field experiment conducted by Nam et al. (2007) also provided a clear evidence that the crack width of CRCP tends to decrease as the pavement age increases (Figure 10.29).

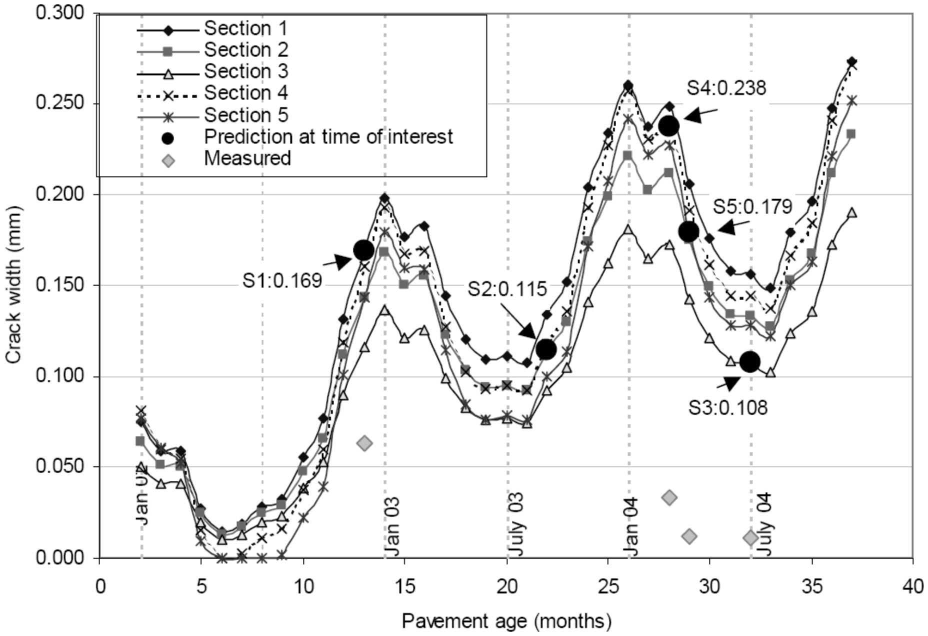

Figure 10.28: *Crack width calculated with MEPDG software* (Kohler, 2005)

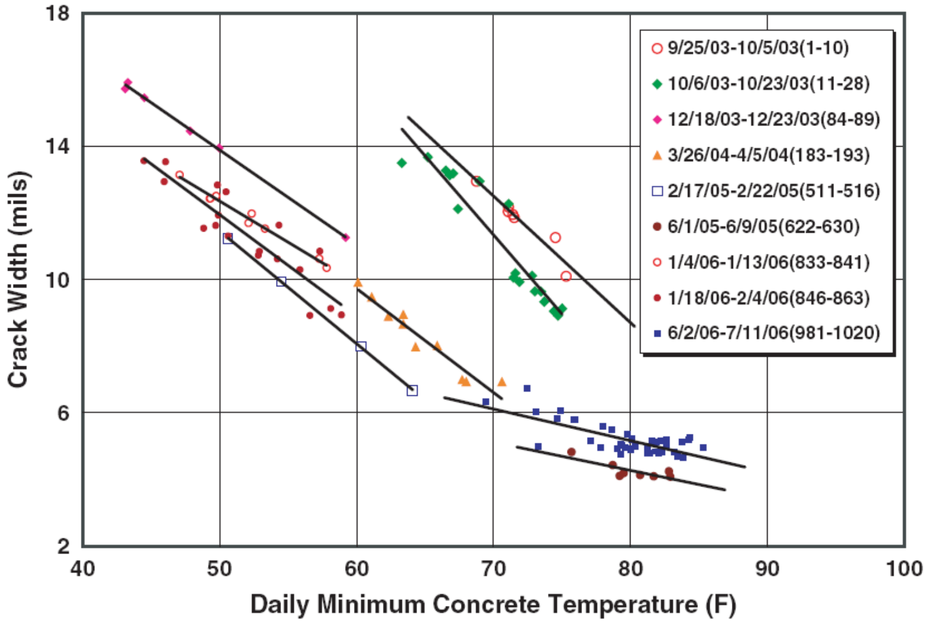

Figure 10.29: *Crack width variations over time* (Nam et al., 2007)

The field condition survey performed under this chapter also indicated that the apparent crack width might not be directly related with the ZST. To see the clearest cases, the survey results obtained from the Houston FM 529 and Dallas IH-45, and Van Horn IH-10 sections were compared each other. As explained previously, the FM 529 and the IH-45 sections were constructed in summer and spring of 2000 (11 and a half years old), respectively, and their ZST were estimated at about 100 °F to 110 °F. On the other hand, the Van Horn IH-10 section was built in March of 2003 (8 and a half years old), and the predicted ZST was around 70 °F. If the above crack width predictive equation works properly under no circumstances, the crack width of the FM 529 and the IH-45 sections should be much larger than that of the IH-10 section because they had about 30 °F to 40 °F higher ZST and experienced three years more drying shrinkage. However, the field condition surveys, as seen in Figures 10.17, 10.18, and 10.26, the apparent crack width observed in the IH-10 section was much larger than those of FM 529 and IH-45.

Also, the survey result from the Cleveland US 59 partly agrees with this finding. The US 59 section was placed in July of 2004, and the estimated ZST was about 107 °F. Even though this section experienced one year less drying shrinkage than the IH-10 section, the crack width would be larger than the IH-10 section in accordance with the Eq. 3.1 because it had about 40 °F higher ZST. The condition survey result, however, showed that the crack width of the US 59 was much tighter than that of the IH-10.

Based on these findings, it might be concluded that the crack width model described in Eq. 3.1 misses some other important parameters affecting the time-dependent crack width variations and thus might not be valid.

Chapter 11: Summary, Conclusions and Recommendations

11.1 SUMMARY

It has been understood that early-age behavior of continuously reinforced concrete pavements (CRCP) has a substantial effect on its long-term performance. The current CRCP design procedures most widely used in the US, the 1993 AASHTO Design Guide, and newly developed mechanistic-empirical pavement design guide (MEPDG), are based on the assumption that CRCP performance depends on the setting temperature of concrete, or zero-stress temperature (ZST), and resulting early-age structural behavior. The primary objective of this dissertation research lies in sound understanding of the effect of early-age structural behavior characteristics of CRCP on its long-term performance to provide researchers, engineers, and practitioners with reliable design and analysis criteria for CRCP.

To achieve this main objective, characterizing the early-age structural response in CRCP was a core task. For this purpose, a zero-stress temperature (ZST), an indicator for characterizing the early-age structural response of CRCP, was evaluated as it may determine the overall history of behavior and response in CRCP. As a beginning point of the entire framework, a series of field experiments were conducted in four new Portland cement concrete pavement (PCCP) construction sections in the state of Texas to evaluate the actual structural response in early-age CRCP. Field experiments were used because a laboratory experiment would have a critical limitation in simulating the actual restraint conditions of CRCP. To expand this core task to the various parametric categories, a computer-aided parametric simulation was carried out using validated numerical models. Based on the data sets obtained from the parametric investigation, a statistical model to quantify the early-age structural response of CRCP was proposed to implement in codes of practice and pavement design guides.

A secondary task was to find a relationship between the early-age structural response and the long-term performance of CRCP structures. Since the experimental and analytical investigations tended to provide quite localized information on the time-dependent behavior of CRCP, the overall performance of CRCP could not be identified solely based on those results. To overcome this limitation, extensive field condition surveys were performed in seven different old CRCP sections with known material and early-age temperature history to find the implications of early-age behavior characteristics on the long-term performance of CRCP from a macroscopic point of view.

11.2 CONCLUSIONS

The current CRCP design procedures are based on the premise that the concrete setting temperature, or ZST, and resulting early-age behavior have substantial effects on the long-term performance of CRCP. However, there is no documented evidence that long-term performance of CRCP in terms of punchouts depends on ZST. The premise was developed based on a perceived notion that the widths of transverse cracks depend on ZST and early-age behavior of CRCP, such as transverse crack spacing. In order to evaluate the validity of this premise, extensive laboratory, field construction, and theoretical studies were conducted. The findings indicate that ZST and resulting early-age behavior of CRCP do not appear to affect long-term structural performance of CRCP. Part of the discrepancy between the premise and the findings in this study stems from the assumptions made in the premise, one of which is that PCC materials are elastic. This study demonstrated that long-term CRCP behavior observed in the field – long-term transverse crack spacing is independent of ZST and crack widths decrese over time – can only be explained when the PCC materials are viscoelastic. The comparison of concrete stresses directly measured in the pavement and those derived from theoretical analysis also confirm the viscoelastic nature of PCC materials.

How the PCC materials behave in CRCP is a fundamental aspect that needs to be correctly addressed in the development of CRCP design procedures. The basic premise made in the development of current CRCP design procedures – PCC materials behavior is elastic – needs to be revised to include the viscoelastic behavior of PCC materials. The changes in the premise will have substantial effects on the CRCP design procedures, one of which will be the effect of ZST.

The current MEPDG exhibits the substantial effect of ZST on slab thickness determination. This puts both state highway agencies (SHAs) and the concrete paving industry in difficult positions. This is due to the fact that when pavement design is developed, design engineers do not have information on when the pavement will be constructed and what mix proportions of concrete will be used for the project, both of which have effects on ZST and thus slab thickness. To make the situation more complicated, there are normally several different phases of CRCP placement in a single paving project due to traffic control issues. CRCP in different phases is placed at different times of the year, resulting in varying ZSTs. Also, even in a single day of concrete placement, ZST varies depending on what time of day the concrete is placed. From a practical standpoint, it is not feasible to change slab thickness depending on when the concrete is placed, because changing the slab thickness during construction requires substantial modifications to the plans with little time and will delay construction, resulting in cost increase. From both technical and practical standpoints, including ZST in the CRCP design procedures is not feasible. There is a strong need for the development of new CRCP design procedures with more reasonable assumptions.

Based on the research efforts presented in this dissertation, the findings can be summarized as follows:

Overall Time-Dependent Behavior of CRCP

A time-dependent behavior of CRCP was reviewed based on numerous field evidence. It was found that CRCP typically experiences the following behavior sequence:

- Occurrence of early-age transverse cracks to relieve the early-age stresses is primarily caused by temperature and moisture variations.

- Horizontal cracking initiates from the transverse crack interface at the steel level. Field and laboratory experiments and numerical investigation revealed that this behavior seems to be caused by curling and the incompatible interaction between longitudinal steel and surrounding concrete at the time of transverse cracking. The horizontal crack can continue to propagate upon further applications of traffic loading.

- Due to the continued incompatible interaction between longitudinal reinforcement and surrounding concrete, later-age longitudinal cracks begin to develop along the longitudinal steel. Also, field observation showed that later-age transverse cracks take place between early-age transverse cracks.

- The continued propagation of horizontal cracking, longitudinal cracking, and later-age transverse cracking isolates a concrete piece in CRCP.

- Under further repetitive traffic loading thereafter, the isolated concrete pieces are ruptured, ultimately resulting in partial-depth punchout distresses.

In-Situ Evaluation of Zero-Stress Temperature in CRCP

An in-situ evaluation of early-age concrete stress development in CRCP was performed to find ZST. Findings from this task were as follows:

- Because the strain directly measured from a concrete element contains both stress-dependent strain and stress-independent strain, decomposition of a stress-dependent strain history out of total strain was required to compute the early-age stress development.

- Specially designed devices called non-stress cylinders (NC) were employed to measure strain-dependent strain components caused by variations in temperature and relative humidity (RH).

- To identify the stress-independent strain at other depths of interest, temperature and RH at various depths were measured using state-of-the-art sensing technologies. These histories were converted to free strains using identified coefficient of thermal expansion (CTE) and hygral shrinkage coefficient.

- Based on the identified strain history, a stress history was calculated with a step-by-step numerical method considering a time-dependent behavior – creep and relaxation – of concrete. A reference stress data monitored with a stressmeter validated the results obtained from the proposed experimental and analysis methodologies.

- To verify the reliability of the current ZST prediction model, the ZST evaluated with the field experiment was compared with the ZST estimated with the current model. The result showed that a difference of about 7 °F to 25 °F existed between the measured and predicted ZST values. This finding suggested a need for a development of a new model or improvements of the current model.

Effect of Time-Dependent CTE on Early-Age Stress Development

CTE in hardening concrete was investigated using NC for accurate prediction of thermal stress developments in CRCP as well as other types of conventional concrete structures. Findings from this task showed:

- The CTE in hardening concrete is age-dependent. The CTE at the time of final setting was about twice as high as that in the stabilized stage.

- After the sudden decrease of CTE in the initial stage, the CTE tended to slightly increase for a certain period of time and then stabilized.

- The results from the numerical investigation revealed that age-dependent characteristics of CTE could remarkably influence early-age thermal stress evolution, and in turn, cracking potential of cast-in-place concrete. The results of case studies showed that the stress values at crack initiation differed about 37 % between the constant CTE and varying CTE cases, although their ZST were nearly identical.

- Delayed thermal deformation induced by moisture redistribution in concrete during and after temperature changes could affect the early and later-age stress developments in concrete structures, especially around temperature inflection points.

Effect of Creep and Built-in-Curing on Stress Development

Effects of creep and built-in-curling (BIC) on restrained stress history of PCC pavements subjected to environmental loading were investigated to propose reliable criteria for stress-related design inputs.

- The result showed that stress relaxation due to creep is not negligible, rather might be important in the design and analysis of PCC pavements. The experimental results presented in this paper showed about 50% ~ 60% of stress relaxation was due to creep at the age of 25 days, which is quite large.

- Creep effect is path-dependent, which is very sensitive to the preceding stress histories.

- Early-age stress development was affected by setting temperature gradient. This indicates that accurate ZST evaluation should be based on consideration of BIC.

- Long-term residual stress might not be significantly affected by BIC because of 1) gradual relaxation of BIC stresses, 2) a large amount of creep in early-age concrete, and 3) low modulus of early-age concrete.

- Based on the findings, it is recommended that stress-related inputs for PCC pavements design need to be developed considering the creep effect because the current design procedures are solely based on the elastic theory, which may lead to overestimation of stresses and conservative design.

- It is also advisable to consider aging effects for more accurate evaluation of long-term stresses. Application of the age-adjusted effective modulus method could be one of the most practical ways incorporating both creep and aging effects into stress analysis.

Development of Numerical Model for ZST Model Development

Theoretical models for temperature and thermal stress predictions were proposed to investigate the effects of various parametric categories on ZST formation.

- The theoretical models were proven to be valid by comparing the results obtained from the numerical analysis with the measured field data sets.

- The proposed theoretical models were implemented in parametric numerical investigations for developing a ZST predictive model.

Development of ZST Predictive Model

- A parametric study showed that ZST depends on diverse factors such as time of day of the placement, placement season, type of coarse aggregate, depth of interest, pavement thickness, cementitious material content, water-to-cement ratio, and wind speed.

- C-value predictive models (and in turn, ZST predictive models) were proposed based on a multivariate linear regression analysis. A total of 1,440 analysis cases were categorized into 24 groups, and regression models for each group were proposed. Data sets for regression analysis were established based on a parametric study using the proposed numerical models. For most cases, a coefficient of determination was higher than 0.90 and a significance level was less than 0.01, which indicate that the proposed models were statistically highly confident.

- General acceptance of the proposed regression models was verified by comparing the original data obtained from the parametric study with the predicted values calculated with the proposed models. The results agreed with each other quite well, which indicates that the proposed multivariate regression models proposed were quite valid to implement in codes of practice and pavement design guides.

Implications of ZST on Punchout Distress in CRCP

- Since punchout is the only structural performance indicator associated with the temperature-related criteria in CRCP structures, the effect of ZST on occurrence of punchout distress was performed based on field condition surveys.

- The field condition surveys were performed in seven selected CRCP sections in the state of Texas. The ages of the surveyed sections ranged from about 7 years to 22 years. Field condition surveys revealed no apparent punchout distress, even a summer-placed CRCP section that was 10.5 years old, or the SRG CRCP section, which accommodates a large volume of heavy traffic on a daily basis, and is 21 years and 9 months old.

- This fact might support the findings from the TxDOT Research Project 0-5832, that rare cases of “real punchout” – which is caused by structural deficiency – have been found in field condition surveys. Field surveys conducted in Dallas, Fort Worth, Wichita Falls, and Childress districts in 2009 showed that true punchouts caused by structural deficiency took only about 33% (31 out of 95) of the total number of punchouts recorded in the Texas PMIS Database.

- The rest of the punchouts recorded (67 %: 64 out of 95) were identified as non-structural punchouts caused by material selection and construction quality control issues.

- This corrected database, under TxDOT Research Project 0-5832, found that punchout distress due to temperature-related criteria much less frequently occurs than has been described by previous research programs.

Implications of ZST on Crack Spacing and Crack Width Variation in CRCP

- The field study indicated that the later-age transverse crack spacing might not be significantly influenced by the ZST level.

- The current crack width model indicates that crack width largely depends on ZST level because it describes that the crack width is in proportion to temperature drop from ZST.

- The field condition survey found that apparent crack width might not be directly related to ZST. The survey results showed that two hot summer-placed CRCP sections (both 11.5 years old and 100-plus ZST in °F) had much tighter transverse cracks than a winter-placed 8.5 year old CRCP section with about 70 °F of ZST. Another case study showed a similar trend.

- Based on these findings, improvements on the current crack width model is recommended.

11.3 RECOMMENDATIONS FOR CHANGES TO MEPDG

The crack width model in the MEPDG assumes that concrete material is elastic, and crack width at any point depends primarily on the concrete temperature difference from the setting temperature. Punchout development model in the MEPDG is based on the assumption that crack stiffness deteriorates as a result of increased crack width over time, resulting in the loss of load transfer efficiency at transverse cracks and eventual punchouts. Accordingly, the basic framework of CRCP performance in MEPDG is rooted in variations in crack widths. Since crack widths depend on the setting temperature of concrete in the MEPDG crack width model, it's not surprising that CRCP performance in the MEPDG depends substantially on the concrete setting temperature. As observed in various CRCP sections in Texas, the majority of the punchouts is due to construction and material quality issues, and to a lesser degree, imperfections in design details. Field evidence indicates non-significant effect of concrete setting temperature on long-term CRCP performance. This study discovered that modeling of CRCP with viscoelastic materials behavior of concrete provides more realistic mechanistic responses. The studies conducted at University of Illinois at Urbana Champaign and at the University of Texas both indicate crack widths actually decrease over time, which is quite contradictory to the assumption made in the MEPDG model. Even though the MEPDG is a quite advanced pavement design program, it needs to be technically improved to address the following issues:

- Concrete materials are not elastic, especially when the loading rate is quite low, as in the case of temperature variations in concrete. Rather, they behave as viscoelastic materials, and the crack width model needs to incorporate the viscoelastic behavior of concrete.

- Concrete creep effect is the largest at the early ages when the stiffness is relatively low, and a substantial portion of concrete stresses dissipates through a stress-relaxation mechanism. Accordingly, the effect of setting temperature on crack widths is reduced.

- The crack width model in the MEPDG assumes that all the transverse cracks occur as soon as concrete is placed, with no subsequent cracks developing. This assumption is not correct, and causes over-estimations in crack width predictions. This assumption over-emphasizes the effect of ZST. Time dependency of transverse crack development needs to be incorporated.

11.4 RECOMMENDATIONS FOR FUTURE RESEARCH

While the research works provided in this dissertation showed some significance, major improvements need to be made in the following aspects:

- Because the creep model used in this study tends to slightly underestimate early-age creep behavior, a more advanced creep model needs to be implemented in the data analysis and numerical simulation.

- As identified from this study, BIC and time-dependent CTE, to some degree, affect the early-age stress development in CRCP. For a more accurate evaluation of concrete stress with numerical analysis, the effects of BIC and time-dependent CTE need to be taken into account by developing appropriate user-supplied subroutines.

- This study only showed early-age strain, temperature, RH, and corresponding stress developments. The measurement period needs to be expanded to monitor the long-term structural response of CRCP.

- In this study, ZST characterization was performed only for Class P concrete typically used in paving in the state of Texas. The parametric investigation could be expanded to more variable categories such as other cement types and SCM replacement ratio.

- The scope of this study did not identify the mechanisms of early-age transverse cracking or the mechanism of later-age longitudinal and transverse cracking. Further research work could be performed in this regard.

- This study could not find a clear relationship between the ZST and punchouts since the surveyed CRCP sections were too young to have punchouts. Field condition surveys for those sections need to be continued throughout the following years to identify the relationship. Also, the field condition survey database needs to be expanded to develop more reliable conclusions.

Appendix A

FIELD CONDITION SURVEY DATA

Table A.1: *Crack spacing data in Houston FM-529 section*

Coordinate of transverse crack		Transverse crack spacing	Coordinate of transverse crack		Transverse crack spacing
[ft.]	[in.]	[ft.]	[ft.]	[in.]	[ft.]
0	0	-	167	2	6.0
4	0	4.0	176	1	8.9
8	3	4.3	181	0	4.9
9	1	0.8	184	5	3.4
15	9	6.7	195	1	10.7
23	8	7.9	201	7	6.5
26	9	3.1	203	0	1.4
32	5	5.7	209	5	6.4
38	0	5.6	214	5	5.0
47	3	9.3	218	5	4.0
52	11	5.7	219	8	1.3
61	1	8.2	221	8	2.0
63	11	2.8	227	0	5.3
66	5	2.5	233	7	6.6
69	3	2.8	240	1	6.5
74	1	4.8	248	3	8.2
81	1	7.0	250	8	2.4
88	3	7.2	254	1	3.4
97	5	9.2	258	4	4.3
104	4	6.9	263	11	5.6
105	1	0.8	273	9	9.8
108	6	3.4	279	11	6.2
115	5	6.9	281	7	1.7
125	6	10.1	285	7	4.0
128	5	2.9	295	7	10.0
136	3	7.8	299	1	3.5
142	9	6.5	304	4	5.3
146	4	3.6	305	6	1.2
147	8	1.3	311	9	6.3
148	4	0.7	321	8	9.9
155	3	6.9	332	7	10.9
156	9	1.5	344	1	11.5
158	7	1.8	348	3	4.2
161	2	2.6	353	11	5.7

Table A.1 (cont.): *Crack spacing data in Houston FM-529 section*

Coordinate of transverse crack		Transverse crack spacing	Coordinate of transverse crack		Transverse crack spacing
[ft.]	[in.]	[ft.]	[ft.]	[in.]	[ft.]
363	0	9.1	553	6	6.0
370	4	7.3	557	6	4.0
373	9	3.4	562	11	5.4
380	3	6.5	569	1	6.2
386	3	6.0	579	3	10.2
392	6	6.3	587	6	8.3
397	9	5.3	594	9	7.3
400	9	3.0	604	0	9.3
407	8	6.9	607	0	3.0
414	7	6.9	611	7	4.6
424	9	10.2	618	0	6.4
435	11	11.2	644	0	26.0
439	5	3.5	653	9	9.8
441	5	2.0	662	3	8.5
448	3	6.8	664	6	2.3
452	5	4.2	671	6	7.0
456	8	4.3	683	2	11.7
463	6	6.8	686	4	3.2
467	0	3.5	688	11	2.6
474	11	7.9	690	0	1.1
477	6	2.6	698	8	8.7
479	1	1.6	704	2	5.5
482	3	3.2	707	4	3.2
488	2	5.9	723	1	15.8
497	1	8.9	727	4	4.3
498	1	1.0	729	2	1.8
506	0	7.9	733	3	4.1
510	11	4.9	741	5	8.2
514	11	4.0	745	2	3.8
518	6	3.6	747	0	1.8
527	1	8.6	749	5	2.4
533	1	6.0	751	5	2.0
539	0	5.9	754	4	2.9
547	6	8.5	758	4	4.0

Table A.1 (cont.): *Crack spacing data in Houston FM-529 section*

Coordinate of transverse crack		Transverse crack spacing	Coordinate of transverse crack		Transverse crack spacing
[ft.]	[in.]	[ft.]	[ft.]	[in.]	[ft.]
763	1	4.8	995	11	6.0
775	11	12.8	998	3	2.3
785	8	9.8	1000	0	1.8
794	8	9.0	1007	2	7.2
807	9	13.1	1011	3	4.1
814	2	6.4	1013	6	2.3
819	9	5.6	1016	5	2.9
825	6	5.8	1022	5	6.0
832	2	6.7	1026	7	4.2
838	11	6.8	1030	4	3.8
847	5	8.5	1035	0	4.7
849	7	2.2	1039	1	4.1
855	0	5.4	1045	4	6.3
860	1	5.1	1058	2	12.8
866	7	6.5	1070	2	12.0
870	8	4.1	1072	6	2.3
880	2	9.5	1075	5	2.9
891	8	11.5	1078	5	3.0
896	4	4.7	1083	1	4.7
902	1	5.8	1095	1	12.0
912	0	9.9	1098	2	3.1
921	6	9.5	1101	0	2.8
926	6	5.0	1107	1	6.1
934	5	7.9	1112	7	5.5
936	6	2.1	1117	2	4.6
940	3	3.8	1124	6	7.3
948	4	8.1	1129	5	4.9
955	1	6.8	1133	1	3.7
959	6	4.4	1139	4	6.3
961	1	1.6	1142	6	3.2
973	1	12.0	1147	7	5.1
978	8	5.6	1149	11	2.3
984	0	5.3	1153	1	3.2
989	11	5.9	1160	0	6.9

Table A.1 (cont.): *Crack spacing data in Houston FM-529 section*

Coordinate of transverse crack		Transverse crack spacing	Coordinate of transverse crack		Transverse crack spacing
[ft.]	[in.]	[ft.]	[ft.]	[in.]	[ft.]
1167	3	7.3	1404	2	15.1
1172	7	5.3	1406	7	2.4
1179	7	7.0	1411	4	4.8
1184	0	4.4	1413	1	1.8
1191	3	7.3	1416	9	3.7
1201	11	10.7	1419	6	2.8
1213	0	11.1	1427	1	7.6
1213	10	0.8	1430	1	3.0
1221	9	7.9	1432	0	1.9
1227	0	5.3	1440	9	8.8
1234	3	7.3	1448	1	7.3
1236	1	1.8	1460	4	12.3
1244	9	8.7	1468	1	7.8
1256	11	12.2	1472	1	4.0
1263	7	6.7	1500	4	28.3
1272	3	8.7	1503	0	2.7
1280	7	8.3	1505	4	2.3
1285	5	4.8	1509	5	4.1
1296	2	10.8	1522	0	12.6
1298	8	2.5	1523	0	1.0
1305	4	6.7	1529	9	6.8
1314	0	8.7	1536	1	6.3
1322	0	8.0	1545	7	9.5
1330	2	8.2	1550	0	4.4
1338	0	7.8	1554	9	4.8
1345	3	7.3	1560	1	5.3
1347	7	2.3	1567	8	7.6
1349	7	2.0	1569	11	2.3
1353	7	4.0	1580	6	10.6
1358	1	4.5	1582	11	2.4
1369	8	11.6	1593	4	10.4
1371	6	1.8	1595	7	2.3
1381	9	10.3	1600	11	5.3
1389	1	7.3	1611	1	10.2

Table A.1 (cont.): *Crack spacing data in Houston FM-529 section*

Coordinate of transverse crack		Transverse crack spacing	Coordinate of transverse crack		Transverse crack spacing
[ft.]	[in.]	[ft.]	[ft.]	[in.]	[ft.]
1612	1	1.0	1752	3	3.8
1618	6	6.4	1755	7	3.3
1623	9	5.3	1760	11	5.3
1630	1	6.3	1766	4	5.4
1632	8	2.6	1769	4	3.0
1636	2	3.5	1773	1	3.8
1638	8	2.5	1779	2	6.1
1642	9	4.1	1784	1	4.9
1648	0	5.3	1789	8	5.6
1653	5	5.4	1799	6	9.8
1663	7	10.2	1804	6	5.0
1669	11	6.3	1813	2	8.7
1671	1	1.2	1817	9	4.6
1680	2	9.1	1820	7	2.8
1684	0	3.8	1826	7	6.0
1693	7	9.6	1827	9	1.2
1697	6	3.9	1833	5	5.7
1702	8	5.2	1836	7	3.2
1710	0	7.3	1838	2	1.6
1719	1	9.1	1843	3	5.1
1728	8	9.6	1854	9	11.5
1741	0	12.3	1863	1	8.3
1744	6	3.5	1865	7	2.5
1748	6	4.0	1875	11	10.3

Table A.2: *Crack spacing data in Dallas IH-45 section*

Coordinate of transverse crack		Transverse crack spacing	Coordinate of transverse crack		Transverse crack spacing
[ft.]	[in.]	[ft.]	[ft.]	[in.]	[ft.]
0	0		228	2	9.5
13	9	13.8	231	3	3.1
14	6	0.8	237	9	6.5
22	9	8.3	245	11	8.2
27	9	5.0	250	0	4.1
34	4	6.6	255	6	5.5
42	1	7.8	259	7	4.1
50	2	8.1	262	0	2.4
52	1	1.9	273	1	11.1
54	6	2.4	276	9	3.7
66	0	11.5	281	1	4.3
69	7	3.6	286	1	5.0
71	1	1.5	287	3	1.2
77	3	6.2	295	1	7.8
80	3	3.0	297	4	2.3
92	6	12.3	298	9	1.4
97	9	5.3	305	9	7.0
107	6	9.8	309	4	3.6
117	8	10.2	315	4	6.0
122	8	5.0	322	4	7.0
132	3	9.6	326	3	3.9
143	4	11.1	333	1	6.8
150	1	6.8	336	7	3.5
154	0	3.9	342	0	5.4
162	6	8.5	349	1	7.1
166	6	4.0	355	7	6.5
171	7	5.1	361	1	5.5
175	11	4.3	365	7	4.5
182	6	6.6	371	5	5.8
188	1	5.6	378	1	6.7
193	8	5.6	382	7	4.5
201	9	8.1	384	3	1.7
209	2	7.4	394	4	10.1
218	8	9.5	401	6	7.2

Table A.2 (cont.): *Crack spacing data in Dallas IH-45 section*

Coordinate of transverse crack		Transverse crack spacing	Coordinate of transverse crack		Transverse crack spacing
[ft.]	[in.]	[ft.]	[ft.]	[in.]	[ft.]
404	3	2.8	451	11	10.6
406	9	2.5	456	9	4.8
409	9	3.0	458	9	2.0
417	2	7.4	463	1	4.3
422	1	4.9	466	9	3.7
426	6	4.4	473	9	7.0
429	6	3.0	483	6	9.8
431	1	1.6	493	9	10.3
438	3	7.2	496	11	3.2
441	4	3.1			

Table A.3: *Crack spacing data in Houston BW 8 section (Subsection A)*

Coordinate of transverse crack		Transverse crack spacing	Coordinate of transverse crack		Transverse crack spacing
[ft.]	[in.]	[ft.]	[ft.]	[in.]	[ft.]
11	10		128	5	6.9
16	0	4.2	135	8	7.3
18	2	2.2	149	4	13.7
23	2	5.0	151	0	1.7
30	0	6.8	160	5	9.4
34	7	4.6	161	8	1.3
39	0	4.4	163	10	2.2
40	10	1.8	166	1	2.3
48	7	7.8	169	9	3.7
59	4	10.8	173	2	3.4
66	1	6.8	175	4	2.2
75	3	9.2	180	1	4.8
80	3	5.0	184	11	4.8
84	0	3.8	192	8	7.8
85	8	1.7	198	9	6.1
90	1	4.4	203	9	5.0
91	3	1.2	205	1	1.3
97	11	6.7	215	3	10.2
102	11	5.0	220	5	5.2
109	10	6.9	225	8	5.3
121	6	11.7			

Table A.3 (cont.): *Crack spacing data in Houston BW 8 section (Subsection B)*

Coordinate of transverse crack		Transverse crack spacing	Coordinate of transverse crack		Transverse crack spacing
[ft.]	[in.]	[ft.]	[ft.]	[in.]	[ft.]
233	6	7.8	353	2	4.9
238	0	4.5	359	6	6.3
249	9	11.8	372	5	12.9
259	2	9.4	377	5	5.0
270	2	11.0	382	0	4.6
274	7	4.4	384	11	2.9
281	0	6.4	390	5	5.5
287	0	6.0	403	9	13.3
293	10	6.8	414	0	10.3
301	1	7.3	419	7	5.6
309	3	8.2	421	8	2.1
316	5	7.2	424	10	3.2
318	3	1.8	426	8	1.8
320	5	2.2	435	9	9.1
331	6	11.1	447	7	11.8
336	6	5.0	454	1	6.5
340	9	4.3	458	7	4.5
348	3	7.5			

Table A.3 (cont.): *Crack spacing data in Houston BW 8 section (Subsection C)*

Coordinate of transverse crack		Transverse crack spacing	Coordinate of transverse crack		Transverse crack spacing
[ft.]	[in.]	[ft.]	[ft.]	[in.]	[ft.]
463	6	4.9	575	6	2.2
467	8	4.2	583	7	8.1
476	4	8.7	597	0	13.4
478	0	1.7	610	11	13.9
485	7	7.6	613	5	2.5
498	9	13.2	615	6	2.1
506	9	8.0	632	4	16.8
511	6	4.8	642	5	10.1
521	4	9.8	651	4	8.9
531	8	10.3	661	5	10.1
535	10	4.2	670	4	8.9
543	10	8.0	678	0	7.7
556	8	12.8	680	3	2.3
560	7	3.9	690	0	9.8
573	4	12.8			

Table A.3 (cont.): *Crack spacing data in Houston BW 8 section (Subsection D)*

Coordinate of transverse crack		Transverse crack spacing	Coordinate of transverse crack		Transverse crack spacing
[ft.]	[in.]	[ft.]	[ft.]	[in.]	[ft.]
699	10	9.8	808	7	10.4
706	2	6.3	813	1	4.5
713	11	7.8	817	4	4.3
717	3	3.3	828	8	11.3
724	6	7.3	831	9	3.1
727	10	3.3	839	7	7.8
730	2	2.3	851	5	11.8
737	0	6.8	859	1	7.7
745	4	8.3	867	8	8.6
753	8	8.3	874	1	6.4
758	10	5.2	884	11	10.8
765	9	6.9	888	11	4.0
773	5	7.7	898	1	9.2
781	4	7.9	910	1	12.0
795	10	14.5	917	1	7.0
798	2	2.3			

Table A.3 (cont.): *Crack spacing data in Houston BW 8 section (Subsection E)*

Coordinate of transverse crack		Transverse crack spacing	Coordinate of transverse crack		Transverse crack spacing
[ft.]	[in.]	[ft.]	[ft.]	[in.]	[ft.]
1129	3		1240	8	8.3
1139	6	10.3	1250	3	9.6
1143	5	3.9	1263	7	13.3
1157	4	13.9	1275	4	11.8
1166	9	9.4	1280	1	4.8
1175	4	8.6	1284	4	4.3
1180	7	5.3	1289	2	4.8
1183	2	2.6	1294	8	5.5
1191	6	8.3	1305	7	10.9
1197	2	5.7	1313	0	7.4
1209	6	12.3	1321	3	8.3
1218	10	9.3	1325	6	4.3
1226	11	8.1	1332	3	6.8
1232	4	5.4	1342	9	10.5

Table A.3 (cont.): *Crack spacing data in Houston BW 8 section (Subsection F)*

Coordinate of transverse crack		Transverse crack spacing	Coordinate of transverse crack		Transverse crack spacing
[ft.]	[in.]	[ft.]	[ft.]	[in.]	[ft.]
1350	8	7.9	1475	0	9.9
1360	2	9.5	1479	8	4.7
1371	9	11.6	1482	1	2.4
1372	11	1.2	1494	10	12.8
1381	5	8.5	1505	8	10.8
1392	3	10.8	1515	9	10.1
1396	11	4.7	1522	10	7.1
1401	11	5.0	1533	4	10.5
1414	5	12.5	1542	1	8.8
1430	3	15.8	1554	0	11.9
1431	11	1.7	1563	1	9.1
1446	0	14.1	1570	6	7.4
1459	2	13.2	1579	5	8.9
1465	1	5.9			

Table A.3 (cont.): *Crack spacing data in Houston BW 8 section (Subsection G)*

Coordinate of transverse crack		Transverse crack spacing	Coordinate of transverse crack		Transverse crack spacing
[ft.]	[in.]	[ft.]	[ft.]	[in.]	[ft.]
1585	10	6.4	1709	6	1.3
1594	4	8.5	1720	10	11.3
1597	3	2.9	1724	6	3.7
1608	7	11.3	1728	5	3.9
1610	4	1.8	1736	9	8.3
1613	7	3.3	1743	10	7.1
1621	10	8.3	1745	7	1.8
1624	9	2.9	1752	4	6.8
1627	9	3.0	1760	6	8.2
1637	1	9.3	1762	6	2.0
1642	9	5.7	1769	7	7.1
1651	1	8.3	1772	4	2.8
1653	10	2.8	1773	6	1.2
1661	3	7.4	1781	7	8.1
1670	5	9.2	1785	4	3.8
1681	0	10.6	1792	1	6.8
1686	1	5.1	1796	1	4.0
1694	6	8.4	1800	6	4.4
1702	4	7.8	1806	3	5.8
1708	2	5.8	1808	7	2.3

Table A.3 (cont.): *Crack spacing data in Houston BW 8 section (Subsection H)*

Coordinate of transverse crack		Transverse crack spacing	Coordinate of transverse crack		Transverse crack spacing
[ft.]	[in.]	[ft.]	[ft.]	[in.]	[ft.]
1820	9	12.2	1931	9	7.3
1824	3	3.5	1935	9	4.0
1827	0	2.8	1943	1	7.3
1829	6	2.5	1953	9	10.7
1839	0	9.5	1960	3	6.5
1845	3	6.3	1967	2	6.9
1850	2	4.9	1975	4	8.2
1858	9	8.6	1980	4	5.0
1866	8	7.9	1981	11	1.6
1873	5	6.8	1994	9	12.8
1882	10	9.4	1998	5	3.7
1893	8	10.8	2007	4	8.9
1900	1	6.4	2009	6	2.2
1908	3	8.2	2012	10	3.3
1910	11	2.7	2021	3	8.4
1914	11	4.0	2024	7	3.3
1920	1	5.2	2034	11	10.3
1922	2	2.1	2040	0	5.1
1924	6	2.3			

Table A.4: *Crack spacing data in Houston IH-45 section (Subsection E)*

Coordinate of transverse crack		Transverse crack spacing	Coordinate of transverse crack		Transverse crack spacing
[ft.]	[in.]	[ft.]	[ft.]	[in.]	[ft.]
5	1		109	3	5.4
9	3	4.2	117	4	8.1
13	8	4.4	124	3	6.9
15	8	2.0	127	1	2.8
17	8	2.0	130	1	3.0
26	5	8.8	133	0	2.9
28	4	1.9	135	1	2.1
29	9	1.4	140	3	5.2
31	1	1.3	146	3	6.0
32	4	1.3	149	6	3.3
34	4	2.0	152	2	2.7
36	10	2.5	154	2	2.0
41	5	4.6	156	8	2.5
48	8	7.3	160	6	3.8
51	3	2.6	165	10	5.3
53	4	2.1	168	6	2.7
56	11	3.6	171	4	2.8
60	6	3.6	179	3	7.9
67	4	6.8	182	3	3.0
69	1	1.8	187	11	5.7
71	6	2.4	190	11	3.0
72	11	1.4	196	0	5.1
77	2	4.3	199	3	3.3
80	2	3.0	201	2	1.9
81	9	1.6	205	5	4.3
86	3	4.5	215	2	9.8
88	7	2.3	219	6	4.3
93	11	5.3	221	10	2.3
96	9	2.8	224	3	2.4
99	7	2.8	228	7	4.3
103	10	4.3	230	0	1.4

Table A.4 (cont.): *Crack spacing data in Houston IH-45 section (Subsection F)*

Coordinate of transverse crack		Transverse crack spacing	Coordinate of transverse crack		Transverse crack spacing
[ft.]	[in.]	[ft.]	[ft.]	[in.]	[ft.]
231	7	1.6	365	6	7.7
232	9	1.2	378	8	13.2
234	4	1.6	391	7	12.9
238	10	4.5	393	6	1.9
247	0	8.2	397	7	4.1
249	10	2.8	398	6	0.9
255	2	5.3	403	11	5.4
257	11	2.8	410	2	6.3
261	4	3.4	413	2	3.0
264	11	3.6	421	1	7.9
269	0	4.1	424	1	3.0
270	11	1.9	424	10	0.8
275	9	4.8	426	2	1.3
280	7	4.8	427	1	0.9
289	2	8.6	430	3	3.2
296	6	7.3	432	6	2.3
309	7	13.1	434	10	2.3
318	8	9.1	437	11	3.1
325	8	7.0	443	4	5.4
332	10	7.2	445	10	2.5
346	8	13.8	452	3	6.4
349	5	2.8	455	7	3.3
357	10	8.4			

Table A.4 (cont.): *Crack spacing data in Houston IH-45 section (Subsection G)*

Coordinate of transverse crack		Transverse crack spacing	Coordinate of transverse crack		Transverse crack spacing
[ft.]	[in.]	[ft.]	[ft.]	[in.]	[ft.]
464	8	9.1	572	11	3.7
470	1	5.4	579	4	6.4
472	3	2.2	580	5	1.1
475	4	3.1	585	10	5.4
477	2	1.8	587	4	1.5
478	4	1.2	590	7	3.3
484	2	5.8	594	1	3.5
489	8	5.5	595	4	1.3
490	3	0.6	601	0	5.7
495	2	4.9	602	7	1.6
500	7	5.4	605	1	2.5
503	5	2.8	609	11	4.8
506	7	3.2	613	7	3.7
511	3	4.7	617	4	3.8
512	11	1.7	622	1	4.8
516	11	4.0	635	11	13.8
519	6	2.6	637	9	1.8
525	11	6.4	641	11	4.2
531	4	5.4	651	3	9.3
538	11	7.6	655	4	4.1
541	6	2.6	656	11	1.6
547	5	5.9	659	4	2.4
553	1	5.7	660	5	1.1
555	10	2.8	664	11	4.5
558	3	2.4	669	3	4.3
561	0	2.8	672	7	3.3
567	3	6.3	677	5	4.8
568	1	0.8	680	0	2.6
569	3	1.2	683	2	3.2

Table A.4 (cont.): *Crack spacing data in Houston IH-45 section (Subsection H)*

Coordinate of transverse crack		Transverse crack spacing	Coordinate of transverse crack		Transverse crack spacing
[ft.]	[in.]	[ft.]	[ft.]	[in.]	[ft.]
693	10	10.7	796	3	2.8
695	4	1.5	798	9	2.5
696	4	1.0	804	1	5.3
699	4	3.0	807	0	2.9
700	4	1.0	810	2	3.2
706	11	6.6	813	6	3.3
710	7	3.7	816	0	2.5
714	6	3.9	818	7	2.6
723	3	8.8	820	9	2.2
728	5	5.2	823	10	3.1
731	5	3.0	827	2	3.3
735	3	3.8	830	2	3.0
737	1	1.8	838	5	8.3
740	2	3.1	841	4	2.9
747	4	7.2	843	7	2.3
753	5	6.1	846	7	3.0
754	5	1.0	848	1	1.5
755	10	1.4	852	3	4.2
757	0	1.2	857	10	5.6
759	10	2.8	872	0	14.2
761	2	1.3	875	4	3.3
765	3	4.1	878	1	2.8
768	8	3.4	883	6	5.4
773	11	5.3	889	2	5.7
776	6	2.6	892	1	2.9
779	3	2.8	897	10	5.8
785	0	5.8	905	11	8.1
788	7	3.6	908	7	2.7
793	5	4.8	914	1	5.5

Table A.4 (cont.): *Crack spacing data in Houston IH-45 section (Subsection A)*

Coordinate of transverse crack		Transverse crack spacing	Coordinate of transverse crack		Transverse crack spacing
[ft.]	[in.]	[ft.]	[ft.]	[in.]	[ft.]
1132	9		1250	3	9.8
1139	8	6.9	1252*	8	2.4
1143	8	4.0	1255	5	2.8
1151*	0	7.3	1258*	2	2.8
1160*	0	9.0	1268*	5	10.3
1162	7	2.6	1273*	7	5.2
1164	11	2.3	1282	6	8.9
1168*	1	3.2	1287*	6	5.0
1169	9	1.7	1289	11	2.4
1173	10	4.1	1295*	10	5.9
1176	6	2.7	1298	6	2.7
1184	10	8.3	1304	10	6.3
1190	1	5.3	1306*	6	1.7
1196*	2	6.1	1308*	4	1.8
1201	1	4.9	1310*	8	2.3
1206	9	5.7	1319	6	8.8
1209	9	3.0	1320	5	0.9
1215*	0	5.3	1327	6	7.1
1218	0	3.0	1330	4	2.8
1225	5	7.4	1332	9	2.4
1226	2	0.8	1334	9	2.0
1227	10	1.7	1336	4	1.6
1229	1	1.3	1339	1	2.8
1233	10	4.8	1341	2	2.1
1237	4	3.5	1344	3	3.1
1240	6	3.2	1351	10	7.6

*Spalling repaired transverse cracks

Table A.4 (cont.): *Crack spacing data in Houston IH-45 section (Subsection B)*

Coordinate of transverse crack		Transverse crack spacing	Coordinate of transverse crack		Transverse crack spacing
[ft.]	[in.]	[ft.]	[ft.]	[in.]	[ft.]
1363	6	11.7	1461	1	9.0
1364	0	0.5	1462	4	1.3
1367[*]	4	3.3	1464	1	1.8
1369	8	2.3	1466	8	2.6
1372	5	2.8	1471	10	5.2
1374	11	2.5	1477	8	5.8
1375	6	0.6	1478	4	0.7
1378	1	2.6	1480	11	2.6
1381	10	3.8	1484	3	3.3
1384	0	2.2	1486	7	2.3
1388	10	4.8	1496	2	9.6
1395[*]	1	6.3	1501	0	4.8
1397[*]	1	2.0	1507	3	6.3
1400[*]	6	3.4	1511	6	4.3
1402[*]	5	1.9	1515	7	4.1
1405	6	3.1	1518	6	2.9
1407	10	2.3	1520	7	2.1
1409	1	1.3	1523[*]	11	3.3
1410	11	1.8	1526	5	2.5
1413	9	2.8	1528	11	2.5
1420	4	6.6	1531	4	2.4
1424	4	4.0	1534	2	2.8
1430[*]	1	5.8	1540[*]	7	6.4
1434	4	4.3	1547	0	6.4
1437[*]	0	2.7	1549[*]	4	2.3
1438	0	1.0	1555	4	6.0
1439	5	1.4	1558	0	2.7
1447	5	8.0	1560[*]	6	2.5
1452	1	4.7	1565	0	4.5

[*] Spalling repaired transverse cracks

Table A.4 (cont.): *Crack spacing data in Houston IH-45 section (Subsection C)*

Coordinate of transverse crack		Transverse crack spacing	Coordinate of transverse crack		Transverse crack spacing
[ft.]	[in.]	[ft.]	[ft.]	[in.]	[ft.]
1567	9	2.8	1683*	5	8.6
1572	4	4.6	1687*	5	4.0
1577	4	5.0	1690	0	2.6
1582	1	4.8	1693	1	3.1
1585*	2	3.1	1697*	9	4.7
1587	10	2.7	1708	4	10.6
1590	7	2.8	1709*	6	1.2
1593	7	3.0	1715	11	6.4
1601*	11	8.3	1717*	5	1.5
1607	8	5.8	1721	6	4.1
1610	8	3.0	1726	0	4.5
1613*	3	2.6	1728	8	2.7
1618	10	5.6	1734	7	5.9
1622*	6	3.7	1737	3	2.7
1629	7	7.1	1739	11	2.7
1636*	8	7.1	1743	1	3.2
1639*	2	2.5	1746	3	3.2
1650	2	11.0	1748	11	2.7
1655*	5	5.3	1754	2	5.3
1658*	2	2.8	1762*	3	8.1
1661	0	2.8	1771*	1	8.8
1663	2	2.2	1774*	10	3.8
1668*	10	5.7	1782	0	7.2
1674	10	6.0			

*Spalling repaired transverse cracks

Table A.4 (cont.): *Crack spacing data in Houston IH-45 section (Subsection D)*

Coordinate of transverse crack		Transverse crack spacing	Coordinate of transverse crack		Transverse crack spacing
[ft.]	[in.]	[ft.]	[ft.]	[in.]	[ft.]
1786	7	4.6	1890	0	2.3
1789	2	2.6	1897*	3	7.3
1792	1	2.9	1904	1	6.8
1794	2	2.1	1906	4	2.3
1798	1	3.9	1911*	8	5.3
1807*	8	9.6	1920	8	9.0
1816	2	8.5	1927	1	6.4
1817*	7	1.4	1932	2	5.1
1820	1	2.5	1933	2	1.0
1821*	2	1.1	1934	11	1.8
1827	10	6.7	1940	2	5.3
1832*	2	4.3	1943*	6	3.3
1838	5	6.3	1946*	0	2.5
1842	5	4.0	1949	5	3.4
1846	7	4.2	1955	3	5.8
1849	2	2.6	1960	5	5.2
1851	10	2.7	1961	5	1.0
1854	7	2.8	1962	11	1.5
1857*	6	2.9	1966	2	3.3
1860	1	2.6	1968	3	2.1
1862	9	2.7	1973	10	5.6
1868	4	5.6	1979*	7	5.8
1869	4	1.0	1984	11	5.3
1873	7	4.3	1991	1	6.2
1878	11	5.3	1996	10	5.8
1885*	1	6.2	2000	7	3.8
1887*	8	2.6	2004	0	3.4

*Spalling repaired transverse cracks

Table A.5: *Crack spacing data in Baytown SPUR 330 section*

Coordinate of transverse crack		Transverse crack spacing	Coordinate of transverse crack		Transverse crack spacing
[ft.]	[in.]	[ft.]	[ft.]	[in.]	[ft.]
8	11		319	6	4.2
18	6	9.6	329	6	10.0
26	6	8.0	341	3	11.8
28	5	1.9	343	3	2.0
43	5	15.0	345	8	2.4
50	1	6.7	350	9	5.1
66	6	16.4	362	6	11.8
72	11	6.4	369	9	7.3
85	6	12.6	382	7	12.8
89	11	4.4	396	2	13.6
95	6	5.6	402	10	6.7
106	3	10.8	412	3	9.4
118	3	12.0	415	2	2.9
122	9	4.5	425	5	10.3
126	11	4.2	437	2	11.8
142	0	15.1	449	4	12.2
155	9	13.8	467	5	18.1
167	11	12.2	470	6	3.1
172	3	4.3	478	6	8.0
180	3	8.0	490	0	11.5
188	9	8.5	505	5	15.4
196	6	7.8	514	0	8.6
202	9	6.3	532	7	18.6
216	3	13.5	541	1	8.5
222	8	6.4	557	5	16.3
237	2	14.5	574	5	17.0
241	7	4.4	586	9	12.3
246	8	5.1	602	1	15.3
257	6	10.8	613	3	11.2
269	9	12.3	616	11	3.7
276	5	6.7	632	1	15.2
284	2	7.8	642	5	10.3
297	8	13.5	658	5	16.0
315	4	17.7	660	2	1.8

Table A.6: *Crack spacing data in Cleveland US 59 section*

Coordinate of transverse crack		Transverse crack spacing	Coordinate of transverse crack		Transverse crack spacing
[ft.]	[in.]	[ft.]	[ft.]	[in.]	[ft.]
4	5		216	11	4.4
10	9	6.3	220	1	3.2
13	5	2.7	227	11	7.8
24	9	11.3	237	4	9.4
28	11	4.2	242	1	4.8
32	1	3.2	251	0	8.9
35	6	3.4	258	11	7.9
40	11	5.4	261	8	2.8
44	5	3.5	274	6	12.8
46	8	2.3	286	6	12.0
51	5	4.8	289	1	2.6
70	0	18.6	296	2	7.1
77	5	7.4	300	6	4.3
84	5	7.0	308	0	7.5
90	7	6.2	310	3	2.3
92	5	1.8	317	3	7.0
100	9	8.3	324	9	7.5
104	8	3.9	331	8	6.9
112	7	7.9	339	7	7.9
118	4	5.8	341	0	1.4
123	1	4.8	347	5	6.4
132	11	9.8	351	4	3.9
141	5	8.5	352	5	1.1
149	5	8.0	356	1	3.7
159	10	10.4	358	11	2.8
163	2	3.3	369	7	10.7
165	11	2.8	375	10	6.3
168	11	3.0	382	3	6.4
174	7	5.7	390	10	8.6
183	5	8.8	400	0	9.2
192	0	8.6	407	6	7.5
200	0	8.0	414	1	6.6
208	4	8.3	423	0	8.9
212	6	4.2	427	5	4.4

Table A.6 (cont.): *Crack spacing data in Cleveland US 59 section*

Coordinate of transverse crack		Transverse crack spacing	Coordinate of transverse crack		Transverse crack spacing
[ft.]	[in.]	[ft.]	[ft.]	[in.]	[ft.]
430	8	3.3	473	4	7.5
438	6	7.8	483	10	10.5
446	3	7.8	490	1	6.3
449	4	3.1	493	4	3.3
457	3	7.9	498	2	4.8
463	9	6.5	504	8	6.5
465	10	2.1			

Table A.7: *Crack spacing data in Van Horn IH-10 section*

Coordinate of transverse crack		Transverse crack spacing	Coordinate of transverse crack		Transverse crack spacing
[ft.]	[in.]	[ft.]	[ft.]	[in.]	[ft.]
1	6		266	11	2.3
6	0	4.5	274	1	7.2
19	3	13.3	276	7	2.5
20	3	1.0	283	9	7.2
31	8	11.4	285	10	2.1
42	10	11.2	293	8	7.8
53	2	10.3	301	5	7.8
54	10	1.7	311	1	9.7
61	10	7.0	315	6	4.4
71	5	9.6	316	9	1.3
79	5	8.0	318	6	1.8
92	0	12.6	330	7	12.1
100	10	8.8	339	9	9.2
104	7	3.8	354	1	14.3
112	8	8.1	359	0	4.9
120	10	8.2	362	9	3.8
129	0	8.2	372	9	10.0
137	7	8.6	380	10	8.1
143	1	5.5	392	5	11.6
150	1	7.0	400	4	7.9
155	6	5.4	409	8	9.3
157	6	2.0	417	8	8.0
167	5	9.9	423	8	6.0
178	4	10.9	437	10	14.2
189	0	10.7	442	4	4.5
193	6	4.5	444	2	1.8
200	4	6.8	447	10	3.7
205	8	5.3	451	9	3.9
216	7	10.9	458	0	6.3
218	5	1.8	466	8	8.7
230	3	11.8	478	7	11.9
243	0	12.8	485	2	6.6
251	8	8.7	493	7	8.4
257	1	5.4	502	1	8.5
264	8	7.6			

Bibliography

AASHTO PP 34-99, "Standard Practice for Estimating Cracking Tendency of Concrete," American Association of State Highway Transportation Officials, 2006.

ACI Committee 209, "Prediction of Creep, Shrinkage, and Temperature Effects in Concrete Structures (ACI 209R-92)," American Concrete Institute, Detroit, 1992.

ACI Committee 318, "Building Code and Commentary (ACI 318-08)," American Concrete Institute, Detroit, 2008.

ACI Committee 318, "Building Code Requirements for Reinforced Concrete, Americal Concrete Institute, Detroit, 1983.

Ali, W., "Finite Element Temperature Development and Moisture Diffusion Prediction Models for Concrete at Early Ages Using MATLAB," Master Thesis, Texas Tech University, 2010.

Amin, M. N., Kim, J. S., Lee, Y., and Kim, J. K., "Simulation of the Thermal Stress in Mass Concrete using a Thermal Stress Measuring Device," Cement and Concrete Research, Vol. 39, No. 3, 2009, pp. 154-164.

ARA, Inc., ERES Consultants Division, "Guide for Mechanistic-Empirical Design of New and Rehabilitated Pavement Structures," Final Report, NCHRP Project 1-37A. Transportation Research Board of the National Academies, Washington, D.C., 2004.

ASTM, "Standard Test Method for Time of Setting of Concrete Mixtures by Penetration Resistance," American Society for Testing and Materials, Philadelphia, 2008.

Bažant, Z. P. and Cedolin, L., "Stability of Structures: Elastic, Inelastic, Fracture, and Damage Theories," Oxford University Press, New York, 1991.

Bažant, Z. P. and Chern, J. C., "Triple Power Law for Concrete Creep," Journal of Engineering Materials, Vol. 3, No. 4, 1985, pp. 63-83.

Bažant, Z. P. and Najjar, L. J., "Nonlinear Water Diffusion in Non-Saturated Concrete," Materials and Structures, Vol. 5, No. 25, 1972, pp. 3-20.

Bažant, Z. P. and Panula, L., "Practical Predictions of Time Dependent Deformations of Concrete," Materials and Structures, Vol. 11, 1978.

Bažant, Z. P., "Delayed Thermal Dilations of Cement Paste and Concrete due to Mass Transport," Nuclear Engineering and Design,Vol. 14, 1970, pp. 308-318.

Bažant, Z. P., "Mathematical Modeling of Creep and Shrinkage of Concrete," John Wiley and Sons, Chichester and New York, 1988.

Bažant, Z. P., "Numerical Determination of Long-Range Stress History from Strain History in Concrete," Material and Structures, Vol. 5, No. 3, 1972a, pp. 135-141.

Bažant, Z. P., "Prediction of Concrete Creep Effects Using Age-Adjusted Effective Modulus Method," American Concrete Institute, Vol. 69, 1972b, pp. 212-217.

Bažant, Z. P., and Wittmann, F. H., "Creep and Shrinkage in Concrete Structures," John Wiley & Sons, Chichester, 1982.

Beckemeyer, C. A., Khazanovich, L., and Yu, H. T., "Determining Amount of Built-in Curling in Jointed Plain Concrete Pavement: Case Study of Pennsylvania I-80," Journal of Transportation Research Board, No, 1809, 2002, pp. 85-92.

Bernander, S. "Practical Measures to Avoiding Early Age Thermal Cracking in Concrete Structures," Prevention of Thermal Cracking in Concrete at Early Ages (Ed.: Springenschmid, R.), RILEM Report 15, E & FN Spon, London, 1998.

Beyer, F. R., "Stresses in Reinforced Concrete Due to Volume Changes," Journal of the ACI, Vol. 20, No. 10, 1949, pp. 713-722.

Bjøntegaard, Ø. and Sellevold, E. J., "Interaction Between Thermal Dilation and Autogenous Deformation in High Performance Concrete," Materials and Structures, Vol. 34, No. 239, 2001, pp. 266-272.

Breitenbücher, R., "Investigation of Thermal Cracking with the Cracking-Frame," Materials and Structures, Vol.23, 1990, pp. 172-177.

Cengel, Y. A., "Heat Transfer: A Practical Approach," 2nd Edition, McGraw Hill, Boston, 2002.

Chapman, A. J., "Fundamentals of Heat Transfer," Macmillan Inc., New York, 1987.

Choi, S. and Won, M., "Design of Tie Bars in Portland Cement Concrete Pavement Considering Nonlinear Temperature Variations," Journal of the Transportation Research Board, No. 2095, 2009, pp. 24-33.

Choi, S. and Won, M., "Thermal Strain and Drying shrinkage of Concrete Structures in the Field," ACI Materials Journal, Vol. 107, No. 5, 2010, pp. 498-507.

Choi, S. and Won, M., "Time-Dependent Behavior of Posttensioned Concrete Pavements under Environmental Loading," Journal of Transportation Research Board, No. 2154, 2010, pp. 44-56.

Choi, S., Ha, S., and Won, M., "Horizontal Cracking of Continuously Reinforced Concrete Pavement under Environmental Loading," Construction and Building Materials, Vol. 25, No. 11, 2011, pp. 4250-4262.

Choktaweekarn, P. and Tangtermsirikul, S., "A Model for Prediction the Coefficient of Thermal Expansion of Cementitious Paste," ScienceAsia, Vol. 35, 2009, pp. 57-63.

Comité Euro-International du Béton-Fédération International de la Précontrainte (CEB-FIP), “CEB-FIP Model Code 1990,” Design Code, Thomas Telford, 1993.

Cusson, D. and Hoogeveen, T. J., “Measuring Early-age Coefficient of Thermal Expansion in High-Performance Concrete,” International RILEM Conference on Volume Changes of Hardening Concrete: Testing and Mitigation, Lyngby, Denmark, 2006.

De Schutter, G., “Finite Element Simulation of Thermal Cracking in Massive Hardening Concrete Elements using Degree of Hydration based Material Laws,” Computers and Structures, Vol. 80, No. 27-30, 2002, pp. 2035-2042.

Emborg, M., “Thermal Stress in Concrete Structures at Early Ages,” Ph.D. Dissertation, Luleå University of Technology, Sweden, 1989.

Ghali, A., Favre, R., and Elbadry, M., “Concrete Structures: Stresses and Deformations,” 3rd Edition, E&FN Spon, London, 2002.

Glisic, B. and Simon, N., “Monitoring of Concrete at Very Early Age using Stiff SOFO Sensor,” Cement and Concrete Composites, Vol. 22, No. 2, 2000, pp. 115-119.

Grasley, Z. C. and Lange, D. A., “A New System for Measuring the Internal Relative Humidity in Concrete.” Cementing the Future, 2004.

Grasley, Z. C. and Lange, D. A., “Modeling Drying Shrinkage Stress Gradent in Concrete,” Cement, Concrete, and Aggregate, V. 26, No.2, 2004, pp. 115-122

Grasley, Z. C. and Lange, D. A., “Thermal Dilation and Internal Relative Humidity of Hardened Cement Paste,” Materials and Structures, Vol. 40, No. 3, 2007, pp. 311-317.

Helmuth, R. A., “Dimensional Changes of Hardened Portland Cement Pastes caused by Temperature Changes,” Proceedings of Highway Research Board, Vol. 40, 1961, pp. 315-336.

Huang, Y. H., “Pavement Analysis and Design,” 2nd Edition, Pearson Education, Inc., New Jersey, 2004.

Kada, H., Lachemi, M., Petrov, N., Bonneau, O., and Aïtcin, P. C., “Determination of the Coefficient of Thermal Expansion of High-Performance Concrete from Initial Setting,” Materials and Structures, Vol. 35, No. 245, 2002, pp. 35-41.

Kim, D. H. and Won, M., “Pilot Implementation of Optimized Aggregate Gradation for Concrete Paving,” Research Report No. 5-9026-01, Center for Transportation Research The University of Texas at Austin, 2007.

Kim, S. M. and Won, M., “Horizontal Cracking in Continuously Reinforced Concrete Pavements,” ACI Structural Journal, Vol. 101, No. 6, 2004, pp. 784-791.

Kohler, E. R., “Experimental Mechanics of Crack Width in Full-Scale Sections of Continuously Reinforced Concrete Pavements,” Ph.D. Dissertation, University of Illinois at Urbana-Champaign, 2005.

Kosmatka, S. H., Kerkhoff, B., and Panarese, W. C., “Design and Control of Concrete Mixtures,” 15th Edition, Portland Cement Association, 2002.

Lienhard J. H., IV and Lienhard J. H., V, “A Heat Transfer Textbook,” 3rd Edition, Phlogiston Press, 2003.

Loser, R., Münch, B., and Lura, P., “A Volumetric Technique for Measuring the Coefficient of Thermal Expansion of Hardening Cement Paste and Mortar,” Cement and Concrete Research, Vol. 40, No. 7, 2010, pp. 1138-1147.

Mackenzie, J. K., “The Elastic Constants of a Solid Containing Spherical Holes,” Proceeding of the Physical Society B, Vol. 63, 1949, pp. 2-11.

Mangold, M., “Determining Thermal Stresses and Crack Sensitivity in the Laboratory,” Prevention of Thermal Cracking in Concrete at Early Ages (Ed.: Springenschmid, R.), RILEM Report 15, E & FN Spon, London, 1998.

Maruyama, I., and Teramoto, A., “Impact of Time-Dependent Thermal Expansion Coefficient on the Early-Age Volume Changes in Cement Pastes,” Cement and Concrete Research, Vol. 41, No. 4, 2011, pp. 380-391.

Mehta, P. K. and Monteiro P. J. M., “Concrete: Microstructure, Properties, and Materials,” 3rd Edition, McGraw-Hill, New York, 2006.

Meyers, S. L., “Thermal Expansion Characteristics of Hardened Cement Paste and Concrete.,” Proceedings of Highway Research Board 30, 1950, pp. 193-203.

Mindess, S., Young, J. F., and Darwin, D., “Concrete,” 2nd Edition, Pearson Education, Inc., Upper Saddle River, 2006.

Nam, J. H, Kim, D. H., Choi, S., and Won, M., “Variation of Crack Width over Time in Continuously Reinforced Concrete Pavement,” Journal of Transportation Research Board, No. 2037, 2007, pp. 3-11.

Nam, J. H., “Early-Age Behavior of CRCP and Its Implications for Long-Term Performance,” Ph.D. Dissertation, The University of Texas at Austin, 2005.

Nam, J. H., Kim, S. M., and Won, M. C., “Measurement and Analysis of Early-Age Concrete Strains and Stresses: Continuously Reinforced Concrete Pavement under Environmental Loading,” Journal of Transportation Research Board, No. 1947, 2006, pp. 79-90.

Neville A. M., “Properties of Concrete,” 4th Edition, Longman, Harlow, 1995.

Popovics, S. and Ujhelyi, J., “Contribution to the Concrete Strength versus Water-Cement Ratio Relationship,” ASCE Journal of Materials in Civil Engineering, Vol. 20, No. 7, 2008, pp. 459-463.

Rao, S. and Roesler, J. R., “Characterizing Effective Built-In Curling from Concrete Pavement Field Measurements,” ASCE Journal of Transportation Engineering, Vol. 131, No. 4, 2005, pp. 320-327.

Richardson, J., Eskildsen, S., Schiller, B., and Jones, M. “Measured Strains in Post-Tensioned Concrete Parking Deck made with Shrinkage-Compensating Concrete,” ACI Structural Journal, Vol. 107, No.6, 2010, pp. 718-725.

Rostácy, F. S., Tanabe, T., and Laube, M., “Assessment of External Restraint,” Thermal Cracking in Concrete at Early Ages (Ed.: Springenschmid, R.), Proceedings of the International RILEM Symposium, E & FN Spon, London, 1995.

Sabri, S. and Illston, J. M., Immediate and Delayed Thermal Expansion of Hardened Cement Paste,” Cement and Concrete Research, Vol. 12, No. 2, 1982, pp. 199-208.

Sant, G.., Lura, P., and Weiss, J., “Measurement of Volume Change in Cementitious Materials at Early Ages: Review of Testing Protocols and Interpretation of Resuslts,”, Journal of Transportation Research Board, No.1979, 2006, pp. 21-29.

Sargand, S., Swanlund, M., Wise, J., and Edwards, W., “Evaluation of Slab Shape under Controlled Environmental Conditions,” ACI Structural Journal, Vol. 102, No. 4, 2005, pp. 588-595.

Scherer, G.. W., “Thermal Expansion Kinetics: Method to Measure Permeability of Cementitious Materials: I, Theory.” Journal of American Ceramic Society, Vol. 83, No. 11, 2000, pp. 2753-2761.

Schinder, A. K., Dossey, T., and McCullough, B. F., “Temperature Control During Construction to Improve the Long Term Performance of Portland Cement Concrete Pavements,” Research Report No. 0-1700-2, Center for Transportation Research The University of Texas at Austin, 2002.

Schindler, A. K., “Concrete Hydration, Temperature Development, and Setting at Early-Ages,” Ph.D. Dissertation, The University of Texas at Austin, 2002.

Sellevold, E. J. and Bjøntegaard, Ø ., “Coefficient of Thermal Expansion of Cement Paste and Concrete: Mechanisms of Moisture Interaction,” Materials and Structures, Vol. 39, No. 9, 2006, pp. 809-815.

Sheibany, F., and Ghaemian, M., “Effects of Environmental Action on Thermal Stress Analysis of Karaj Concrete Arch Dam,” ASCE Journal of Engineering Mechanics, Vol. 132, No. 5, 2006, pp. 532-544.

Springenschmid, R. (Ed.), “Prevention of Thermal Cracking in Concrete at Early Ages,” RILEM Report 15, E & FN Spon, London, 1998.

Springenschmid, R. (Ed.), “Thermal Cracking in Concrete at Early Ages,” Proceedings of the International RILEM Symposium, E & FN Spon, London, 1995.

Springenschmid, R. and Breitenbücher, R., “Influence of Constituents, Mix Proportions and Temperagure on Cracking Sensitivity of Concrete,” Prevention of Thermal Cracking in Concrete at Early Ages (Ed.: Springenschmid, R.), RILEM Report 15, E & FN Spon, London, 1998.

Suh, Y. C., Hankins, K., and McCullough, B. F., “Early-Age Behavior of Continuously Reinforced Concrete Pavement and Calibration of the Failure Prediction Model in the CRCP-7 Program,” Research Report No. 1244-3, Center for Transportation Research The University of Texas at Austin, 1992.

Tazawa, E. (Ed.), “Autogenous Shrinkage of Concrete,” Proceeding of the International Workshop Organized by JCI, E & FN Spon, London, 1999.

Texas Department of Transportation, “Standard Specifications for Construction and Maintenance of Highways, Streets, and Bridges,” Texas Department of Transportation, 2004.

TNO Building Construction, “DIANA 8.1.2 User’s Manual,” Delft, The Netherlands, 2003.

Wang, C. and Dilger, W. H., “Prediction of Temperature Distribution in Hardening Concrete,” Thermal Cracking in Concrete at Early Ages (Ed.: Springenschmid, R.), Proceedings of the International RILEM Symposium, E & FN Spon, London, 1995.

Westergaard, H. M., “Analysis of Stress in Concrete Roads Caused by Variations of Temperature,” Public Roads, Vol. 8, No. 3, 1927, pp. 54-60.

Wittmann F. and Lukas, J., “Experimental Study of Thermal Expansion of Hardened Cement Paste,” Materials and Structures, Vol. 7, No. 40, 1974, pp. 247-252.

Won, M., “Evaluation of MEPDG with TxDOT Rigid Pavement Database,” Research Report 5445-3, Center for Transportation Research, The University of Texas at Austin, 2009.

Won, M., “Improvement of Testing Procedures for Concrete Coefficient of Thermal Expansion,” Journal of Transportation Research Board, No. 1919, 2005, pp. 23-28.

Won, M., Cho, B. H., Ha, S., Yeon, J. H., Jung, Y., and Zollinger, D. G., “Develop Mechanistic/Empirical Design for CRCP,” Research Report No. 0-5832, Center for Transportation Research, The University of Texas at Austin, 2011.

Wu, W. Y. and McCullough, B. F., Terminal Movement in Continuously Reinforced Concrete Pavements,” Research Report 1169-4, Center for Transportation Research, The University of Texas at Austin, 1992.

Yan, P. Y., Chen, J. C., Wang, J. C., and Zheng, F., "Autogenous Shrinkage of Concrete Prepared with the Binders Containing Different Kinds of Mineral Admixture," Proceedings of the 12th International Conference of Cement Chemistry, Montreal, Canada, 2007.

Yang, S., Kim, N., Kim, J., and Park, J., "Experimental Measurement of Concrete Thermal Expansion," Journal of the Eastern Asia Society for Transportation Studies, Vol. 5, 2003, pp. 1035-1048.

Yeon, J. H., Choi, S., and Won, M. C., "Effect of Relative Humidity on Coefficient of Thermal Expansion of Hardened Cement Paste and Concrete," Journal of Transportation Research Board, No. 2113, 2009, pp. 83-91.

Yu, H. T., Khazanovich, L., Darter, M. I., and Ardani, A., "Analysis of Concrete Pavement Responses to Temperature and Wheel Loads Measured from Instrumented Slab," Journal of the Transportation Research Board, No. 1639, 1998, pp. 94-101.

Yuan, Y. and Wan, Z. L., "Prediction of Cracking within Early-Age Concrete due to Thermal, Drying and Creep Behavior," Cement and Concrete Research, Vol. 32, No. 7, pp .1053-1059.

Zollinger, D. G., Personal Correspondence, 2011.

Vita

Jung Heum Yeon was born in Chuncheon, Korea on December 5, 1983 as the son of Kyu-Seok Yeon and Byoung-Ok Kang. After completing his work at Chuncheon High School, Chuncheon, Korea, he studied at the School of Civil and Environmental Engineering at Yonsei University, Seoul, Korea. He received the degree of Bachelor of Science from Yonsei University in February, 2006. He then entered a graduate school at the Department of Civil, Architectural, and Environmental Engineering at The University of Texas at Austin, where he worked as a graduate research assistant for Drs. David W. Fowler and Moon C. Won at the Center for Transportation Research. He earned the degree of Master's of Science in Engineering from The University of Texas at Austin in August, 2008 with a thesis entitled "Effect of Internal Relative Humidity on Coefficient of Thermal Expansion of Hardened Concrete and Cement Paste".

Permanent address: 102-1501 Daewoo Apt., Seoksa-dong, Chuncheon, Gangwon-do, 200-936, Republic of Korea.

This dissertation was typed by the author.